UNIVERSITY OF CALIFORNIA,
IRVINE

Enhancing Coupling of Electromagnetic Waves with Artificial Materials

DISSERTATION

submitted in partial satisfaction of the requirements
for the degree of

DOCTOR OF PHILOSOPHY

in Electrical and Computer Engineering

by

Caner Guclu

Dissertation Committee:
Associate Professor Filippo Capolino, Chair
Professor H. Kumar Wickramasinghe
Associate Professor Ozdal Boyraz

2016

"A taste for truth at any cost is a passion which spares nothing"

Albert Camus

TABLE OF CONTENTS

LIST OF FIGURES

LIST OF TABLES

Page

ACKNOWLEDGMENTS

My time spent at UC Irvine was not only a PhD program to fulfill certain requirements to earn a degree. It was a long journey through which I had to learn a lot about my field of study, the academia, and also the life itself. I established myself in a new country and started a new life from scratch. No human being, I believe, is capable of achieving these without any support. Therefore, I feel obliged to acknowledge the people whose support helped me successfully complete this journey.

I express my deepest gratitude to my advisor Prof. Filippo Capolino. I appreciate his high standards in research and in the quality of work we produced. I always felt his support to pursue research independently and rely on my skills.

I would like to thank the doctoral committee members, Prof. Ozdal Boyraz and Prof. Kumar Wickramasinghe who also provided guidance and support in our collaborations constantly. I would like to thank Prof. Regina Ragan for her guidance on practical aspects of our research and ensuring realizability of our designs. I am grateful to Dr. Willie Luk for the great chance he has given me as a visiting researcher at Sandia National Laboratories, his dedication in overcoming obstacles by learning ever more taught me a lot.

The most special people in my doctoral adventure were my labmates and friends. I thank Dr. Salvatore Campione, Dr. Ali Hosseini and his wife Dr. Yasmin Ghochani, Mehdi Veysi, and Dr. Shiji Pan for being my family. Our research group and the graduate students in EECS department were always like an ever growing close-knit community, I thank them all, in particular to Davit Hovhannisyan, Dmitry Oshmarin, Farshad Yazdi, Saman Kabiri, and Evangelos Kornaros. I am grateful to the friendship of Frederik Guyon and his family. I present special thanks to Mohamad Othman and Hassan Sedighy whose collaborations also contributed to this dissertation.

The former and current staff at the department always kept an eye on the graduate students' wellbeing and helped us in most urgent conditions. Therefore, I am grateful to the best staff ever, especially to Susan Staebell, Loretta Waltemeyer, Patricia Collette, Elvia Salas, and Amy Pham.

I am grateful to the friendship of Cemil Can Coskun, Kumru Arslan, Fulya Ozcan, Duygu Akdevelioglu, Dr. Tolga Oztan, Ecehan Uludag, Dr. Kemal Davaslioglu, Dr. Thania Muñoz, and Deanna Kashani. I am thankful to all of them for being my family in Irvine.

My girlfriend Ayça Çavcı was the essential source of love and encouragement whenever I needed, I am grateful to her for being my best friend and my inspiration. I owe a debt of gratitude to my friend Emre Tatlı for always being there when I need someone to talk to.

Finally, I am deeply grateful to my mother Ayhan Güçlü, my father Bülent Hilmi Güçlü, and my brother Tansel Güçlü whose belief in me and endless love gave me the strength to pursue my goals.

My graduate studies were partially supported by the National Science Foundation and Sandia National Laboratories. I also thank the publishers APS, OSA, IEEE, AIP and ACS for granting the permissions to include material in this dissertation from our peer-reviewed journal articles published by them.

CURRICULUM VITAE

Caner Guclu

2016 Ph.D in Electrical and Computer Engineering, University of California, Irvine

2010 M.S. in Electrical and Electronics Engineering, Middle East Technical University, Ankara, Turkey

2008 B.S in Electrical and Electronics Engineering, Middle East Technical University, Ankara, Turkey

EXPERIENCE

2013/2014 Visiting Researcher, Sandia National Labs, Albuquerque, New Mexico

2010-2016 Graduate Student Researcher, Electrical Engineering and Computer Science, University of California Irvine, Advisor: Prof. Filippo Capolino

2009 Visiting Researcher, Centre Tecnològic de Telecomunicacions de Catalunya, Barcelona, Spain, Supervisor: Dr. Julien Perruisseau-Carrier

2008-2010 Teaching and Research Assistant, Middle East Technical University, Ankara, Turkey, Advisor: Prof. Ozlem Aydin Civi

FIELD OF STUDY

Metamaterials, reflectarray and phased-array antennas, plasmonic arrays in optics, nano engineered materials, optical leaky wave antennas, metasurfaces, electromagnetic modeling, numerical methods

PUBLICATIONS

[22] Q. Zhao, C. Guclu, Y. Huang, F. Capolino, and O. Boyraz, ""Experimental Demonstration of Directive Si_3N_4 Optical Leaky Wave Antennas with Semiconductor Perturbations", *J. Lightwave Technology* in print (DOI 10.1109/JLT.2016.2608801).

[21] C. Guclu, M. Veysi, and F. Capolino, "Photoinduced Magnetic Nanoprobe Excited by Azimuthally Polarized Vector Beam", *ACS Photonics*, in print. (DOI 10.1021/acsphotonics.6b00329)

[20] M. Veysi, C. Guclu, and F. Capolino, “Focused Azimuthally Polarized Vector Beam and Spatial Magnetic Resolution below the Diffraction Limit”, *JOSA B*, vol. 32, pp. 345-354, 2016

[19] Q. Zhao, C. Guclu, Y. Huang, F. Capolino, and O. Boyraz, “Silicon Nitride Waveguides for Plasmon Optical Trapping and Sensing Applications”, *JOSA B*, vol. 33, pp. 1182-1189, 2016

[18] C. Guclu, O. Boyraz, and F. Capolino, "Theory of Optical Leaky-Wave Antenna Integrated in a Ring Resonator for Radiation Control," submitted *to J. Lightwave Technology* in print (DOI 10.1109/JLT.2016.2626982,).

[17] C. Guclu, V. A. Tamma, H. K. Wickramasinghe, and F. Capolino, "Photoinduced Magnetic Force Between Nanostructures," *Physical Review B*, vol. 92, p. 235111, 2015.

[16] M. Veysi, C. Guclu, O. Boyraz, and F. Capolino, "Vortex beams with strong longitudinally polarized magnetic field and their generation by using metasurfaces," *JOSA B*, vol. 32, pp. 345-354, 2015.

[15] M. Veysi, C. Guclu, O. Boyraz, and F. Capolino, "Thin anisotropic metasurfaces for simultaneous light focusing and polarization manipulation," *JOSA B*, vol. 32, pp. 318-323, 2015.

[14] F. Tork Ladani, S. Campione, C. Guclu, and F. Capolino, "Critical excitation-rate enhancement of a dipolar scatterer close to a plasmonic nanosphere and importance of multipolar self-coupling," *Physical Review B*, vol. 90, p. 125127, 2014.

[13] C. Guclu, T. S. Luk, G. T. Wang, and F. Capolino, "Radiative emission enhancement using nano-antennas made of hyperbolic metamaterial resonators," *Applied Physics Letters*, vol. 105, p. 123101, 2014. (Featured on the cover of the issue)

[12] S. Campione, D. de Ceglia, C. Guclu, M. A. Vincenti, M. Scalora, and F. Capolino, "Enhanced Fano collective resonance as complex mode in a two-dimensional planar metasurface of plasmonic nanoparticles," *Applied Physics Letters*, vol. 105, p. 191107, 2014.

[11] S. Campione, C. Guclu, R. Ragan, and F. Capolino, "Enhanced magnetic and electric fields via Fano resonances in metasurfaces made of circular nanoclusters of plasmonic nanoparticles," *ACS Photonics*, vol. 1, pp. 254-260, 2014.

[10] C. Guclu, S. Campione, and F. Capolino, "Array of dipoles near a hyperbolic metamaterial: Evanescent-to-propagating Floquet wave transformation," *Physical Review B*, vol. 90, p. 125127, 2014.

[09] C. Guclu, S. Campione, and F. Capolino, "Theory of a directive optical leaky wave antenna integrated into a resonator and enhancement of radiation control," *J. Lightwave Technology*, vol. 32, pp. 1741-1749, 2014.

[08] S. Campione, C. Guclu, R. Ragan, and F. Capolino, "Fano resonances in metasurfaces made of linear trimers of plasmonic nanoparticles," *Optics Letters*, vol. 38, pp. 5216-5219, 2013.

[07] S.H. Sedighy, C. Guclu, S. Campione, K. Amirhoseini, and F. Capolino, "Wideband planar transmission line hyperbolic metamaterial for subwavelength focusing and resolution," *IEEE Trans. Microw. Theory Techn.*, vol. 61, pp. 4110-4117, 2013.

[06] M. A. K. Othman, C. Guclu, and F. Capolino, "Graphene–dielectric composite metamaterials: evolution from elliptic to hyperbolic wavevector dispersion and the transverse epsilon-near-zero condition," *Journal of Nanophotonics*, vol. 7, p. 073089, 2013.

[05] M. A. K. Othman, C. Guclu, and F. Capolino, "Graphene-based tunable hyperbolic metamaterials and enhanced near-field absorption," *Optics Express*, vol. 21, pp. 7614–7632, 2013.

[04] C. Guclu, S. Campione, and F. Capolino, "Hyperbolic metamaterial as super absorber for scattered fields generated at its surface," *Physical Review B*, vol. 86, p. 205130, 2012.

[03] S. Campione, C. Guclu, Q. Song, O. Boyraz, and F. Capolino, "An optical leaky wave antenna with Si perturbations inside a resonator for enhanced optical control of the radiation," *Optics Express*, vol. 20, pp. 21305–21317, 2012.

[02] C. Guclu, J. Perruisseau-Carrier, O. Aydin Civi, "Proof of Concept of a Dual-Band Circularly-Polarized RF MEMS Beam-Switching Reflectarray," *IEEE Transactions on Antennas and Propagation*, vol. 60, pp. 5451–5455, Nov. 2012

[01] C. Guclu, J. Sloan, S. Pan, and F. Capolino, "Direct Use of the High Impedance Surface as an Antenna Without Dipole on Top," *IEEE Antennas and Wireless Propagation Letters*, vol. 10, pp. 1536 – 1539, Nov. 2011

ABSTRACT OF THE DISSERTATION

Enhancing Coupling of Electromagnetic Waves with Artificial Materials

By

Caner Guclu

Doctor of Philosophy in Electrical and Computer Engineering

University of California, Irvine, 2016

Associate Professor Filippo Capolino, Chair

Metamaterials are composites that are engineered purposefully for realizing electromagnetic characteristics that do not occur naturally in mineral or organic form. These characteristics are realized by regular arrangements of meta atoms, the building blocks of metamaterials, that mimic the atoms in an element. The electric and magnetic responses of these building blocks are engineered in such a way that the effective permittivity and permeability of metamaterials can be tuned. Similarly, the anisotropy of constitutive electromagnetic parameters can also be controlled efficiently. This dissertation focuses on the enhancement of the interaction between light and matter using bulk anisotropic metamaterials and magnetic meta atoms, in order to enhance, control and/or isolate electric and magnetic nature of emitters. This is achieved first through utilization of hyperbolic metamaterials (HMs) which are a subcategory of uniaxially anistotropic materials exhibiting opposite signs of permittivity or permeability along and orthogonal the axis of anisotropy. HMs host a wide spatial spectrum of propagating waves, i.e., high gradient field features can be transferred in HMs owing to the propagating waves in ideally *indefinitely* large spatial spectrum. Optical HMs are mainly constructed by

periodic alternating layers of plasmonic metals and dielectrics. The power emitted by point sources (and arrays of point sources) in the vicinity of HMs is highly boosted compared to regular dielectric media. Moreover, most of the power is absorbed by the HM. Similar characteristics can be realized using graphene layers instead of metals in the infrared regime, where the chemical potential can be an effective means of controlling emission enhancement. Thereafter, a reactively loaded transmission line grid is presented as an example of a two-dimensional HMs, where the canalization of large spectral waves leads to transferring high resolution features. HMs can also be molded into resonators that provide high-quality resonances even in subwavelength dimensions. These extraordinary resonances are demonstrated to boost radiative emission of dipolar emissions. Another exotic property of anisotropic metamaterials is investigated with near-zero permittivity conditions where huge electric field enhancements are achieved in larger intensities than those demonstrated using isotropic near-zero permittivity materials. Lastly, a circular cluster of plasmonic nanospheres under azimuthally polarized vector beams are studied as a way of boosting local magnetic field and isolating it from electric field, which is promising for studying weak magnetic transitions in high frequency range.

CHAPTER 1

INTRODUCTION

Sec. 1.1 The Concept of Metamaterials

This dissertation is based on metamaterial concepts developed over the course of electromagnetics engineering in a quest to realize materials which exhibit characteristics not available in nature as a direct resource such as minerals or organic materials.

Metamaterials are artificial composite materials whose structure are engineered in order to achieve certain constitutive electromagnetic parameters, such as permittivity, permeability and conductivity, in macro scale. They are usually made of meta atoms, which are the building blocks arranged in a periodic order in a scale much smaller than the wavelength of intended operation. The meta atoms mimic the atoms or molecules as in natural elements and compounds whose electromagnetic responses are established based on the response of the atoms' nuclei and electrons to the external electromagnetic waves in a collective manner. Moreover, alternating layers of regular materials may be also employed to realized desired constitutive parameters.

The science of composite electromagnetic metamaterials seeks to engineer the frequency response, spatial variation, anisotropic properties of permittivity, permeability and/or conductivity of a bulk material or a surface.

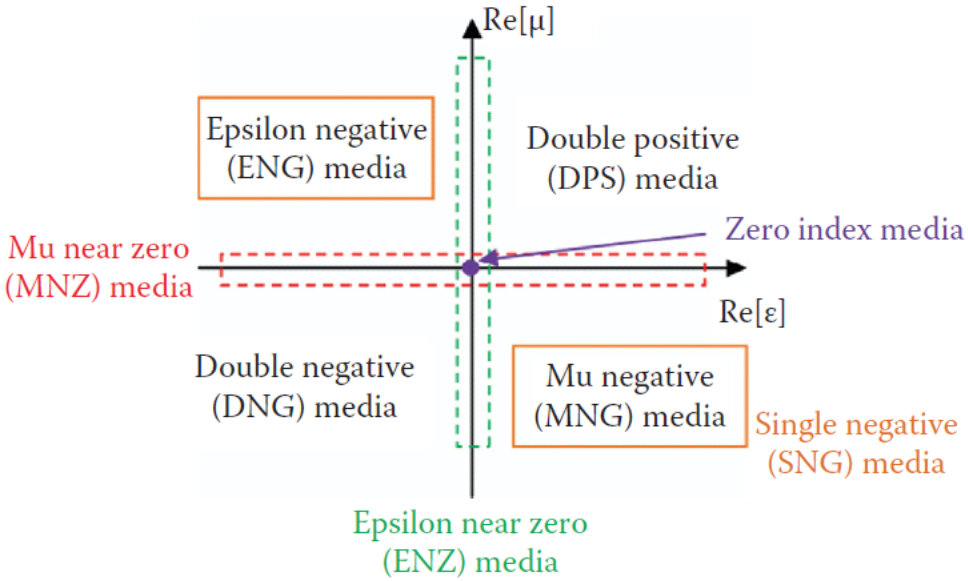

Fig. 1.1 The classification of media with respect to the real parts of the effective permittivity and permeability (© 2012 CRC Press, from William A. Goddard, *Handbook of Nanoscience, Engineering, and Technology 3rd ed.*. With permission.)

A very prominent example of metamaterial design is the double negative media whose permittivity and permeability are negative in real part. These structures find potential use in inverting the refraction direction of light rays and also in super resolutions applications that substantially revolutionized the way the metamaterials are perceived by not only the scientists but also the general public. However, there is much more than this to the science of metamaterials including but not limited to improving performance of antennas, artificial magnetic surfaces, band-gap metamaterials, chirality engineering, realization of invisibility cloaks. The theory and applications of metamaterials have been published in several books [1-12].

Any point on the permittiviy/permeability space depicted in Fig. 1.1, represents a specific form of material with exotic properties. Note that metamaterials may be isotropic in permittivity and permeability with a range of properties as in Fig. 1.1. Interestingly, and relevant to the presented work in this dissertation it is also possible to tailor anisotropic permittivity and/or permeability with control on its response to a specific field (electric or magnetic) polarized in a specific direction (*x, y, z* directions). The fundamental goal of this dissertation lies in that the interaction of emitters and light beams with metamaterials and/or meta atoms of anisotropic nature can enable engineering of their power emission, near-field and far field featuress. To this aim, uniaxially anisotropic metamaterials and anisotropic magnetic meta atoms are utilized. In the following, these concepts are briefly introduced, the content of chapters are explained, leaving the detailed introduction and literature survey of each method to the motivation sections of respective chapters.

Sec. 1.2 The Main Concepts

The main frame of the dissertation is based on the concept of hyperbolic metamaterials that are utilized for engineering the emission of sources nearby them. A bulk material with uniaxially anisotropic relative permittivity, represented as $\underline{\boldsymbol{\varepsilon}}_r = \varepsilon_t \left(\hat{\mathbf{x}}\hat{\mathbf{x}} + \hat{\mathbf{y}}\hat{\mathbf{y}} \right) + \varepsilon_z \hat{\mathbf{z}}\hat{\mathbf{z}}$, and an isotropic relative permeability μ_r , responds to transverse electric to *z* and the transverse magnetic to *z* plane waves (TE and TM) differently. The wavevector dispersion relations of TE and TM wave are different in that, TE waves only have transverse electric field component and does not respond to the anisotropy of the host material. On the other hand, TM waves experience the anisotropy and the dispersion relation takes, in general, an elliptic form as in Fig. 1.2. Moreover when the signs of permittivity along the transverse (*t*) and the normal (*z*)

directions are opposite, $\varepsilon_t \varepsilon_z < 0$, the dispersion relation of the TM wave turns into a hyperbolic equation. Ideally these waves show extraordinary dispersion, thus called extraordinary waves, where any plane wave component with an "*indefinitely*" large transverse wavenumber (i.e., high spatially oscillatory field components) can propagate and carry power. This exotic property is ideally not dependent on any resonant behavior, thus when proper materials are utilized, it can present itself over a wide range of frequencies. The example above is explained over uniaxially anisotropic permittivity, however a similar case can be constructed using TE waves and uniaxially anisotropic permeability too. Here it is intended to give a conceptual introduction, whereas any specific design and hyperbolic metamaterial synthesis will be presented in detail in the relevant chapter's motivation section.

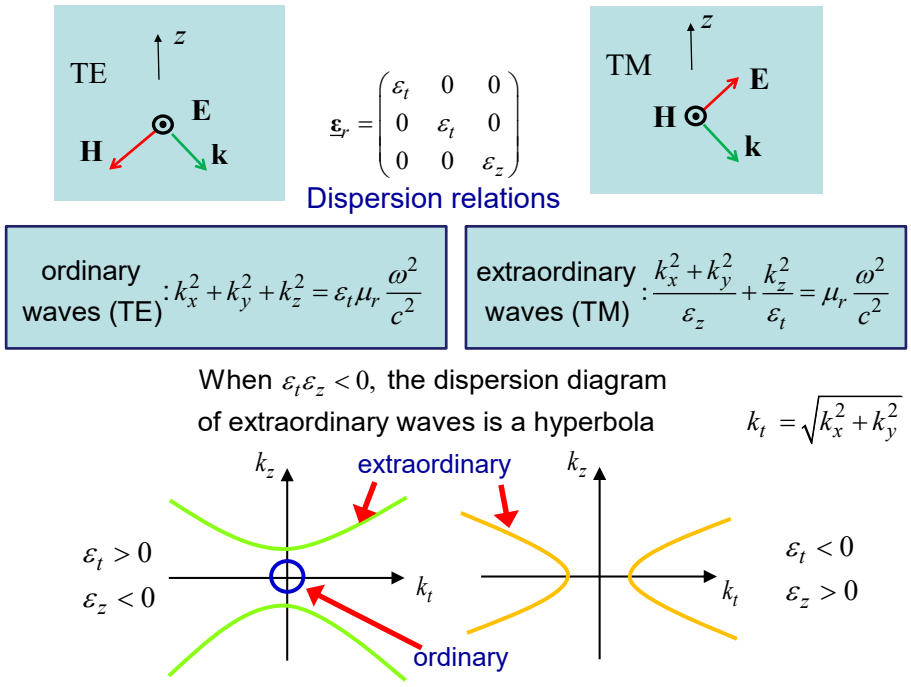

Fig. 1.2 The hyperbolic metamaterial basics, based on the anisotropy permittivity engineering.

To achieve uniaxial anisotropy, especially hyperbolic metamaterial as in the top left quadrant of Fig. 1.3, one may utilize alternating layers of plasmonic metals and dielectrics, infinitely thing inductive admittance layers separated by dielectric spacers, and wire medium as illustrated in Fig. 1.3. Even though not shown for brevity in the illustration, one can also implement hyperbolic dispersion in 2-D metamaterials which can be realized by simple transmission line grids loaded with reactive components as presented in Chapter 4.

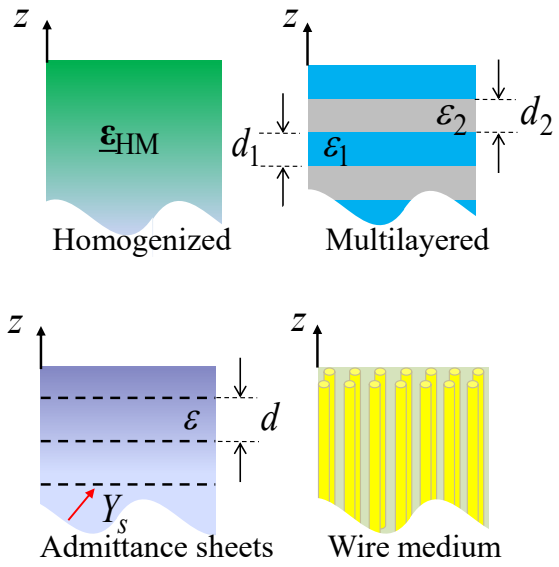

Fig. 1.3 Fundamental ways of achieving anisotropic metamaterials, particularly those hosting hyperbolic dispersion and very large spatial frequency of wave propagation.

Here it is helpful to introduce the idea of multilayered metamaterials since it is the most commonly used method of realization throughout this dissertation. Looking at the illustration in Fig. 1.4, the multilayer structure can be homogenized and thus be represented with an anisotropic, spatially invariant effective medium. The validity of such a homogenization applies to frequency range and the spectral range where one can make sure that the wavelength of the hosted waves in the heterogeneous original composite (solution to exact wave equations) is always much larger than individual layer thicknesses (and thus

also the period) of the multilayered medium. In the chapters of the dissertation, the results are not obtained relying only on the homogenization of the metamaterial, but also on accurate multilayer Green's function and transfer matrix formulations. It is, however, of utmost practicality to represent the metamaterials with simple homogenized effective parameters to convey the principles of their functionality.

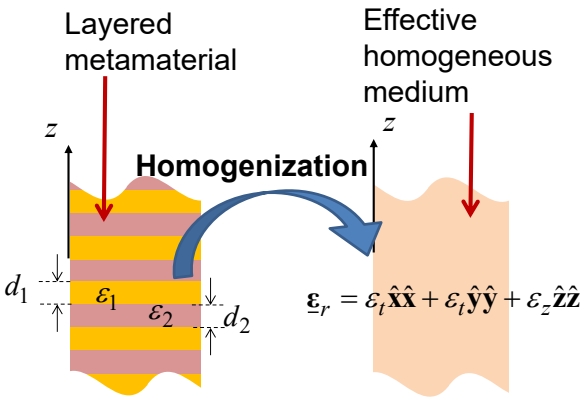

Fig. 1.4 The most commonly utilized method of achieving anisotropy is the illustrated way of stacking alternating layers of two distinct materials. The optical regime of metals with negative permittivity together with dielectric layers lead to realization of hyperbolic metamaterials. This is the main way of obtaining hyperbolic dispersion in this dissertation.

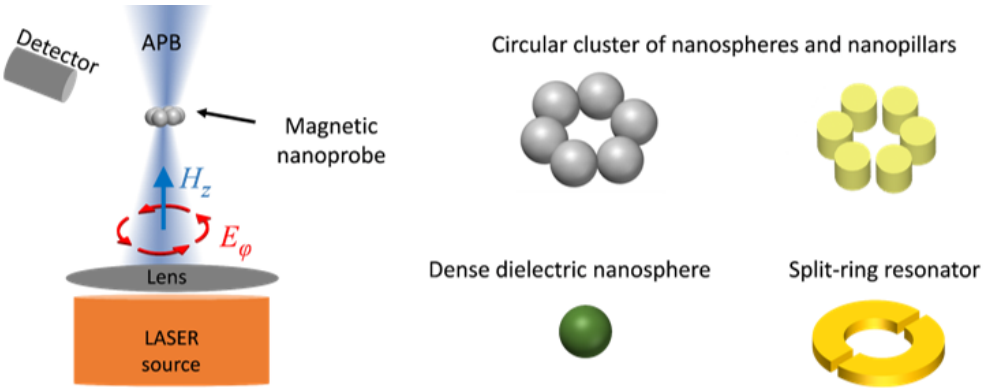

Fig. 1.5 The interaction of a vector beam with a magnetic nanoprobe, i.e. meta atom of a magnetic metamaterial, for boosting and studying the magnetism, by creating a magnetic dominant spatial reason. This constitutes a very special case of utilizing magnetic meta atoms, shown in the right panel.

By approaching from another perspective, an example to the ways to utilize a magnetic meta atom to investigate the weak magnetism optical regime is presented in Chapter 8. The magnetism becomes an exotic phenomenon in high frequency spectrum, thus the study thereof requires engineering specific setups which do not only enhance light matter interactions, but must also isolate the magnetism from the dominant electric phenomena. For this purpose, one can require both a specific form of light, called vector beams in addition to the use of magnetic meta atoms. Specifically, azimuthally polarized beams, having E-fields with circulating vectors disposition and donut-shaped intensity along with a purely longitudinal magnetic field along the beam axis is ideal. The availability of exotic structured beams opens new scenarios for studying near fields, specifically magnetism for spectroscopy and microscopy applications as in the system of vector beams and meta atoms depicted in Fig. 1.5. In Chapter 8, a road map to how to combine azimuthally polarized beam a magnetic meta atom made of plasmonic nanospheres is investigated.

Sec. 1.3 The Content of Chapters

The dissertation is organized into Chapters that involve specific methods of studying interaction of emitters and light beams with metamaterials and meta atoms.

Chapter 2: The hyperbolic metamaterials (HMs) hosting hyperbolic wave-vector dispersion solutions are studied in detail demonstrating two important features related to super absorption: The total power scattered by a nanosphere is (i) greatly enhanced when placed at the HM surface, compared to other material surfaces, and (ii) almost totally directed into the HM. These two features are peculiar of HM interfaces, and we support them using a spectral theory study of transverse-electric and magnetic waves scattered by a

subwavelength nanosphere. The nanosphere's scattered power absorbed by various substrate configurations are investigated and categorized with realizations in mind, specifically for the multilayer composition and the nano scatterer material.

Chapter 3: A novel implementation of hyperbolic metamaterial (HM) at far-infrared frequencies composed of stacked graphene sheets separated by thin dielectric layers is presented. Using the surface conductivity model of graphene, the homogenization formula for the multilayer structure by treating graphene sheets are derived as lumped layers with complex admittances. Homogenization results and limits are investigated by comparison with a transfer matrix formulation for the HM constituent layers. We show that infrared iso-frequency wavevector dispersion characteristics of the proposed HM can be tuned by varying the chemical potential of the graphene sheets via electrostatic biasing. Accordingly, reflection and transmission properties for a film made of graphene-dielectric multilayer are shown to be tunable at terahertz frequencies. The graphene-based HM is also studied as a super absorber for near-fields generated at its surface. The power emitted by a dipole near the surface of a graphene-based HM is increased dramatically (up to 5×10^2 at 2 THz), furthermore we show that most of the scattered power is directed into the HM. The validity and limits of the homogenized HM model are assessed also for near-fields and show that in certain conditions it overestimates the dipole radiated power into the HM.

Chapter 4: Subwavelength focusing by using a planar hyperbolic metamaterial (HM) at microwave frequencies is investigated oth theoretically and experimentally. The proposed HM consists of microstrip transmission lines (TLs) loaded by lumped components and exhibits a very flat wave vector iso-frequency dispersion diagram over a wide frequency range, and thus able to transport spectral component with large wavenumbers. This flatness

is here exploited to provide subwavelength focusing with a full width half maximum (3-dB power width) of about $\lambda_g/31$ and $\lambda_g/19$ at 0.5 and 1 GHz, respectively, where λ_g is the guided wavelength in the TL microtrip grid. Numerical simulation results are in good agreement with measurement ones. Moreover, we also investigate the capability of the proposed HM to resolve sources with subwavelength distance of about $\lambda_g/6$ and $\lambda_g/3$ at 0.5 and 1 GHz, respectively.

Chapter 5: The capabilities of hyperbolic metamaterials (HMs) to couple near-fields (i.e., evanescent waves) emitted by a two-dimensional periodic array of electric dipoles to propagating waves is demonstrated. In particular, large-order Floquet harmonics with transverse-magnetic polarization that would be evanescent in free space, and therefore confined near the array surface, are transformed into a propagating spectrum inside the HM and thus carry power away. Because of this property, independent of the finite or infinite extent of the HM, the power generated by an array of elementary electric dipoles is strongly enhanced and is mostly directed into the HM when the array is located near a HM surface. In particular, the power coupled to the HM exhibits narrow frequency features that can be employed in detection applications. The results shown in this chapter provide a clear signature on wave dynamics in HMs. A link between the results pertaining to the case of an isolated dipole on top of HM and the planar array is found to be convenient in explaining both wave dynamics and spectral power distribution. The narrow frequency emission features appear in the array case only; they depend on its spatial periodicity and remarkably on the HM thickness.

Chapter 6: A hyperbolic metamaterial (HM) resonator is analyzed as a nano-antenna for enhancing the radiative emission of quantum emitters in its vicinity. It has been shown that

the spontaneous emission rate by an emitter near a hyperbolic metamaterial substrate is enhanced dramatically due to very large density of states. However, enhanced coupling to the free-space, which is central to applications such as solid-state lighting, has not been investigated significantly. Here, it is numerically demonstrated that approximately 100 times enhancement of the free-space radiative emission at 660 nm wavelength by utilizing a cylindrical HM resonator with a radius of 54 nm and a height of 80 nm on top of an opaque silver-cladded substrate. It is also shown that the free-space radiation enhancement factor depends on the dipole orientation and the location of the emitter near the subwavelength resonator. Furthermore, an array of HM resonators with subwavelength spacings is shown to be able to maintain most of the enhancement effect of a single resonator.

Chapter 7: The concept of longitudinal epsilon-near-zero (LENZ) film for giant field enhancement is presented. LENZ films are uniaxially anisotropic films where the relative permittivity along the normal direction to the film is much smaller than unity, while the permittivity in the transverse plane of the film is not near zero. The LENZ condition is exceedingly superior to the standard ENZ condition in isotropic materials for generating large field enhancement in thin films. Specifically, giant field enhancement near the interface of LENZ films under TM-polarized plane wave incidence. It is proved that in comparison to the (isotropic) ENZ case the LENZ film's field enhancement is not only extremely larger but it also occurs for a wider range of angles of incidence. Furthermore the field enhancement in LENZ does not exhibit significant dependence on the film thickness unlike the isotropic ENZ case. The effect of loss on the value of the field enhancement is also investigated emphasizing the advantages of LENZ versus ENZ. Finally, it is demonstrated that radiative emission in LENZ films is much higher than in IENZ films.

Chapter 8: The concept of magnetic nanoprobes (or magnetic nanoantennas), their excitation, and the capability of providing a magnetic near-field enhancement and vanishing electric field is presented and investigated. It is established that a particular type of cylindrical vector beam called an azimuthally electric polarized vector beam yields a strong longitudinal magnetic field on the beam axis where the electric field is ideally null. These beams, with an electric polarization vortex and cylindrical symmetry, are important in generating high magnetic to electric field contrast, i.e., large local field admittance, and in allowing selective excitation of magnetic transitions in matter located on the beam axis. We demonstrate that azimuthally polarized vector beam excitation of a photoinduced magnetic nanoprobe made of a magnetically polarizable nanocluster leads to an enhanced magnetic near field with resolution beyond the diffraction limit. Two figures of merit are introduced to quantify the meta atom / beam interaction: magnetic field enhancement and local field admittance normalized to that of a plane wave. The performance of magnetic nanoprobes and azimuthal polarized beams is quantified in comparison to other illumination schemes and with several defect scenarios. The proposed probes may be useful in spectroscopy and scanning probe microscopy applications.

References

[1] F. Capolino, Ed., *Metamaterials Handbook*. Boca Raton, FL: CRC Press, 2009, p.^pp. Pages.

[2] N. Engheta and R. W. Ziolkowski, *Metamaterials: Physics and Engineering Explorations*. New York: Wiley, 2006.

[3] A. Sihvola, "Electromagnetic Mixing Formulas and Applications," ed. London: IEE Publishing, 1999.

[4] S. Tretyakov, *Analytical Modeling in Applied Electromagnetics*. Norwood, MA: Artech House, 2003.

[5] S. A. Ramakrishna and T. M. Grzegorczyk, *Physics and Applications of Negative Refractive Index Materials*. Boca Raton, FL: CRC Press and SPIE Press, 2009.

[6] B. Banerjee, *An Introduction to Metamaterials and Waves in Composites*. Boca Raton, FL: CRC Press, 2011.

[7] T. J. Cui, D. Smith, and R. Liu, Eds., *Metamaterials: Theory, Design, and Applications*. New York: Springer, 2009, p.^pp. Pages.

[8] L. Solymar and E. Shamonina, *Waves in Metamaterials*. New York: Oxford, 2009.

[9] R. Marques, F. Martin, and M. Sorolla, *Metamaterials with Negative Parameters: Theory, Design and Microwave Applications*. New York: Wiley, 2008.

[10] V. M. Shalaev and A. K. Sarychev, *Electrodynamics of Metamaterials*. Hackensack, NJ: World Scientific, 2007.

[11] G. V. Eleftheriades and K. G. Balmain, Eds., *Negative-Refraction Metamaterials*. Hoboken, NJ: John Wiley and Sons, 2005, p.^pp. Pages.

[12] C. Caloz and T. Itoh, *Electromagnetic Metamaterials. Transmission Line Theory and Microwave Applications*. Hoboken, NJ: Wiley, 2006.

CHAPTER 2

HYPERBOLIC METAMATERIAL AS NEAR FIELD ABSORBER

Sec. 2.1 Motivation

We show that hyperbolic metamaterials (HMs) that exhibit hyperbolic wavevector dispersion diagrams possess two important features related to super absorption: the total power scattered by a nanosphere is (i) greatly enhanced when placed at the HM surface, compared to other material surfaces and (ii) almost totally directed into the HM. We show that these two features are peculiar of HM interfaces, and support them using a spectral theory study of transverse-electric and magnetic waves emitted by a subwavelength nanosphere. We analyze the nanosphere's scattered power absorbed by various substrate configurations, and various nanosphere materials.

Composite hyperbolic metamaterials (HMs) are a particular kind of uniaxial anisotropic materials with iso-frequency hyperbolic-like wavevector dispersion diagram [1, 2] (as stated in the following, the wavevector dispersion curve of a realistic HM is not an exact hyperbola).

The aim of this chapter is to use a spatial spectrum approach [1] to show that a HM may exhibit the potential to act as a super absorber for scattered fields generated by a

nanoparticle near its surface. In other words, two important phenomena occur: (i) the nanoparticle's scattered fields will be enhanced by the presence of the HM, and (ii) fields are mainly directed into the HM, and hence there almost totally absorbed. Implicitly, this means that the local density of states, related to the total emitted power of a dipole, is greatly increased. These physical properties are of key importance and allow us to foresee broadband wide-angle absorption when scattering is created at the HM surface, by either purposely roughening a HM surface or, equivalently, locating many nano-scatterers at the HM surface.

The use of spectral theory enables us to carefully analyze the radiation capabilities of elementary dipoles or small objects located close to HMs for different physical conditions including, but not limited to, distance from the HM, materials, shapes, and source power spectra. In particular, we analyze systematically all the physical parameters that affect absorption capabilities, and quantify their effect. This work aims at providing a clear and exhaustive analysis of the interaction between a single dipole, or a nano-scatterer, with a HM. This analysis may lead to possible developments of innovative ways to absorb fields at microwaves as well as millimeter-wave, infrared, and optical frequencies, since HM fabrication using composite materials is simple and does not require extreme, unfeasible material parameters. The HM considered here is either made by a multilayered metal-dielectric composite or is a homogeneous HM. In both cases we demonstrate the HM suitability to super absorption capabilities, which are consistent also with other HM implementations as well (e.g., wire medium). We show that when a homogeneous HM is considered, the absorption properties discussed in this chapter are slightly overestimated when compared to a multilayered HM implementation. The formulation shown here is

general and can be applied to other envisioned applications involving HMs, not limited to absorption properties. Note that the design of a practical absorber would require the analysis of many nanoscatterers in proximity of the HM, and as such we postpone this discussion to a future effort.

Multilayered structures as in Fig. 2.1 are practical implementations of HMs at optical frequencies and have been investigated for negative refraction [3], subwavelength field focusing and superlensing applications [4-10]. The spontaneous emission patterns of electric and magnetic dipoles above a multilayer HM surface were estimated using the dyadic Green's function technique in [9]. An increased rate of spontaneous emission near nanostructured HMs has been reported in [11]. The absorption of thin dye-doped polymeric films located on top of several substrates (glass, silver, gold and multilayered HMs) has been shown in [12], concluding that absorption can be tuned and enhanced by controlling the substrate geometry and composition. As a result of a recent experiment in [13], corrugated surfaces of HMs lead to a very low reflectance and ultimate dark appearance, providing a further incentive to the analysis here proposed.

The outline of the chapter is as follows. We first model multilayered HMs in Sec. 2.2using both effective medium approximation (EMA) and Bloch theory, showing that the former is applicable under certain limitations, and in general overestimates results for the multilayered systems. Then we study in Sec. 2.3 the power emitted by an impressed dipole close to HMs via spectral theory. We then extend in Sec. 2.4 the developed theory to analyze the power scattered by a nanoparticle close to HMs. Conclusions and final remarks are stated in Sec. 2.5.

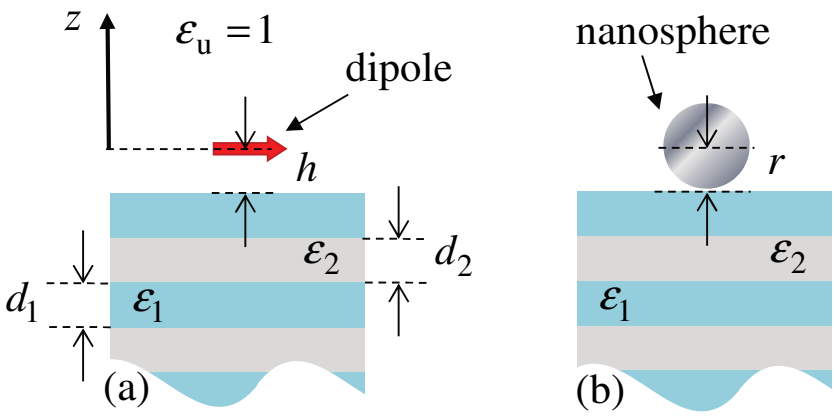

Fig. 2.1 (a) Elementary dipole at a distance *h* from the interface between free space (upper space, denoted with subscript 'u') and a multilayered HM. (b) A silver nanosphere with radius *r*, located at the HM surface.

Sec. 2.2 Layered Hyperbolic Metamaterial and Limitation of Effective Medium Approximation

Consider a structure made by a stack of two homogeneous layers as in Fig. 2.1, with subwavelength thicknesses d_1 and d_2, with relative permittivity $\varepsilon_1 = \varepsilon_1' + i\varepsilon_1''$ and $\varepsilon_2 = \varepsilon_2' + i\varepsilon_2''$ (a prime and a double prime denote real and imaginary parts, respectively). This multilayered structure can be approximated by a homogeneous HM via EMA having the anisotropy axis coincident with the *z* axis and permittivity tensor

$$\underline{\boldsymbol{\varepsilon}}_{\mathrm{HM}} = \varepsilon_t(\hat{\mathbf{x}}\hat{\mathbf{x}} + \hat{\mathbf{y}}\hat{\mathbf{y}}) + \varepsilon_z\hat{\mathbf{z}}\hat{\mathbf{z}} \tag{2.1}$$

where the expressions for $\varepsilon_t = \varepsilon_t' + i\varepsilon_t''$ and $\varepsilon_z = \varepsilon_z' + i\varepsilon_z''$ are [14]

$$\varepsilon_t = \frac{\varepsilon_1 d_1 + \varepsilon_2 d_2}{d_1 + d_2} \qquad \varepsilon_z^{-1} = \frac{\varepsilon_1^{-1} d_1 + \varepsilon_2^{-1} d_2}{d_1 + d_2} \tag{2.2}$$

Assume for the moment absence of material losses (i.e., $\varepsilon'' = 0$): a HM can be easily realized by choosing $\varepsilon_1 < 0$ (metallic layer at optical frequencies) and $\varepsilon_2 > 0$ (dielectric layer). In general, two categories of plane waves, namely ordinary and extraordinary waves, are present in a uniaxial anisotropic medium propagating with $\exp\left[i\left(k_x x + k_y y + k_z z\right)\right]$, as described in [15], where k_z and $k_t = (k_x^2 + k_y^2)^{1/2}$ are the *z* and the *transverse to z* components of the wavevector $\mathbf{k} = k_x\hat{\mathbf{x}} + k_y\hat{\mathbf{y}} + k_z\hat{\mathbf{z}}$. As shown already in [15], when considering a homogeneous HM with uniaxial anisotropy of permittivity, ordinary waves are TE (*E* field transverse to *z*) and related to ε_t. Similarly, extraordinary waves are TM (*H* field transverse to *z*) and exhibit a hyperbolic wavevector dispersion when $\varepsilon_t \varepsilon_z < 0$ [15]. The dispersion relations of ordinary and extraordinary waves are given by

$$\begin{aligned} \text{TE (ordinary):} \quad & \frac{k_t^2 + k_z^2}{\varepsilon_t} = k_0^2 \\ \text{TM (extraordinary):} \quad & \frac{k_t^2}{\varepsilon_z} + \frac{k_z^2}{\varepsilon_t} = k_0^2 \end{aligned} \tag{2.3}$$

where k_0 is the wavenumber in free space. In principle, the case with $\varepsilon_z < 0$, $\varepsilon_t > 0$ allows the extraordinary waves to propagate (carry power) in the HM for any k_t, whereas the ordinary waves propagate only for $k_t < k_0\sqrt{\varepsilon_t}$, provided EMA holds (see the discussion regarding Fig. 2.3). When $\varepsilon_z > 0$, $\varepsilon_t < 0$, instead, extraordinary waves propagate in the HM for any $k_t > k_0\sqrt{\varepsilon_z}$ whereas ordinary waves are evanescent in the whole spectrum, provided EMA holds. This latter HM case is investigated here because its realistic design is achievable over a wide bandwidth at optical frequencies when using metallic (with large negative

relative permittivity values) and dielectric layers. It is fundamental to observe that TM waves can propagate in the HM up to very large values of k_t that would otherwise be evanescent in the upper isotropic half-space, resulting in the energy transfer from the evanescent spectrum into a propagating one in the HM.

Consider now a lossy multilayered HM shown in Fig. 2.1 made of $d_1 = d_2 = 5$ nm-thick silver (complex permittivity obtained from [16]) and silica ($\varepsilon_{\mathrm{SiO_2}} = 2.2$) layers. This leads to the permittivity tensor entries ε_t and ε_z evaluated by EMA shown in Fig. 2.2 with $\varepsilon_t' < 0$ and $\varepsilon_z' > 0$ for the entire frequency band analyzed here, thus imposing hyperbolic dispersion diagrams. It has been recently reported in [17] that the power directed toward the metal–dielectric multilayers is over estimated by EMA, and we provide here a discussion on the reasons behind this phenomenon. We employ Bloch theory [18] to determine the dispersion diagram complex k_z versus real k_t (with $k_z = \beta_z + i\alpha_z$) for TM waves inside the HM at 400 THz, reported in Fig. 2.3 (solid blue curve) and compared to the dispersion diagram obtained by EMA (dashed red curve). In Fig. 2.3 we only show the mode with $\beta_z > 0$ and $\alpha_z < 0$ because it is the only one decaying (carrying power) in the –*z* direction, inside the HM. The curve shows that the wave propagating inside the HM is backward because $\beta_z \alpha_z < 0$ [19, 20]. The $-k_z$ solution, with $\beta_z < 0$ and $\alpha_z > 0$, would be the equivalent solution decaying in the +*z* direction. We note that similar diagrams are preserved at other frequencies as well (see the discussion in Sec. 2.3 and Fig. 2.6). We observe that for a wide k_t spectrum the real part of the wavenumber β_z computed by Bloch theory is close to the hyperbola obtained by EMA, confirming a hyperbolic-like dispersion (Fig. 2.3). However, for larger k_t the dispersion

curve significantly deviates from the one from EMA and it is not hyperbolic anymore. Indeed, close to $k_t \approx 14.3k_0$, β_z approaches the Brillouin zone edge ($\beta_z \approx 37.5k_0 \approx \pi / d$ at 400 THz, where $d = d_1 + d_2$ is the periodicity) and thereafter the attenuation constant α_z increases dramatically (behavior not modeled by EMA), marking a mainly evanescent spectrum in the HM. It is observed that even for small constituent-layer thicknesses and for large k_t it is important to take into account the heterogeneity of layered structures because a large wavenumber k_z implies a short wavelength in the z direction. Hence, a maximum propagating k_t spectral limit can be determined. Therefore one should not rely on EMA for large wavenumbers because EMA does not introduce any limitation for the propagating spectrum, i.e., theoretically all $k_t \in (k_{t,\min}, \infty)$ would propagate in the HM, where $k_{t,\min}$ is determined following the discussion after (2.3). In other words, according to EMA the emitted power spectrum coupled to the HM is limited only by the spatial spectrum of the field at the HM interface, and therefore EMA could lead to overestimation of the power emitted by physically very small sources (characterized by a very wide spatial spectrum of emission). It is for these reasons that in the following, we mainly treat the HM as a non-homogeneous medium modeled via Bloch theory and we also provide results regarding the HM modeled by EMA in order to determine its validity range.

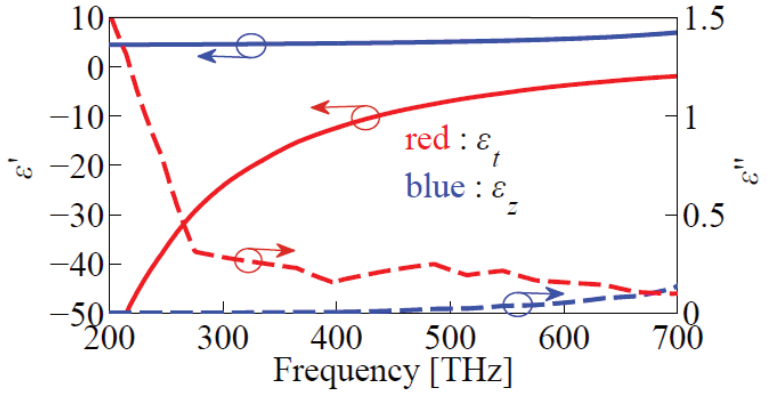

Fig. 2.2 Effective $\varepsilon_t = \varepsilon_t' + i\varepsilon_t''$ and $\varepsilon_z = \varepsilon_z' + i\varepsilon_z''$ evaluated by EMA versus frequency, pertaining to the HM made of silica ($\varepsilon_{SiO_2} = 2.2$) and silver layers, with thicknesses $d_1 = d_2 = 5$ nm.

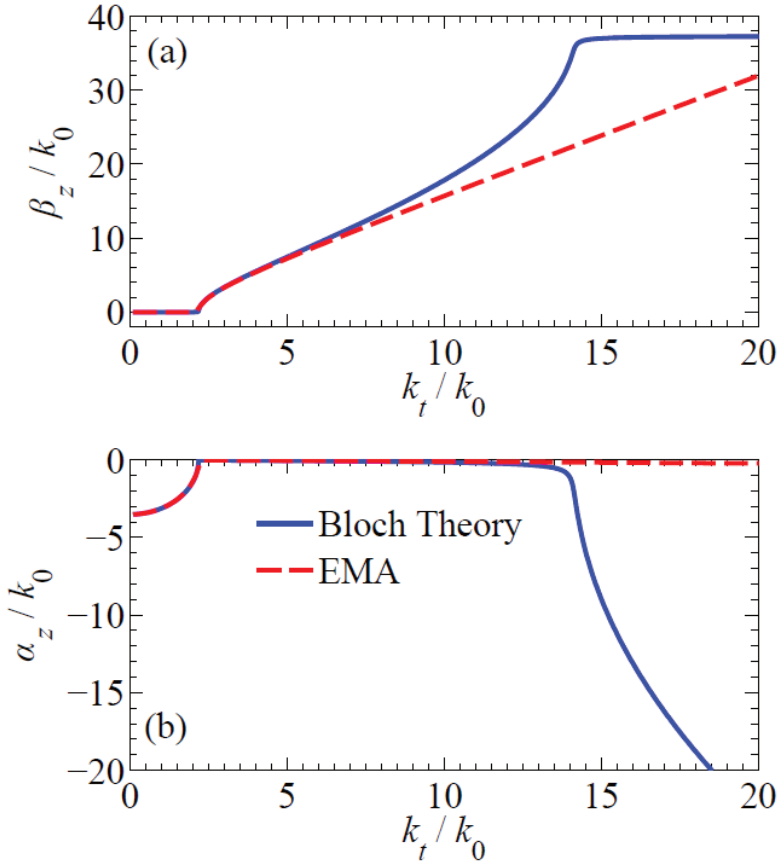

Fig. 2.3 $k_z - k_t$ dispersion diagram normalized by k_0. (a) Real and (b) imaginary parts of the wavenumber $k_z = \beta_z + i\alpha_z$ in the multilayered HM with periodicity $d = d_1 + d_2 = 10$ nm $\approx \lambda_0 / 75$ at 400 THz obtained via Bloch theory and EMA.

Sec. 2.3 Spectral Theory and the Power Emitted by an Impressed Dipole near Hyperbolic Metamaterial

We consider first the power emitted by a transverse elementary dipole with electric polarization $\mathbf{P} = p_x \hat{\mathbf{x}} \delta(\mathbf{r})$ located close to the interface between free space and the HM as illustrated in Fig. 2.1(a). To gain physical insight into the super absorption of the emitted power, we decompose the emitted power spectrum due to TE and TM polarized-field spatial harmonics and analyze their interaction with the HM. We use the equivalent transmission line theory in chapters 2, 3 and 5 in [1]. The total power $P_{\text{tot}} = P_{\text{u}} + P_{\text{d}}$ coupled to TE and TM waves (where 'u' and 'd' subscripts denote upward and downward directions, respectively) is computed by spectral integrals as

$$P_{\text{u,d}} = \frac{\omega^2 |p_x|^2}{8\pi} \int_0^{+\infty} p_{\text{u,d}}(k_t)\, dk_t \tag{2.4}$$

where

$$p_{\text{u,d}}(k_t) = \frac{\text{Re}\left[Y_{\text{u,d}}^{\text{TM}*}(k_t) \right]}{\left| Y_{\text{tot}}^{\text{TM}}(k_t) \right|^2} k_t + \frac{\text{Re}\left[Y_{\text{u,d}}^{\text{TE}*}(k_t) \right]}{\left| Y_{\text{tot}}^{\text{TE}}(k_t) \right|^2} k_t \tag{2.5}$$

are the upward and downward directed power spectra, respectively, where "*" indicates complex conjugate operation. The terms $Y_{\text{u,d}}^{\text{TM,TE}}$ represent equivalent spectral admittances at the dipole location, looking upward ($+z$ direction) or downward ($-z$ direction), for TE and TM waves. Following [1], where their expressions and physical interpretation are provided, we recall that the wave admittances relative to the upper half-space are simply given by

$$Y_{\mathrm{u}}^{\mathrm{TM}}=\frac{\omega\varepsilon_{\mathrm{u}}\varepsilon_0}{k_{z,\mathrm{u}}},\quad Y_{\mathrm{u}}^{\mathrm{TE}}=\frac{k_{z,\mathrm{u}}}{\omega\mu_0} \tag{2.6}$$

where $k_{z,\mathrm{u}}=\sqrt{\varepsilon_{\mathrm{u}}k_0^2-k_t^2}$. The downward admittances $Y_{\mathrm{d}}^{\mathrm{TM}}$ and $Y_{\mathrm{d}}^{\mathrm{TE}}$ in (2.5) (evaluated at the dipole location) in the case of a homogeneous HM half-space have to be calculated using transfer matrix method [18] and the TM and TE wave admittances

$$Y^{\mathrm{TM}}=\frac{\omega\varepsilon_t\varepsilon_0}{k_{z,\mathrm{d}}^{\mathrm{TM}}},\quad Y^{\mathrm{TE}}=\frac{k_{z,\mathrm{d}}^{\mathrm{TE}}}{\omega\mu_0} \tag{2.7}$$

where $k_{z,\mathrm{d}}^{\mathrm{TE,TM}}$ is calculated using either the TE or TM dispersion relation in (2.3). In the case of multilayered HM, instead, the downward admittances $Y_{\mathrm{d}}^{\mathrm{TM}}$ and $Y_{\mathrm{d}}^{\mathrm{TE}}$ in (2.5) are calculated applying Bloch theorem to the multilayered structure and transfer matrix method [18]. Following [1], the total admittance in (2.5) is defined as

$$Y_{\mathrm{tot}}^{\mathrm{TM,TE}}\left(k_t\right)=Y_{\mathrm{d}}^{\mathrm{TM,TE}}\left(k_t\right)+Y_{\mathrm{u}}^{\mathrm{TM,TE}}\left(k_t\right) \tag{2.8}$$

Analogous calculations can be performed also for the power emitted by a *z*-directed dipole p_z , not reported here for brevity. Note that with these expressions one can calculate the spectral power content of TE/TM waves, independently, and to the authors' knowledge this exact spectral analysis has not been previously investigated for composite HMs. Moreover, this formalism can also model the effect induced by the periodic nature of the HM via Bloch theory [18], as was explained in regard to Fig. 2.3. The ratio $P_{\mathrm{tot}}/P_{\mathrm{free\ space}}$ of the total power emitted by an elementary dipole located at a distance $h=15$ nm from the interface between free space ($\varepsilon_{\mathrm{u}}=1$) and five different kinds of bottom media, namely bulk silica, bulk silver,

HMm (HM with metal as the topmost layer), HMd (HM with dielectric as the topmost layer), and HM EMA (HM modeled by EMA) is plotted versus frequency in Fig. 2.4(a). $P_{\text{free space}}$ is the total power emitted by the same dipole in free space. Similarly in Fig. 2.4(b) the ratio $P_{\text{tot}} / P_{\text{free space}}$ is plotted versus the dipole distance h from the interface, at 400 THz. In the HM cases, we assume the period equal to $d = d_1 + d_2$ =10 nm, as in Sec. 2.2.

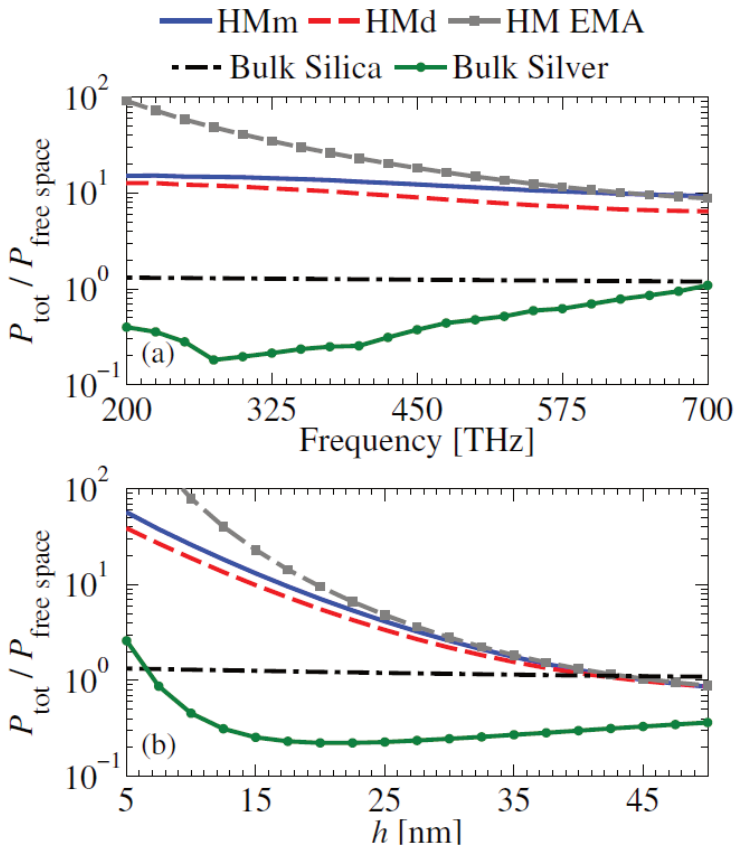

Fig. 2.4 The ratio $P_{\text{tot}} / P_{\text{free space}}$ related to an elementary transverse dipole located near the interface between free space and five kinds of media: bulk silica, bulk silver, HMm (HM with metal as the topmost layer), HMd (HM with dielectric as the topmost layer) , and HM EMA (HM modeled by EMA). The multilayered HM is composed of 5-nm-thick silver and silica layers. (a) The dipole is located at a distance $h = 15$ nm and frequency is varied. (b) The dipole location h is varied at 400 THz.

Looking at the ratio $P_{\text{tot}} / P_{\text{free space}}$ in Fig. 2.4, without considering the HM EMA result for the moment, the highest emitted power occurs for the HMm case (slightly larger than the HMd case), and the smallest for the bulk silver case, over a wide frequency band. We note however that HM EMA overestimates scattered power amounts for low frequencies or low distances *h*, and the explanation behind this fact will be provided in the discussion regarding Fig. 2.5. The power emitted by an elementary dipole at a distance $h = 15\ \text{nm}$ is about 7 to 15 times higher than the power emitted by the same dipole in free space in the case of HM bottom half-space [Fig. 2.4(a)]. Moreover, for the HM case, the ratio $P_{\text{tot}} / P_{\text{free space}}$ increases almost exponentially if *h* is decreased, as shown in Fig. 2.4(b), thanks to the coupling of power between evanescent spectrum in free space and propagating spectrum in the HM. This clearly indicates that a large boost of emitted power occurs when the dipole is very close to the HM.

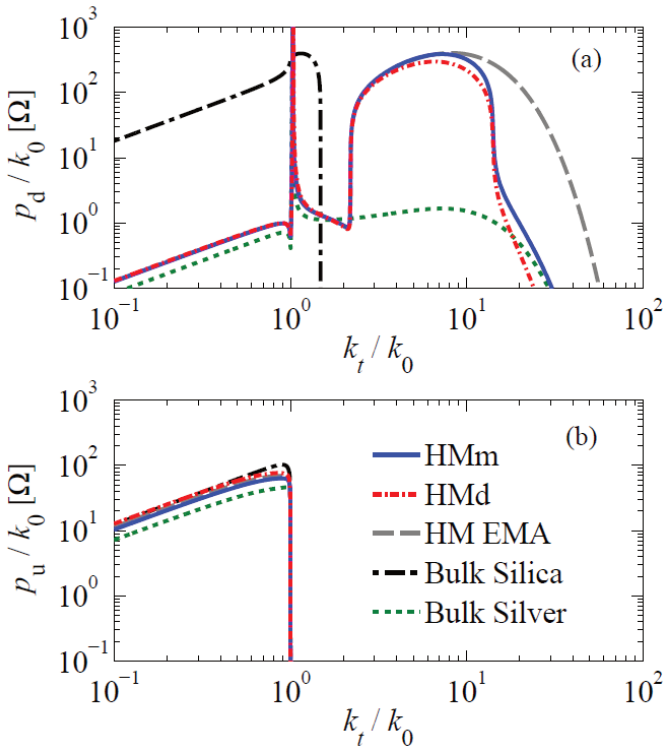

Fig. 2.5 (a) Downward, p_{d}, and (b) upward, p_{u}, spectral power emitted by a transverse dipole located at $h = 15$ nm at 400THz, for the same case considered in Fig. 2.4. Note the large power spectrum p_{d} for k_t / k_0 between 2.1 and 14.3, for the bottom HMm and HMd cases, and between 2.1 and 36.5, for the bottom HM EMA case.

To investigate the physical mechanism causing the enhancement of the power emission by a dipole in proximity of a HM, and the suitability to super absorption capabilities, we report in Fig. 2.5 the downward and upward spectra p_{d} and p_{u} in (2.5) normalized by k_0. The very wide spectrum of $p_{\mathrm{d}}(k_t)$ coupled to the HM, from $k_t \approx 2.1 k_0$ to $k_t \approx 14.3 k_0$, is clearly seen in Fig. 2.5(a), in agreement with the dispersion relation plotted in Fig. 2.3 that shows the k_t spectrum where TM waves have relatively small α_z and thus are mainly propagating. The upward power spectrum is instead present only for $k_t < k_0$, the propagating spectrum in free space. Also note that EMA results in a wider propagating spectrum inside the HM,

from $k_t \approx 2.1k_0$ to $k_t \approx 36.5k_0$, eventually in disagreement with Bloch theorem for large k_t spectrum, specifically in the region $14.3k_0 < k_t < 36.5k_0$. As mentioned in Sec. 2.2, EMA predicts that any $k_t > k_0\sqrt{\varepsilon_z}$ is allowed to propagate in the HM, however due to the dipole distance from the HM interface, large k_t spectrum cannot couple power into the HM because of the free space evanescent field decay proportional to $\exp\left(-\sqrt{k_t^2 - k_0^2}h\right)$. It is this evanescent decay that leads to power spectrum $p(k_t)$ decay after $k_t \approx 36.5k_0$ in the HM EMA case in Fig. 2.5(a). This fact implies that the closer the distance *h* of the dipole from the HM, the larger the power coupled into the HM.

Observing the power spectrum in Fig. 2.5 is also useful to explain why the total scattered power evaluated with EMA as in Fig. 2.4(a) is overestimated when compared to the one calculated with Bloch theory, in the low frequency region. The power spectrum difference between EMA and Bloch theory is mainly in the interval $k_{t,\max}^{\text{Bloch}} < k_t < k_{t,\max}^{\text{EMA}}$, where $k_{t,\max}^{\text{Bloch}}$ and $k_{t,\max}^{\text{EMA}}$ are evaluated as follows. The largest spectral component k_t of the field emitted by the source and coupled to the HM under EMA is determined assuming that the power spectrum decays as $\exp\left(-\sqrt{k_t^2 - k_0^2}h\right)$ and it is considered negligible when $\sqrt{k_t^2 - k_0^2}h > \xi$, where $\xi \geq 1$ is a predetermined number. This shows that the upper boundary of the k_t-spectrum coupled to the HM under EMA (i.e., $k_t < k_{t,\max}^{\text{EMA}}$) is $k_{t,\max}^{\text{EMA}} = \sqrt{k_0^2 + (\xi/h)^2} \approx \xi/h$. Note that this upper limit is independent of frequency in the assumption $\xi^2/h^2 >> k_0^2$ (fully verified in our case).

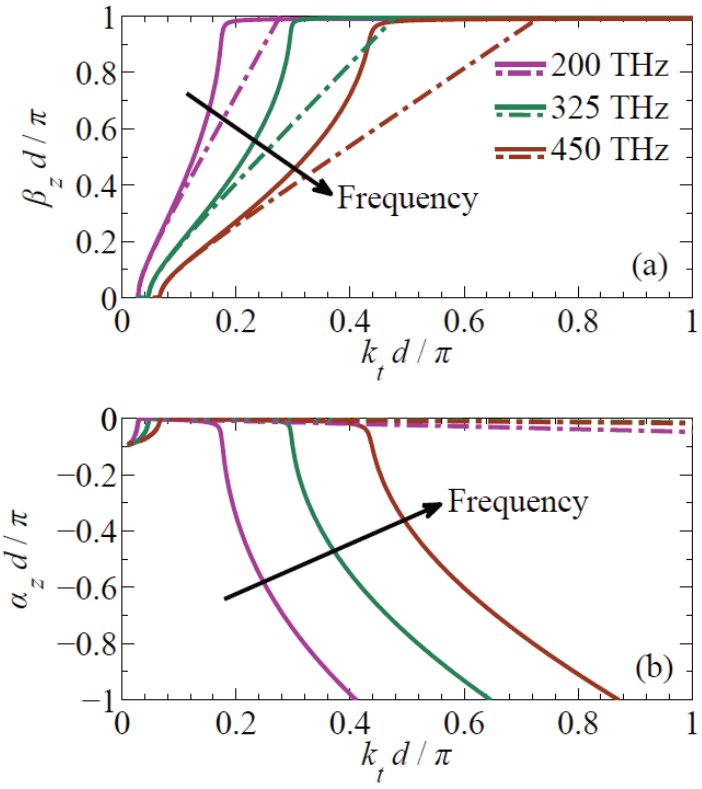

Fig. 2.6 $k_z - k_t$ dispersion diagram normalized by π/d, at the three frequencies shown in the legend, obtained via Bloch theory (solid) and EMA (dashed dotted). (a) Real and (b) imaginary parts of the wavenumber $k_z = \beta_z + i\alpha_z$ in the multilayered HM with periodicity $d = d_1 + d_2 = 10$ nm.

The upper spectral limit $k_{t,\max}^{\text{Bloch}}$ denotes the maximum spectrum able to propagate in the HM using the more precise Bloch theory and it is determined by β_z approaching the Brillouin zone edge. By looking at the dispersion diagrams in Fig. 2.6 relative to different frequencies, one can observe that the $k_{t,\max}^{\text{Bloch}}$ decreases for decreasing frequency. However, since the ratio $k_{t,\max}^{\text{Bloch}} / k_0$ remains almost constant and equal to about 14, as in Sec. 2.2 for the multilayer HM under analysis, we can say that $k_{t,\max}^{\text{Bloch}} \approx K k_0$, where K is a proportionality constant determined mainly by the periodicity of the multilayered HM (see the discussion

regarding Fig. 2.7). This means that the difference between power spectra able to couple power into the HM under EMA and Bloch theory is as wide as $\Delta k_t = k_{t,\max}^{\mathrm{EMA}} - k_{t,\max}^{\mathrm{Bloch}} \approx \xi / h - K k_0$. We note that Δk_t increases for decreasing frequency, hence leading to higher disagreement between EMA and Bloch theory at lower frequencies, explaining the power overestimation by EMA in Fig. 2.4(a) in the low frequency region of the plot.

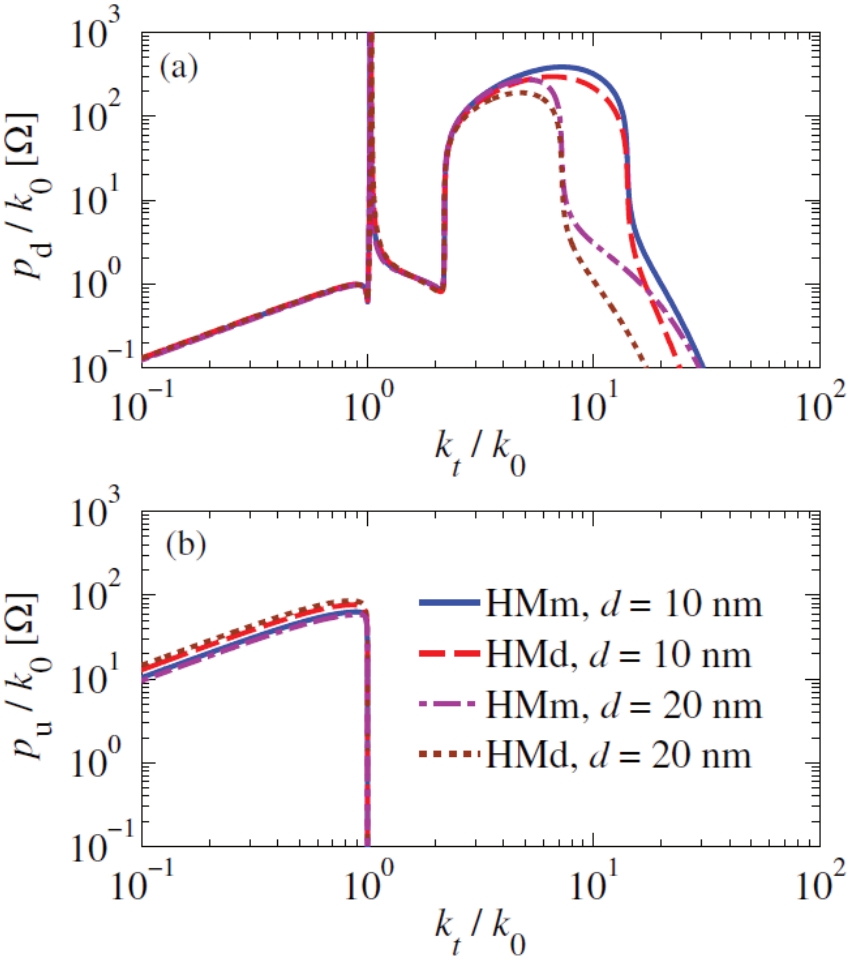

Fig. 2.7 (a) Downward, p_{d}, and (b) upward, p_{u}, spectral power emitted by a transverse dipole located at $h = 15$ nm at 400THz, for the same case considered in Fig. 2.4, considering the two periods in the legend (individual silver and silica layers are assumed with equal thicknesses).

In Fig. 2.7, we analyze the power spectra of the HM for two illustrative cases: the one shown in Fig. 2.5 with a metamaterial period $d = d_1 + d_2$=10 nm, and another one with doubled period $d = d_1 + d_2$=20 nm (still keeping the same d_1 / d_2 of the case in Fig. 2.5). This analysis is performed to stress that the metamaterial physical parameters impact the propagating spectrum inside the HM, which tends to be narrower as the period of the HM is increased. The upper edge of the propagating spectrum inside the HM shifts from $k_t \approx 14.3k_0$ (10 nm period) to $k_t \approx 7.1k_0$ (20 nm), showing that the period of the HM needs to be minimized for having a wide propagating spectrum inside the HM that can be employed to couple power coming from the evanescent spectrum in free space.

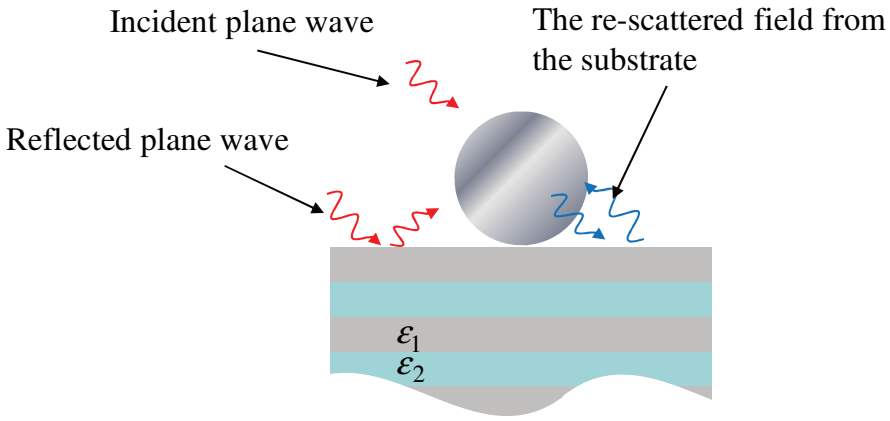

Fig. 2.8 The illustration showing the scattering problem and the contribution to the local electric field which excites the scaterrer.

Sec. 2.4 Power Scattered by a Nanoparticle Close to Hyperbolic Metamaterial

We show and explain now the phenomenon of strong absorption by the HM when a passive nanoscatterer in proximity of the HM interface is illuminated. Inspired by the experimental results in [21], we focus on understanding how a nanosphere's scattered power is affected by its size and material properties. Hence, consider a silver nanosphere

located as in Fig. 2.1(b), excited by a linearly polarized (say along the *x* direction) plane wave with normal incidence. The nanosphere is modeled as an equivalent electric dipole via the single dipole approximation [22, 23], and its induced dipole moment located at the center of the nanosphere (thus at a distance from the HM equal to the radius *r*) is given by $p_x = \alpha_{xx} E_x^{\mathrm{loc}}$, where α_{xx} is the electric polarizability (Clausius-Mossotti expression reported in [22, 23]) and E_x^{loc} is the local electric field acting on the nanosphere. In particular,

$$E_x^{\mathrm{loc}} = E_x^{\mathrm{pw}} + E_x^{s}, \tag{2.9}$$

where E_x^{pw} is the total plane wave field, sum of the incident plane wave and the one reflected at the HM interface, evaluated at the nanosphere's center. Furthermore, $E_x^{s} = G_{xx}^{s} p_x$ represents the field produced by the dipole itself, and evaluated at its location, that accounts for the scattering by the bottom half-space. Accordingly, the term G_{xx}^{s} is the $\hat{\mathbf{x}}\hat{\mathbf{x}}$ component of the regularized dyadic Green's function, i.e., it does not account for the free-dipole field but includes all the spectral terms reflected by the HM interface. Accordingly, it is given by the spectral representation

$$G_{xx}^{s} = \frac{i\omega}{4\pi} \int_0^{+\infty} \left[\frac{\Gamma_{\mathrm{d}}^{\mathrm{TM}}(k_t)}{2Y_{\mathrm{u}}^{\mathrm{TM}}(k_t)} + \frac{\Gamma_{\mathrm{d}}^{\mathrm{TE}}(k_t)}{2Y_{\mathrm{u}}^{\mathrm{TE}}(k_t)} \right] k_t dk_t, \tag{2.10}$$

where

$$\Gamma_{\mathrm{d}}^{\mathrm{TM,TE}}(k_t) = \frac{Y_{\mathrm{u}}^{\mathrm{TM,TE}}(k_t) - Y_{\mathrm{d}}^{\mathrm{TM,TE}}(k_t)}{Y_{\mathrm{u}}^{\mathrm{TM,TE}}(k_t) + Y_{\mathrm{d}}^{\mathrm{TM,TE}}(k_t)} \tag{2.11}$$

are the plane-wave reflection coefficients [1] of TE and TM spectral component with transverse wavenumber k_t , looking towards the $-z$ direction, and evaluated at the nanosphere center location. By solving for the scatterer's dipole moment one obtains the closed form expression

$$p_x = \frac{\alpha_{xx}}{1-\alpha_{xx}G^s_{xx}} E^{\mathrm{pw}}_x \ . \tag{2.12}$$

The total plane field at the nanosphere's center is given by $E^{\mathrm{pw}}_x = E^{\mathrm{inc}}_x \left[1+\Gamma_{\mathrm{d}}(0)\right]$, where E^{inc}_x is the incoming normally incident plane wave and $\Gamma_{\mathrm{d}}(0)$ is its reflection coefficient evaluated at the nanosphere's center. This method is accurate when the nanosphere is very subwavelength and not far from its first Fröhlich resonance [22], so that the electric dipolar term is dominant compared to the field due to higher multipolar terms. Once the dipole moment p_x of the nanosphere is determined, its scattered power toward the upper (free space, P^s_{u}) and lower (P^s_{d}) spaces is evaluated by using (2.4). The advantage of this semi-analytical method is that it breaks down each scattering process into its basic components and provides a clear physical insight.

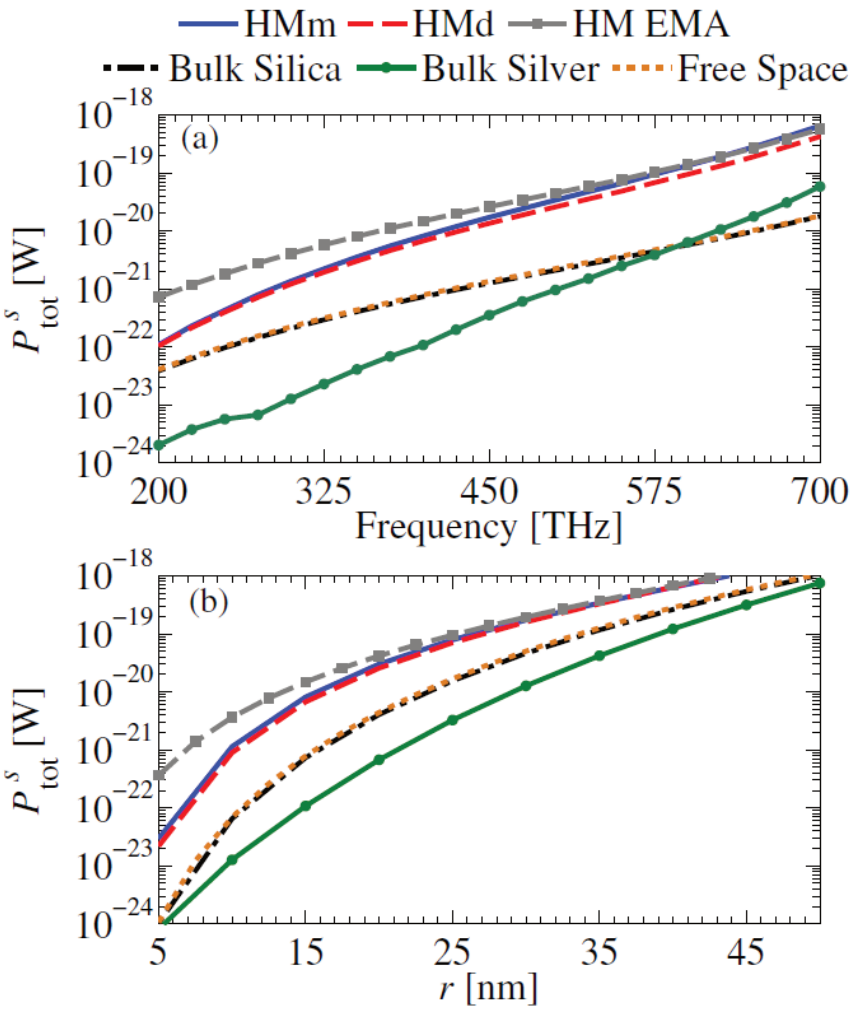

Fig. 2.9 Total power P^s_{tot} scattered by a silver nanosphere located on the surface of six kinds of media: bulk silver, bulk silica ($\varepsilon_{\text{SiO}_2} = 2.2$), free space, HMm, HMd, and HM EMA composed of silver and silica layers of thickness 5nm, under plane wave incidence ($\left|E_x^{\text{inc}}\right| = 1$ V/m) when (a) $r = 15$ nm and frequency is varied and (b) at 400 THz varying the nanosphere radius r.

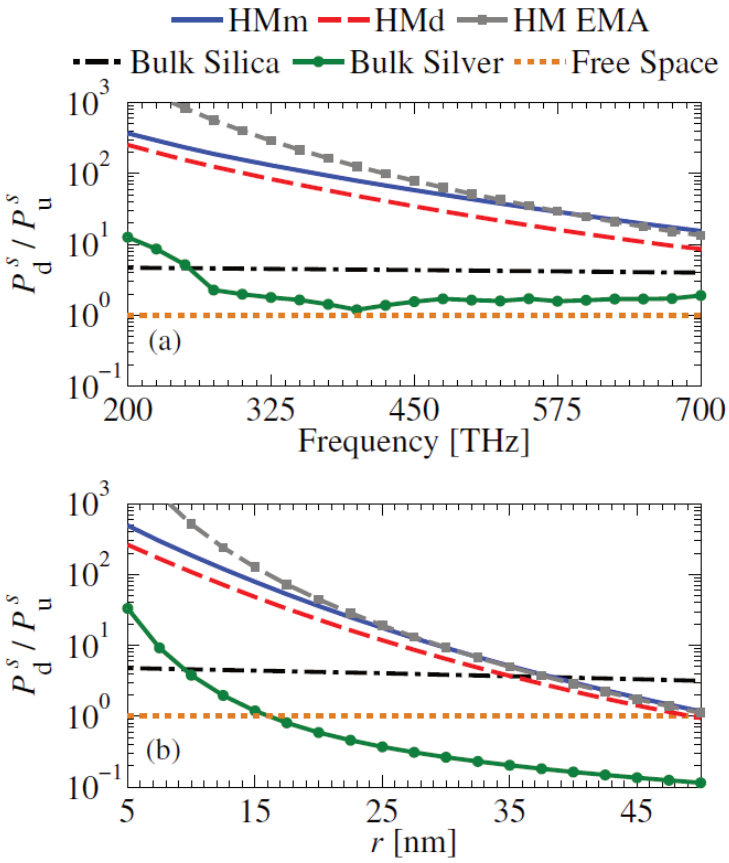

Fig. 2.10 Ratio of downward over upward power $P_{\mathrm{d}}^{s} / P_{\mathrm{u}}^{s}$, for the same case considered in Fig. 2.9.

The total scattered power $P_{\mathrm{tot}}^{s} = P_{\mathrm{u}}^{s} + P_{\mathrm{d}}^{s}$ due to a silver nanosphere located on top of six possible substrates (HMd, HMm, HM EMA, bulk silver, bulk silica, and free space) under linearly-polarized, normally incident plane wave E_x^{inc} (with 1 V/m electric field amplitude) is shown in Fig. 2.9(a) for a nanosphere radius $r = 15$ nm versus frequency, and in Fig. 2.9(b) versus the nanosphere radius *r* at 400 THz. The passive silver nanosphere on top of HMd and HMm apparently scatters one or two orders of magnitude more total power than when on top of bulk silica, free space or bulk silver, between 200 THz and 700 THz (in agreement with the total power emitted by an elementary transverse dipole shown in Fig. 2.4(a). Note also

that HM EMA gives overestimated scattered power amounts for smaller frequency/radius ranges in agreement with the discussion in Sec. 2.3 above Fig. 2.5.

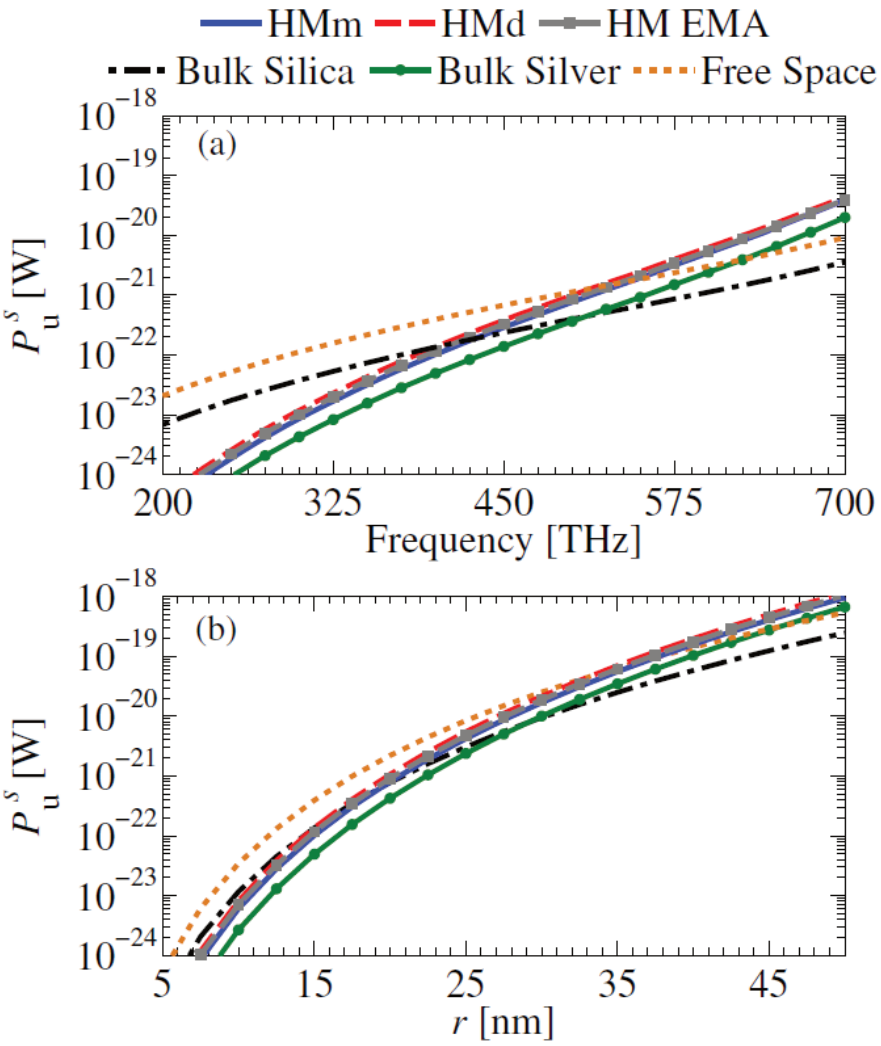

Fig. 2.11 The upward scattered power P_u^s, for the same case considered in Fig. 2.9.

The difference in scattered power among all substrate cases is less evident when the nanosphere radius is increased, as shown in Fig. 2.9(b), though the total power scattered by the nanosphere in the case of the HM substrates is still significantly larger than in the other bulk substrate cases. In Fig. 2.10, the ratio P_d^s / P_u^s is plotted (a) for a nanosphere with

$r = 15$ nm versus frequency, and (b) at 400 THz versus the nanosphere radius *r*. One shall notice the remarkable effect that the scattered power into the bottom space P_{d}^{s} is much larger than the power scattered into the upper space ($P_{\mathrm{d}}^{s} >> P_{\mathrm{u}}^{s}$) for HMm and HMd (where HMm has a larger ratio) indicating that the nanosphere's scattered field is mainly absorbed by the HM (and giving direct proof of super absorption capabilities). Note that HM EMA gives overestimated results for smaller frequencies or radii, as explained in Sec 3. The case with bulk silver bottom space yields the lowest $P_{\mathrm{d}}^{s} / P_{\mathrm{u}}^{s}$ ratio in most of the shown frequency band when compared to all other substrates except free space, where power is evenly scattered and thus $P_{\mathrm{d}}^{s} / P_{\mathrm{u}}^{s} = 1$. When the radius of the metal nanosphere is decreased, the ratio $P_{\mathrm{d}}^{s} / P_{\mathrm{u}}^{s}$ increases for cases with HMd, HMm, HM EMA, and bulk silver bottom spaces because the power coupled to these media is related to a wide k_t spectrum that is purely evanescent in free space (where HM hosts mainly propagating waves, and bulk silver hosts mainly evanescent waves related to losses), whereas the case with bulk silica bottom space is slightly affected. For small nanospheres, e.g., $r = 15$ nm or smaller, the downward power exceeds the upward power by at least two orders of magnitude. Therefore, we can observe that a proper distance and size shall be selected for the nanosphere to enhance its scattered power, and direct it toward the HM: if the nanosphere is much smaller than the wavelength, it will not scatter light efficiently; whereas if it is too large, it does not couple efficiently to the HM's high density of states and the scattering directed toward the HM is weak (i.e., less power will be coupled into the HM). For the sake of completeness, we show in Fig. 2.11 the power scattered by the nanosphere into the upper space for the cases reported in Fig. 2.9 and Fig. 2.10. When looking at Fig. 2.11(a), we note that in the HM cases the nanosphere

scatters less power (up to two orders of magnitude) into the upper space until 450 THz. For the remaining frequency range, as well as for the result in Fig. 2.11(b), the power scattered in the upper half-space in the presence of the HM is comparable to the one scattered when the nanosphere is in free space. Moreover, the amount of the scattered power into the upper space increases as the radius is increased. We however know from Fig. 2.9 that the total scattered power is about 1 to 2 orders of magnitude larger than the one in free space. This is a promising quality of the metamaterial under study: not only the downward power scattered by the nanosphere on top of HM is increased (remarking suitability to absorption capabilities) but also the upward scattered power is reduced or comparable to the one scattered in free space over a wide frequency band.

Lastly, we inspect the influence of the nanosphere's material on the scattered power. We consider the HMd substrate in Fig. 2.9 and nanospheres with radius r = 15 nm made of four materials, namely silver (Ag, with negative and large permittivity [16]), silica (SiO_2 with small and positive permittivity $\varepsilon_{SiO_2} = 2.2$), silicon carbide (SiC, positive and moderate permittivity [24]), and gallium phosphide (GaP, large positive permittivity with losses [24, 25]) and show their scattered total power in Fig. 2.12. Apparently, when the permittivity of the nanosphere's material increases in absolute value (Ag, GaP), the total power scattered by the nanosphere increases as well. Although the $P_{\mathrm{d}}^{s} / P_{\mathrm{u}}^{s}$ ratio does not depend on the excitation of the dipole itself, the material of the scatterer effectively determines how much power of the incident plane wave is scattered. Further conclusions about the usage of sets of scatterers on top of HM for achieving low reflectance need modeling of distributed scatterers on a HM surface and will be the object of future work.

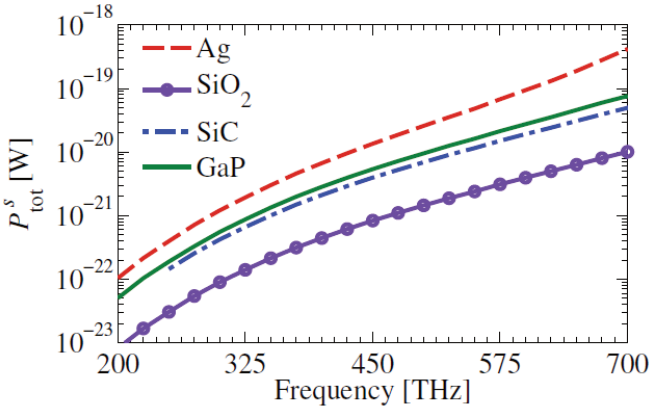

Fig. 2.12 Total power P^s_{tot} scattered by a silver (Ag), silica (SiO_2), silicon carbide (SiC), and gallium phosphide (GaP) nanosphere (r = 15nm) located on top of the HMd in Fig. 2.9 composed of silver and silica layers of thickness 5nm varying frequency under plane wave incidence ($\left|E^{\text{inc}}_x\right|$ = 1 V/m).

Sec. 2.5 Conclusion

We have shown via spectral theory that: (i) the power scattered by a passive nanosphere located in the proximity of a HM is increased; (ii) scatterers located on top of HMs emit almost all power toward the HM. Both HM EMA and multilayer implementations (HMm, HMd) lead to similar super absorption properties (in some frequency range EMA overestimates absorption). Therefore, HMs have a clear potential of enhancing the decay rate of emitters near its surface and also for designing efficient and innovative absorbers. A list of foreseen applications of this "super absorber" with unprecedented performance in terms of bandwidth and wide angle of operations includes radar cross section reduction, near field absorbers, improved solar spectrum absorption, infrared absorbers.

This chapter is reproduced based on the material in [C. Guclu, S. Campione, and F. Capolino, "Hyperbolic metamaterial as super absorber for scattered fields generated at its surface," *Phys. Rev. B*, Vol. 86, 205130, Nov. 2012], © 2012 American Physical Society.

References

[1] L. B. Felsen and N. Marcuvitz, *Radiation and Scattering of Waves*: Prentice-Hall, NJ, 1973.

[2] D. R. Smith and D. Schurig, "Electromagnetic Wave Propagation in Media with Indefinite Permittivity and Permeability Tensors," *Physical Review Letters,* vol. 90, p. 077405, 2003.

[3] G. V. Naik, J. Liu, A. V. Kildishev, V. M. Shalaev, and A. Boltasseva, "Demonstration of Al:ZnO as a plasmonic component for near-infrared metamaterials," *Proceedings of the National Academy of Sciences,* May 18, 2012 2012.

[4] J. B. Pendry and S. A. Ramakrishna, "Refining the perfect lens," *Physica B-Condensed Matter,* vol. 338, pp. 329-332, Oct 2003.

[5] K. J. Webb and M. Yang, "Subwavelength imaging with a multilayer silver film structure," *Optics Letters,* vol. 31, pp. 2130-2132, Jul 2006.

[6] X. Li and F. Zhuang, "Multilayered structures with high subwavelength resolution based on the metal-dielectric composites," *Journal of the Optical Society of America a-Optics Image Science and Vision,* vol. 26, pp. 2521-2525, Dec 2009.

[7] Y. Jin, "Improving subwavelength resolution of multilayered structures containing negative-permittivity layers by flatting the transmission curves," *Progress in Electromagnetics Research-Pier,* vol. 105, pp. 347-364, 2010.

[8] C. Della Giovampaola, M. Albani, and F. Capolino, "Investigation on subwavelength focusing properties of metal-dielectric multilayer," in *Metamaterials Congress, Barcelona, Spain, October 10-15, 2011*, 2011.

[9] R. Kotyński, T. Stefaniuk, and A. Pastuszczak, "Sub-wavelength diffraction-free imaging with low-loss metal-dielectric multilayers," *Applied Physics A: Materials Science & Processing,* vol. 103, pp. 905-909, 2011.

[10] Z. Liu, Z. Liang, X. Jiang, X. Hu, X. Li, and J. Zi, "Hyper-interface, the bridge between radiative wave and evanescent wave," *Applied Physics Letters,* vol. 96, pp. 113507-3, 2010.

[11] H. N. S. Krishnamoorthy, Z. Jacob, E. Narimanov, I. Kretzschmar, and V. M. Menon, "Topological Transitions in Metamaterials," *Science,* vol. 336, pp. 205-209, April 13, 2012 2012.

[12] T. U. Tumkur, L. Gu, J. K. Kitur, E. E. Narimanov, and M. A. Noginov, "Control of absorption with hyperbolic metamaterials," *Applied Physics Letters,* vol. 100, p. 161103, 2012.

[13] E. E. Narimanov, H. Li, Y. A. Barnakov, T. U. Tumkur, and M. A. Noginov, "Darker than black: radiation-absorbing metamaterial," *arXiv:1109.5469v1,* 2011.

[14] P. A. Belov and Y. Hao, "Subwavelength imaging at optical frequencies using a transmission device formed by a periodic layered metal-dielectric structure operating in the canalization regime," *Physical Review B,* vol. 73, p. 113110, 2006.

[15] L. D. Landau, E. M. Lifshitz, and L. P. Ptaevskii, "Electromagnetic Waves in Anisotropic Media," in *Electrodynamics of Continuous Media*, 2nd ed: Butterworth-Heinemann, 1984, p. 339.

[16] P. B. Johnson and R. W. Christy, "Optical Constants of the Noble Metals," *Physical Review B,* vol. 6, pp. 4370-4379, 1972.

[17] O. Kidwai, S. V. Zhukovsky, and J. E. Sipe, "Dipole radiation near hyperbolic metamaterials: applicability of effective-medium approximation," *Optics Letters,* vol. 36, pp. 2530-2532, 2011.

[18] D. M. Pozar, *Microwave Engineering*, 3rd ed.: John Wiley & Sons, 2005.

[19] S. Campione, S. Steshenko, M. Albani, and F. Capolino, "Complex modes and effective refractive index in 3D periodic arrays of plasmonic nanospheres," *Opt. Express,* vol. 19, pp. 26027-26043, 2011.

[20] S. Campione, S. Steshenko, and F. Capolino, "Complex bound and leaky modes in chains of plasmonic nanospheres," *Opt. Express,* vol. 19, pp. 18345-18363, 2011.

[21] T. U. Tumkur, J. K. Kitur, B. Chu, L. Gu, V. A. Podolskiy, E. E. Narimanov*, et al.*, "Control of reflectance and transmittance in scattering and curvilinear hyperbolic metamaterials," *Applied Physics Letters,* vol. 101, pp. 091105-4, 2012.

[22] C. F. Bohren and D. R. Huffman, *Absorption and Scattering of Light by Small Particles*. New York: Wiley, 1983.

[23] S. Steshenko and F. Capolino, "Single dipole approximation for collections of nanoscatterers," in *Theory and Phenomana of Metamaterials*, F. Capolino, Ed., ed FL: CRC Press, 2009.

[24] E. Palik, *Handbook of Optical Constants of Solids*. New York: Academic Press, 1985.

[25] D. E. Aspnes and A. A. Studna, "Dielectric functions and optical parameters of Si, Ge, GaP, GaAs, GaSb, InP, InAs, and InSb from 1.5 to 6.0 eV," *Physical Review B,* vol. 27, pp. 985-1009, 1983.

CHAPTER 3

GRAPHENE-BASED TUNABLE HYPERBOLIC METAMATERIAL

Sec. 3.1 Motivation

A stack of graphene sheets, separated by subwavelength dielectric spacers, can be regarded as a composite material with uniaxial electric properties. Graphene layers strongly affect the complex effective permittivity of the composite for electric field components polarized parallel to the graphene sheets. Uniaxial anisotropic materials in general offer a variety of interesting electromagnetic properties. In particular, here a subcategory denoted as hyperbolic metamaterials (HMs) is investigated, which is named after the hyperbolic iso-frequency wavevector dispersion curves that arise due to the negative permittivity experienced by the electric field component along either the axis of anisotropy or a direction orthogonal to the axis of anisotropy [1,2].

Strong interest in HMs is based on their specific property that enables propagation of a very wide spatial spectrum, that would be otherwise evanescent in free space, which is in principle unbounded for the ideal case of purely hyperbolic iso-frequency wavevector dispersion. In case of realistic hyperbolic-like dispersion, the spatial spectrum allowed for

propagation can still be extremely wide, as shown in [3–5]. This property is shared with uniaxial anisotropic materials with elliptic iso-frequency dispersion diagram, with a very large axial ratio. Though in practical cases purely hyperbolic dispersion cannot be obtained, effective medium models based on hyperbolic dispersion proves to be a very useful tool for understanding the physics behind the interesting electromagnetic properties of these metamaterials with extremely subwavelength features.

Recently, metal-dielectric multilayers were proposed as candidates to realize HMs at optical frequencies [3,6,7]. This wide spatial spectrum of propagation can lead to novel phenomena as increasing the power scattered by imposed dipoles [3,8] or nanoparticles [3,9] on HM surfaces, and this power is mostly directed into HMs. This exotic property of HMs enables features like focusing with very subwavelength resolution [10,11], controlling absorption [12], enhancement of spontaneous emission [13], increasing the decay rate of emitters [6], designing quantum and thermal emitters [14]. HMs can also host backwards waves and thus they are utilized for achieving negative refraction as in [15]. As stated in [4], HMs are considered to be promising materials for advancement in the fields of tunable surface plasmon polaritons, super Planckian thermal emission [5], radiative decay engineering [16], and nano-imaging.

HMs attract attention also because they are easy to fabricate using metal-dielectric multilayers or metallic nanowires embedded in dielectric substrates. Also, doped semiconductors [17,18] and conductive oxides used for generating surface plasmons can be used for HM designs in near- and mid-IR frequency bands [15]. In multilayer structures, metal is used as a negative permittivity layer-spaced by dielectric layers, overall creating a

negative permittivity effect for the electric field components tangential to the layers. This effect does not rely on any resonant behavior and thus is a very wide-frequency-band.

In this chapter a multilayer HM design based on stacking dielectric layers and graphene sheets is investigated. A graphene sheet (a one-atom-thick carbon layer) is able to support surface plasmon modes at terahertz frequencies [19–23]. A recent work in [24] introduced the idea of a HM based on graphene-dielectric multilayers, assuming a semi-infinite structure studied at a temperature of 4 K, thus assuming graphene losses negligible, leading to purely real permittivity and wavenumbers. Our analysis instead accounts for losses at a room temperature of 300 K and their effect on (i) the effective permittivity that assumes indeed complex values, (ii) the hyperbolic-like dispersion (it is not exactly hyperbolic), and (iii) on the radiated power by a dipole near the HM surface, where losses play an important role. Moreover, the investigation is focused on practical cases with a finite number of graphene-dielectric layers, and quantitatively show tunability aspects of graphene-based HMs using electrostatic biasing. The study is mainly presented with a detailed study about the dependence of power spectrum emitted by a dipole source in the proximity of the graphene-based HM on the number of layers, as well as on frequency. Alternative to the HM implemented as a graphene-dielectric multilayer studied here, in [25] graphene stripes analogous to a metallic wire medium, are utilized for realizing hyperbolic dispersion in cylindrical wavenumber coordinates, with the aim of designing a hyperlens. The peculiar electronic properties of graphene [26,27], have been investigated for different electromagnetic applications such as lensing [28], transformation optics [29], nanomechanical resonators [30], and solar cells [31]. Moreover, based upon periodic patterning of graphene, bi-periodic and/or multilayered graphene structures were

extensively studied for enhanced transmission [32], optical absorption [33], and tunable metasurfaces in [34], as well as isolators and polarizers in the microwave regime [35–37]. It was shown that crystalline Graphite (the 3D parent of graphene) possess indefinite permittivity at UV frequencies [38].

A graphene sheet, in this chapter, has properties at THz frequencies similar to those of a thin metal film at optical frequencies. In principal, any inductive infinitesimally-thin layer can be used to realize HMs, however, at the terahertz regime, designing inductive layers is difficult due to metallic losses and dispersion introduced by periodically patterned conductive layers. For this aim, metallic meshes are mainly effective only in lower microwave regime [39–41]. On the other hand, the use of highly dispersive metals is practical the optical frequencies below the plasma frequency. Here it is shown that stacking graphene sheets can be utilized for designing tunable HMs in a wide frequency spectrum ranging from millimeter-waves up to tens of terahertz frequencies, encompassing the whole far-infrared band. In Sec. 3.2, the main content is the development of an effective medium approximation (EMA) to facilitate the characterization of graphene-based multilayer structure and its use in possible devices and its limits are assessed. Moreover, in Sec. 3.2 the basic properties of graphene and the associated hyperbolic wavenumber dispersive behavior of multilayer structures composed of graphene-dielectric layers are discussed. In Sec. 3.3 investigation is presented regarding plane wave transmission and reflection for a thin slab made of several graphene sheets, as well as their tunability features, and we also show how EMA is able to describe these properties. In Sec. 3.4 the main aim is to study the radiation of a dipole at the interface of a finite thickness HM and it is shown that the HM is able to enhance the total power radiated by several orders of magnitude, reporting enhancement in the order of 5×10^2

at 2 THz. It is also shown that most of the power is directed into the HM, offering a viable route for wide band and wide incidence-angle super absorption interfaces at far-infrared frequencies, as previously discussed in [3,9,13,42] for optical frequencies. This large enhancement of power emission is shown to be associated to the wide spatial spectrum being able to propagate inside the HM, that would be otherwise evanescent in free space.

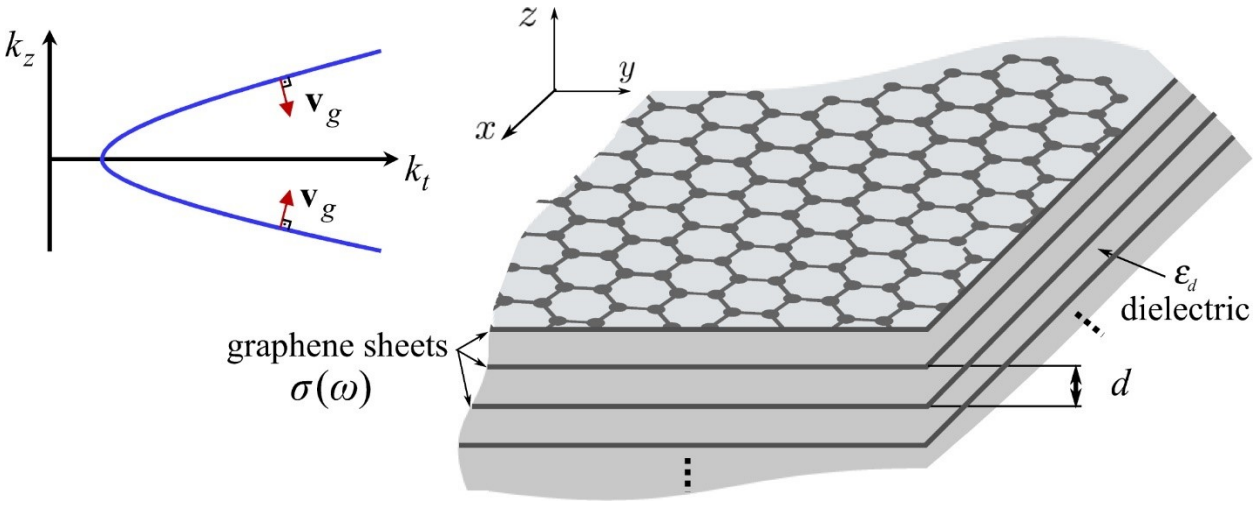

Fig. 3.1 Composite multilayer material made by stacking graphene sheets and dielectric layers. Under certain conditions it exhibits hyperbolic-like iso-frequency wavevector dispersion as depicted in the inset, where v_g indicates the direction of the group velocity.

Sec. 3.2 Tunability of Hyperbolic Metamaterial Made of Graphene and Dielectric Layers

A graphene monolayer is electrically characterized by its surface conductivity $\sigma(\omega, \mu_c)$, where μ_c is the chemical potential related to the electrostatic biasing, which quantifies the electronic transport properties [43]. The frequency dependent conductivity follows the interband (boundelectrons) and the intraband (free-electrons) sum rules [44,45]. Spatial dispersion of graphene has negligible effects, since the graphene lattice constant a ≈0.246 nm is extremely subwavelength at THz frequencies [34]. Therefore, a graphene layer is

modeled by the local isotropic surface conductivity $\sigma(\omega,\mu_c)=\sigma'+j\sigma''$ (assuming time-harmonic fields of the form $e^{j\omega t}$) that is calculated by the Kubo formula

$$\sigma(\omega,\mu_c)=\frac{-j4\pi e^2 k_B T}{h^2(\omega-j2\Gamma)}\left(\frac{\mu_c}{k_B T}+2\ln\left[e^{-\mu_c/(k_B T)}+1\right]\right) - \frac{j4\pi e^2(\omega-j2\Gamma)}{h^2}\int_0^\infty \frac{f_D(-\zeta)-f_D(\zeta)}{(\omega-j2\Gamma)^2-16(\pi\zeta/h)^2}d\zeta, \tag{3.1}$$

where k_B is the Boltzmann constant, *h* is the Planck constant, $f_D(\zeta)=\left[e^{(\zeta-\mu_c)/(k_B T)}+1\right]^{-1}$ is the Fermi-Dirac distribution, and Γ is the phenomenological scattering rate. Throughout our discussion, assuming Γ=0.1 meV, which is within the range of values considered in other studies [21, 37, 46, 47], at room temperature *T*= 300 K. Consider a periodic stack of graphene-dielectric layers, as depicted in Fig. 3.1. Each dielectric spacer has a subwavelength thickness *d* and relative permittivity ε_d. In this premise, it is assumed that graphene sheets are electronically isolated, i.e., the electronic band structure of a graphene sheet is not affected by the neighboring graphene sheets (interlayer electronic coupling mechanisms as well as tunneling effects are ignored, due to the significant thickness of the dielectric with respect to quantum scales). Graphene sheets are modeled as complex lumped admittance layers, due to their extremely subwavelength thickness. Wave propagation in the multilayer structure, depicted in Fig. 3.1, can be modeled using (i) EMA that models the multilayer as a homogeneous medium and (ii) by applying Bloch theory (Chapter 8 in [48]) using the transfer matrix of a unit cell. When applying EMA, the multilayered structure is modeled as a homogeneous uniaxial anisotropic medium (with axis of anisotropy along *z*) whose

effective relative permittivity tensor $\underline{\boldsymbol{\varepsilon}}_{\text{eff}}$ is a diagonal matrix in Cartesian coordinates given as

$$\underline{\boldsymbol{\varepsilon}}_{\text{eff}} = \varepsilon_t \left(\hat{\mathbf{x}}\hat{\mathbf{x}} + \hat{\mathbf{y}}\hat{\mathbf{y}} \right) + \varepsilon_z \hat{\mathbf{z}}\hat{\mathbf{z}}. \tag{3.2}$$

Since a graphene sheet is infinitesimally thin with respect to the dielectric thickness, one may assume that $\varepsilon_z = \varepsilon_d$, because a *z*−directed electric field would not excite any current in the graphene sheet. The transverse effective relative permittivity ε_z is determined as follows, considering a unit cell made of a dielectric layer with dielectric constant ε_d between $z = 0$ and $z = d$, and a graphene sheet at $z = 0$. Within this unit cell one can write $\nabla \times \mathbf{H} = j\omega\varepsilon_0\varepsilon_d \mathbf{E} + \mathbf{J} = j\omega\varepsilon_0 \underline{\boldsymbol{\varepsilon}}_d \mathbf{E}$, where the current density $\mathbf{J}$ [A/m^2] in the graphene sheet is reduced to the surface current along the sheet $\mathbf{J} = \delta(z)\sigma\mathbf{E}_t$, where $\mathbf{E}_t$ is the transverse component of the electric field. Therefore, one has $\underline{\boldsymbol{\varepsilon}}_d = \varepsilon_d \underline{\mathbf{I}} + j\left[\sigma\delta(z) / (\omega\varepsilon_0) \right] \left(\hat{\mathbf{x}}\hat{\mathbf{x}} + \hat{\mathbf{y}}\hat{\mathbf{y}} \right)$, that when averaged over a period along *z* leads to the effective relative "transverse" permittivity ε_t,

$$\varepsilon_t = \varepsilon_t' - j\varepsilon_t'' = \varepsilon_d - j\frac{\sigma(\omega, \mu_c)}{\omega\varepsilon_0 d}. \tag{3.3}$$

The formula for ε_t in Eq. (3.3) could be obtained alternatively by following the method used for homogenization involving thin metal-dielectric layers [49]. Accordingly, a graphene sheet may be treated as a layer with extremely subwavelength, but finite, thickness with bulk properties. Exploiting the continuity of the electric field, along *x* and *y*, at the boundaries between graphene and dielectric layers, and averaging the transverse component of the effective displacement current over a period *d* also leads to Eq. (3.3) (here the effective

displacement current account for the displacement current in the dielectric and the conduction current in the graphene sheets). In Eq. (3.3), it is highlighted that the graphene conductivity is strongly dependent on the frequency and chemical potential. It is important to note that if a graphene sheet has a sufficiently large inductive susceptance, i.e., if $\sigma'' < -\omega\varepsilon_0\varepsilon_d d$, then the effective relative permittivity term $\varepsilon_t = \varepsilon_t' - j\varepsilon_t''$ has a negative real part, i.e., $\varepsilon_t' < 0$. Under this condition, and recalling that $\varepsilon_z' = \varepsilon_d' > 0$, extraordinary waves, with TM^z polarization (magnetic field transverse to z), are allowed to propagate inside the HM, with wavevectors exhibiting iso-frequency hyperbolic dispersion as explained in [3]; whereas ordinary waves with TE^z polarization (electric field transverse to z) are mainly evanescent. This allows for the propagation of TE^z waves with transverse wavenumber $k_t > \omega\sqrt{\mu_0\varepsilon_0\varepsilon_d}$, that would otherwise be evanescent in free space.

To better illustrate the possible homogenized parameters that can be obtained, it is reported in Fig. 3.2 the real and imaginary parts of $\varepsilon_t = \varepsilon_t' - j\varepsilon_t''$ using the EMA formula Eq. (3.3), assuming that graphene sheets are spaced by silica layers with permittivity $\varepsilon_d = 2.2$ and thickness d = 0.1 μm. Note that ε_t' approaches ε_d at higher frequencies due to saturation of the graphene conductivity to its universal value $\pi e^2/(2h)$ [44] which gives a negligible contribution compared to ε_d. Moreover, the imaginary part of the effective permittivity term (ε_t) is remarkably small in a certain frequency band, showing that waves in this composite material can propagate large distances. Indeed, it is known that a graphene layer may support weakly attenuated plasmonic modes in at terahertz frequencies [45]. It is noted that ε_t is very sensitive to the chemical potential μ_c, and it is shown that the zero-crossing

frequency of ε_t', when $\sigma'' = -\omega\varepsilon_0\varepsilon_d d$, occurs at 6.6, 11, and 24.6 THz, for different values of μ_c = 0, 0.1, and 0.4 eV, respectively. The tunability of the proposed HM structure is then quantified, as seen in Fig. 3.3(a) and (b), where the chemical potential and stacking density (thickness of dielectric layer *d*) are varied assuming a frequency of 12 THz. When the dielectric thickness *d* is increased, one should note that ε_t' increases toward 0. Note also that as the chemical potential (tuned by electrostatic biasing) increases ε_t' takes smaller values. Hence, at 12 THz, ε_t' is positive (≈ 2.2) for zero chemical potential, and at higher chemical potential values, ε_t' becomes negative: for example at $\mu_c = 0.5$ eV, with *d*= 0.1 μm, one has $\varepsilon_t' = 9.5$. In summary, a composite material made by layered graphene sheets possesses interesting performance in terms of losses, inductive response, and tunability from millimeter-waves up to mid-infrared frequencies, hard to find in any other known material. This makes it a good candidate for realizing HM designs in the THz range.

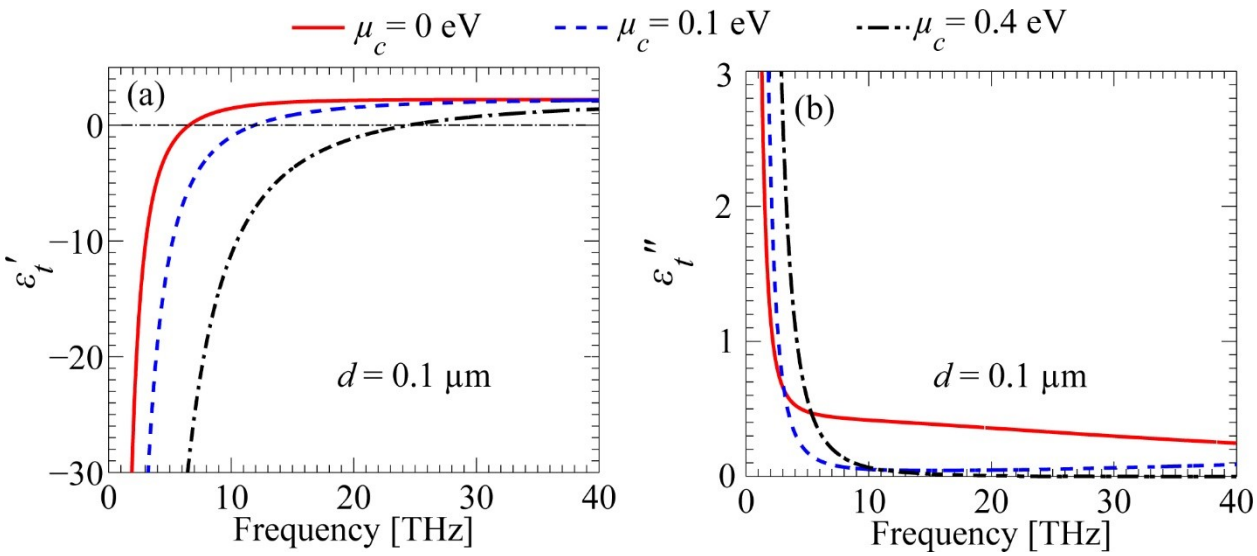

Fig. 3.2 Effective medium complex relative permittivity term $\varepsilon_t = \varepsilon_t' - j\varepsilon_t''$ for biased and unbiased graphene multilayer configuration

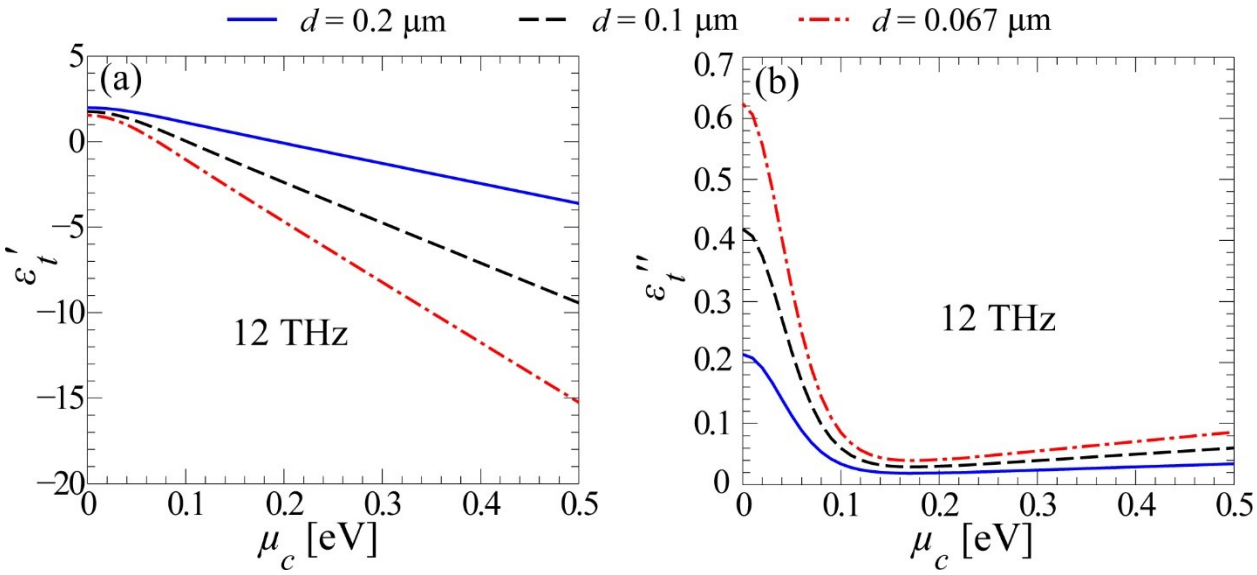

Fig. 3.3 Relative effective medium complex permittivity term $\varepsilon_t = \varepsilon_t' - j\varepsilon_t''$ of graphene HM versus the graphene sheets' chemical potential for various spacer thicknesses at 12 THz.

When considering plane waves propagating in a homogeneous uniaxial anisotropic medium it is useful to decompose them into the modal polarizations TE^z and TM^z. A description using EMA, when valid, gives a neat physical insight into wave propagation in this structure. Wavevector dispersion relations for ordinary (TE^z) and extraordinary (TM^z) waves in a uniaxial anisotropic materials are written as

$$k_z^2 + k_t^2 = \varepsilon_t k_0^2, \quad \text{TE}^z \tag{3.4}$$

$$\frac{k_z^2}{\varepsilon_t} + \frac{k_t^2}{\varepsilon_z} = k_0^2, \quad \text{TM}^z \tag{3.5}$$

where $k_0 = \omega\sqrt{\varepsilon_0\mu_0}$ is the wavenumber in vacuum, and $k_t = \sqrt{k_x^2 + k_y^2}$ thanks to symmetry about the z axis. It is apparent that TM^z waves in a medium with $\varepsilon_t < 0$ exhibit an iso-frequency wavenumber dispersion with hyperbolic shape, as explained in [3,5,50]. This allows the propagation of the extraordinary waves (TM^z) with any transverse wavenumber

$k_t > \sqrt{\varepsilon_d} k_0$ that would be otherwise evanescent in a homogeneous dielectric with permittivity ε_d. However, one should note that TE^z waves are mainly evanescent when $\varepsilon_t < 0$, for any k_t. The proposed graphene-dielectric metamaterial can be used for realizing hyperbolic dispersion with $\varepsilon_t < 0$ and $\varepsilon_z > 0$, and with the present implementation it is not possible to have anisotropy such that $\varepsilon_t > 0$ and $\varepsilon_z < 0$. Elliptic dispersion regime occurring when both $\varepsilon_t > 0$ and $\varepsilon_z > 0$, inherently implies a propagating spectrum with $k_t < \sqrt{\varepsilon_z} k_0$. Considering the multilayered structure depicted in Fig. 3.1, considering the root of k_z^2, solution of Eq. (3.5), that corresponds to a wave whose Poynting's vector is directed toward the graphene-based HM, i.e, in the $-z$ direction, as shown with $\mathbf{v}_g$ in Fig. 3.1. It is assumed here that the z-directed wavenumber may assume complex values, i.e., $k_z = \beta_z - j\alpha_z$, since the graphene conductivity σ is complex, modeling the inhomogeneous plane wave spectrum. Accordingly, a wave that carries power in the $-z$ direction shall have the attenuation constant (α_z) with negative sign, associated to field decay (due to possible losses) along the $-z$ direction. In general, β_z can have both signs, though in our case it is positive, implying that the TM^z mode is a backward wave for $k_t < \sqrt{\varepsilon_d} k_0$, since $\beta_z \alpha_z < 0$ [51, 52].

With the aim of assessing the validity of EMA in Eq. (3.4), we calculate the iso-frequency wavevector dispersion with the more accurate Bloch theory for the periodic structures. This is done by treating each graphene layer as a complex lumped admittance $Y_s = \sigma$ (where the subscript "s" denotes surface) as a shunt load in a transverse equivalent network (TEN, see

Chapters 2 and 3 in [1]). This leads to the dispersion relation as (see Appendix A for more details)

$$\cos\left(k_z d\right) = \cos\left(\kappa_d d\right) + j\frac{1}{2}\sigma Z_d \sin(\kappa_d d), \tag{3.6}$$

where $\kappa_d = \sqrt{\varepsilon_d k_0^2 - k_t^2}$ is the *z*-directed wavenumber of a wave inside the dielectric, $Z_d^{\mathrm{TE}} = \omega\mu_0 / \kappa_d$ and $Z_d^{\mathrm{TM}} = \kappa_d / \left(\omega\varepsilon_0\varepsilon_d\right)$ are the characteristic wave impedances for TE^z and TM^z waves, respectively. Here we report only the dispersion curves that belong to TM^z modes for brevity, since they are those exhibiting hyperbolic-like dispersion. We report in Fig. 3.4(a)-(b), and Fig. 3.4(c)-(d) the plots of $k_z = \beta_z - j\alpha_z$ versus k_t for TM^z waves at 2 and 12 THz, respectively, by applying EMA Eq. (3.5) and Bloch theory Eq. (3.6), for the graphene-dielectic HM (with $\varepsilon_d = 2.2$ and *d*= 0.1 μm), for various chemical potentials μ_c. We plot only the dispersion branch relative to power propagation in the downward direction (see Fig. 3.1). However one should note the $\pm k_z$ symmetry in the solutions of Eq. (3.6). One can observe in Fig. 3.4 that EMA and Bloch theory are in very good agreement for a wide range of transverse wavenumber k_t showing a hyperbolic relation, whereas the curves obtained from the two methods diverge for large k_t and the dispersion curve obtained via Bloch theory shows a switching to a mainly evanescent spectrum after certain k_t. This observation is in accordance with the simplification of the dispersion relation obtained from Bloch theory as follows. Let us consider the special but important case with $\left|\kappa_d d\right| << 1$ and $\left|k_z d\right| << 1$, i.e., the period *d* is subwavelength, with respect to the wavenumber in the dielectric and with respect to the Bloch wavenumber (the second inequality also implies that k_z is far from the

edge of the first Brillouin zone where $\beta_z = \pm\pi / d$). Thus, we approximate Eq. (3.6) by taking into account the first and second order Taylor expansion terms corresponding to the approximations $\cos(\kappa_d d) \approx 1-(\kappa_d d)^2 / 2$ and $\sin(\kappa_d d) \approx \kappa_d d$, that lead to

$$1-\frac{(k_z d)^2}{2} \approx 1-\frac{(\kappa_d d)^2}{2} + j\frac{\sigma}{2} Z_d \kappa_d d. \tag{3.7}$$

After substituting the characteristic impedance by its corresponding value for TE^z and TM^z waves, Eq. (3.7) leads to

$$k_z^2 = \kappa_d^2 - j\frac{\sigma\omega\mu_0}{d}, \qquad \text{TE}^z \tag{3.8}$$

$$k_z^2 = \kappa_d^2 - j\frac{\sigma\kappa_d^2}{\omega\varepsilon_0\varepsilon_d d}. \quad \text{TM}^z \tag{3.9}$$

Substituting $\kappa_d = \sqrt{\varepsilon_d k_0^2 - k_t^2}$ we find that for TE^z

$$k_z^2 = \left[\varepsilon_d - j\frac{\sigma}{\omega\varepsilon_0 d}\right] k_0^2 - k_t^2, \tag{3.10}$$

Similarly for TM^z

$$k_z^2 = \left[\varepsilon_d - j\frac{\sigma}{\omega\varepsilon_0 d}\right] k_0^2 - \left[\varepsilon_d - j\frac{\sigma}{\omega\varepsilon_0 d}\right] k_t^2, \tag{3.11}$$

Note that if one defines an effective transverse permittivity as in (3.3), the wavenumber dispersion just found above become

$$k_z^2 = \varepsilon_t k_0^2 - k_t^2, \qquad \text{TE}^z \tag{3.12}$$

$$k_z^2 = \varepsilon_t k_0^2 - \frac{\varepsilon_t}{\varepsilon_z} k_t^2, \qquad \text{TM}^z \tag{3.13}$$

which are identical to the wavevector dispersion relations provided in (3.4) and (3.5) using EMA.

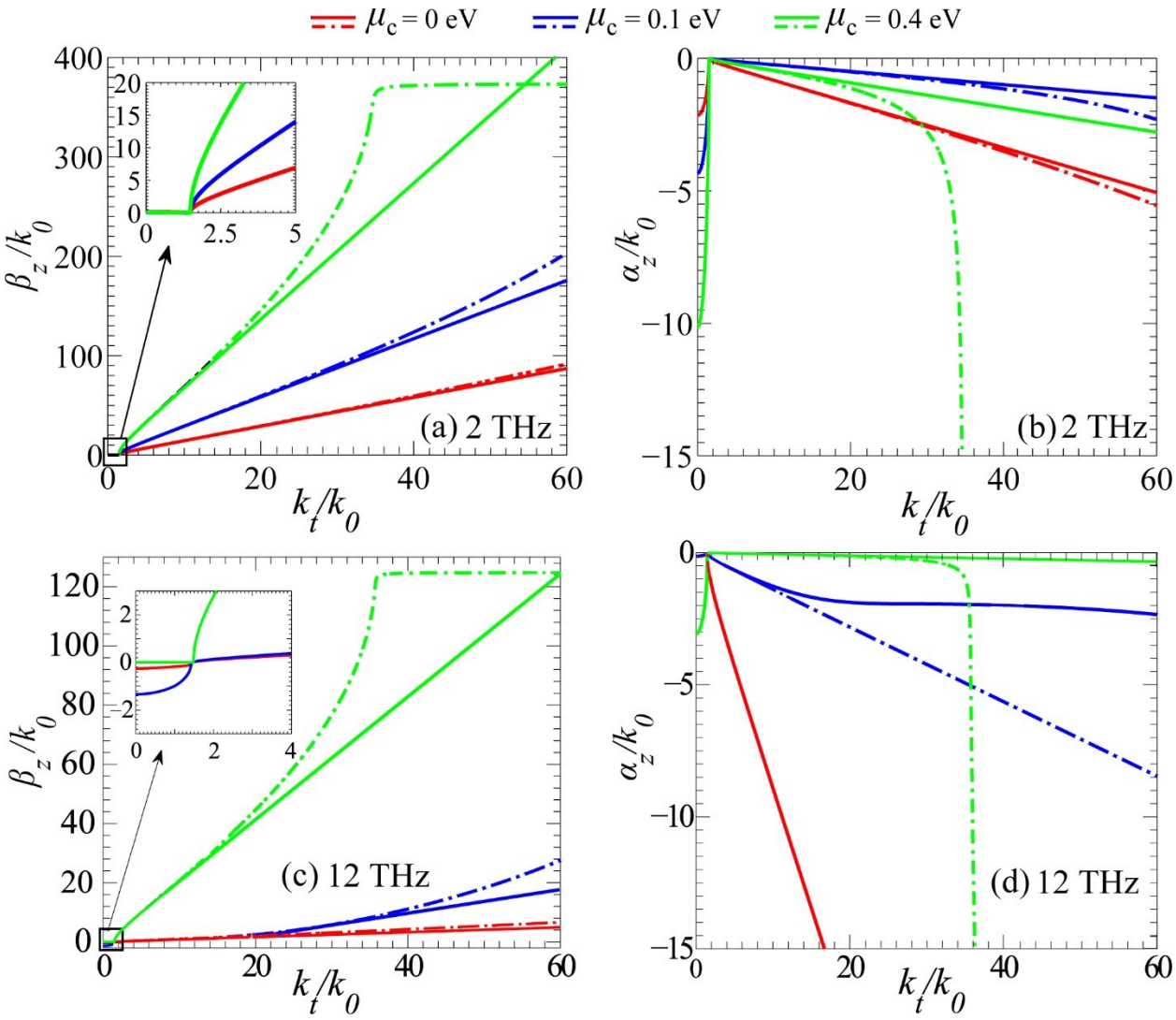

Fig. 3.4 Iso-frequency wavevector dispersion ($k_z = \beta_z - j\alpha_z$) versus k_t computed by both Bloch theory (dashed-dotted lines) and EMA (solid lines), for different chemical potential levels at 2 THz (a,b), and at 12 THz (c,d).

It is clear from the analytical analysis above and from Fig. 3.4 that EMA well describes the wavevector dispersion when $|\kappa_d d| << 1$ and $|k_z d| << 1$, which can be verified when the transverse wavenumber k_t is not too large. For larger and larger values of k_t, the two assumptions would not be valid anymore. In Fig. 3.4, we also report the evolution of the dispersion curves by varying the chemical potential μ_c at 2 THz and 12 THz. For example at 2 THz, when $\mu_c =$ 0.4 eV, the spatial spectrum is bounded by $k_t = 36k_0$ after which α_z increases dramatically. However, by increasing the chemical potential, ε_t' assumes larger negative values and $\beta_z - k_t$ dispersion in Fig. 3.4 evolves to a flatter curve, thus the Brillouin zone edge is reached at larger values of k_t. Note that at larger spatial spectrum, the attenuation constant α_z increases due to finite losses, as shown in Fig. 3.4(b). By tuning the chemical potential, the dispersion characteristics can be controlled, for example, at 12 THz the dispersion for unbiased graphene is elliptic as well as when $\mu_c =$ 0.1 eV. This behavior appears since ε_t' exhibits zero crossing and becomes positive at 6.6 THz and 11 THz, when $\mu_c =$ 0 and $\mu_c =$ 0.1 eV, respectively. However, when the chemical potential is increased to 0.4 eV, hyperbolic dispersion arises at 12 THz, as shown in Fig. 3.4(c)-(d) where the inset of Fig. 3.4(c) shows the elliptic behavior for $k_t > \sqrt{\varepsilon_d} k_0$. At high frequencies where the conductivity saturates to its universal value, the TM^z plasmonic modes are extremely confined to graphene layers (σ'' becomes very small) and higher frequencies, once $\sigma'' > 0$, graphene layers are incapable of supporting those modes [21]. Hence, the spectrum $k_t > \sqrt{\varepsilon_d} k_0$ becomes mainly evanescent at frequencies with $\varepsilon_t' > 0$. In other words, after ε_t' exhibits a zero-crossing and becomes positive, the wavevector dispersion becomes elliptic.

Sec. 3.3 Plane-wave Scattering Through a Thin Film of Graphene-based Hyperbolic Metamaterial

A finite thickness graphene-dielectric multilayer film is considered comprising *N* graphene sheets stacked with silica SiO_2 dielectric spacer, such that a graphene sheet is at the topmost layer. The thickness of each SiO_2 spacer is 0.1 μm, and the total multilayered film thickness is $D = Nd$. For simplicity, all graphene layers are biased equally using a constant electrostatic potential [34]. For practical consideration, suppose that a thin film of silica (in the order of 100 nm) is deposited on an epitaxially-grown graphene monolayer repeatedly until creating an *N* layer stack; though larger thicknesses could be considered, it is rather simple to achieve the biasing range (μ_c up to 0.5 eV) using relatively lower electrostatic potential for smaller thicknesses [34, 53].

We investigate reflection and transmission under normal plane wave incidence, and at 30° oblique incidence for both TE^z and TM^z polarizations (here $k_t = k_0 \sin\left(\theta^i\right)$, where θ^i is the incidence angle). Reflection and transmission coefficients are reported using the transfer matrix method (solid lines), and using EMA (circles) as well, for the two cases with $N = 10$ ($D = 1$ μm) and $N = 20$ ($D = 2$ μm), when $\mu_c = 0$ eV and 0.4 eV in Fig. 3.5 and Fig. 3.6, respectively. As discussed in Sec. 3.2, at lower frequencies, TE^z waves are evanescent for any k_t when $\varepsilon_t' < 0$, while for TM^z waves the iso-frequency wavenumber dispersion is hyperbolic (when $\varepsilon_t' < 0$), consequently, a plane wave impinging on the structure with $k_t < \sqrt{\varepsilon_d} k_0$ is very weakly transferred, specifically by evanescent coupling. This property is demonstrated in Fig. 3.5 at frequencies lower than 6 THz, and in Fig. 3.6 at frequencies lower than 24.6 THz. However,

after ε_t' exhibits a zero-crossing and becomes positive, the plane wave is able to propagate, and the hyperbolic wavevector dispersion turns into elliptic (thus waves with $k_t < \sqrt{\varepsilon_d} k_0$ can propagate).

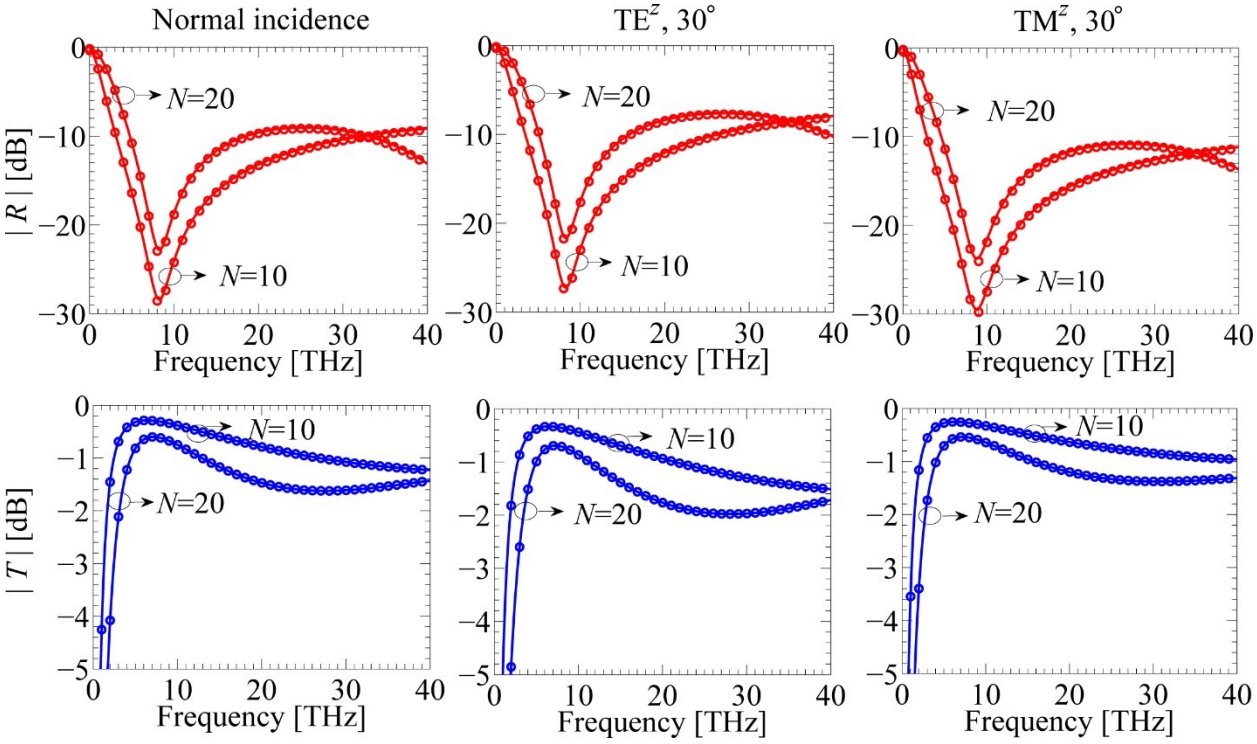

Fig. 3.5 Reflection and transmission versus frequency for a finite thickness graphene-silica multilayered HM, at normal, and oblique incidence for both TE^z and TM^z polarizations, calculated by transfer matrix method (solid lines) and EMA (circles) when graphene layers are unbiased, i.e., $\mu_c = 0$ eV.

The transmission peak for normal incidence occurs when the effective ε_t' is near unity (matched to the free space, where the losses are negligible) for $\mu_c = 0$ eV at ≈ 8 THz (reported in Fig. 3.5) and for $\mu_c = 0.4$ eV at ~ 33 THz (reported in Fig. 3.6); this is in accordance with the effective ε_t' plotted in Fig. 3.2(a). It is clear that changing the chemical potential of the graphene layers offers great tunability and possibility to control the transmission peak and spectrum. EMA is a good tool to describe plane wave interaction with a graphene-dielectric multilayer thin film, for small

dielectric thickness d. In order to explore the validity of EMA for thicker dielectric spacers, we report in Fig. 3.7 the reflection and transmission coefficients for 10 layers of graphene-dielectric layers with varying thickness d, at 10 THz, assuming $\mu_c = 0.4$ eV. It is shown that EMA yields a noticeable deviation from transfer matrix calculations when $d > 0.2\lambda_0$. Note that in Fig. 3.7 the transition from hyperbolic to elliptic dispersion occurs at $d = 0.02\lambda_0$, which implies $\varepsilon_t' \approx 0$.

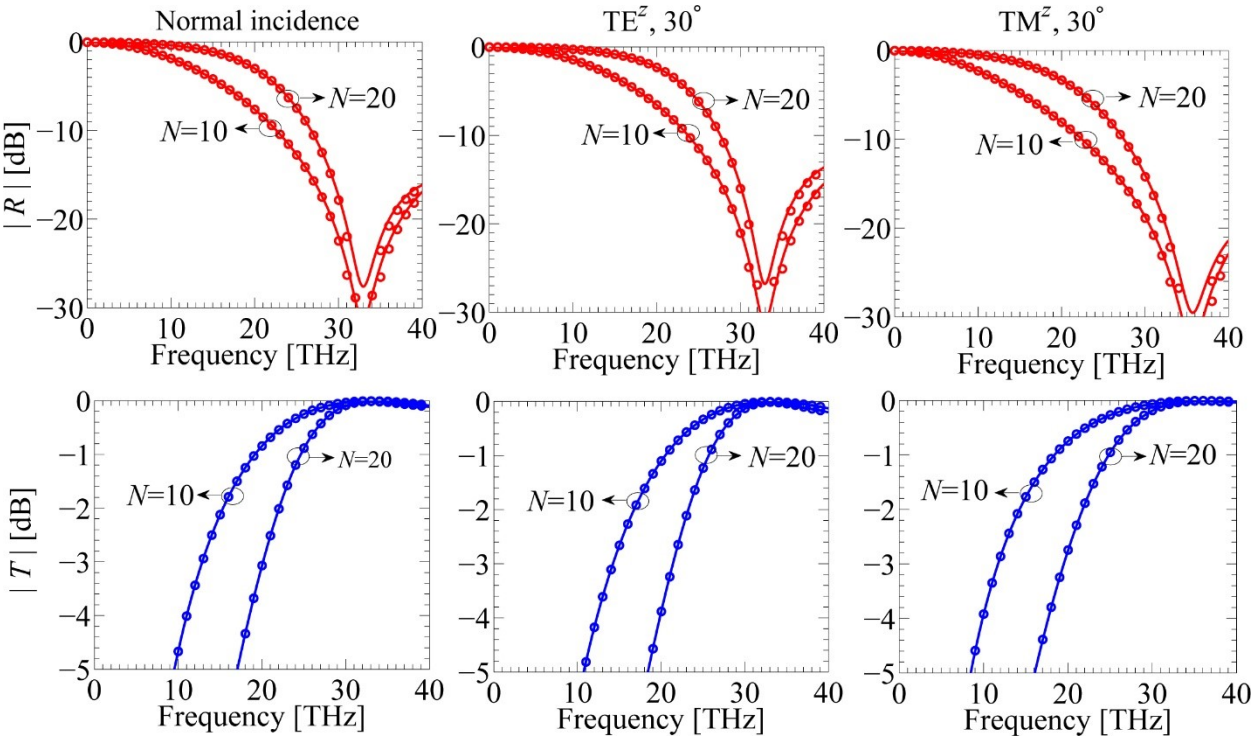

Fig. 3.6 Reflection and transmission versus frequency, for the same set of parameters as Fig. 3.5, except that now graphene layers are biased with $\mu_c = 0.4$ eV.

In particular, these results show two remarkable facts: (i) EMA agrees well with transfer matrix calculations for a wide range of frequencies and dielectric thicknesses, (ii) transmission and reflection by the graphene-based multilayered structure can be effectively tuned by electrostatic biasing. It is evident that graphene layers despite controlling

transmission with such small thicknesses, at the same time can be designed to be almost transparent to plane wave excitation [32].

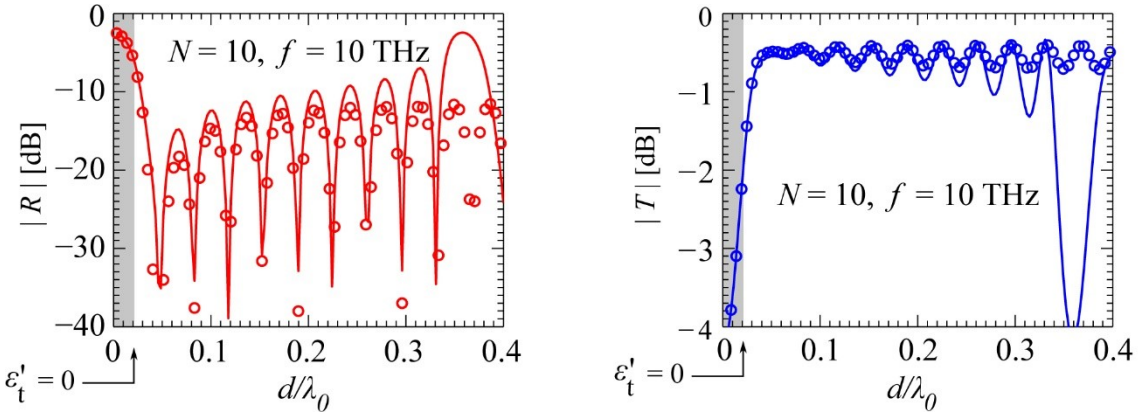

Fig. 3.7 Reflection and transmission of a 30° TM^z wave from a 10 layer graphene-dielectric stack at 10 THz with variable spacer *d*, based on transfer matrix (solid lines) and EMA (circles).

In this Section we have investigated reflection and transmission, and how this is predicted by EMA, for an incident plane wave, however a source or scatterer near the HM interface is able to generate a very wide spatial spectrum of plane waves, including the spectrum with $k_t > k_0$, which would be evanescent in free space. In the next Section we show how this wide spectrum is able to propagate inside the HM, similarly to what was done in [3] for a HM at optical frequencies made of dielectric and metallic layers.

Sec. 3.4 Enhancement of Emitted Power by an Impressed Dipole on the Surface of Graphene-based Hyperbolic Metamaterial

We investigate the power emitted by a transverse dipole located at a distance *h* above the graphene-silica multilayered HM as depicted in Fig. 3.8(a), over a silicon substrate (sufficiently thick to be assumed infinitely long, with relative permittivity $\varepsilon_{\mathrm{Si}} = 11.7$). We assume here a unit cell of the HM consisting of a 0.1-μm thick silica layer stacked with a sheet

of graphene sheet on top. We calculate the power emitted by the transverse dipole located at z = 0 as in Fig. 3.8(a), by using the spatial spectral formalism of TE^z and TM^z waves as outlined in [1]. The total power $P_{\text{tot}} = P_{\text{up}} + P_{\text{down}}$ emitted by the transverse dipole illustrated in Fig. 3.8 is decomposed into the power terms directed toward the +z and −z directions (P_{up} and P_{down}, respectively) that are found by the spectral integrals

$$P_{\text{up,down}} = \frac{\omega^2 |\mathbf{p}_t|^2}{8\pi} \int_0^\infty \left(p_{\text{up,down}}^{\text{TE}} + p_{\text{up,down}}^{\text{TM}} \right) dk_t, \tag{3.14}$$

and $p(k_t)$ is the spectral power either in the "up" or "down" direction, with transverse wavenumber k_t and $|\mathbf{p}_t|$ is magnitude of the transverse electric dipole moment. The spectral power $p_{\text{up,down}}^{\text{TE,TM}}(k_t)$ can be written as

$$p_{\text{up,down}}^{\text{TE,TM}}(k_t) = \frac{\text{Re}\left\{ Y_{\text{up,down}}^{\text{TE,TM*}}(k_t) \right\}}{\left| Y_{\text{up,down}}^{\text{TE,TM*}}(k_t) \right|^2} k_t. \tag{3.15}$$

Here Y represents the equivalent admittance of TE^z/TM^z waves seen at the location of the dipole either toward free space or toward the HM (indicated by the subscripts "up" and "down", respectively), whereas $Y_{\text{tot}} = Y_{\text{up}} + Y_{\text{down}}$, and "*" denotes the complex conjugate. In particular, for what concerns free space (up), the terms $Y_{\text{up}}^{\text{TE,TM}}$ are straightforwardly the TE^z and TM^z wave admittances in free space given by $Y_{\text{up}}^{\text{TE}} = \kappa_0 / (\omega\mu_0)$, and $Y_{\text{up}}^{\text{TM}} = (\omega\varepsilon_0) / \kappa_0$ where $\kappa_0 = \sqrt{k_0^2 - k_t^2}$ is the wavenumber along the z axis in free space. The calculation of the admittance Y_{down}, for either TE^z or TM^z waves, is done by translating $Y_{\text{HM},N}$ which is the

admittance toward $-z$ direction, shown in Fig. 3.8(b), evaluated at the surface of HM (at $z=-h$), to z = 0 by the simple formula

$$Y_{\text{down}} = Y_0 \frac{jY_0 \sin(\kappa_0 h) + \cos(\kappa_0 h) Y_{\text{HM},N}}{Y_0 \cos(\kappa_0 h) + j \sin(\kappa_0 h) Y_{\text{HM},N}}. \tag{3.16}$$

The calculation of $Y_{\text{HM},N}$ (see Fig. 3.8), for either TE^z or TM^z waves, is done by using the transfer matrix of N unit cells, and representing the silicon substrate at the bottom with a TE^z/TM^z wave admittance, as detailed in Appendix B. When using EMA, the multilayer structure is treated as an anisotropic dielectric with relative permittivity in Eq. (3.2). In Fig. 3.9 and Fig. 3.10 (for $\mu_c = 0$ eV and $\mu_c = 0.4$ eV, respectively, and assuming a dipole distance h = 2 μm) we report two power ratios aiming at showing their enhancement: (i) the total power $P_{\text{tot}} = P_{\text{up}} + P_{\text{down}}$ emitted by the dipole normalized by the power emitted by the same dipole in free space $P_{\text{free space}}$; (ii) the ratio of the power directed downward to the HM, P_{down} , and the power directed into the upper free space, P_{up}, for four different cases where the number of graphene sheets is changed as N = 1, 3, 10 and $N \to \infty$, as well as for a transverse dipole at a distance h above a silicon substrate (dashed lines) for comparison purposes.

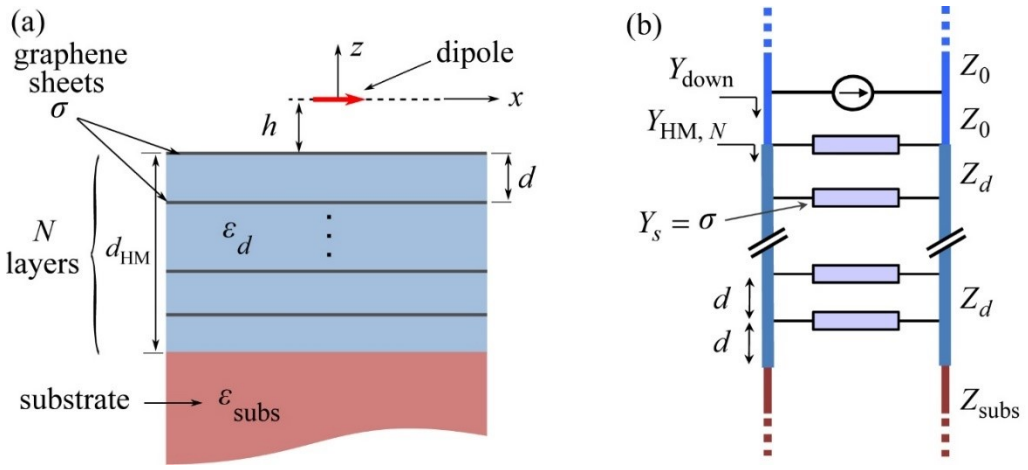

Fig. 3.8 (a) Dipole near-field emission over a finite thickness multilayer graphene HM over of a substrate, and (b) the its transverse equivalent network (TEN) for every spectral wave (both TE^z and TM^z).

The ratio $P_{\text{tot}} / P_{\text{free space}}$ also represents the increase of the local density of states (LDOS) with respect to LDOS at a point in free space [5, 50, 54], and this is also referred to as Purcell effect [6, 24]. We model the HM with thickness *Nd* via both the more accurate transfer matrix method (denoted by lines in the figure) and EMA (denoted by circles), and provide the results in Fig. 3.9(a) and (b) for unbiased graphene ($\mu_c = 0$ eV), and in Fig. 3.10 for biased graphene ($\mu_c = 0.4$ eV). In Fig. 3.9 one can observe that, at the lowest frequency 0.1 THz, there is a clear trend showing that when the number of layers (*N*) increases the ratio $P_{\text{down}} / P_{\text{up}}$ also increases from ~ 10^6 up to ~ 2.7×10^8, when using calculations based on the transfer matrix method. Moreover, in the lower frequency range, EMA overestimates $P_{\text{down}} / P_{\text{up}}$ by almost one order of magnitude, as also discussed in [3] for a different HM configuration; however, as the frequency increases EMA and the transfer matrix method agree well. In Fig. 3.9(b), we observe the same disagreement of the transfer matrix calculations and EMA at lower frequencies, and it is clearly seen that the normalized emitted

power ($P_{\text{tot}} / P_{\text{free space}}$) is ~ at the lowest frequency 0.1 THz and drops linearly as the frequency increases. $P_{\text{down}} / P_{\text{up}}$ exhibits a very sharp drop for N = 1 after around 1 THz, for N = 3 after about 2 THz, for N = 10 after 4 THz, and for $N \to \infty$ after 6 THz (note that the hyperbolic to elliptic dispersion curve transformation occurs at 6.6 THz when $\mu_c = 0$ eV obtained via EMA, see Fig. 3.2, in very good agreement with the $N \to \infty$ case).

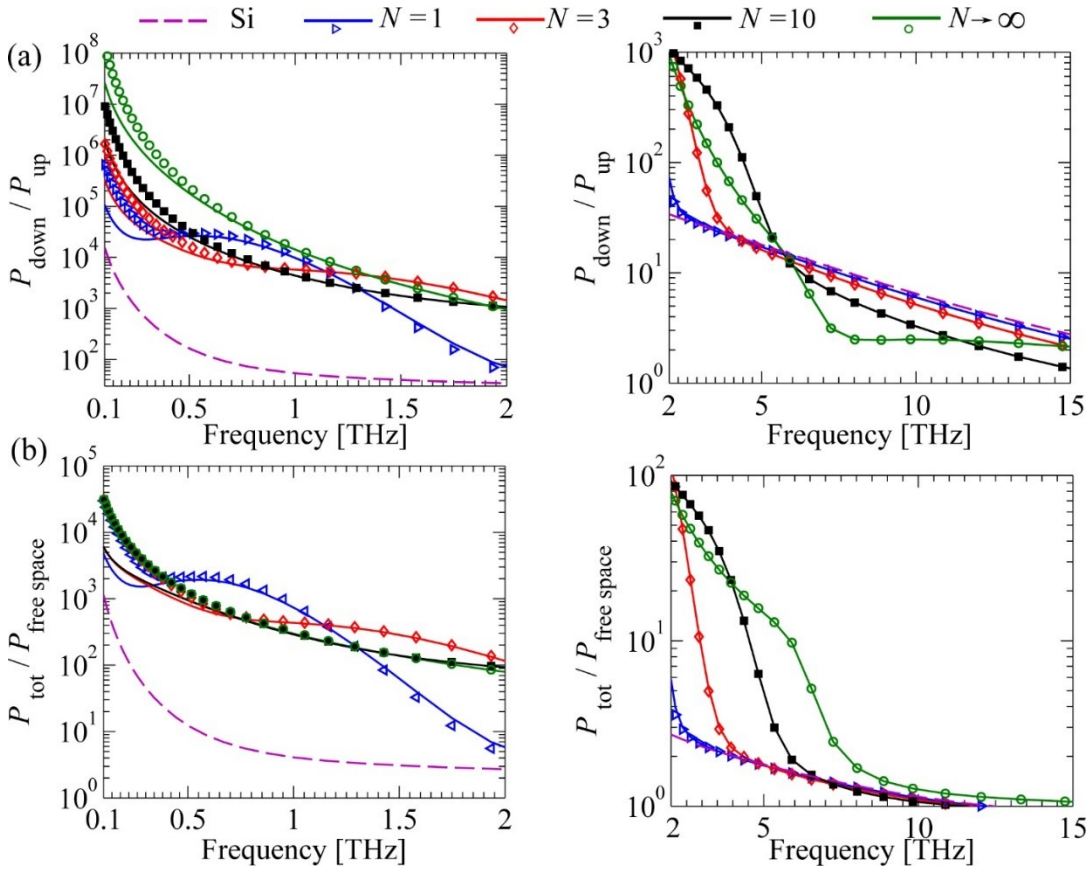

Fig. 3.9 (a) Ratio between power emitted in the lower space with the one in the upper space, $P_{\text{down}} / P_{\text{up}}$, and (b) the ratio $P_{\text{tot}} / P_{\text{free space}}$ related to the transverse dipole located near the interface of free space and graphene-based HM made by N graphene layers on top of Si substrate. Calculations done via multilayer transfer matrix method (lines) and via EMA (markers) when chemical potential is $\mu_c = 0$ eV.

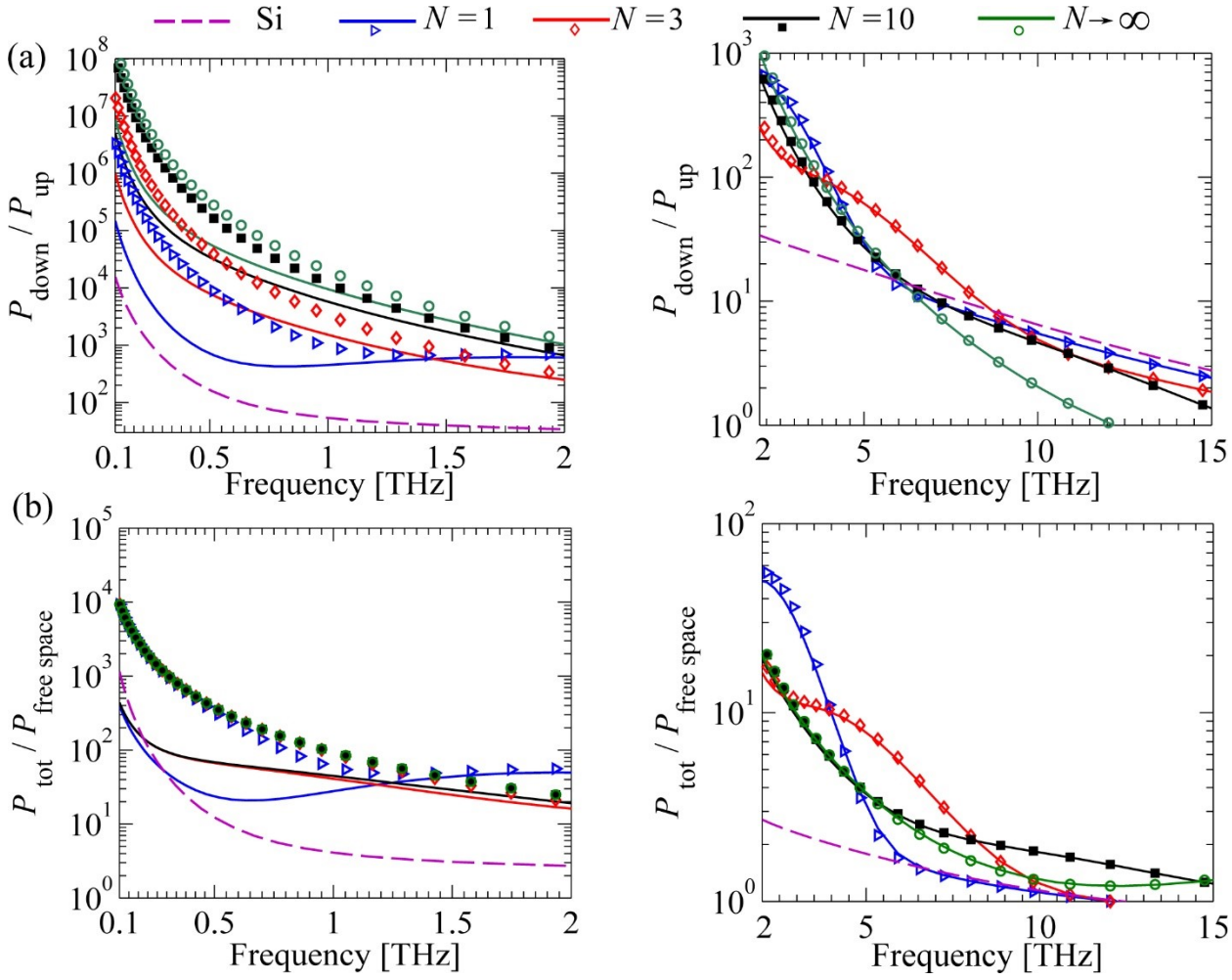

Fig. 3.10 (a) Ratio $P_{\text{down}} / P_{\text{up}}$ and (b) ratio $P_{\text{tot}} / P_{\text{free space}}$ for the same set of parameters in Fig. 3.9, but when chemical potential is $\mu_c = 0.4$ eV.

When the chemical potential is increased to $\mu_c = 0.4$ eV, the "transverse" permittivity ε'_t decreases to further negative values and the frequency of hyperbolic to elliptic dispersion curve transformation shifts from 6.6 THz ($\mu_c = 0$ eV) to 24.6 THz ($\mu_c = 0.4$ eV). In Fig. 3.10(a), at lower frequencies one can observe that $P_{\text{down}} / P_{\text{up}}$ is increased by one order of magnitude for all cases whereas $P_{\text{tot}} / P_{\text{free space}}$ decreases by almost one order of magnitude when compared to the case with $\mu_c = 0$ eV. Moreover the frequency where $P_{\text{tot}} / P_{\text{free space}}$

exhibits a sharp decrease shifts to a higher frequency when the chemical potential is increased to 0.4 eV in agreement with the change in the frequency of hyperbolic to elliptic dispersion curve transformation, as illustrated from Fig. 3.4(c). As seen in Fig. 3.10(a) and (b) both the enhancement of emitted power and the ratio of power directed to the $-z$ direction are much larger than the Si-substrate case for a wide frequency band (1–6 THz) in the presence of graphene-dielectric. The interesting features in Fig. 3.9 and Fig. 3.10 are related to the power spectrum in Eq. (3.15), which is described in the following.

We report the emitted power spectrum for TM^z waves (solid lines), $p^{\mathrm{TM}}(k_t) = p_{\mathrm{up}}^{\mathrm{TM}}(k_t) + p_{\mathrm{down}}^{\mathrm{TM}}(k_t)$, versus normalized transverse wavenumber $k_t d/\pi$ at 0.1 in Fig. 3.11(a) and 3 THz in Fig. 3.11(b), varying the number of graphene-dielectric layers assuming $\mu_c =$ 0 eV, and for a better visualization we provide Fig. 3.11(a) and (b) in both logarithmic and linear scales for the horizontal axis, in the left and right panels, respectively. For comparison we also show the power spectrum $p^{\mathrm{TE}}(k_t) = p_{\mathrm{up}}^{\mathrm{TE}}(k_t) + p_{\mathrm{down}}^{\mathrm{TE}}(k_t)$ for N =1 and $N \to \infty$ (dashed lines). At these two frequencies the composite multilayer exhibits hyperbolic dispersion for TM^z waves and propagation inside the HM occurs for $k_t > \sqrt{\varepsilon_d} k_0$. We observe in Fig. 3.11(b) that in the high k_t spectrum, there are a larger number of spectral peaks when N increases; eventually yielding a continuous distribution of large spectral intensities when $N \to \infty$. This explain the advantage of having a large number of layers. Moreover when $N \to \infty$, one can notice that the power spectrum starts to rise strongly after $k_t = \sqrt{\varepsilon_d} k_0$, in agreement with the propagating spectrum's lower limit in the hyperbolic dispersion diagrams in Fig. 3.4. We would like to emphasize that plots in linear scale in Fig.

3.11 clearly show that the propagating power spectrum in the large k_t region is very wide and therefore it strongly contributes to the spectral integral in Eq. (3.14). Note that the upper limit of the power spectrum, cut-off at $k_{t,\max}$, can be determined by evaluating the evanescent decay in free space between the dipole at $z = 0$ and the surface of the composite material at $z = -h$, given by $\exp\left(-\sqrt{k_t^2 - k_0^2}h\right)$. For example, by setting $\exp\left(-\sqrt{k_t^2 - k_0^2}h\right) = \xi$, where ξ is a predetermined small number, we can consider the power spectrum negligible when $k_t > k_{t,\max}$. It is important to note that for $h \ll \lambda_0$ this upper wavenumber limit $k_{t,\max}$ is independent of the operating frequency when $k_{t,\max} >> k_t$, because in this case $\exp\left(-\sqrt{k_{t,\max}^2 - k_0^2}h\right) \approx \exp\left(-k_{t,\max}h\right)$. These considerations explain why all spectral curves decay with very similar profile for very large k_t and therefore it is imposed mainly by the dipole distance h, for both frequencies examined in Fig. 3.11(a) and (b), i.e., at 0.1 and 3 THz.

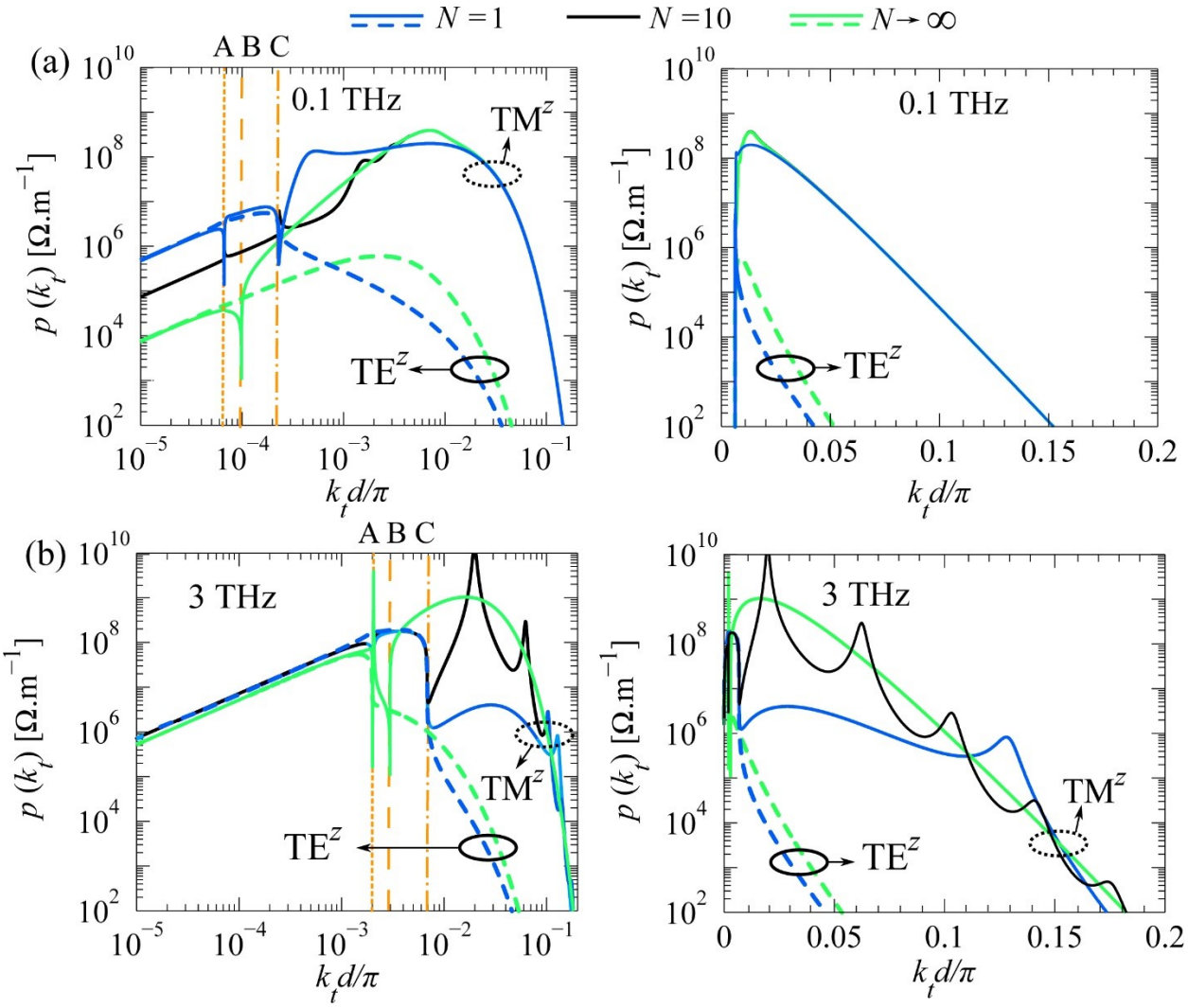

Fig. 3.11 Emitted power spectrum $p^{\mathrm{TM}}(k_t) = p_{\mathrm{up}}^{\mathrm{TM}}(k_t) + p_{\mathrm{down}}^{\mathrm{TM}}(k_t)$ in Eq. (3.15), solid lines, versus normalized traverse wavenumber $k_t d/\pi$ at (a) 0.1 THz, and (b) 3 THz, for different number of graphene-dielectric layers: N = 1, 10, and $N \to \infty$. For comparison we also show the power spectrum $p^{\mathrm{TE}}(k_t) = p_{\mathrm{up}}^{\mathrm{TE}}(k_t) + p_{\mathrm{down}}^{\mathrm{TE}}(k_t)$ for N =1 and $N \to \infty$ (dashed lines). The points A, B, and C denote the spectrum points $k_0 d/\pi$, $\sqrt{\varepsilon_d}\,k_0 d/\pi$, and $\sqrt{\varepsilon_{\mathrm{Si}}}\,k_0 d/\pi$, respectively. Left panel plots have a horizontal logarithmic scale whereas right panel plots have a horizontal linear scale.

At low frequency, in Fig. 3.11(a) all curves with different N, tend to exhibit the same behavior at the large k_t in particular when $(k_t d/\pi) > 10^{-2}$. The reason of this low frequency

property, that does not occur at higher frequency in Fig. 3.11(b), is explained as follows. Propagation inside such multilayer stack consists in strong evanescent coupling between adjacent graphene sheets [23, 32], that is approximately proportional to $\exp\left(-\sqrt{k_t^2-\varepsilon_d k_0^2}\,d\right)$. Considering now the large k_t region where the power spectrum $p^{\mathrm{TM}}(k_t)$ is intense in Fig. 3.11(a), the exponential interlayer decay becomes stronger, at fixed k_t, when the frequency decreases (i.e., when $\varepsilon_d k_0^2$ decreases). Thus, at low frequencies, less power is coupled to lower graphene layers, whereas most of the power is coupled to losses in the first graphene sheet closest to the dipole, implying that the number of layers becomes less effective on the power spectrum for large k_t and hence on the total emitted power integral in Eq. (3.14). For example, the case with 0.1 THz in Fig. 3.11(a), the total TM^z power emitted by the dipole is dominated by the wide power spectrum region $\left(5\times10^{-3}\pi/d\right)<k_t<k_{t,\max}$ which is weakly dependent on the number of layers. Under this low frequency condition, we observe that the total TM^z emitted power becomes proportional to ω^2, independently on the number of layers, in agreement with the findings in [21] for a single graphene layer. A similar trend occurs for the power emitted as TE^z waves at these lower frequencies, though it is several orders of magnitude weaker than TM^z cases for large k_t (see the dashed curves in Fig. 3.11). Note that, instead, the free space emitted power by a dipole $|\mathbf{p}_t|\omega^4\eta_0/\left(12\pi c^2\right)$ is proportional to ω^4. Comparing the low frequency trends of the power emitted in free space with the one in presence of the HM one can explain the strong increase of the power ratio $\left(P_{\mathrm{tot}}/P_{\mathrm{free\ space}}\right)\propto\omega^{-2}$ in Fig. 3.10(b) as frequency decreases.

It is also important to provide a physical insight into the effect of the distance h on the power emitted by the impressed transverse dipole. In Fig. 3.12, we provide the plots of $P_{\text{tot}} / P_{\text{free space}}$ and $P_{\text{down}} / P_{\text{up}}$ at 2 THz versus the dipole's distance h for the semi-infinitely periodic ($N \to \infty$) graphene-dielectric multilayered structure with $\mu_c = 0$ eV and $\mu_c = 0.4$ eV, obtained both via EMA (markers) and the transfer matrix method (lines). In Fig. 3.12(a) and (b) we report the power ratios $P_{\text{down}} / P_{\text{up}}$ and $P_{\text{tot}} / P_{\text{free space}}$ for both HMg and HMd configurations, denoting a HM with graphene (HMg) and dielectric (HMd) as topmost layer, respectively [3,49]. We notice that the responses of both HMg and HMd configurations are very similar while the HMg has a slightly larger $P_{\text{down}} / P_{\text{up}}$ and $P_{\text{tot}} / P_{\text{free space}}$ for smaller h, in agreement with the observations in [49]. For the smallest reported distance h = 0.2 μm, the emitted power ($P_{\text{tot}} / P_{\text{free space}}$) and $P_{\text{down}} / P_{\text{up}}$ are maximum. However, for small h, EMA overestimates the reported parameters by one to two orders of magnitude for small h, as demonstrated in [49], whereas for h > 1 μm both methods agree well at the given frequency. Using the transfer matrix method we find the maximum ratio $P_{\text{down}} / P_{\text{up}} \approx 2 \times 10^6$ when $\mu_c =$ 0 eV, and it decreases to $P_{\text{down}} / P_{\text{up}} \approx 5 \times 10^5$ as a result of increasing $Y_{\text{down}}^{\text{TM}}$ when ε_t' possesses more negative values. A similar change is also observed such that the maximum ratio $P_{\text{tot}} / P_{\text{free space}}$ becomes $\approx 2 \times 10^4$ when $\mu_c = 0$ eV, and it decreases to $P_{\text{tot}} / P_{\text{free space}} \approx 4 \times 10^2$ when $\mu_c = 0.4$ eV. The total emitted power decreases as the distance h increases, due to the stronger evanescent decay of high k_t spectrum. However, since the distance h is subwavelength, still a lot of power is able to couple into the HM. The power ratio

$P_{\text{down}} / P_{\text{up}}$ also exhibits a decrease with increasing h showing the key role of the coupling of the evanescent spectrum in free space to the propagating spectrum in the HM. We finally note from the observations in Fig. 3.12 that the accuracy of EMA is influenced by changing the values of μ_c, implying the effect of ε_t on EMA's validity.

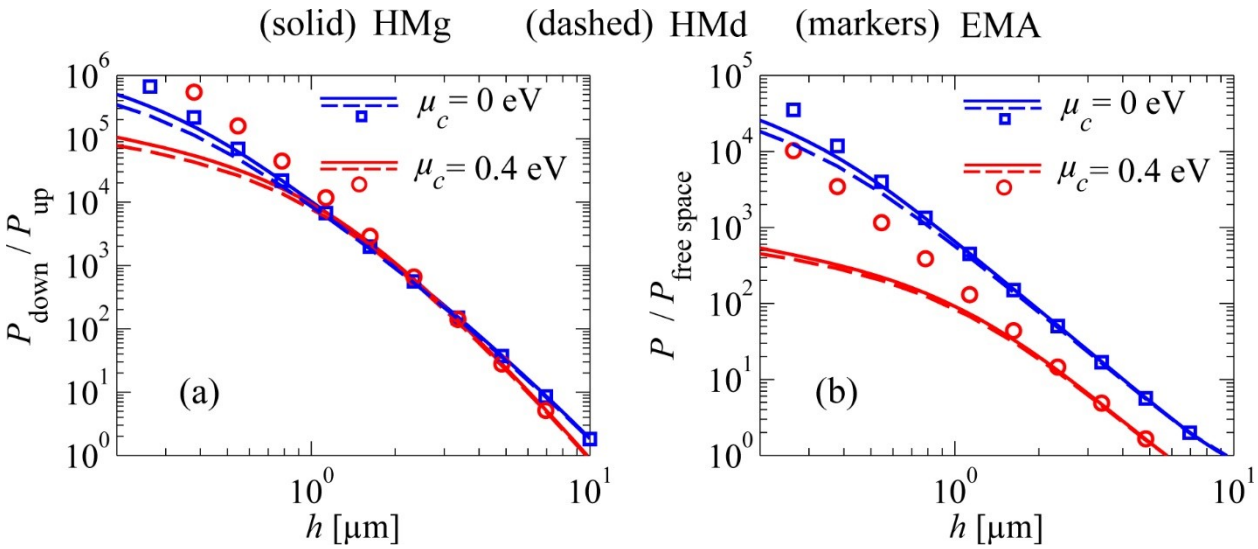

Fig. 3.12 (a) Ratio $P_{\text{down}} / P_{\text{up}}$ and (b) ratio $P_{\text{tot}} / P_{\text{free space}}$ related to the transverse dipole located near the interface of free space and a semi-infinite graphene-based HM at 2 THz plotted versus dipole distance h, for different chemical potential μ_c values obtained via transfer matrix method (lines) and EMA (markers).

In summary, we have shown that the power emitted by a dipolar source in the proximity of a graphene-based HM is strongly enhanced, and that it can be effectively tuned by electrostatically biasing the graphene sheets, which makes this HM a promising candidate for tunable applications in the far-infrared frequencies.

Sec. 3.5 Conclusion

We have investigated a novel design of HM for far-infrared frequencies based on graphene layers. The multilayer structure has been analyzed using EMA which, based on a permittivity

homogenization model, predicts the HM features at far-infrared frequencies. We have quantitatively shown the capability of tuning the composite material properties via chemical potential of graphene. We have investigated plane wave interaction with a thin film made by few graphene sheets, and showed how the transmission frequency spectrum can be tuned. We have assessed the validity of EMA for both plane wave incidence and near-field radiation from a dipole, and we have shown that under certain conditions EMA is in good agreement with the transfer matrix analysis. In the last part of the chapter, we have shown that a very wide spatial spectrum emitted by an electric dipole is allowed to couple into the graphene-based HM, that would be otherwise evanescent in free space. This generates two interesting main features: (i) the power emitted by the dipole is strongly enhanced (up to several orders of magnitude) by the presence of the graphene-based HM, and (ii) most of the power is directed into the HM, also for relative subwavelength HM thicknesses realized with only a few graphene sheets. These properties seem to enable the use of this tunable graphene-based HM to efficiently absorb mm-waves and terahertz frequencies, and give rise to other possible applications including super resolution lenses.

Appendix A Derivation Steps Regarding Transfer Matrix Method

The transfer matrix [T_{unit}] of a unit cell composed of a graphene sheet (modeled as a lumped shunt complex admittance $Y_s = \sigma$) and a dielectric layer of thickness *d* (modeled as a transmission line) for TE^z/TM^z waves can be written as (assuming time-harmonic fields of the form $e^{j\omega t}$)

$$
\begin{aligned}
\left[\mathrm{T}_{\mathrm{unit}}\right] &= \begin{bmatrix} A_{\mathrm{unit}} & B_{\mathrm{unit}} \\ C_{\mathrm{unit}} & D_{\mathrm{unit}} \end{bmatrix} = \\
&= \begin{bmatrix} 1 & 0 \\ \sigma & 1 \end{bmatrix} \begin{bmatrix} \cos(\kappa_d d) & jZ_d \sin(\kappa_d d) \\ \dfrac{j}{Z_d}\sin(\kappa_d d) & \cos(\kappa_d d) \end{bmatrix} = \\
&= \begin{bmatrix} \cos(\kappa_d d) & jZ_d \sin(\kappa_d d) \\ \dfrac{j}{Z_d}\sin(\kappa_d d) + \sigma\cos(\kappa_d d) & j\sigma Z_d \sin(\kappa_d d) + \cos(\kappa_d d) \end{bmatrix},
\end{aligned}
\tag{3.17}
$$

where $\kappa_d = \sqrt{\varepsilon_d k_0^2 - k_t^2}$ is wavenumber along the *z* axis inside the dielectric, and for TE^z and TM^z waves: $Z_d^{\mathrm{TE}} = \omega\mu_0 / \kappa_d$ and $Z_d^{\mathrm{TM}} = \kappa_d / \omega\varepsilon_d\varepsilon_0$, respectively. We are interested in determining the Bloch wavenumber k_z in the *z*-direction, that describes layer to layer propagation. Following the simple procedure in [48], the wavevector dispersion relation can be obtained from the solution of the eigenvalue problem $\left|\left[\mathrm{T}_{\mathrm{unit}}\right] - e^{-jk_z d}\left[\mathrm{I}\right]\right| = 0$, where [I] is the identity matrix. This leads to the simple dispersion relation in Eq. (3.6).

Appendix B Calculation of the Admittance Toward Hyperbolic Metamaterial

The calculation of the admittance looking toward the −*z* direction $Y_{\mathrm{HM},N}$ (see Fig. 3.8) can be straightforwardly carried out by constructing the transfer matrix of the HM film made of *N* unit cells [T_N], between the bottom-most material, i.e., the silicon substrate at *z* = −(*Nd* + *h*), and the surface of HM at *z* = −*h*. By knowing the transfer matrix of the unit cell [$\mathrm{T}_{\mathrm{unit}}$], given in Eq. (3.17), one has

$$
\left[\mathrm{T}_N\right] = \begin{bmatrix} A_N & B_N \\ C_N & D_N \end{bmatrix} = \left[\mathrm{T}_{\mathrm{unit}}\right]^N . \tag{3.18}
$$

Then $Y_{\mathrm{HM},N}$ is evaluated using the entries of the transfer matrix [T_N] and the wave admittance inside silicon substrate, Y_{subs}, as

$$Y_{\mathrm{HM},N} = \frac{C_N + D_N Y_{\mathrm{subs}}}{A_N + B_N Y_{\mathrm{subs}}}, \tag{3.19}$$

where $Y_{\mathrm{subs}}^{\mathrm{TE}} = \kappa_{\mathrm{subs}} / (\omega\mu_0)$ and $Y_{\mathrm{subs}}^{\mathrm{TM}} = \omega\varepsilon_{\mathrm{subs}}\varepsilon_0 / \kappa_{\mathrm{subs}}$ are the TE^z and TM^z wave impedances in the substrate, $\kappa_{\mathrm{subs}} = \sqrt{\varepsilon_{\mathrm{subs}} k_0^2 - k_t^2}$ is the z-directed wavenumber, and $\varepsilon_{\mathrm{subs}} = \varepsilon_{\mathrm{Si}}$ is the relative permittivity of silicon. When we consider the semi-infinite case, $N \to \infty$, the admittance $Y_{\mathrm{HM},N}$ becomes the Bloch admittance Y_{Bloch} of the periodic multilayer evaluated using the unit cell's transfer matrix entries in Eq. (3.17) as

$$Y_{\mathrm{Bloch}} = \frac{A_{\mathrm{unit}} - D_{\mathrm{unit}} \pm \sqrt{(A_{\mathrm{unit}} + D_{\mathrm{unit}})^2 - 4}}{-2B_{\mathrm{unit}}}. \tag{3.20}$$

Here one should pick the root of Y_{Bloch} such that $\mathrm{Re}\{Y_{\mathrm{Bloch}}\} > 0$, representing waves that carry power in the $-z$ direction.

Acknowledgment

We thank the anonymous reviewers for their useful comments. We also would like to thank Salvatore Campione (University of California, Irvine) for fruitful discussions. This chapter is reproduced based on the material in [M. A. K. Othman, C. Guclu, and F. Capolino, "Graphene-based tunable hyperbolic metamaterials and enhanced near-field absorption," *Optics Express*, vol. 21, pp. 7614-7632, 2013], © 2013 Optical Society of America.

References

[1] L. Felsen and N. Marcuvitz, *Radiation and Scattering of Waves* (Prentice-Hall, NJ, 1973).

[2] D. R. Smith and D. Schurig, "Electromagnetic wave propagation in media with indefinite permittivity and permeability tensors," *Phys. Rev. Lett.*, vol. 90, p. 077405 (2003).

[3] C. Guclu, S. Campione, and F. Capolino, "Hyperbolic metamaterial as super absorber for scattered fields generated at its surface," *Phys. Rev. B*, vol. 86, p. 205130 (2012).

[4] Y. Guo, W. Newman, C. Cortes, and Z. Jacob, "Applications of hyperbolic metamaterial substrates," *Adv. OptoElectron*., vol. 2012, p. 452502 (2012).

[5] Y. Guo, C. L. Cortes, S. Molesky, and Z. Jacob, "Broadband super-planckian thermal emission from hyperbolic metamaterials," *Appl. Phys. Lett.*, vol. 101, p. 131106 (2012).

[6] Z. Jacob, I. I. Smolyaninov, and E. E. Narimanov, "Broadband purcell effect: Radiative decay engineering with metamaterials," *Appl. Phys. Lett.*, vol. 100, p. 181105 (2012).

[7] I. Smolyaninov and E. Narimanov, "Metric signature transitions in optical metamaterials," *Phys. Rev. Lett.*, vol. 105, p. 67402 (2010).

[8] O. Kidwai, S. V. Zhukovsky, and J. E. Sipe, "Dipole radiation near hyperbolic metamaterials: applicability of effective-medium approximation," *Opt. Lett.*, vol. 36, pp. 2530–2532 (2011).

[9] T. U. Tumkur, J. K. Kitur, B. Chu, L. Gu, V. A. Podolskiy, E. E. Narimanov, and M. A. Noginov, "Control of reflectance and transmittance in scattering and curvilinear hyperbolic metamaterials," *Appl. Phys. Lett.*, vol. 101, p. 091105 (2012).

[10] J. Pendry and S. Ramakrishna, "Refining the perfect lens," *Physica B.*, vol. Condensed Matter 338, pp. 329 – 332 (2003).

[11] K. J. Webb and M. Yang, "Subwavelength imaging with a multilayer silver film structure," *Opt. Lett.*, vol. 31, pp. 2130– 2132 (2006).

[12] T. Tumkur, L. Gu, J. Kitur, E. Narimanov, and M. Noginov, "Control of absorption with hyperbolic metamaterials," *Appl. Phys. Lett.*, vol. 100, pp. 161103–161103 (2012).

[13] A. N. Poddubny, P. A. Belov, P. Ginzburg, A. V. Zayats, and Y. S. Kivshar, "Microscopic model of purcell enhancement in hyperbolic metamaterials," *Phys. Rev. B.*, vol. 86, p. 035148 (2012).

[14] C. L. Cortes, W. Newman, S. Molesky, and Z. Jacob, "Quantum nanophotonics using hyperbolic metamaterials,"*J. Opt.*, vol. 14, p. 063001 (2012).

[15] G. V. Naik, J. Liu, A. V. Kildishev, V. M. Shalaev, and A. Boltasseva, "Demonstration of al:zno as a plasmonic component for near-infrared metamaterials," *Proc. of the National Academy of Sciences*, vol.109, pp. 8834–8838 (2012).

[16] J. Kim, V. Drachev, Z. Jacob, G. Naik, A. Boltasseva, E. Narimanov, and V. Shalaev, "Improving the radiative decay rate for dye molecules with hyperbolic metamaterials," *Opt. Express*, vol. 20, pp. 8100–8116 (2012).

[17] G. Naik and A. Boltasseva, "Semiconductors for plasmonics and metamaterials," *Phys. Status Solidi Rapid Res. Lett*., vol. 4, pp. 295–297 (2010).

[18] C. Rizza, A. Ciattoni, E. Spinozzi, and L. Columbo, "Terahertz active spatial filtering through optically tunable hyperbolic metamaterials," *Opt. Lett*., vol. 37, pp. 3345–3347 (2012).

[19] A. Vakil and N. Engheta, "One-atom-thick reflectors for surface plasmon polariton surface waves on graphene," *Opt. Comm*., vol. 285, pp. 3428 – 3430 (2012).

[20] F. Rana, "Graphene terahertz plasmon oscillators," *IEEE Trans. Nano*., vol. 7, pp. 91–99 (2008).

[21] G. W. Hanson, A. B. Yakovlev, and A. Mafi, "Excitation of discrete and continuous spectrum for a surface conductivity model of graphene," *J. Appl. Phys*., vol. 110, p. 114305 (2011).

[22] M. Tamagnone, J. Gomez-Diaz, J. Mosig, and J. Perruisseau-Carrier, "Analysis and design of terahertz antennas based on plasmonic resonant graphene sheets," *J. Appl. Phys*., vol. 112, p. 114915 (2012).

[23] B. Wang, X. Zhang, F. J. Garcia-Vidal, X. Yuan, and J. Teng, "Strong coupling of surface plasmon polaritons in monolayer graphene sheet arrays," *Phys. Rev. Lett*., vol. 109, p. 073901 (2012).

[24] I. V. Iorsh, I. S. Mukhin, I. V. Shadrivov, P. A. Belov, and Y. S. Kivshar, "Hyperbolic metamaterials based on multilayer graphene structures," *Phys. Rev. B*, vol. 87, p. 075416 (2013).

[25] A. Andryieuski, A. V. Lavrinenko, and D. N. Chigrin, "Graphene hyperlens for terahertz radiation," *Phys. Rev. B*, vol. 86, p. 121108 (2012).

[26] V. P. Gusynin and S. G. Sharapov, "Unconventional integer quantum hall effect in graphene," *Phys. Rev. Lett*., vol. 95, p. 146801 (2005).

[27] A. B. Kuzmenko, E. van Heumen, F. Carbone, and D. van der Marel, "Universal optical conductance of graphite," *Phys. Rev. Lett*., vol. 100, p. 117401 (2008).

[28] L. Gerhard, E. Moyen, T. Balashov, I. Ozerov, M. Portail, H. Sahaf, L. Masson, W. Wulfhekel, and M. Hanbucken, "A graphene electron lens," *Appl. Phys. Lett*., vol. 100, p. 153106 (2012).

[29] A. Vakil and N. Engheta, "Transformation optics using graphene," Science, vol. 332, pp. 1291–1294 (2011).

[30] C. Chen, S. Rosenblatt, K. Bolotin, W. Kalb, P. Kim, I. Kymissis, H. Stormer, T. Heinz, and J. Hone, "Performance of monolayer graphene nanomechanical resonators with electrical readout," *Nat. nano*, vol. 4, pp. 861–867 (2009).

[31] X. Wang, L. Zhi, and K. Mullen, "Transparent, conductive graphene electrodes for dye-sensitized solar cells," *Nano Lett*., vol. 8, pp. 323–327 (2008).

[32] C. S. R. Kaipa, G. W. P. Y. R. Yakovlev, Alexander Hanson, and M. F. Medina, F., "Enhanced transmission with a graphene-dielectric microstructure at low-terahertz frequencies," *Phys. Rev. B*, vol. 85, p. 245407 (2012).

[33] S. Thongrattanasiri, F. H. L. Koppens, and F. J. Garcia de Abajo, "Complete optical absorption in periodically patterned graphene," *Phys. Rev. Lett*., vol. 108, p. 047401 (2012).

[34] A. Fallahi and J. Perruisseau-Carrier, "Design of tunable biperiodic graphene metasurfaces," *Phys. Rev*. B, vol. 86, p. 195408 (2012).

[35] D. Sounas and C. Caloz, "Gyrotropy and nonreciprocity of graphene for microwave applications," *IEEE Trans. Microw. Theory Techn*., vol. 60, pp. 901 –914 (2012).

[36] D. L. Sounas and C. Caloz, "Electromagnetic nonreciprocity and gyrotropy of graphene," *Appl. Phys. Lett*., vol. 98, p. 021911 (2011).

[37] G. Lovat, "Equivalent circuit for electromagnetic interaction and transmission through graphene sheets," *IEEE Trans. Electromagn. Compat*., vol. 54, pp. 101 –109 (2012).

[38] J. Sun, J. Zhou, B. Li, and F. Kang, "Indefinite permittivity and negative refraction in natural material: Graphite," *Appl. Phys. Lett*., vol. 98, p. 101901 (2011).

[39] C. S. Kaipa, A. B. Yakovlev, F. Medina, F. Mesa, C. Butler, and A. P. Hibbins, "Circuit modeling of the transmissivity of stacked two-dimensional metallic meshes," *Opt. Express*, vol. 18, pp. 13309–13320 (2010).

[40] Y. R. Padooru, A. B. Yakovlev, C. S. Kaipa, F. Medina, and F. Mesa, "Circuit modeling of multiband highimpedance surface absorbers in the microwave regime," *Phys. Rev. B*, vol. 84, p. 035108 (2011).

[41] C. S. R. Kaipa, A. B. Yakovlev, F. Medina, and F. Mesa, "Transmission through stacked 2d periodic distributions of square conducting patches," *J. Appl. Phys*., vol. 112, p. 033101 (2012).

[42] X. Ni, G. Naik, A. Kildishev, Y. Barnakov, A. Boltasseva, and V. Shalaev, "Effect of metallic and hyperbolic metamaterial surfaces on electric and magnetic dipole emission transitions," *Appl. Phys. B*, vol. 103, pp. 553–558 (2011).

[43] K. Novoselov, A. Geim, S. Morozov, D. Jiang, Y. Zhang, S. Dubonos, I. Grigorieva, and A. Firsov, "Electric field effect in atomically thin carbon films," *Science*, vol. 306, pp. 666–669 (2004).

[44] V. P. Gusynin, S. G. Sharapov, and J. P. Carbotte, "Sum rules for the optical and hall conductivity in graphene*," Phys. Rev. B*, vol. 75, p. 165407 (2007).

[45] G. W. Hanson, "Dyadic green's functions and guided surface waves for a surface conductivity model of graphene," J. *Appl. Phys*., vol. 103, p. 064302 (2008).

[46] R. A. Jishi, M. S. Dresselhaus, and G. Dresselhaus, "Electron-phonon coupling and the electrical conductivity of fullerene nanotubules," *Phys. Rev. B*, vol. 48, pp. 11385–11389 (1993).

[47] Y.-W. Tan, Y. Zhang, K. Bolotin, Y. Zhao, S. Adam, E. H. Hwang, S. Das Sarma, H. L. Stormer, and P. Kim, "Measurement of scattering rate and minimum conductivity in graphene," *Phys. Rev. Lett*., vol. 99, p. 246803 (2007).

[48] D. Pozar, *Microwave engineering* (John Wiley & Sons, 2009).

[49] O. Kidwai, S. V. Zhukovsky, and J. E. Sipe, "Effective-medium approach to planar multilayer hyperbolic metamaterials: Strengths and limitations," *Phys. Rev. A*, vol. 85, p. 053842 (2012).

[50] H. N. S. Krishnamoorthy, Z. Jacob, E. Narimanov, I. Kretzschmar, and V. M. Menon, "Topological transitions in metamaterials," *Science*, vol. 336, pp. 205–209 (2012).

[51] S. Campione, S. Steshenko, M. Albani, and F. Capolino, "Complex modes and effective refractive index in 3d periodic arrays of plasmonic nanospheres," *Opt. Express*, vol. 19, pp. 26027–26043 (2011).

[52] F. Capolino and M. Albani, "Truncation effects in a semi-infinite periodic array of thin strips: A discrete wienerhopf formulation," *Radio Sci*., vol. 44, p. RS2S91 (2009).

[53] P.-Y. Chen and A. Alu, "Atomically thin surface cloak using graphene monolayers," *ACS Nano*, vol. 5, pp. 5855–5863 (2011).

[54] Z. Jacob, J. Kim, G. Naik, A. Boltasseva, E. Narimanov, and V. Shalaev, "Engineering photonic density of states using metamaterials," *Appl. Phys. B*, vol. 100, pp. 215–218 (2010).

CHAPTER 4

WIDEBAND PLANAR TRANSMISSION LINE HYPERBOLIC METAMATERIAL

Sec. 4.1 Motivation

The analysis here is presented both theoretically and experimentally pertaining to the subwavelength focusing by using a planar hyperbolic metamaterial (HM) at microwave frequencies. The proposed HM consists of microstrip transmission lines loaded by lumped components and exhibits a very flat wavevector iso-frequency dispersion diagram, over a wide frequency range, and thus able to transport spectral component with large wavenumbers. This flatness is here exploited to provide subwavelength focusing with a full width half maximum (3 dB power width) of about $\lambda_g/31$ and $\lambda_g/19$ at 0.5 and 1 GHz, respectively, where λ_g is the guided wavelength in the transmission line (TL) microtrip grid. Numerical simulation results are in good agreement with the measurement ones. Moreover, the investigations regarding the capability of the proposed HM to resolve sources with subwavelength distance of about $\lambda_g/6$ and $\lambda_g/3$ at 0.5 and 1 GHz, respectively, are presented.

The resolution of a conventional lens is limited by the Abbe diffraction limit [1] that imposes a maximum resolution of $d = \lambda_0 / (2n)$, with λ_0 the free-space wavelength and *n* the refractive index of the medium. This limitation rises from the fact that conventional lenses cannot transfer the evanescent spectrum emitted by a source, which is essential to reconstruct subwavelength information [2]. In other words, to overcome the diffraction limit one should transfer a very wide spatial spectrum of waves, including both propagating and evanescent components. The propagating (evanescent) spectrum includes all the spatial spectral components with transverse (to the lens axis) wavenumber k_t smaller (larger) than $k_0 n$, where $k_0 = 2\pi / \lambda_0$ is the free space wavenumber.

Transfer of both propagating and evanescent spectra has been achieved through the use of negative refractive index (NRI) materials. The "perfect lens" introduced by Pendry in [3] is a direct example of the fact that a slab of NRI material is able to *amplify* the evanescent spectral components emitted by a source, in addition to provide the standard focusing of the propagating spectrum. A NRI slab is thus able to compensate the evanescent decay in free space, overcoming the diffraction limit. However, the performance of a perfect lens is largely diminished by the presence of losses as outlined in [4, 5]. Transmission line (TL) implementations of Pendry's lens have been reported in [6-9], where the NRI medium has been achieved via a periodically *LC*-loaded transmission line medium. The authors of [6-9] have demonstrated sub-diffraction focusing whose resolution limit is imposed by the periodicity of the implemented metamaterial NRI lens.

Another way of transferring both propagating and evanescent spectra is by using wire media [10-12], photonic crystals [13], and metal-dielectric multilayers [14-17] without

involving the use of negative refraction or amplification of evanescent spectral components. All the artificial materials mentioned above support the propagation of a wide spatial spectrum of waves generated by one or more scatterers in their vicinity, otherwise evanescent in free space, due to the presence of a hyperbolic dispersion (see for example [16] for more details). In the following, such artificial materials are referred to as hyperbolic metamaterials (HMs). It has been shown in [10, 13, 14, 17, 18] that when these media possess a flat dispersion relation, in a regime referred to as *canalization regime*, they can be used to obtain subwavelength focusing. In other words, the canalization regime occurs when a wide spatial spectrum is allowed to propagate with almost the same phase constant inside the artificial medium. It is this peculiar regime that the proposed designs are going to exploit in two dimensional (2D) TL HM implementations for subwavelength focusing purposes. It is noted that, to the authors' knowledge, the use of very flat dispersion diagrams in 2D TL HMs to achieve subwavelength focusing has not been demonstrated before.

In alternative to the canalization regime here investigated, in the 2D TL HM scenario, a *LC*-loaded TL grid capable of forming "resonance cones" [19, 20] has been experimentally demonstrated in [19] to achieve subwavelength focusing. Also unloaded TL grids with unequal periods along the principal directions, creating anisotropy, have been proven to support hyperbolic dispersion [21]. There, by interfacing two identical HMs, but one with 90-degree rotation, negative refraction and subwavelength focusing have been achieved. In [22], the use of periodic circuits with unit cells comprising series capacitor or inductor in orthogonal directions led to extraordinary reflection and refraction phenomena including negative refraction.

Very recently, another experimental realization of HMs using 2D TLs made of lumped capacitors and inductors has been reported in [23], with the goal of classifying the different configurations that lead to hyperbolic dispersion, however without dealing with subwavelength focusing or with very flat dispersion.

In this chapter, a planar TL HM with very flat dispersion is utilized and it allows the subwavelength focusing by means of the above mentioned canalization regime. The flatness of the HM dispersion curve is easy to design and realize experimentally in a 2D TL grid, and this is a great motivation of our analysis. It is thus demonstrated theoretically and experimentally that the subwavelength focusing capabilities can be obtained by a HM with extremely flat dispersion diagram over a wide frequency range implemented by using loaded microstrip TLs. The wide frequency range of operation, without the change of focus location, constitutes the main advantage of the proposed design when compared to previous literature.

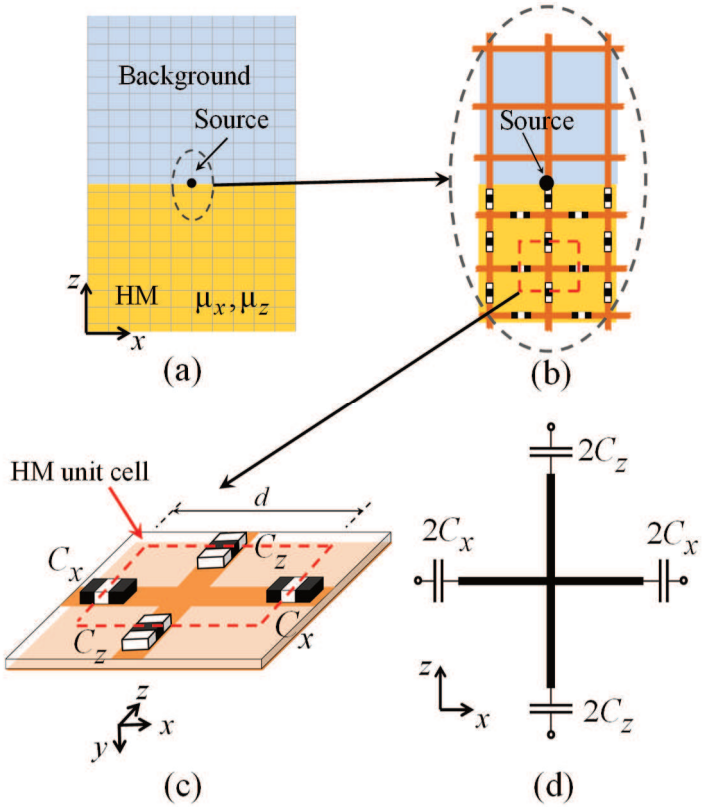

Fig. 4.1 (a) Schematic of the two-dimensional periodic transmission line implementation of HM; (b) a close-up view of the schematic in (a); (c) illustration of the HM region unit cell; (d) the network representation of the HM region unit cell. Note that in the unit cell choice in (d), each microstrip segment is loaded by twice the capacitance in the relative direction.

The outline of the chapter is as follows. In Sec. 4.2 the theoretical model is constructed and it is required to calculate the wavenumber dispersion diagram in the planar HM implemented via TLs. Both Bloch theory and homogenization theory are employed, and the comparisons of two methods are presented. The developed model is then adopted to design a HM with very flat iso-frequency dispersion diagram used in the subsequent sections. The proposed finite structure with HM is simulated in Sec. 4.3 using a microwave circuit simulation package [Agilent Advanced Design System (ADS)], and it is shown to exhibit subwavelength focusing capabilities. It is also shown that the HM allows for the

discrimination of two sources with subwavelength relative distance. Sec. 4.4 documents the fabricated proposed HM design and experimental results exhibiting subwavelength focusing capabilities, in good agreement with simulation results. The required steps to achieve the iso-frequency dispersion diagrams according to both Bloch theory and homogenization theory are reported in Appendix A and B, respectively.

Sec. 4.2 Hyperbolic Dispersion Diagrams in HMs Implemented via Planar Transmission Lines

4.2.1 Analytical Model

The 2D microstrip TL grid implementation here proposed for subwavelength focusing and resolution is illustrated in Fig. 4.1. The upper 2D "isotropic region", referred to as background medium [light blue in Fig. 4.1(a-b)], is made by a 2D microstrip TL grid with square unit cells. The lower HM region [light brown in Fig. 4.1(a-b)] is realized by periodically loaded (by series lumped capacitors) microstrip lines, whose unit cell is shown in Fig. 4.1(c). In the following, consider a square unit cell with period *d* along the *x* and *z* axes. The infinitely periodic representation of the HM design in Fig. 4.1(c) is here studied by using Bloch theory, following the formulation presented in [8]. The HM dispersion relation of the *z*-component of the wavevector k_z versus the *x*-component of the wavevector k_x is given by (see Appendix A for more details)

$$\frac{\sin^2\left(\frac{k_z d}{2}\right)}{B^z}+\frac{\sin^2\left(\frac{k_x d}{2}\right)}{B^x}+j2Y_0\sin\left(\frac{\beta d}{2}\right)=0 \tag{4.1}$$

where

$$B^{x,z} = jZ_0 \sin\left(\frac{\beta d}{2}\right) + \frac{1}{j2\omega C_{x,z}} \cos\left(\frac{\beta d}{2}\right) \tag{4.2}$$

The coefficients $B^{x,z}$ are the "B" entries of the ABCD matrices of the microstrip branches of length $d/2$ along the x and z axes in the unit cell that are loaded by capacitors C_x and C_z, respectively, as illustrated in Fig. 4.1(c,d). Furthermore, $Z_0 = \sqrt{L_{\text{dis}} / C_{\text{dis}}}$ and $\beta = \omega\sqrt{L_{\text{dis}} C_{\text{dis}}}$ are the characteristic impedance and the propagation constant of the microstrip lines used in the grid implementation, respectively, where L_{dis} [H/m] and C_{dis} [F/m] are the distributed (per-unit-length) inductance and capacitance of the microstrip line (for simplicity here it is assumed that TL segments along x and z are identical). As shown in Appendix B, in the particular case of TL-grid period much smaller than the guided wavelength in the HM (i.e., $k_{x,z} d \ll 1$) and the microstip TL (i.e., $\beta d \ll 1$), the dispersion relation in (4.1) can be simplified to

$$\frac{k_z^2}{\mu_x} + \frac{k_x^2}{\mu_z} = \omega^2 \varepsilon \tag{4.3}$$

where

$$\mu_x = L_{\text{dis}} - \frac{1}{\omega^2 C_z d}, \quad \mu_z = L_{\text{dis}} - \frac{1}{\omega^2 C_x d}, \quad \varepsilon = 2C_{\text{dis}}. \tag{4.4}$$

Equation (4.3) is the wavevector dispersion relation in an effective homogeneous material with anisotropic (absolute) magnetic permeability represented by the diagonal tensor $\underline{\boldsymbol{\mu}} = \mu_x \hat{\mathbf{x}}\hat{\mathbf{x}} + \mu_z \hat{\mathbf{z}}\hat{\mathbf{z}}$ and the absolute effective permittivity ε.

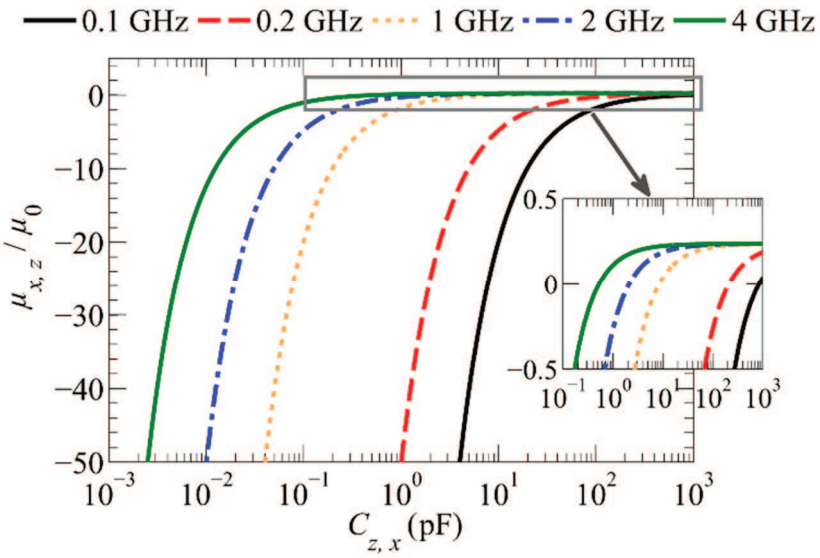

Fig. 4.2 (a) Relative permeability $\mu_{x,z}/\mu_0$ versus capacitance $C_{z,x}$ calculated by the homogenized medium approach (4) for various frequency values. The inset shows the region of small $\mu_{x,z}/\mu_0$ where zero crossing occurs.

Based on (4.4), one can realize a positive μ_x and a negative μ_z or, vice versa, a positive μ_z and a negative μ_x, by proper loading the 2D microstrip line with capacitors C_x and C_z. To show this feature, plots show the relative permeabilities $\mu_{x,z}/\mu_0$ versus $C_{z,x}$ in Fig. 4.2 (where μ_0 and ε_0 are the free space absolute permeability and permittivity, respectively) for different frequencies, assuming 1.5mm-wide microstrip lines on top of a grounded dielectric substrate (i.e., FR4) with relative permittivity $\varepsilon_{\text{FR4}} = 4.5$ and thickness $h = 0.76\,\text{mm}$, and square unit cells with d = 1 cm. This microstrip line is modeled by the distributed inductance $L_{\text{dis}} = 298\,\text{nH/m}$ and capacitance $C_{\text{dis}} = 127\,\text{pF/m}$ leading to the characteristic impedance $Z_0 = 48.4\Omega$. Under these assumptions, the background region (comprising the unloaded TL grid) corresponds to an effective isotropic medium with relative permeability $\mu_b/\mu_0 \approx 0.237$ and relative permittivity $\varepsilon_b/\varepsilon_0 \approx 28.7$ (where the

subscript "*b*" stands for "background"). One can see from that depending on the adopted capacitances $C_{z,x}$, the relative permeabilities $\mu_{x,z}/\mu_0$ cross zero for different capacitance values depending on the frequency. For any frequency, there is a capacitance value C_{res}

$$C_{res} = \frac{1}{\omega^2 L_{\text{dis}} d} \tag{4.5}$$

responsible for a series resonance of the loaded microstrip branch (for example, $C_{res} = 8.5\,\text{pF}$ at 1 GHz). When $C_{z,x} < C_{res}$ at a given frequency, the relative *permeability is negative* and has a steep behavior, i.e., it varies largely with small capacitance variations. On the contrary, for capacitance values $C_{z,x} > C_{res}$, the relative permeability $\mu_{x,z}/\mu_0$ changes rather slowly and it approaches the unloaded microstrip line's permeability μ_b/μ_0 as $C_{z,x} \to \infty$, as the inset in Fig. 4.2 shows.

A hyperbolic dispersion diagram is obtained only when the ratio μ_z / μ_x is negative, as dictated by (4.3), i.e., when one of the two conditions is verified:

$$C_x < C_{res} < C_z \;\text{ or }\; C_z < C_{res} < C_x \tag{4.6}$$

where the first or second condition corresponds to HM with either μ_z or μ_x negative value. The rest is carried on by assuming the condition $C_x < C_{res} < C_z$ (i.e., $\mu_z < 0$, $\mu_x > 0$) as it leads to a canalization regime. It is also stressed that the frequency band of canalization is intimately related to the chosen capacitance values: the low (high) frequency edge is determined by C_z (C_x) as for lower (higher) frequencies C_{res} increases (decreases) in view of (5). Thus, the condition $C_x < C_{res} < C_z$ may be satisfied only for a wide though limited

frequency band. To outline a design procedure, it is noted that a large ratio μ_z / μ_x is determined by either having μ_z large or μ_x small, or both at the same time. It is observed that a very small μ_x (governed by C_z) cannot be achieved in a wide frequency band. For this reason, it will be assumed that in the experimental verification there is the condition $\mu_x \approx \mu_b$, realizable over a wide band, achieved with $C_z \to \infty$ (i.e., large), whereas μ_z large and negative can be easily achieved in a large frequency band by selecting a proper C_x, as it will be illustrated next (for the sake of knowledge, start by assuming a finite value for C_z).

Table 4.1 Permeability ratios for four representative cases of capacitances C_x at 1 GHz for the HM under investigation when $C_z = 13.5$ pF ($\mu_x = 0.0877\mu_0$)

Case	C_x	μ_z / μ_x
A	0.005 pF	−4600
B	1.5 pF	−12.6
C	4.6 pF	−2.30
D	6 pF	−1.13

By properly choosing the series loading capacitors for the HM TL region, one can then achieve different hyperbolic dispersion curves, including extremely flat ones. To stress this capability, in Fig. 4.3 the four representative cases of C_x summarized in Table I at 1 GHz are

analyzed under the assumption $C_z = 13.5\,\text{pF}$ ($\mu_x = 0.0877\mu_0$), considering that for these cases $C_{res} \approx 8.5\,\text{pF}$.

In Fig. 4.3 one finds the normalized dispersion diagrams by using (4.1) based on Bloch theory, and by using (4.3) based on homogenization theory. The plots show that the dispersion diagram evolves from a flat curve (Case A) to a steep hyperbola (Case D). In particular, Case A is characterized by a C_x smaller than the other cases, thus exhibiting a negative μ_z and $|\mu_z / \mu_x| \approx 4600$ much larger than the other three cases. Case D is instead characterized by a C_x larger than the other cases, still satisfying $C_x < C_{res}$ and thus still exhibiting HM with a negative μ_z and $|\mu_z / \mu_x| \approx 0.535$, smaller than the other three cases. Accordingly, when keeping both C_z and frequency constant, a smaller C_x is required to achieve a very flat dispersion curve. In turn the very flat dispersion curve assures that spatial spectral components with any k_x generated by a source at the interface of the HM region are able to propagate inside the HM with almost the same k_z, as can be ascertained by looking at Case A in Fig. 4.3 where for any k_x, $k_z d / \pi \approx 0.1$.

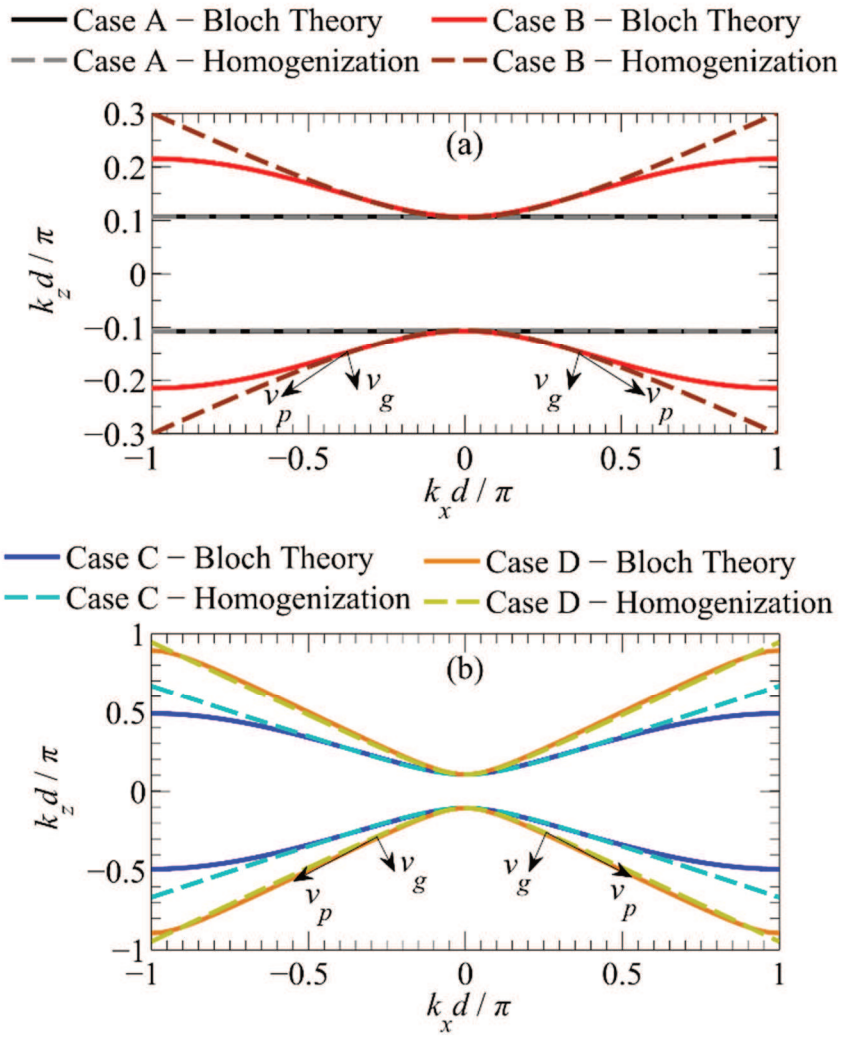

Fig. 4.3 $k_z - k_x$ wavenumber dispersion diagram at 1 GHz using Bloch theory (solid) and homogenization theory (dashed) of the 2D TL HM for (a) cases A, and B, and (b) cases C and D, described in Table I. The group and phase velocities are drawn to indicate the direction of power flow and phase propagation, respectively. The group velocity is along the frequency gradient of the dispersion surface, so the Poynting vector is normal to the dispersion surface.

4.2.2 Proposed HM TL Design

Both background and HM TL grids are here made of 1.5mm-wide microstrip lines above on a FR4 grounded dielectric substrate (the microstrip lines are as in Subsec. 4.2.1). The upper 12×23 unit cells represent the background medium and the bottom 11×23 unit cells

the HM. The unit cell dimension is 1cm×1cm ($0.0869\lambda_g \times 0.0869\lambda_g$), whereas the whole board size is 23cm×23cm ($2\lambda_g \times 2\lambda_g$), where $\lambda_g = 11.5\,\text{cm}$ is the guided wavelength in the background medium at 1 GHz. The microstrip line segments are the same as inSubsec. 4.2.1 thus modeled by the same L_{dis} and C_{dis} values provided in Subsec. 4.2.1. The microstrips in the HM region are loaded in series with capacitances for achieving here a very flat dispersion curve.

Consider now Case A in Table I ($C_x = 0.005\text{pF}$) that exhibits a very flat dispersion diagram as reported in Fig. 4.3. It can be inferred from Fig. 4.2 that μ_x/μ_0 varies from 0.0877 to 0.237 when C_z is increased from 13.5 pF to infinity (short circuit). Also, replacing the capacitor C_z with a short circuit decreases the ratio $|\mu_z / \mu_x|$ from 4600 to 1700 at 1 GHz and this change implies a slightly less flat dispersion diagram, though still much flatter than the other three cases in Table 4.1. Therefore, for simplicity of realization it is shown that if one increases C_z from 13.5 pF to infinity, the $k_z - k_x$ dispersion curves remain still very flat as reported in Fig. 4.4 (obtained by Bloch theory) at 1 GHz. Note that k_z varies due to the change in μ_x/μ_0 ; in particular, $k_z d/\pi$ goes from 0.1 to about 0.2. This is still good for the purpose of employing the canalization regime, and the choice of $C_z \to \infty$ (short circuit) eases a fabrication realization. Regarding C_x, instead, the one reported in Table 4.1 for Case A ($C_x = 0.005\text{pF}$), is kept which is realized simply by a 1-mm gap in the *x*-directed TL branches (the value of this gap capacitance has been verified by using the finite element method full-wave solver, HFSS by Ansys Inc.). It is further shown that this design is characterized by a very flat

dispersion diagram for a wide frequency band (0.1– 4 GHz) as reported in Fig. 4.5(a) (obtained by Bloch theory), where only the propagating k_z value varies from case to case. The obtained very flat iso-frequency dispersion diagrams imply that the reported 2D TL HM can be in principle used for subwavelength focusing applications with large bandwidth of operation. In contrast, we show in Fig. 4.5(b) the dispersion diagram at various frequencies for Case C. Below 0.8 GHz, both μ_x and μ_z are negative for Case C, implying that the 2D TL grid hosts only evanescent waves. However, above 0.8 GHz we observe hyperbolic dispersion because μ_x becomes positive. As the frequency increase also μ_z turns positive and thus the hyperbolic dispersion is lost as depicted by the dot-dashed black elliptic curve at 2 GHz in Fig. 4.5(b). This strengthens our choice of the flat dispersion for which we have a wider frequency band of operation.

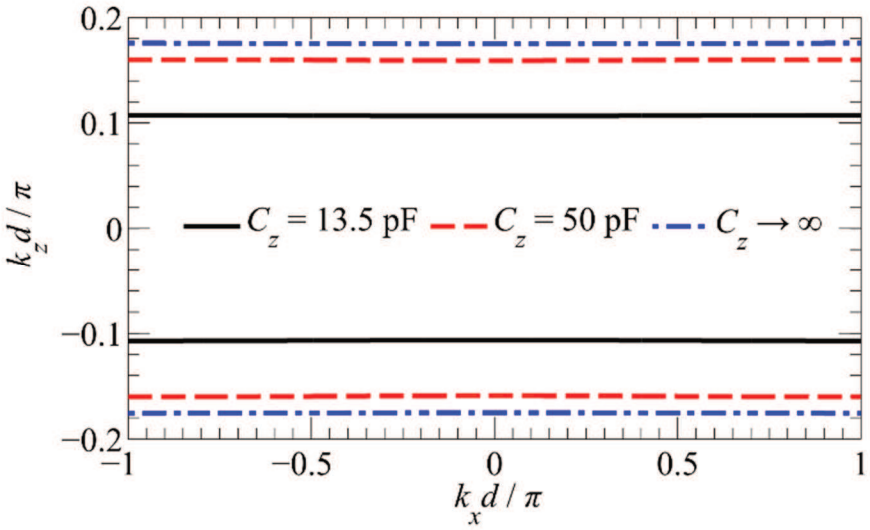

Fig. 4.4 $k_z - k_x$ wavenumber dispersion diagram obtained by Bloch theory for the 2D TL HM medium versus lumped capacitance C_z. Other design parameters are as in Case A in Fig. 4.3.

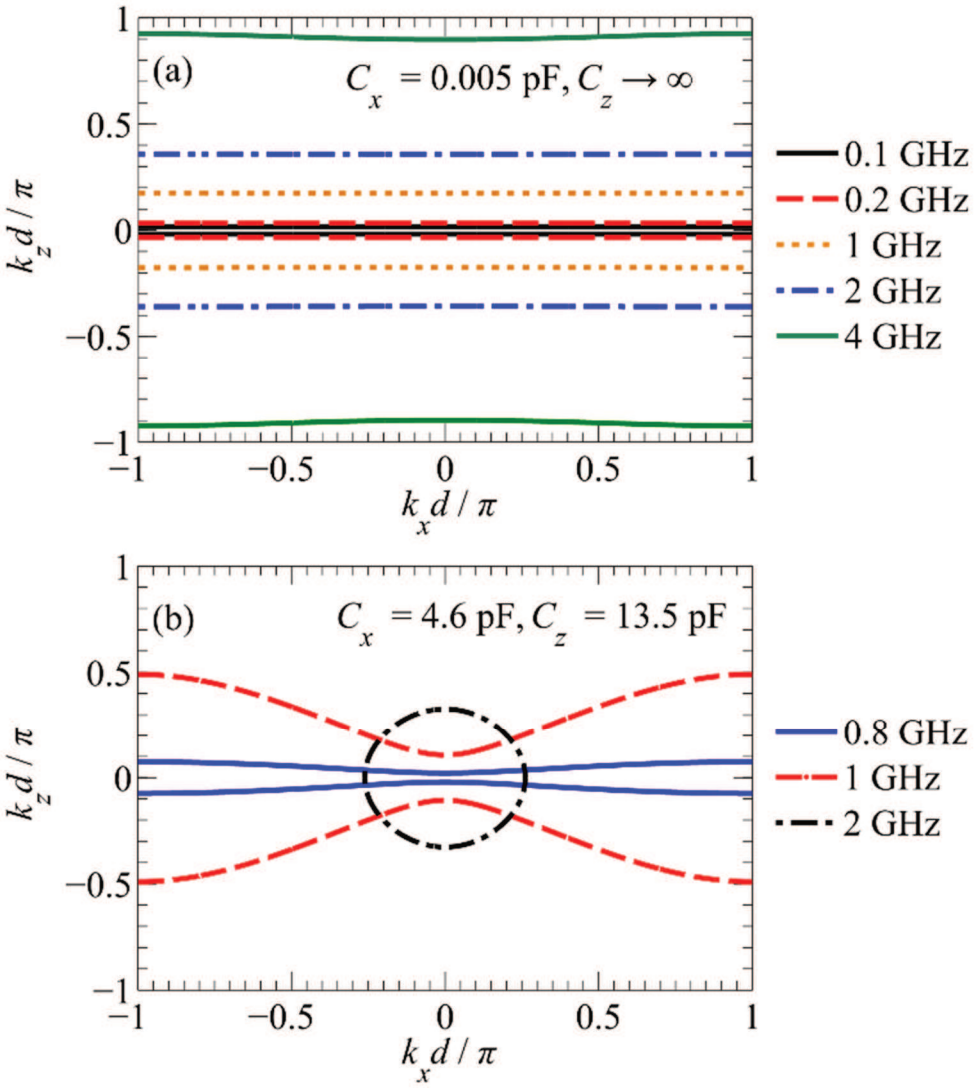

Fig. 4.5 $k_z - k_x$ wavenumber dispersion diagram obtained by Bloch theory for the 2D TL HM medium for various representative frequencies, for (a) Case A in Fig. 4.3, using $C_z \to \infty$ (i.e., short circuit), and (b) Case C . Note that in (a) the curves remain flat for a wide frequency range, whereas in (b) the hyperbolic dispersion varies considerably with frequency and is even lost, becoming elliptic, for instance, at 2 GHz.

4.2.3 Evaluation of Transmission Line Termination Impedances via Bloch Theory

Due to the finite size of the designed board, the reflection from the board edges should be avoided in order to mimic semi-infinite HM and background half-spaces. For this reason, the

TL grids (for both background and HM) need to be terminated to proper impedances. Here, similarly to what done in [8], the proper termination impedances are equal to the Bloch impedances

$$Z_{x,z} = \frac{Z_0 \tan(\beta d / 2) - \dfrac{1}{2\omega C_{x,z}}}{\tan(k_{x,z} d / 2)} \tag{4.7}$$

where the subscripts "*x*" and "*z*" of *Z* indicate the direction of the termination (i.e., Z_x is the Bloch impedance for terminating the transmission lines along the *x* direction).

As discussed in the previous section, because of the flat dispersion diagram, all the spectral waves in the HM propagate with almost the same wavenumber along the *z* direction as $k_z = \omega\sqrt{\mu_x \varepsilon}$. By using (4.7) and the TL parameters introduced in the previous sections, the HM Bloch termination is 33 Ω, which matches waves propagating along the –*z* direction. Note that since the power inside the HM is canalized mainly into the –*z* direction, the power propagating in the +/– *x* directions is negligible, hence we can leave the TL endings along *x* as open circuit. For the background medium, that is characterized by a circular iso-frequency dispersion wavenumber curve, the Bloch impedances in the *x* and *z* directions vary for any wavenumber pair (k_x, k_z), i.e., with the angle of propagation. Based on the background medium dimensions, the waves excited at the center of the board, that are, in turn, incident on the three edges of the upper background region in Fig. 4.1, have an angle of incidence between 0° and 45°. This in turn means that the ratio $k_{x,z}/k_b$, with $k_b = \omega\sqrt{\mu_b \varepsilon_b} = \omega\sqrt{L_{dis} 2C_{dis}}$, changes between 0 and $1/\sqrt{2}$. Thus, using (4.7) and the TL parameters from the previous section, the Bloch impedances in the *z* and *x* direction change

from a minimum of 29 Ω, for $k_{x,z}/k_b = 0$ to a maximum of 42 Ω for $k_{x,z}/k_b = 1/\sqrt{2}$. For simplicity we chose to terminate all TLs in the background part with a constant resistance of 33 Ω. A detailed analysis of this choice has been carried out proving that this constant termination impedance causes negligible reflection from the boundaries (not reported here for brevity) and this does not hinder the subwavelength focusing capabilities.

Sec. 4.3 Numerical Simulations of Subwavelength Focusing and Resolution

We use a microwave circuit simulator (Agilent's Advanced Design System, ADS) to simulate the design discussed in Subsecs. 4.2.2 and 4.2.3. A shunt voltage source is exerted between the ground and the TL grid at the center of the interface between the background and the HM, as illustrated in Fig. 4.1(b). The voltage of the nodes (intersection points of microstrip lines along *x* and *z*) toward the ground, in the case of a single voltage source excitation at 1 GHz, is shown in Fig. 4.6(a). The color of each square represents the node voltage (in dB) of the board normalized with respect to the maximum voltage in the board, which occurs to be the voltage of the closest node to the source on the HM side. The canalization regime is clearly observed in Fig. 4.6(a). We also report the normalized node voltages versus the cell number along *x*, at the interface between the HM and the background, at the top (background) edge, and at the bottom (HM) edge in Fig. 4.6(b, c), at 0.5 and 1 GHz, respectively. These plots show that the voltage profile along the HM–background interface is transferred to the bottom edge of the HM region with almost the same pattern, indicating that the HM is able to transport all the large wavenumber spectral components generated by the voltage source. Instead, the voltage profile at the top egde of the background region (the isotropic region) shows that focusing is lost because waves with large spectral wavenumbers

are evanescent and thus do not propagate away from the source. In summary, the source information in free space is lost due to evanescent decay, whereas it is kept in the HM because waves with large wavenumbers are propagating in the HM. We annotate the full width half maximum (FWHM) by arrows and the result in Fig. 4.6(b, c) clearly shows that subwavelength focusing with FWHM of $\lambda_g/31$ and $\lambda_g/19$ at 0.5 and 1 GHz is achieved, respectively.

Next, we consider the case of two point sources with subwavelength distance of 4 cm (equal to $\lambda_g/6$ and $\lambda_g/3$ at 0.5 and 1 GHz, respectively) to verify the potential of subwavelength resolution. Fig. 4.6(d) shows the voltage color map of the case with two voltage sources, and we show that the voltage of each source is clearly canalized in the HM. Moreover the normalized voltage profiles at the interface, top edge, and bottom edge of the background and HM media are reported in Fig. 4.6(e, f), at 0.5 and 1 GHz, respectively. It can be seen that the peaks of the two sources are clearly resolved and a resolution of sources with an inter-distance of at least $\lambda_g/6$ at 0.5 GHz and $\lambda_g/3$ at 1 GHz is achieved.

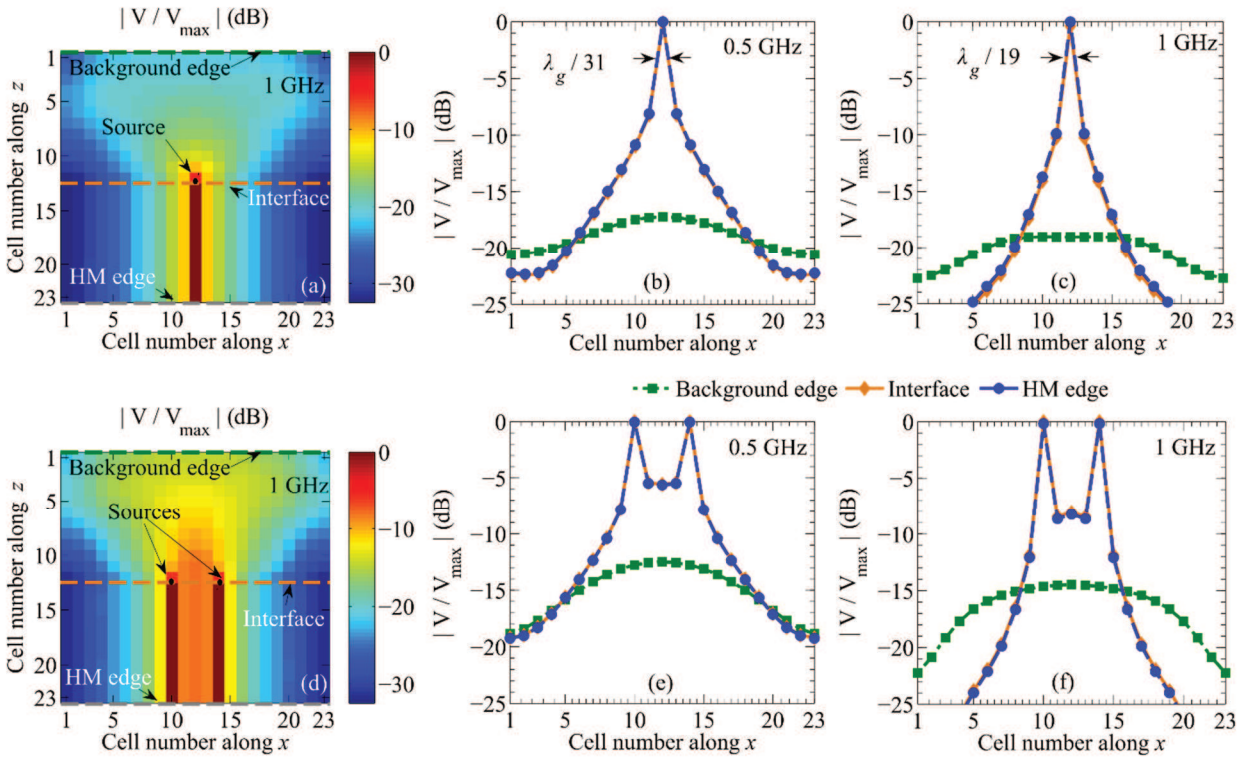

Fig. 4.6 The simulated voltage magnitude distribution, normalized by the maximum voltage V_{max} on the designed board, at 1 GHz for (a) one and (d) two excitation point sources. Normalized voltage magnitude at the interface, top and bottom boundary of the structure for (b) one point source at 0.5 GHz, (c) one point source at 1 GHz, (e) two point sources at 0.5 GHz, and (f) two point sources at 1 GHz.

Sec. 4.4 Measurement Results of Subwavelength Focusing

In this section we elaborate on the fabrication and measurement of the design whose specifications and simulation results were provided in Secs. II and III. For implementation purposes, we used a TL grid printed with placement pads left for surface mounted devices (SMDs). The fabricated circuit board with FR4 grounded dielectric substrate is depicted in Fig. 4.7. We used 0 Ω SMD resistors in the *z* direction for realization of $C_z \to \infty$, whereas the microstrip gap capacitance on the SMD placement pads were sufficient along the *x* direction to achieve the designed capacitance value of $C_x = 0.005$ pF in Case A in Table I and Fig. 4.5

(designed to achieve a very flat wavenumber dispersion diagram). At the center of the board, a SMA connector is mounted from the bottom side and is connected to one port of the vector network analyzer (VNA, Rhode Schwarz ZVA67). The second port of the VNA is connected to an in-house built probe (which is a modified SMA edge-mount connector with two points of contact, one for ground and one for signal to ensure low-resistance contacts across the termination resistors). Then S_{21} is recorded along the HM (bottom) and the background (top) edges by sampling S_{21} for each termination resistor. Note that all the termination resistors have the same value of 33 Ω, therefore S_{21} values are indicative of the voltage along the edges. We first start discussing the measurement across the bottom edge of the HM. Simulation have been carried out in order to assure that the probe impedance (as a parallel 50 Ω to the termination impedance) does not have a significant impact on the results and this method is sufficiently accurate for the purpose of showing subwavelength focusing. Fig. 4.8 shows the measurement and simulated voltage profiles (normalized to the maximum value at the HM bottom edge) at the HM bottom edge of the structure at 0.5, 0.75, 1, 1.25, and 1.5 GHz, respectively. It is clear that the voltage profile at the bottom edge of the HM is almost a replica of the voltage profile along the *x* direction at the interface between the two grid media, therefore exhibiting a focus with subwavelength dimension. Similarly to what done for the HM bottom edge, we have also reported the simulation and experimental results relative to a scan line at the background top edge. The presence of very flat voltage profile shows that focusing is lost, as expected, due to evanescent decay of large spectral component in the isotropic region (i.e., the background grid) generated by the voltage source. The small disagreement, in the $-15 \div -20$ dB range, may be due to the non-perfect contact between the probe and the metallization on the circuit board, to the 5%-10% tolerance in termination

resistances, and to the probe loading the termination resistors (in particular the latter might affect the recorded signal along HM and background edges differently). In summary, after comparing the voltage profiles along the HM bottom and background top edges, these results numerically and experimentally verify the subwavelength focusing capabilities of the proposed HM-based device over a wide frequency band.

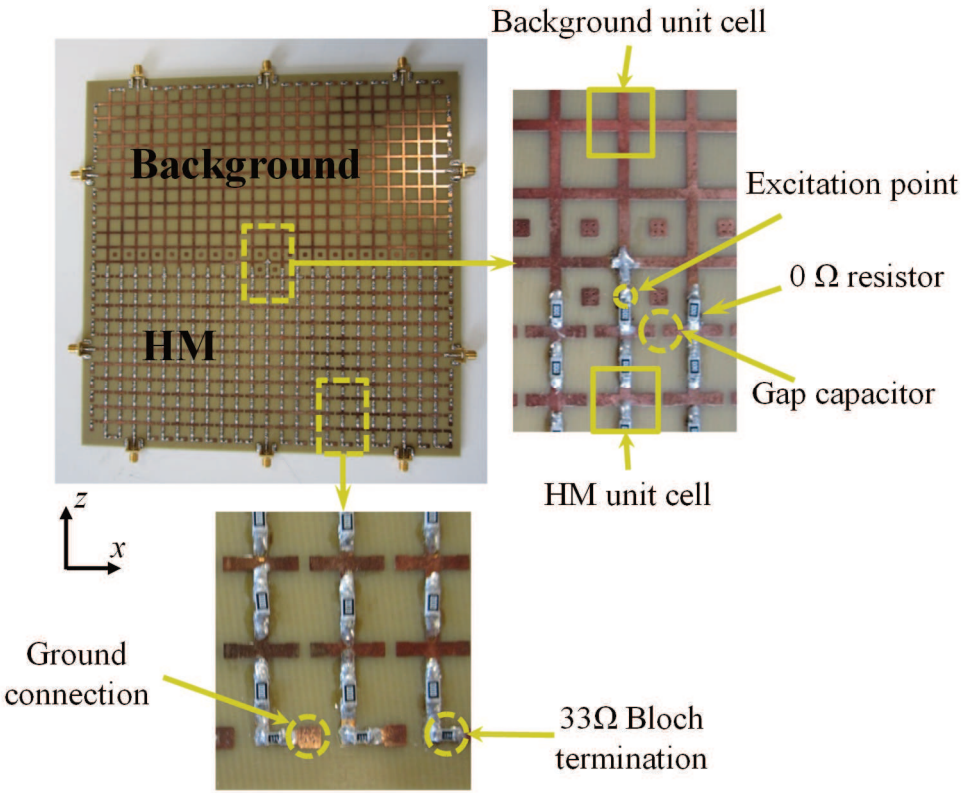

Fig. 4.7 Fabricated TL grid over a grounded dielectric substrate. The background and HM are represented by the upper and lower half parts of the TL grid, respectively. Each component is indicated by yellow lines.

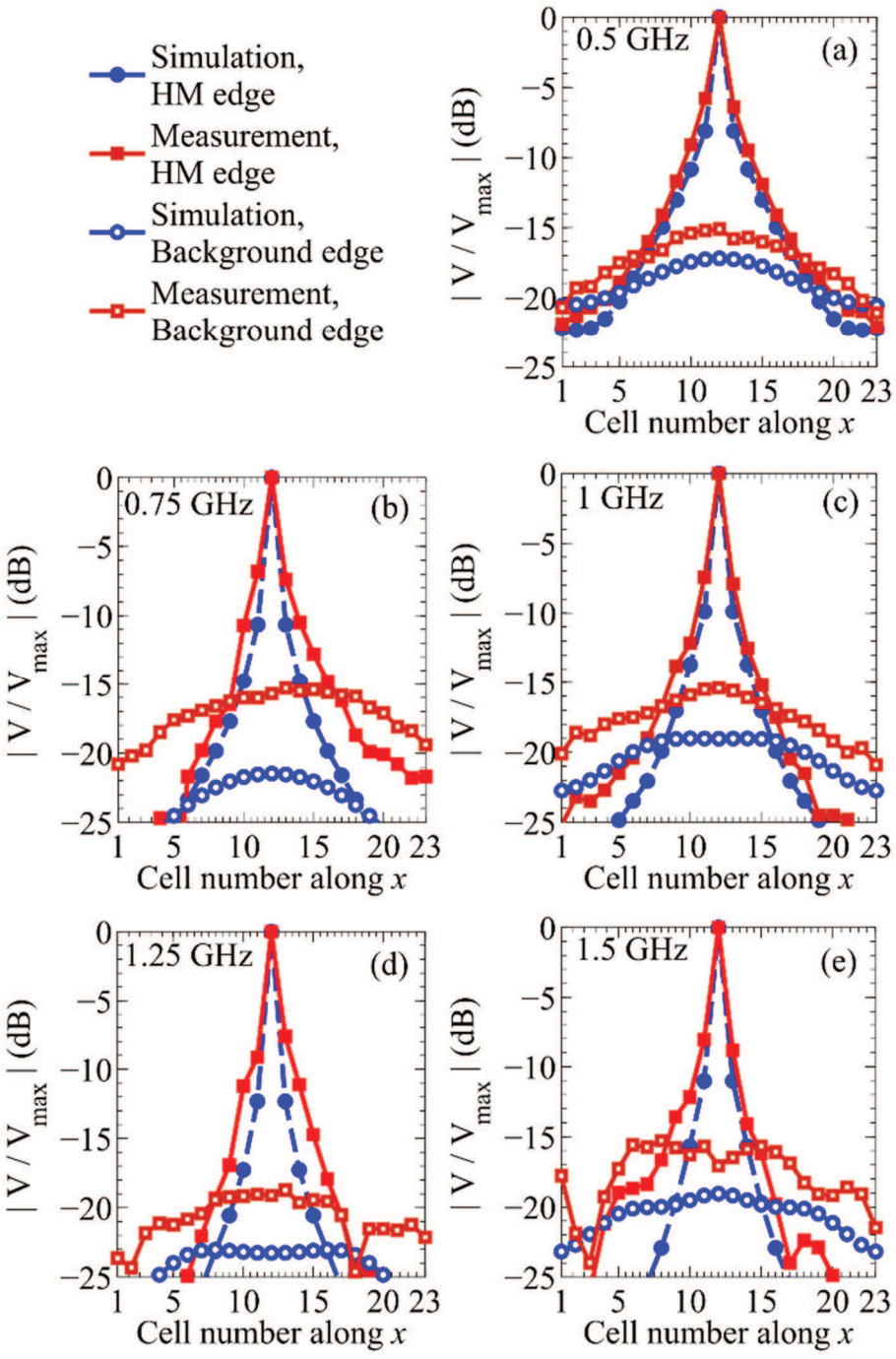

Fig. 4.8 Simulation and measurement results of the voltage magnitude profile at the HM bottom edge and at the Background top edge normalized by the maxima V_{max} at the HM bottom edge for simulation and measurements respectively at 0.5, 0.75, 1, 1.25, and 1.5 GHz. Measured and simulated results, in good agreement, show that subwavelength focusing is preserved across the HM.

Sec. 4.5 Conclusion

This chapter shows a practical implementation of a planar (2D) HM able to transport waves with large spectral wavenumber. In particular, the planar HM is realized using microstrip transmission lines, and is designed to achieve subwavelength focusing over a wide frequency range by engineering very flat, and stable-with-frequency, wavenumber hyperbolic dispersion curves. This has been achieved by loading a transmission line grid with capacitors in the *x* and *z* directions, leading to a canalization regime for the node voltage in the HM region. We have shown that the HM design can provide subwavelength focusing of $\lambda_g/31$ and $\lambda_g/19$ at 0.5 and 1 GHz, respectively, with good agreement between simulation and measurement results. We have also shown that the proposed HM can be used to resolve two sources separated by subwavelength distance of $\lambda_g/6$ and $\lambda_g/3$ at 0.5 and 1 GHz, respectively.

Appendix A Derivation of the Dispersion Relation via Bloch Theory

According to Bloch theory applied to 2D TLs [8], the wave-vector dispersion relation of a loaded 2D TL grid is obtained by solving the equation

$$\begin{aligned} B^x D^x \left[\cos\left(k_z d\right) - \left(C^z B^z + A^z D^z \right) \right] + \\ B^z D^z \left[\cos\left(k_x d\right) - \left(C^x B^x + A^x D^x \right) \right] = 0 \end{aligned} \tag{4.8}$$

where

$$A^{x,z} = \cos\left(\frac{\beta d}{2}\right) + \frac{1}{Z_0 \omega 2 C_{x,z}} \sin\left(\frac{\beta d}{2}\right), \tag{4.9}$$

$$B^{x,z} = jZ_0 \sin\left(\frac{\beta d}{2}\right) + \frac{1}{j\omega 2C_{x,z}} \cos\left(\frac{\beta d}{2}\right), \tag{4.10}$$

$$C^{x,z} = jY_0 \sin\left(\frac{\beta d}{2}\right), \tag{4.11}$$

$$D^{x,z} = \cos\left(\frac{\beta d}{2}\right) \tag{4.12}$$

are the transfer (ABCD) matrix entries of the microstrip lines of length $d/2$ (with characteristic impedance $Z_0 = 1/Y_0$ and wavenumber β) along the *x* and *z* axes (indicated by the superscripts *x* and *z*) loaded by capacitors $2C_{x,z}$ in a $d \times d$ unit cell as depicted in Fig. 4.1(c). Due to the reciprocity of the unit cell, it follows that $A^{x,z}D^{x,z} - B^{x,z}C^{x,z} = 1$, thus

$$\begin{aligned} B^x D^x \left[\cos\left(k_z d\right) - \left(2C^z B^z + 1\right)\right] + \\ B^z D^z \left[\cos\left(k_x d\right) - \left(2C^x B^x + 1\right)\right] = 0 \end{aligned} \tag{4.13}$$

Moreover, due to the symmetry of the unit cell in our setup, $C^z = C^x$ and $D^z = D^x$, thus the dispersion relation can be further simplified as

$$B^x \left[\sin^2\left(\frac{k_z d}{2}\right) + C^x B^z\right] + B^z \left[\sin^2\left(\frac{k_x d}{2}\right) + C^x B^x\right] = 0 \tag{4.14}$$

By dividing all the terms in (4.14) by $B^x B^z$ and substituting C^x from (4.11), we arrive at the dispersion relation in (4.1).

Appendix B Effective Medium Approach as a Particular Case of Bloch Theory

It is interesting how the effective medium model can be derived from the Bloch formulation based on the transfer matrix approach. We can simplify the dispersion relation in (4.1) by assuming $k_{x,z}d \ll 1$ and $\beta d \ll 1$. After using the approximation $\sin\left(k_{x,z}d/2\right) \approx k_{x,z}d/2$, expression (4.1) is rewritten as

$$\frac{\left(\frac{k_z d}{2}\right)^2}{B^z} + \frac{\left(\frac{k_x d}{2}\right)^2}{B^x} = -j2Y_0 \sin\left(\frac{\beta d}{2}\right) \tag{4.15}$$

Then, by using the approximations $\sin\left(\beta d/2\right) \approx \beta d/2$ and $\cos\left(\beta d/2\right) \approx 1$, the expressions $B^{x,z}$ [given in (4.2)] are simplified as

$$B_{x,z} \approx jZ_0 \frac{\beta d}{2} + \frac{1}{2j\omega C_{x,z}}. \tag{4.16}$$

The right-hand side of (4.15) is also simplified as

$$-j2Y \sin\left(\frac{\beta d}{2}\right) \approx -jY_0 \beta d \tag{4.17}$$

By replacing approximations (4.16) and (4.17) into (4.15) and using the definitions $\beta = \omega\sqrt{L_{\text{dis}}C_{\text{dis}}}$ and $Z_0 = \sqrt{L_{\text{dis}}/C_{\text{dis}}}$, we reach the dispersion relation of the HM effective medium approach as given in (4.3).

Note that for the background isotropic region, where we can assume $C_{x,z} = \infty$, the dispersion relation (4.3) leads to the wavenumber in the background region $k_b = \sqrt{k_x^2 + k_z^2} = \omega\sqrt{\mu_b \varepsilon_b} = \omega\sqrt{L_{\text{dis}} 2C_{\text{dis}}} = \beta\sqrt{2}$, where $\mu_b = \mu_x = \mu_z = L_{dis}$ and $\varepsilon_b = 2C_{dis}$.

Acknowledgment

The authors are thankful to Rhode Schwarz for the measurement system, to Ansys Inc. for providing HFSS, and to Agilent for providing ADS, instrumental in the present analysis. We thank K. Rice, S. Park, and K. Vuong from the University of California Irvine, for their contribution to the experimental setup. This chapter is reproduced based on the material in [S. H. Sedigy, C. Guclu, S. Campione, M. K. Amirhosseini, and F. Capolino, "Wideband Planar Transmission Line Hyperbolic Metamaterial for Subwavelength Focusing and Resolution," *IEEE Trans. on Microwave Theory and Techn*., vol. 61, pp. 4110 - 4117, 2013], © 2013 IEEE.

References

[1] M. Born and E. Wolf, *Principles of Optics*, 7th ed., Cambridge, United Kingdom, Cambridge Univ. Press, 1999.

[2] P. A. Belov and M. G. Silveirinha, "Resolution of subwavelength transmission devices formed by a wire medium," *Phys. Rev. E*, vol. 73, p. 056607, May 2006.

[3] J. B. Pendry, "Negative Refraction Makes a Perfect Lens," *Phys. Rev. Lett.*, vol. 85, pp. 3966–3969, Oct. 2000.

[4] D. R. Smith, D. Schurig, M. Rosenbluth, S. Schultz, S. A. Ramakrishna, and J. B. Pendry, "Limitations on subdiffraction imaging with a negative refractive index slab," *Appl. Phys. Lett.*, vol. 82, p. 1506, Mar. 2003.

[5] D. Maystre and S. Enoch, "Perfect lenses made with left-handed materials: Alice's mirror?," *J. Opt. Soc. Am. A*, vol. 21, pp. 122–131, Jan 2004.

[6] A. Grbic and G. V. Eleftheriades, "Negative refraction, growing evanescent waves, and sub-diffraction imaging in loaded transmission-line metamaterials," *IEEE Trans. Microw. Theory Techn.*, vol. 51, pp. 2297–2305, Dec. 2003.

[7] A. Grbic and G. V. Eleftheriades, "Growing evanescent waves in negative-refractive-index transmission-line media," *Appl. Phys. Letters*, vol. 82, p. 1815, Mar 2003.

[8] A. Grbic and G. V. Eleftheriades, "Periodic analysis of a 2-D negative refractive index transmission line structure," *IEEE Trans. Antennas Propagat.*, vol. 51, pp. 2604–2611, Oct 2003.

[9] A. K. Iyer, P. C. Kremer, and G. V. Eleftheriades, "Experimental and theoretical verification of focusing in a large, periodically loaded transmission line negative refractive index metamaterial," *Opt. Express*, vol. 11, pp. 696–708, Apr. 2003.

[10] P. A. Belov, Y. Hao, and S. Sudhakaran, "Subwavelength microwave imaging using an array of parallel conducting wires as a lens," *Phys. Rev. B*, vol. 73, p. 033108, Jan. 2006.

[11] X. Radu, A. Lapeyronnie, and C. Craeye, "Numerical and Experimental Analysis of a Wire Medium Collimator for Magnetic Resonance Imaging," *Electromagnetics*, vol. 28, pp. 531–543, Sept. 2008.

[12] X. Radu, D. Garray, and C. Craeye, "Toward a wire medium endoscope for MRI imaging," *Metamaterials*, vol. 3, pp. 90–99, Oct. 2009.

[13] P. A. Belov, C. R. Simovski, and P. Ikonen, "Canalization of subwavelength images by electromagnetic crystals," *Phys. Rev. B*, vol. 71, p. 193105, May 2005.

[14] Y. Jin, "Improving Subwavelenght Resolution of Multilayered Structures Containing Negative-Permittivity Layers by Flatting the Transmission Curves," *PIER*, vol. 105, pp. 347-364, 2010.

[15] R. Smith and D. Schurig, "Electromagnetic Wave Propagation in Media with Indefinite Permittivity and Permeability Tensors," *Phys. Rev. Lett.*, vol. 90, p. 077405, Feb. 2003.

[16] C. Guclu, S. Campione, and F. Capolino, "Hyperbolic metamaterial as super absorber for scattered fields generated at its surface," *Phys. Rev. B*, vol. 86, p. 205130, Nov. 2012.

[17] P. A. Belov and Y. Hao, "Subwavelength imaging at optical frequencies using a transmission device formed by a periodic layered metal-dielectric structure operating in the canalization regime," *Phys. Rev. B*, vol. 73, Mar 2006.

[18] W. Yan, N. A Mortensen, and M. Wubs, "Hyperbolic metamaterial lens with hydrodynamic nonlocal response," *Opt. Express*, vol. 21, pp. 15026-15036, Jun. 2013.

[19] K. G. Balmain, A. A. E. Luttgen, and P. C. Kremer, "Resonance cone formation, reflection, refraction, and focusing in a planar anisotropic metamaterial," *IEEE Antennas Wireless Propag. Lett.*, vol. 1, pp. 146-149, Nov. 2002.

[20] J. K. H. Wong, K. G. Balmain, and G. V. Eleftheriades, "Fields in planar anisotropic transmission-line metamaterials," *IEEE Trans. Antennas Propag.*, vol. 54, pp. 2742-2749, Oct. 2006.

[21] G. V. Eleftheriades and O. F. Siddiqui, "Negative refraction and focusing in hyperbolic transmission-line periodic grids," *IEEE Trans. Microw. Theory Techn.*, vol. 53, pp. 396-403, Jan. 2005.

[22] Y. Feng, X. Teng, Y. Chen, and T. Jiang, "Electromagnetic wave propagation in anisotropic metamaterials created by a set of periodic inductor-capacitor circuit networks," *Phys. Rev. B*, vol. 72, p. 245107, Dec. 2005.

[23] P. V. K. Alyona V. Chshelokova, Alexander N. Poddubny, Dmitry S. Filonov, Alexey P. Slobozhanyuk, Yuri S. Kivshar, and Pavel A. Belov, "Hyperbolic transmission-line metamaterials," *J. Appl. Phys.*, vol. 112, p. 073116, Oct. 2012.

CHAPTER 5

ARRAY OF DIPOLES NEAR HYPERBOLIC METAMATERIAL

Sec. 5.1 Motivation

We investigate the capabilities of hyperbolic metamaterials (HMs) to couple near-fields (i.e., evanescent waves) emitted by a two-dimensional periodic array of electric dipoles to propagating waves. In particular, large order Floquet harmonics with transverse magnetic (TM) polarization, that would be evanescent in free space and therefore confined near the array surface, are transformed into propagating spectrum inside the HM, and thus carry power away. Because of this property, independent of the finite or infinite extent of the HM, the power generated by an array of elementary electric dipoles is strongly enhanced when the array is located near a HM surface and is mostly directed into the HM. In particular, the power coupled to the HM exhibits narrow frequency features that can be employed in detection applications. The results shown in this chapter provide a clear signature on wave dynamics in HMs. A link between the results pertaining to the case of an isolated dipole on top of HM and the planar array is found convenient to explain both wave dynamics and

spectral power distribution. The narrow frequency emission features appear in the array case only; they depend on its spatial periodicity and remarkable on the HM thickness.

Hyperbolic metamaterials (HMs) are a subcategory of artificial uniaxial anisotropic materials that exhibit hyperbolic isofrequency wave-vector dispersion diagram [1-3]. HMs allow for engineering the spatial spectrum of propagating waves and thus power emission exploiting a wide propagating spectrum when compared to common dielectrics. This unusually wide spatial spectrum of power emission leads to novel phenomena such as the enhancement of the power scattered by nanospheres [1] or of the one emitted by imposed dipoles [1-3] located above HM surfaces. Furthermore, HMs are capable of absorbing (in the form of propagating waves) the power emitted by sources in their proximity. This, in turn, means that decay rate of emitters can be controlled without resorting to substrate's loss engineering. For this reason, HMs have been used to engineer the Purcell effect and emission decay rate, as well as the enhancement of spontaneous emission [4-11]. Moreover, the wide spatial spectrum supported by HMs leads to applications such as focusing with extreme subwavelength resolution and superlensing [6, 12-18], as well as absorption and reflection control [19-21]. HMs have also been shown to exhibit negative refraction [22-25] and epsilon-near-zero capabilities [26, 27], and the latter could be for example employed to improve nonlinear processes. In [28] the formation of second harmonic double-resonance cones has been proven. Moreover, efficient second harmonic generation has been reported in [29] through the use of micrometer-thick slabs with hyperbolic permittivity tensor.

HMs can be fabricated at infrared and optical frequencies using metal-dielectric multilayers [6, 30], dielectric-semiconductor multilayers [31], graphene-dielectric multilayers [2, 24, 27, 32] or metallic wires embedded in dielectric substrates [21, 33]. In

particular, the emergence of hyperbolic dispersion in multilayered HMs does not rely on any resonant behavior and thus occurs in a wide frequency band. A review of certain wave properties in HMs is reported in [1, 34-36]. We stress that practical HM realizations alter the ideal hyperbolic wavevector dispersion curve, and limit the propagating spectrum in contrast to what is predicted by the effective medium approximation (EMA) that does not introduce any limitation for the propagating spectrum in HMs [1, 3, 37].

In this study, we carry for the first time an analysis of electromagnetic waves generated by a two-dimensional (2D) periodic array of electric dipoles located above a HM. This study is a precursor to the investigation of the scattered power upon an array of passive, polarizable particles on top of HM, as for example done in [1] for a single spherical nanoparticle. Once the resulting linear system is solved for the induced dipole moments of the particles, the scattered power evaluation would follow a similar procedure to the one reported here. We first show how Floquet waves (FWs) emanating from such an array, that would be otherwise evanescent in free space, are instead transformed into propagating extraordinary waves inside a HM. We then investigate the enhancement of the power radiated by a 2D periodic array of impressed electric dipoles above a HM substrate, motivated by earlier work in which small scatterers on top of HMs (which can be modeled using single dipole approximation) or roughness on HM surfaces are shown to realize unprecedented absorption of plane waves [19, 21]. We show that most of the power generated by the 2D periodic array is directed towards the HM. We investigate how the array periodicity plays a critical role in the possibility to allocate wave propagation in the ideally indefinite spectral propagating channels of the HM. We further show the effect of HM substrate's thickness on the properties mentioned above. For the first time, for the case of a

2D periodic array of sources on top of HM, we show the existence of very narrow-frequency emission peaks in both infinite and finite-thickness HMs, and then explain the theory thereof. Such peaks can be useful for sensing applications. Finally the discrete dipole approximation and its limitations are discussed over a representative example of array of rectangular current sheets (i.e., with limited physical domain).

Sec. 5.2 Coupling and Propagation of large-index Floquet Waves to a HM

The 2D periodic array of elementary electric dipoles is located above a HM at a distance *h* from its surface as in Fig. 5.1(a). Electric dipolar sources in the array are located at $\mathbf{r}_{mn} = \mathbf{r}_{00} + ma\hat{\mathbf{x}} + nb\hat{\mathbf{y}}$ ($m, n = 0, \pm 1, \pm 2, \ldots$), where a and b are the periods along the *x* and *y* directions, respectively, and $\mathbf{r}_{00} = x_{00}\hat{\mathbf{x}} + y_{00}\hat{\mathbf{y}} + z_{00}\hat{\mathbf{z}}$ is the location of the reference dipole. In the following, the 00th reference dipole is assumed to be located at $\mathbf{r}_{00} = \mathbf{0}$ (here we implicitly assume the time harmonic convention $e^{-i\omega t}$). Thus an electric dipole at $\mathbf{r}_{mn}$ has a dipole moment $\mathbf{p}_{mn} = \mathbf{p}_{00}\exp\left(i\mathbf{k}_t \cdot \mathbf{r}_{mn}\right)$, where $\mathbf{k}_t = k_x\hat{\mathbf{x}} + k_y\hat{\mathbf{y}}$ is the wavevector defining the progressive phasing of the dipoles on the *x,y* plane, and $\mathbf{p}_{00} = p_x\hat{\mathbf{x}} + p_y\hat{\mathbf{y}} + p_z\hat{\mathbf{z}}$ is the electric dipole moment of the 00th reference dipole.

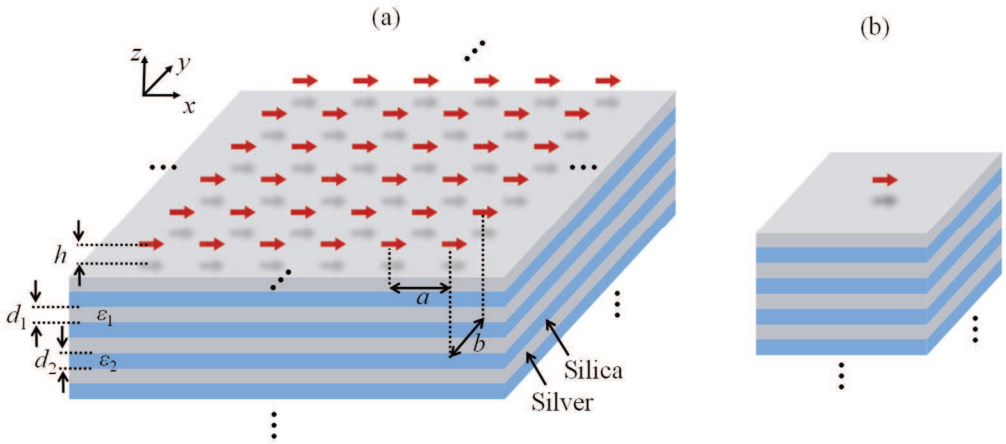

Fig. 5.1 (a) Schematic of an array of electric dipoles at a distance h from the surface of a hyperbolic metamaterial. Example of HM made of a stack of dielectric and silver layers with thicknesses d_1 and d_2 and relative permittivities ε_1 and ε_2. (b) Schematic of single dipole at a distance h from the surface of a hyperbolic metamaterial as in part (a).

We demonstrate here that near fields, in the form of FWs, emitted by a 2D periodic array of electric dipolar sources are coupled to propagating waves inside the HM substrate. It is well known that, in general depending on the array periodicity, only a certain (finite) number of FWs are propagating in a common dielectric, and thus carry power away from the array. The remaining FWs are in general evanescent and are confined mostly to the array plane forming the near field.

Consider for example the *direct* electric field produced by a 2D periodic array of elementary electric dipoles in free space, represented in terms of transverse-to-z polarized electric (TE) and magnetic (TM) pq-indexed FWs as

$$\mathbf{E}(\mathbf{r}) = \sum_{p,q=-\infty}^{\infty} \left(\mathbf{E}_{pq}^{\mathrm{TM}} + \mathbf{E}_{pq}^{\mathrm{TE}} \right). \tag{5.1}$$

Each FW in free space is given by [38]

$$\mathbf{E}_{pq}^{\mathrm{TM,TE}}(\mathbf{r}) = \frac{i}{2ab\varepsilon_0}\frac{e^{i\left(\mathbf{k}_{t,pq}\cdot\mathbf{r}+k_{z0,pq}|z|\right)}}{k_{z0,pq}}\mathbf{e}_{pq}^{\mathrm{TM,TE}}, \tag{5.2}$$

with

$$\begin{aligned}\mathbf{e}_{pq}^{\mathrm{TM}} &= \left\{\begin{array}{l}\left[\dfrac{k_{z0,pq}^2}{k_{t,pq}^2}\mathbf{k}_{t,pq} \mp k_{z0,pq}\hat{\mathbf{z}}\right]\mathbf{k}_{t,pq} \\ +\left[k_{t,pq}^2\hat{\mathbf{z}} \mp k_{z0,pq}\mathbf{k}_{t,pq}\right]\hat{\mathbf{z}}\end{array}\right\}\cdot\mathbf{p}_{00}, \\ \mathbf{e}_{pq}^{\mathrm{TE}} &= \frac{k_0^2}{k_{t,pq}^2}\left(\mathbf{k}_{t,pq}\times\hat{\mathbf{z}}\right)\left(\mathbf{k}_{t,pq}\times\hat{\mathbf{z}}\right)\cdot\mathbf{p}_{00},\end{aligned} \tag{5.3}$$

where the minus (plus) sign in Eq. (5.3) is used when the observation point is above (below) the array plane. Longitudinal wavenumbers in free space, $k_{z0,pq}$, will be denoted with '0' in the subscript. The transverse wavevector of a *pq*-indexed FW is defined as

$$\mathbf{k}_{t,pq} = \mathbf{k}_{t,00} + \frac{2\pi p}{a}\hat{\mathbf{x}} + \frac{2\pi q}{b}\hat{\mathbf{y}}, \tag{5.4}$$

and $k_{t,pq}^2 = \mathbf{k}_{t,pq}\cdot\mathbf{k}_{t,pq}$. It is clear that the field in Eqs. (5.1-3)is intimately related to the transverse and longitudinal wavenumbers, $k_{t,pq}$ and $k_{z0,pq}$, respectively. In free space the relation of $k_{t,pq}$ and $k_{z0,pq}$ follows the free space isofrequency wavenumber dispersion equation, $k_{t,pq}^2 + k_{z0,pq}^2 = k_0^2$, with $k_0 = \omega/c$ the free space wavenumber, ω the angular frequency and *c* the speed of light in vacuum. Therefore, for large *pq*-indexed FWs, the longitudinal wavenumber in free space $k_{z0,pq} = i\sqrt{k_{t,pq}^2 - k_0^2}$ is purely imaginary, with $\mathrm{Im}\left(k_{z0,pq}\right) > 0$ to satisfy the radiation boundary condition at infinity (for "proper" waves, detailed information on proper and improper wave can be found in [38-41]). Such FWs are

evanescent waves decaying exponentially away from the array plane (on the other hand, improper waves have opposite sign and grow exponentially toward infinity).

Consider now the scenario in Fig. 5.1(a), where the FWs generated by a 2D periodic array of electric dipoles with transverse wavenumber $\mathbf{k}_{t,pq}$ couple to a homogeneous HM characterized by the relative permittivity tensor

$$\underline{\boldsymbol{\varepsilon}}_{\mathrm{HM}} = \varepsilon_t \left(\hat{\mathbf{x}}\hat{\mathbf{x}} + \hat{\mathbf{y}}\hat{\mathbf{y}} \right) + \varepsilon_z \hat{\mathbf{z}}\hat{\mathbf{z}}, \tag{5.5}$$

with $\varepsilon_t \varepsilon_z < 0$ in an ideal lossless case, where ε_t and ε_z (both real numbers) represent the transverse and longitudinal entries of the diagonal relative permittivity tensor, respectively. Inside the HM, TM waves are extraordinary waves that satisfy the hyperbolic isofrequency dispersion relation [1, 42, 43] (assuming non-magnetic materials, thus relative permeability is taken as unity in the following)

$$\frac{k_{t,pq}^2}{\varepsilon_z} + \frac{\left(k_{z1,pq}^{\mathrm{TM}} \right)^2}{\varepsilon_t} = k_0^2, \tag{5.6}$$

where $k_{t,pq}$ is matched to that of the FWs in free space above the HM (longitudinal wavenumbers in HM are denoted with '1' in the subscript). Isofrequency hyperbolic wavevector dispersion occurs when $\varepsilon_t \varepsilon_z < 0$, and we recall that two possible scenarios may occur, with either $\varepsilon_z < 0$ or $\varepsilon_t < 0$. The latter will be treated in Sec. 5.4 pertaining to discussion and illustrative examples because it can be obtained at optical frequencies by simply stacking metal and dielectric layers of subwavelength thicknesses [1, 3, 25, 30].

Following Eq. (5.6), the *pq*-indexed TM FWs in the HM have longitudinal wavenumbers given by

$$k_{z1,pq}^{\mathrm{TM}} = \sqrt{\varepsilon_t \left(k_0^2 - \frac{1}{\varepsilon_z} k_{t,pq}^2 \right)}, \tag{5.7}$$

with sign of the square root chosen regarding the condition explained in the following. In general, assuming the presence of losses in the HM, the longitudinal wavenumber is complex and given as

$$k_{z1,pq}^{\mathrm{TM}} = \beta_{z1,pq}^{\mathrm{TM}} + i\alpha_{z1,pq}^{\mathrm{TM}}. \tag{5.8}$$

A FW generated by the array at z = 0, with transverse wavenumber $k_{t,pq}$, assumes the wave propagator $\exp(ik_{z1,pq}^{\mathrm{TM}}|z|) = \exp(-ik_{z1,pq}^{\mathrm{TM}} z)$ along the $-z$ direction inside the HM underneath. The condition $\alpha_{z1,pq}^{\mathrm{TM}} > 0$ is necessary to satisfy the boundary condition when z tends to $-\infty$. Also, as explained in [1, 23, 25], waves in the HM are backward when $\varepsilon_t < 0$ and $\varepsilon_z > 0$ and hence characterized by $\beta_{z1,pq}^{\mathrm{TM}} < 0$, i.e., phase propagation occurs along $+z$ while power flows along $-z$. Indeed, as specified in [38-41] backward waves are characterized by a wavenumber that satisfies the relation $\beta_{z1,pq}^{\mathrm{TM}}\, \alpha_{z1,pq}^{\mathrm{TM}} < 0$.

Note that observing Eq. (5.7), when assuming absence of losses inside the HM, $k_{z1,pq}^{\mathrm{TM}}$ is *purely real* for *large pq* index values since the ratio $\varepsilon_t / \varepsilon_z$ is negative. This means that any TM FW with sufficiently large *pq* order is able to propagate inside the HM with a real longitudinal wavenumber $k_{z1,pq}^{\mathrm{TM}}$. Note that FWs with small *pq* indexes, in particular the

fundamental one with $(p,q)=(0,0)$, may or may not be propagating. Low order FWs are propagating if $\varepsilon_t > 0$ whereas they are evanescent when $\varepsilon_t < 0$. Nevertheless, the most important phenomenon is that in theory an infinite number of FWs are able to propagate in an ideal HM with unlimited hyperbolic isofrequency wavevector dispersion curve. In practical realization of HMs however, the HM periodicity along a coordinate would restrict the range of FWs are able to propagate, as it will be briefly discussed in Sec. 5.4, and the power in FWs would strongly depend on the distance of the array from the HM and the presence of losses

Having clarified the propagation of TM and TE FWs inside a HM, we now analyze their excitation generated by a 2D periodic array of dipoles located at a distance *h* below the array. We first assume that the HM is homogenous with relative permittivity tensor as in Eq. (5.5) and it is semi-infinite. As previously described, the direct field produced by the array is represented as a sum of *pq*-indexed FWs (i.e., plane waves) as in Eqs. (5.1-3)for an array in free space. Each *pq*-indexed FW generated by the array and directed towards –*z* is partly reflected at the free-space/HM interface, with TM/TE Fresnel reflection coefficient

$$\Gamma_{pq}^{\mathrm{TM,TE}} = \frac{Z_{\mathrm{HM}}^{\mathrm{TM,TE}}\left(\mathbf{k}_{t,pq}\right) - Z_{0}^{\mathrm{TM,TE}}\left(\mathbf{k}_{t,pq}\right)}{Z_{\mathrm{HM}}^{\mathrm{TM,TE}}\left(\mathbf{k}_{t,pq}\right) - Z_{0}^{\mathrm{TM,TE}}\left(\mathbf{k}_{t,pq}\right)}, \tag{5.9}$$

conveniently given in terms of the characteristic wave impedances of free space

$$Z_{0}^{\mathrm{TM}}\left(\mathbf{k}_{t,pq}\right) = \frac{k_{z0,pq}}{\omega\varepsilon_0}, \qquad Z_{0}^{\mathrm{TE}}\left(\mathbf{k}_{t,pq}\right) = \frac{\omega\mu_0}{k_{z0,pq}}, \tag{5.10}$$

and the characteristic wave impedances

$$Z_{\mathrm{HM}}^{\mathrm{TM}}\left(\mathbf{k}_{t,pq}\right)=\frac{k_{z1,pq}^{\mathrm{TM}}}{\omega\varepsilon_0\varepsilon_t},\qquad Z_{\mathrm{HM}}^{\mathrm{TE}}\left(\mathbf{k}_{t,pq}\right)=\frac{\omega\mu_0}{k_{z1,pq}^{\mathrm{TE}}},\tag{5.11}$$

for the extraordinary (TM) and ordinary (TE) waves inside the HM, here assumed homogeneous. Note that $k_{z1,pq}^{\mathrm{TM}}$ for the extraordinary wave (TM) inside the HM is evaluated as in Eq. (5.7), whereas $k_{z1,pq}^{\mathrm{TE}}$ for the ordinary (TE) wave is evaluated by the ordinary wave dispersion relation $k_{t,pq}^2+\left(k_{z1,pq}^{\mathrm{TE}}\right)^2=\varepsilon_t k_0^2$, and thus

$$k_{z1,pq}^{\mathrm{TE}}=\sqrt{\varepsilon_t k_0^2-k_{t,pq}^2}\tag{5.12}$$

As discussed above, for TM waves with large *pq* indexes, $k_{z1,pq}^{\mathrm{TM}}$ is real, assuming a lossless HM, and thus also $Z_{\mathrm{HM}}^{\mathrm{TM}}\left(\mathbf{k}_{t,pq}\right)$ is real. Furthermore, in the case of a HM with $\varepsilon_t<0$ considered here we conclude after observing Eq. (5.11) that $Z_{\mathrm{HM}}^{\mathrm{TM}}\left(\mathbf{k}_{t,pq}\right)$ is real positive because a TM wave in the HM is backward (i.e., $\beta_{z1,pq}^{\mathrm{TM}}<0$) as discussed previously. Therefore, in a HM, including the occurrence of losses, the characteristic wave impedance $Z_{\mathrm{HM}}^{\mathrm{TM}}\left(\mathbf{k}_{t,pq}\right)$ as in Eq. (5.11) has a positive real part which is associated to power flowing in the HM in the −*z* direction. [Here, the general expression of a characteristic wave impedance $Z\left(\mathbf{k}_{t,pq}\right)$ is defined assuming that the real part of the *z*-directed (in the positive or negative *z* direction) Poynting vector emitted by the array of dipoles in absence of reflections is given by $S\left(\mathbf{k}_{t,pq}\right)=\frac{1}{2}\mathrm{Re}\left[\left|\mathbf{E}_{t,pq}\right|^2/Z_0^*\left(\mathbf{k}_{t,pq}\right)\right]$, where $\mathbf{E}_{t,pq}$ is the transverse field of the harmonic, yielding always positive $S\left(\mathbf{k}_{t,pq}\right)$ for waves carrying power away from the array (note that

a '*' denotes complex conjugation).] We recall that the total power propagating in the +/-z direction is the sum of power of all the Floquet harmonics, given as

$$P_{\pm z} = \iint_A \frac{1}{2}\mathrm{Re}\left(\mathbf{E}\times\mathbf{H}^*\right)\cdot\left(\pm\hat{\mathbf{z}}\right)dA = \\ = \frac{1}{2}\mathrm{Re}\left(\sum_{p,q=-\infty}^{\infty}\left[\frac{\left|\mathbf{E}_{t,pq}^{\mathrm{TM}}\right|^2}{Z_0^{\mathrm{TM}*}\left(\mathbf{k}_{t,pq}\right)}+\frac{\left|\mathbf{E}_{t,pq}^{\mathrm{TE}}\right|^2}{Z_0^{\mathrm{TE}*}\left(\mathbf{k}_{t,pq}\right)}\right]\right)ab \tag{5.13}$$

owing to the spatial orthogonality of Floquet harmonics with different orders and the vectorial orthogonality of TM and TE waves with same harmonic order (details can be found in Sec. 2.2 of [42]). Here A is the unit cell cross-section orthogonal to the z direction.

Each FW generated by the array above the HM is partly transmitted into the HM with transmission coefficient $T_{pq}^{\mathrm{TM,TE}} = 1+\Gamma_{pq}^{\mathrm{TM,TE}}$. We recall that all reflection and transmission coefficients $\Gamma_{pq}^{\mathrm{TM,TE}}$ and $T_{pq}^{\mathrm{TM,TE}}$ are defined with respect to transverse electric fields [44]) Therefore the transverse field at any location $\mathbf{r}$ above the 2D periodic array of dipoles (i.e., $z > 0$) is represented as

$$\mathbf{E}_t\left(\mathbf{r}\right) = \sum_{p,q=-\infty}^{\infty}\left[\begin{array}{l}\left(\mathbf{E}_{t,pq}^{\mathrm{TM}+}+\mathbf{E}_{t,pq}^{\mathrm{TM}-}\Gamma_{pq}^{\mathrm{TM}}e^{i2k_{z0,pq}h}\right)+\\ +\left(\mathbf{E}_{t,pq}^{\mathrm{TE}+}+\mathbf{E}_{t,pq}^{\mathrm{TE}-}\Gamma_{pq}^{\mathrm{TE}}e^{i2k_{z0,pq}h}\right)\end{array}\right]e^{ik_{z0,pq}z}, \tag{5.14}$$

where the subscript t denotes the transverse component of the *direct* electric field $\mathbf{E}_{pq}^{\mathrm{TM,TE}}$ in Eq. (5.2) and +/− superscripts denote that the respective quantity is evaluated at the limit $z\to 0^+$ and $z\to 0^-$, respectively [the array plane is assumed at $z=0$]. Note that the transverse component of $\mathbf{E}_{pq}^{\mathrm{TE}}$ is always continuous across the array plane, i.e. $\mathbf{E}_{t,pq}^{\mathrm{TE}+} = \mathbf{E}_{t,pq}^{\mathrm{TE}-}$

, and TE FWs are only emitted by transverse-to-z dipole components. On the other hand, the transverse component of $\mathbf{E}_{pq}^{\mathrm{TM}}$ should be treated carefully. For example when $\mathbf{p}_{00}$ is transverse to z, the transverse component of $\mathbf{E}_{pq}^{\mathrm{TM}}$ is continuous across the array plane, i.e. $\mathbf{E}_{t,pq}^{\mathrm{TM}+}=\mathbf{E}_{t,pq}^{\mathrm{TM}-}$; however when $\mathbf{p}_{00}$ is along z, the transverse component of $\mathbf{E}_{pq}^{\mathrm{TM}}$ follows the relation $\mathbf{E}_{t,pq}^{\mathrm{TM}+}=-\mathbf{E}_{t,pq}^{\mathrm{TM}-}$ [dictated by Eq. (5.3)].

At any location $\mathbf{r}$ below the array of dipoles and above the HM (i.e., $-h<z<0$) the transverse electric field is

$$\mathbf{E}_t(\mathbf{r})=\sum_{p,q=-\infty}^{\infty}\begin{bmatrix}\mathbf{E}_{t,pq}^{\mathrm{TM}-}\left(e^{-ik_{z0,pq}z}+\Gamma_{pq}^{\mathrm{TM}}e^{ik_{z0,pq}(2h+z)}\right)+\\ +\mathbf{E}_{t,pq}^{\mathrm{TE}-}\left(e^{-ik_{z0,pq}z}+\Gamma_{pq}^{\mathrm{TE}}e^{ik_{z0,pq}(2h+z)}\right)\end{bmatrix}. \tag{5.15}$$

The transverse field transmitted to a homogeneous HM (i.e., at any location $\mathbf{r}$ belonging to the HM, with $z<-h$) is represented as

$$\mathbf{E}_t(\mathbf{r})=\sum_{p,q=-\infty}^{\infty}\begin{bmatrix}\mathbf{E}_{t,pq}^{\mathrm{TM}-}T_{pq}^{\mathrm{TM}}e^{-ik_{z1,pq}^{TM}(z+h)}+\\ +\mathbf{E}_{t,pq}^{\mathrm{TE}-}T_{pq}^{\mathrm{TE}}e^{-ik_{z1,pq}^{TE}(z+h)}\end{bmatrix}e^{ik_{z0,pq}h}. \tag{5.16}$$

Looking at Eq. (5.16), it is clear that the distance h plays a fundamental role in determining the spectrum of evanescent waves in free space that can be coupled to propagating waves in the HM. In particular, when the array is located at a certain distance h from the HM surface, waves will decay with the propagator $e^{ik_{z0,pq}h}$, resulting in a decay factor $e^{-\mathrm{Im}(k_{z0,pq})h}$, in free space, and this will prevent high pq-indexed FWs from transferring power to the HM underneath.

Sec. 5.3 Power generated by a 2-D Periodic array of Electric dipoles above a HM

The real power density (the real part of the Poynting vector) of each *pq*-th FW in (+*z*) upward direction above the array is expressed as

$$S_{\text{up}}\left(\mathbf{k}_{t,pq}\right)=\frac{1}{2}\text{Re}\left[\frac{\left|\mathbf{E}_{t,pq}^{+}+\mathbf{E}_{t,pq}^{-}\Gamma_{pq}e^{i2k_{z0,pq}h}\right|^{2}}{Z_{0}^{*}\left(\mathbf{k}_{t,pq}\right)}\right], \tag{5.17}$$

where $Z_0\left(\mathbf{k}_{t,pq}\right)$ is the TM/TE wave impedance in vacuum.

Analogously, the real power density of each *pq*-th FW evaluated at the HM interface in the downward direction, and thus entering the HM, is given by

$$\begin{aligned}
&S_{\text{down}}\left(\mathbf{k}_{t,pq}\right)= \\
&=\frac{1}{2}\text{Re}\left[\frac{\left|\mathbf{E}_{t,pq}^{-}\right|^{2}\left[\left(1+\Gamma_{pq}e^{i2k_{z0,pq}h}\right)\left(1-\Gamma_{pq}e^{i2k_{z0,pq}h}\right)^{*}\right]}{Z_{0}^{*}\left(\mathbf{k}_{t,pq}\right)}\right]= \\
&=\frac{1}{2}\text{Re}\left[\frac{\left|\mathbf{E}_{t,pq}^{-}e^{ik_{z0,pq}h}\right|^{2}\left[\left(1+\Gamma_{pq}\right)\left(1-\Gamma_{pq}\right)^{*}\right]}{Z_{0}^{*}\left(\mathbf{k}_{t,pq}\right)}\right]= \\
&=\frac{1}{2}\text{Re}\left[\frac{\left|\mathbf{E}_{t,pq}^{-}T_{pq}e^{ik_{z0,pq}h}\right|^{2}}{Z_{\text{HM}}^{*}\left(\mathbf{k}_{t,pq}\right)}\right]
\end{aligned}, \tag{5.18}$$

where $Z_{\text{HM}}\left(\mathbf{k}_{t,pq}\right)$ is the wave impedance in HM. In Eq. (5.18) through the 1st to the 3rd expression, the power density in the –*z* direction is given (1st) at the array level, (2nd) in vacuum side of the HM-vacuum interface, and (3rd) in the HM side of the same interface,

respectively. Note that, in Eqs. (5.17) and (5.18), $k_{z0,pq}$ and $Z_0^*\left(\mathbf{k}_{t,pq}\right)$ are both either purely real or purely imaginary in vacuum and thus the three expressions yield equal results. In the 1st expression, $\Gamma_{pq}e^{i2k_{z0,pq}h}$ [appearing in both Eqs. (5.17) and (5.18)] is the reflection coefficient Γ_{pq} evaluated at the array plane, observing the downward direction, and $\mathbf{E}_{t,pq}^{-}e^{ik_{z0,pq}h}$ represents the transverse field of the downward-propagating wave evaluated at the HM's top surface in both 2nd and 3rd expressions. The superscript TM/TE is omitted in Eqs. (5.17) and (5.18) since both expressions are valid for both TM and TE waves, assuming all quantities are evaluated accordingly. The superscripts +/− follow the same convention introduced in Sec. 5.2.

In Eqs. (5.17) and (5.18) numerators are real valued; in contrast, denominators may be complex valued, depending on the medium where each FW is propagating into and the transverse wavevector $\mathbf{k}_{t,pq}$. In particular, $Z_0\left(\mathbf{k}_{t,pq}\right)$ is real only when $k_{t,pq}^2 < k_0^2$ and purely imaginary otherwise (for both TM and TE waves). In other words, only low *pq*-indexed FWs, with real $k_{z0,pq}$, carry power away from the array in the upward direction. Similarly, $Z_{\mathrm{HM}}^{\mathrm{TE}}\left(\mathbf{k}_{t,pq}\right)$ is (assuming lossless HM) either purely imaginary for any $k_{t,pq}$ (when $\varepsilon_t < 0$ and $\varepsilon_z > 0$), or purely real only for the spectrum $k_{t,pq}^2 < \varepsilon_t k_0^2$ (when $\varepsilon_t > 0$ and $\varepsilon_z < 0$). However for extraordinary waves with TM polarization inside the HM, the situation is rather different. The term $Z_{\mathrm{HM}}^{\mathrm{TM}}\left(\mathbf{k}_{t,pq}\right)$ has a real part (purely real for a lossless HM as discussed in Sec. 5.2) for large *pq*-indexed FWs because $k_{z1,pq}^{\mathrm{TM}}$ has a real part (purely real for a lossless HM) for large *pq* indexes as described in Sec. 5.2. Therefore, the total power coupled from

the array in free space to the HM underneath is determined by the power carried by a very large number (infinite for an ideal lossless HM) of propagating FWs hosted by HM (however, note that the power coupled to FW with large *pq* is also limited by the decay along the distance *h* as described in Sec. 5.2). Indeed, as it will be discussed in later sections, practical HM implementations based on periodic arrangement of layers or other configurations (e.g., wire medium) limit the maximum *pq* indexes of FWs that can propagate in HM, thus limiting the maximum amount of power coupled to HM. Equation (5.18) is valid for a homogeneous HM (that includes losses) and it is generalized to the case of multilayer HM by substituting T_{pq} with $1+\Gamma_{pq}$, and $Z_{\mathrm{HM}}\left(\mathbf{k}_{t,pq}\right)$ with the impedance at the multilayer HM interface, in the downward direction, $Z_{\mathrm{down}}(\mathbf{k}_{t,pq})$, as explained in [2]. The field inside the HM multilayer can be evaluated via transfer matrix method.

We now investigate in detail the power coupled to TM and TE plane wave spectra, based on [42, 45, 46], adapted to periodic structures, as in [47], for modeling the power emitted by a 2D periodic array of impressed (transverse or vertical) electric dipoles located slightly above an infinitely extended HM as in Fig. 5.1(a). Then we establish the relation between the plane wave spectra emanating from an array and a single dipole [as in Fig. 5.1(b)] above the same HM. Note that this TL formalism represents the solution of Maxwell's equations in the analyzed environment, i.e., it is an exact representation [42, 45, 46].

We are interested in the power emitted in +*z* and –*z* directions, in the following denoted by superscripts "up" and "down", respectively. The power emitted in a *unit cell* directed up/down for an array of *transverse dipoles* with $\mathbf{p}_{00} = p_x\hat{\mathbf{x}} + p_y\hat{\mathbf{y}}$ is given as a sum of TM and TE contributions as

$$P_{\text{up/down}} = \frac{\omega^2}{2ab} \sum_{p,q=-\infty}^{\infty} \left[\begin{matrix} U_{\text{up/down}}^{\text{TM}} \left(\mathbf{k}_{t,pq} \right) + \\ + U_{\text{up/down}}^{\text{TE}} \left(\mathbf{k}_{t,pq} \right) \end{matrix} \right]. \tag{5.19}$$

expressed in [W]. The TM and TE power spectra in Eq. (5.19) (normalized by angular frequency squared, ω^2) directed toward the $+/-z$ directions are

$$\begin{aligned} U_{\text{up/down}}^{\text{TM}} \left(\mathbf{k}_{t,pq} \right) = & \frac{\left| \mathbf{p}_{00} \cdot \mathbf{k}_{t,pq} \right|^2}{\left| \mathbf{k}_{t,pq} \right|^2} \\ & \times \frac{\text{Re} \left(Y_{\text{up/down}}^{\text{TM}*} \left(\mathbf{k}_{t,pq} \right) \right)}{\left| Y_{\text{up}}^{\text{TM}} \left(\mathbf{k}_{t,pq} \right) + Y_{\text{down}}^{\text{TM}} \left(\mathbf{k}_{t,pq} \right) \right|^2}, \end{aligned} \tag{5.20}$$

$$\begin{aligned} U_{\text{up/down}}^{\text{TE}} \left(\mathbf{k}_{t,pq} \right) = & \frac{\left| \mathbf{p}_{00} \cdot \left(\hat{\mathbf{z}} \times \mathbf{k}_{t,pq} \right) \right|^2}{\left| \mathbf{k}_{t,pq} \right|^2} \\ & \times \frac{\text{Re} \left(Y_{\text{up/down}}^{\text{TE}*} \left(\mathbf{k}_{t,pq} \right) \right)}{\left| Y_{\text{up}}^{\text{TE}} \left(\mathbf{k}_{t,pq} \right) + Y_{\text{down}}^{\text{TE}} \left(\mathbf{k}_{t,pq} \right) \right|^2}. \end{aligned} \tag{5.21}$$

The power emitted in a unit cell in an array of *vertical dipoles* with $\mathbf{p}_{00} = p_z \hat{\mathbf{z}}$ is instead

$$P_{\text{up/down}} = \frac{\omega^2}{2ab} \sum_{p=-\infty}^{\infty} \sum_{q=-\infty}^{\infty} W_{\text{up/down}}^{\text{TM}} \left(\mathbf{k}_{t,pq} \right), \tag{5.22}$$

where the power spectrum (normalized by angular frequency squared, ω^2), which has contribution only from TM waves, is

$$W_{\text{up/down}}^{\text{TM}}\left(\mathbf{k}_{t,pq}\right)=\frac{\left|\mathbf{p}_{00}\cdot\hat{\mathbf{z}}\right|^2}{\omega^2\left|\varepsilon\right|^2}\left|\mathbf{k}_{t,pq}\right|^2 \times\frac{\text{Re}\left(Z_{\text{up/down}}^{\text{TM}}\left(\mathbf{k}_{t,pq}\right)\right)}{\left|Z_{\text{up}}^{\text{TM}}\left(\mathbf{k}_{t,pq}\right)+Z_{\text{down}}^{\text{TM}}\left(\mathbf{k}_{t,pq}\right)\right|^2}. \tag{5.23}$$

Here $Y_{\text{up/down}}^{\text{TM/TE}}=\left(Z_{\text{up/down}}^{\text{TM/TE}}\right)^{-1}$, and the impedances $Z_{\text{up/down}}^{\text{TM/TE}}$ are defined by the ratio of transverse field components [42]

$$Z_{\text{up/down}}^{\text{TM}}\left(\mathbf{k}_{t,pq}\right)=\lim_{z\to 0^{\pm}}\frac{\pm\mathbf{E}_{pq}^{\text{tot}}\left(z\right)\cdot\mathbf{k}_{t,pq}}{\mathbf{H}_{pq}^{\text{tot}}\left(z\right)\cdot\left(\hat{\mathbf{z}}\times\mathbf{k}_{t,pq}\right)} \tag{5.24}$$

$$Z_{\text{up/down}}^{\text{TE}}\left(\mathbf{k}_{t,pq}\right)=\lim_{z\to 0^{\pm}}\frac{\pm\mathbf{E}_{pq}^{\text{tot}}\left(z\right)\cdot\left(\mathbf{k}_{t,pq}\times\hat{\mathbf{z}}\right)}{\mathbf{H}_{pq}^{\text{tot}}\left(z\right)\cdot\mathbf{k}_{t,pq}} \tag{5.25}$$

where the "tot" superscript indicates that the E/H-field is the sum of both the direct and the reflected fields of the respective *pq*-th Floquet harmonic and here in the limit operation, the sign + (–) is taken for the "up" ("down") direction. Note that in this case $Z_{\text{up}}^{\text{TM/TE}}=Z_0^{\text{TM/TE}}$, because there is no wave reflected from the upper space; whereas $Z_{\text{down}}^{\text{TM/TE}}\left(\mathbf{k}_{t,pq}\right)$ needs to be computed via transfer matrix method, since it accounts for the reflection at the HM interface. Equations (5.19-23) are derived by lengthy though straightforward substitutions of Eqs. (5.1-3) into Eqs. (5.17) and (5.18) utilizing the reflection coefficients evaluated at the array plane based on $Y_{\text{up/down}}^{\text{TM/TE}}$ and $Z_{\text{up/down}}^{\text{TM/TE}}$ for particular dipole orientations as $\mathbf{p}_{00}=p_x\hat{\mathbf{x}}+p_y\hat{\mathbf{y}}$ or as $\mathbf{p}_{00}=p_z\hat{\mathbf{z}}$. Accordingly, the power carried in a FW harmonic is $\iint_A S\left(\mathbf{k}_{t,pq}\right)dA=\left[\omega^2/\left(2ab\right)\right]U\left(\mathbf{k}_{t,pq}\right)$ for transverse dipoles' excitation and

$\iint_A S\left(\mathbf{k}_{t,pq}\right) dA = \left[\omega^2 / (2ab)\right] W\left(\mathbf{k}_{t,pq}\right)$ for vertical dipoles' excitation (Since these expressions are applied to either TM or TE polarizations, and either the up or down directions, the common TM/TE superscripts, and up/down subscripts have been omitted). In Appendix B, the derivation steps for $U_{\text{down}}^{\text{TM}}$ are provided as an example. Those for the other terms can be derived in an analogous way.

In the following we establish a relation between the power expressions related to the 2D periodic array of electric dipoles to that of a single electric dipole on top of HM as in Fig. 5.1(b), analyzed in [1] for example. According to the expressions presented in [1] for the *single dipolar source* case, the upward and downward directed power emitted by a *transverse dipole* are

$$P_{\text{up/down}} = \frac{\omega^2}{8\pi^2} \iint \begin{bmatrix} U_{\text{up/down}}^{\text{TM}}\left(\mathbf{k}_t\right) + \\ + U_{\text{up/down}}^{\text{TE}}\left(\mathbf{k}_t\right) \end{bmatrix} dk_x dk_y . \tag{5.26}$$

The power emitted by a *vertical dipole* is

$$P_{\text{up/down}} = \frac{\omega^2}{8\pi^2} \iint W_{\text{up/down}}^{\text{TM}}\left(\mathbf{k}_t\right) dk_x dk_y . \tag{5.27}$$

Note that the functions *U* and *W* within the summations in Eqs. (5.19) and (5.23), for the periodic array case, are the same functions as the integrands in Eqs. (5.26) and (5.27), for the single dipole. In other words, the radiation from the array corresponds to a spectral sampling of the continuous spectrum of waves emanating from a single source. This fact emphasizes the importance of array periodicity to control effectively the sampling in the band of propagating FWs in HM, as it will be pointed out in what follows.

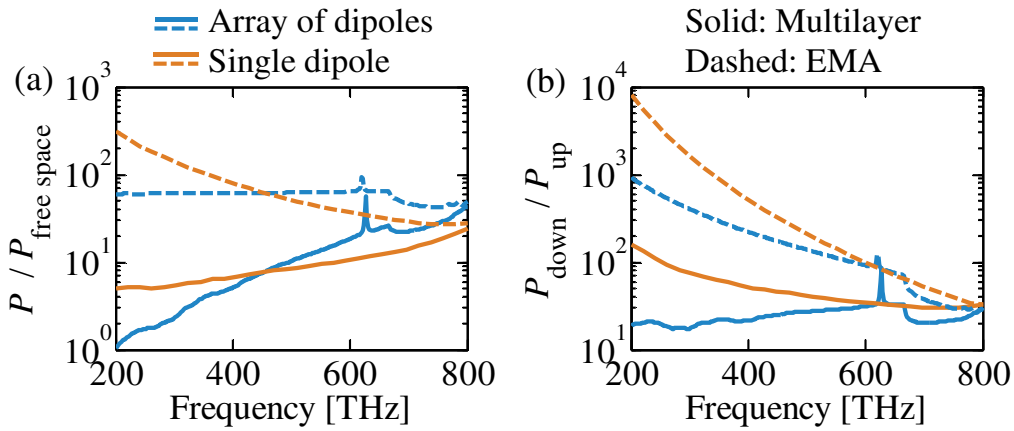

Fig. 5.2 (a) Enhancement of the power $P = P_{\text{up}} + P_{\text{down}}$ emitted by an array of dipoles ($a = b = 300$ nm) with a HM underneath with respect to that emitted in free space. Dipoles are polarized along *x*, with $\mathbf{k}_{t,00} = 0.5k_0\hat{\mathbf{x}}$. For comparison, also the power enhancement pertaining to a single dipole over the HM is provided. (b) Ratio of power emitted by the array and a single dipole towards HM (down) and towards the upper homogeneous isotropic space (up) versus frequency. Dashed lines are obtained for a homogeneous HM (via EMA) made of silver and silica layers with equal thicknesses $d_1 = d_2 = 10$ nm whereas solid lines are obtained using a rigorous multilayer Green's function implementation for the same HM. Silver permittivity ε_2 is from [48] and dielectric relative permittivity ε_1 is equal to 2.2. Source distance from the HM is assumed as $h = 10$ nm.

Before going into the details of the wave dynamics of the system under analysis, we provide two preliminary examples showing how the HM impacts the emitted power and the ratio of the power directed toward the HM for an array of dipoles against a single dipole for an infinitely extended HM substrate. Here we utilize a semi-infinite practical HM implementation consisting of a stacked bi-layers made of silver (whose dielectric relative permittivity function ε_2 is taken from the experimental results including losses in [48]) and silica ($\varepsilon_1 = 2.2$) layers with equal thicknesses $d_1 = d_2 = 10$ nm. The power evaluations are carried out using HMs modeled with two methods: the effective medium approximation (EMA) as given in [49] where

$$\varepsilon_t = \frac{\varepsilon_1 d_1 + \varepsilon_2 d_2}{d_1 + d_2} \qquad \varepsilon_z^{-1} = \frac{\varepsilon_1^{-1} d_1 + \varepsilon_2^{-1} d_2}{d_1 + d_2}. \tag{5.28}$$

and the more accurate multilayer Bloch analysis [44] based on the transfer matrix method in evaluation of the impedances $Z_{\text{down}}\left(\mathbf{k}_{t,pq}\right)$.

In Fig. 5.2(a), we report the enhancement of the total power $P = P_{\text{up}} + P_{\text{down}}$ emitted by an array of dipoles with respect to the total power emitted by the array in free space. The power enhancement for an array of dipoles in general increases as the frequency is increased. As a comparison we also provide the enhancement for a single dipole which exhibits less dependence on frequency and the enhancement is larger than the one in the array case at lower frequencies whereas at higher frequencies, the array case shows more enhancement due to periodicity of the sources as will be shown in Sec. 5.4. Moreover the EMA vastly overestimates the power enhancement at lower frequencies for both cases. We will recall the reasons behind this overestimation in the next section using a spatial spectrum interpretation. This is a well-known shortcoming of EMA [1, 3, 37], which was recently discussed in [50] by showing that the presence of surface plasmon modes supported by multilayer HMs limits the validity of EMA. In our multilayer HM we have used a silver layer as the topmost layer. If we were to use a silica layer instead, its effect would result to an increased distance of the dipole array from the HM, which would in turn reduce the coupling of power from the array of dipoles to the HM. We refer the reader to detailed investigations on the topic reported in [1, 3]. When using the rigorous multilayer Bloch theory (it is exact when assuming ideally smooth surface boundaries), the enhancement for the array case is between 10 to 30 folds for frequencies between 500 and 800 THz, where EMA yields at least

one order more enhancement at low frequency. In Fig. 5.2(b), we report the ratio $P_{\text{down}} / P_{\text{up}}$ for the cases in Fig. 5.2(a). When using the Bloch model, we observe that the array has $P_{\text{down}} / P_{\text{up}}$ ratio between 20 and 30 over the whole frequency range whereas the ratio is higher for the single dipole case especially at the lower frequencies. The overestimation of $P_{\text{down}} / P_{\text{up}}$ by the homogenized HM model (EMA) is also observed, particularly at low frequency. We further show in Fig. 5.3 the ratios $P / P_{\text{free space}}$ and $P_{\text{down}} / P_{\text{up}}$ by changing the period of the array of dipoles along the *x* and *y* axes, calculated assuming a multilayer HM. We observe that as the period increases both $P / P_{\text{free space}}$ and $P_{\text{down}} / P_{\text{up}}$ increase. A period of $a = b = 300$ nm (half a wavelength at 500 THz) leads to an enhancement almost more than 10 folds above 500 THz and it increases at higher frequencies; the power is mostly directed to the HM over the whole frequency range shown here (300-800 THz), especially for larger period.

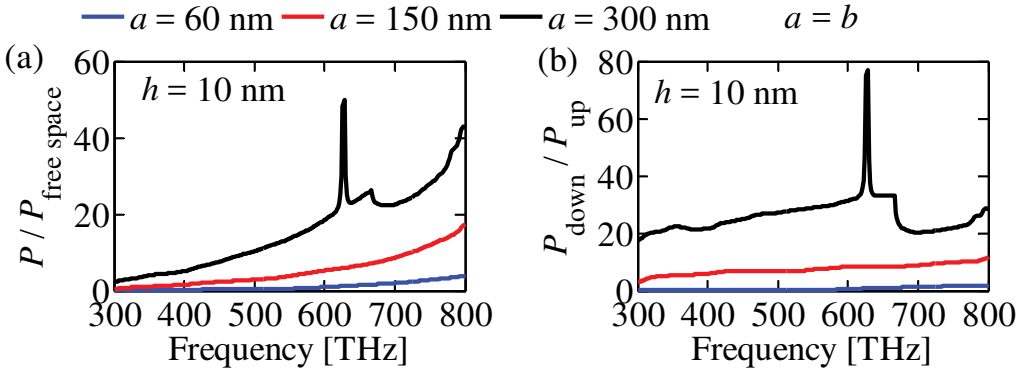

Fig. 5.3 (a) Emitted power $P = P_{\text{up}} + P_{\text{down}}$ by an array of dipoles (polarized along *x* and with $\mathbf{k}_{t,00} = 0.5k_0\hat{\mathbf{x}}$) and (b) the ratio of power emitted by the array towards HM and towards free space versus frequency with respect to different array periods $a = b$. The HM is as in Fig. 5.2. This result is calculated assuming a multilayer HM.

It is important to note for the array case the occurrence of the peaks at about 627 THz for $a = b = 300$ nm case only; we attribute this peak to the surface plasmon polariton (SPP) at the interface of free space and HM for which the modal wavenumber elaboration is provided in the Appendix A. Moreover similar narrow-frequency peaks are also present at many more frequencies when considering finite-thickness HMs. These peaks are particular to the array of dipoles, and are not observed for the single dipole emission on top of HM. The reasons of these peaks will be explained in Sec. 5.5. In the next section it is proven that we can achieve enhanced, coupled power toward HM by proper design of the array on top of HM.

Sec. 5.4 Discussion and Illustrative Examples

We consider here the same HM as introduced in the previous section assumed to have semi-infinite extent in *z*, and investigate the dynamics of the FWs emitted by an array of dipoles. The array of electric dipoles oscillating at 650 THz (i.e., a free-space wavelength of $\lambda_0 = 462$ nm) is assumed to be located in free space at a distance $h = 10$ nm from the HM (subwavelength proximity).

We first recall the case for a single emitting dipole as in Fig. 5.1(b) that will be helpful in subsequent analyses. The total power spectra (in logarithmic scale) are given in Fig. 5.4 versus k_x and k_y for both a transverse unit electric dipole located as in Fig. 5.1(b) with $\mathbf{p}_{00} = (\hat{\mathbf{x}} + \hat{\mathbf{y}})//\sqrt{2}$ Cm [evaluated as $U_{\text{up}}^{\text{TM}} + U_{\text{down}}^{\text{TM}} + U_{\text{up}}^{\text{TE}} + U_{\text{down}}^{\text{TE}}$, terms taken from Eqs. (5.20) and (5.21)] and a vertical unit electric dipole $\mathbf{p}_{00} = \hat{\mathbf{z}}$ [evaluated as $W_{\text{up}}^{\text{TM}} + W_{\text{down}}^{\text{TM}}$, terms taken from Eq. (5.23)].

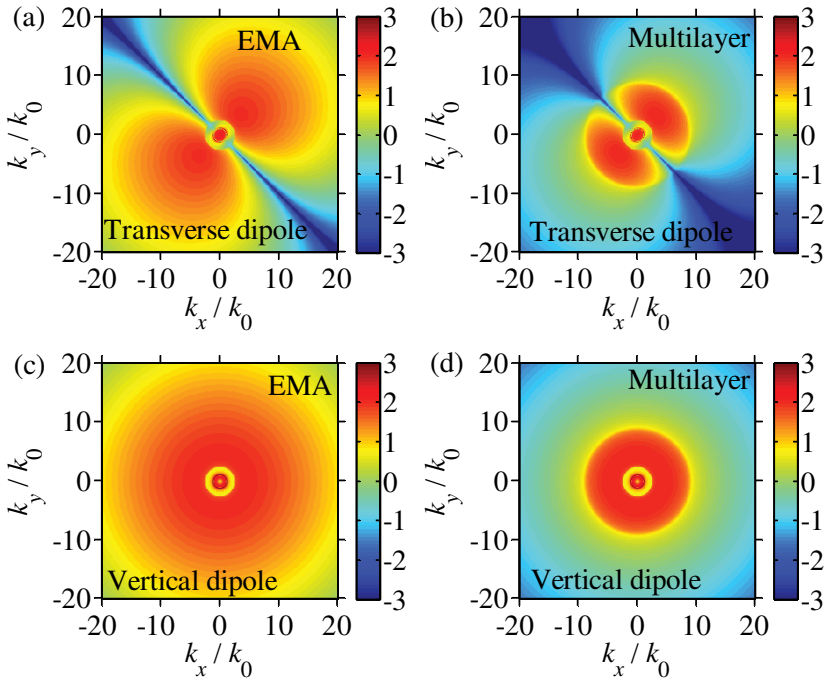

Fig. 5.4 Total spectral power versus k_x and k_y (a, b) $\log_{10}\left[\left(U_{\text{up}}^{\text{TM}}+U_{\text{down}}^{\text{TM}}+U_{\text{up}}^{\text{TE}}+U_{\text{down}}^{\text{TE}}\right)/\left(\text{Wm}^2\,\text{s}^2\right)\right]$ emitted by the unit transverse electric dipole $\mathbf{p}_{00}=\left(\hat{\mathbf{x}}+\hat{\mathbf{y}}\right)//\sqrt{2}$ Cm, (c, d) $\log_{10}\left[\left(W_{\text{up}}^{\text{TM}}+W_{\text{down}}^{\text{TM}}\right)/\left(\text{Wm}^2\text{s}^2\right)\right]$ emitted by the unit vertical dipole $\mathbf{p}_{00}=\hat{\mathbf{z}}$. In (a) and (c) EMA is used in HM modeling whereas in (b) and (d) multilayer HM is assumed, at 650 THz.

We first note in Fig. 5.4 the strong power spectrum for large transverse wavevectors. We also observe a strong dependence on the transverse wavevector direction for the transverse dipole, and no dependence for the vertical one due to symmetry reasons. Fundamentally, for metal-dielectric HMs the spectra provided in Fig. 5.4 is a wide-frequency phenomenon that does not rely on resonant characteristics, and it is provided for a representative frequency.

Moreover, we note the presence of a much wider spectrum of waves carrying power in the HM when looking at EMA results than multilayer ones. This result clearly explains that EMA overestimates power quantities, and is in agreement with previous investigations [1, 3,

37]. Since Bloch analysis models accurately the HM dispersion properties and EMA overestimates features for high spectral regions we will use Bloch multilayer modeling from this point on.

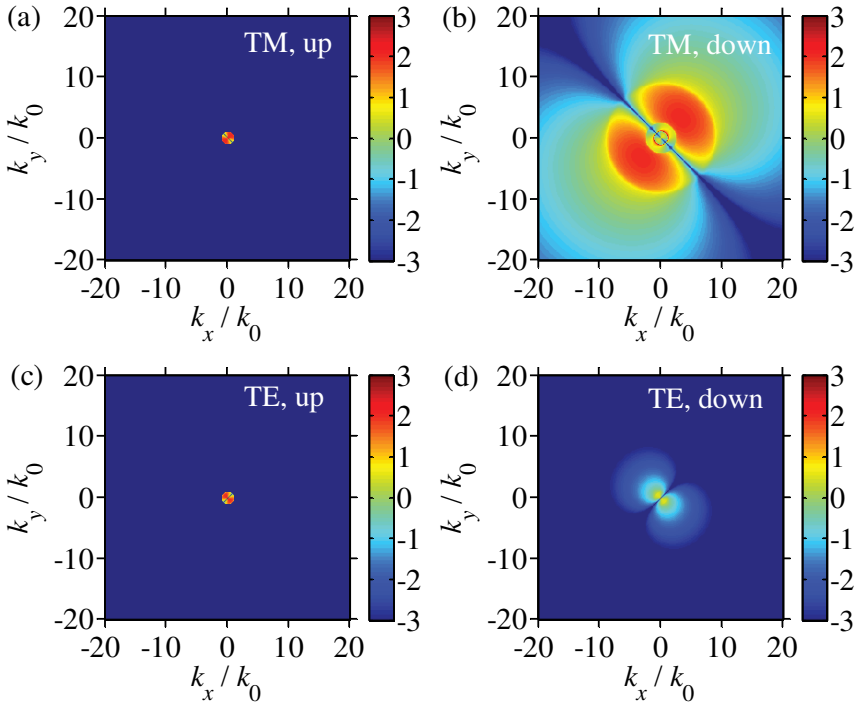

Fig. 5.5 Spectral power $\log_{10}\left[U_{\text{up/down}}^{\text{TM/TE}} / \left(\text{Wm}^2\text{s}^2\right)\right]$ versus k_x and k_y emitted by the unit transverse dipole $\mathbf{p}_{00} = \left(\hat{\mathbf{x}} + \hat{\mathbf{y}}\right) / /\sqrt{2}$ Cm in (a) $U_{\text{up}}^{\text{TM}}$: TM polarization and +$z$ direction, (b) $U_{\text{down}}^{\text{TM}}$: TM polarization and −$z$ direction, (c) $U_{\text{up}}^{\text{TE}}$: TE polarization and +$z$ direction, and (d) $U_{\text{down}}^{\text{TE}}$: TE polarization and −$z$ direction. This result is calculated assuming a multilayer HM.

We then turn our attention to understanding which waves carry most of the power. To do so, we plot in Fig. 5.5the spectral power $U_{\text{up/down}}^{\text{TM/TE}}$ in Eqs. (5.20) and (5.21) coupled to TM and TE waves toward both upper and bottom half spaces at 650 THz for the transverse dipole case in Fig. 5.4(b). It is clear that the power is mostly emitted in TM spectrum in −z direction,

i.e., towards the HM. A similar situation is encountered when analyzing the spectral power $W_{\text{up/down}}^{\text{TM}}$ in Eq. (5.23) for a vertical dipole (not shown for brevity).

The information in Fig. 5.4 and Fig. 5.5 will be now used to study the case of a 2D periodic array of electric dipoles on top of HM as in Fig. 5.1(a). Indeed, the spectral power quantities discussed in Figs. 4 and 5 are subject to sampling in the case of an array of dipoles as mentioned in Sec. 5.2. Here we assume the array's progressive phasing is governed by $\mathbf{k}_{t,00} = 0.5k_0\hat{\mathbf{x}}$ where k_0 is the free-space wavenumber, and we investigate the spectral power for three sets of periods (assuming square lattice): 150, 300, and 600 nm. On the left panels of Fig. 5.6, the power in FW harmonics (normalized by angular frequency squared ω^2) is reported versus FW indices *p* and *q*. The larger the period, the more is the number of propagating FWs carrying power away as discussed in Sec. 5.2. On the right panels of Fig. 5.6, we show the spectral power map pertaining to a single transverse dipole on top of HM where we superimpose the sampling points due to array periodicity (white circles) [the sampling procedure was mentioned in Sec. 5.3]. It is clear that as the period increases the spectral power in the case of the array resembles that of the single dipole. This result indeed demonstrates that, for increasing periods, dipoles in the array experience less and less coupling between each other, therefore the array response tends to be very similar to an isolated dipole. Moreover, it is evident that periodicity can be optimized to couple most of the power to propagating extraordinary waves in HM.

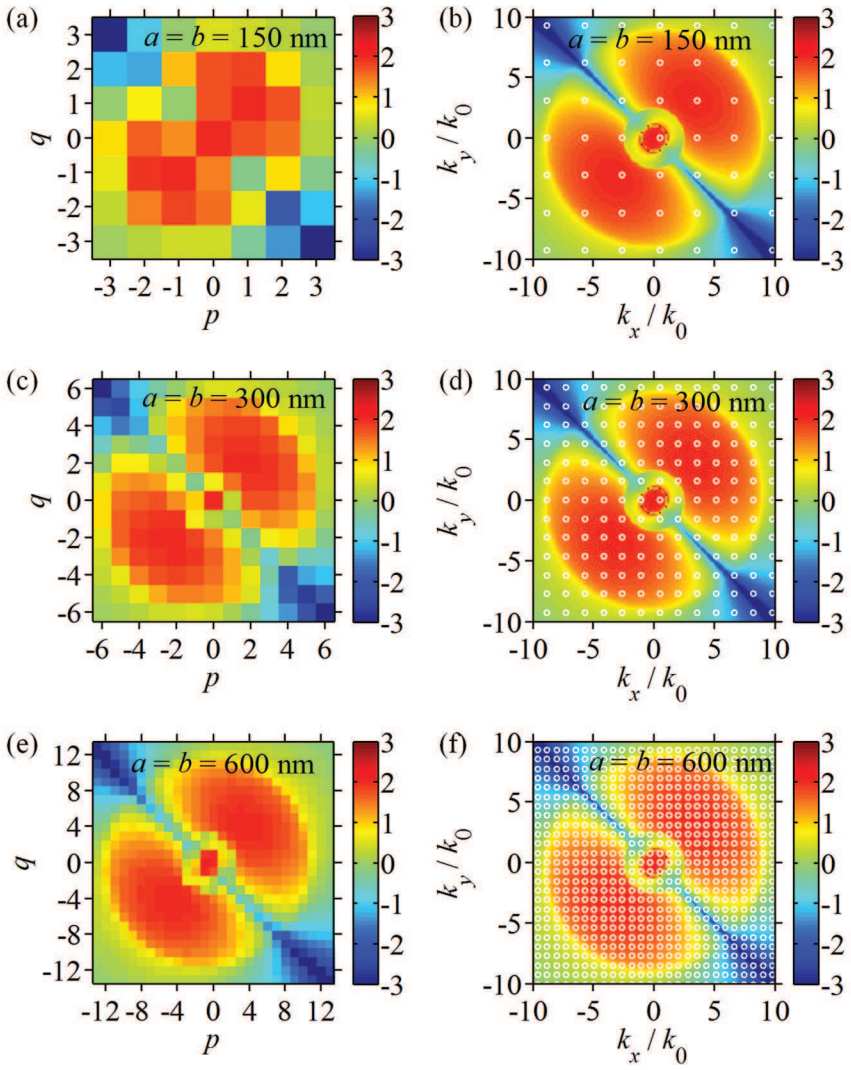

Fig. 5.6 (a, c, e) The spectral power of the Floquet harmonics versus the indices p and q for the array periods $a = b =$ 150, 300, 600 nm; (b, d, f) total spectral power ($\log_{10}\left[\left(U_{\text{up}}^{\text{TM}} + U_{\text{down}}^{\text{TM}} + U_{\text{up}}^{\text{TE}} + U_{\text{down}}^{\text{TE}}\right)/\left(\text{Wm}^2\text{s}^2\right)\right]$) versus k_x and k_y emitted by the unit transverse dipole $\mathbf{p}_{00} = \left(\hat{\mathbf{x}} + \hat{\mathbf{y}}\right)/\sqrt{2}$ Cm at 650 THz where the white circles denote the Floquet harmonic sampling locations on k_x-k_y plane in the array case for various array periods as in (a, c, e). This result is calculated assuming a multilayer HM.

Indeed, the impact of the period, thus the sampling of the spatial spectral power, manifests itself in the enhancement and upward/downward redistribution of the emitted power. In order to achieve enhancement of emitted power with respect to free space, $P / P_{\text{free space}}$, one

needs to sample at as many points as possible inside the propagating spectrum of HM with high k_x and k_y. The increase in the period realizes this with a large ratio of $P_{\text{down}} / P_{\text{up}}$ as well. On the other hand if an array of dipolar sources were to represent induced dipoles modeling polarized scatterers, the fraction of the scattered power to the power impinging on a unit cell would decrease with increasing period, thus this decrease would undesirably downplay the coupling to the propagating spectrum in HM. A critical balance must be determined for this situation and will be studied in the future.

Sec. 5.5 Floquet waves Coupled to Modes in HM: Array Over Finite-thickness HM Substrates

We analyze the effect of finite HM thickness as in Fig. 5.7 on the power emission enhancement and redistribution. The impact of the number of the bi-layer unit cells *N* on the spectral power and then on the enhancement and redistribution of the emitted power is demonstrated.

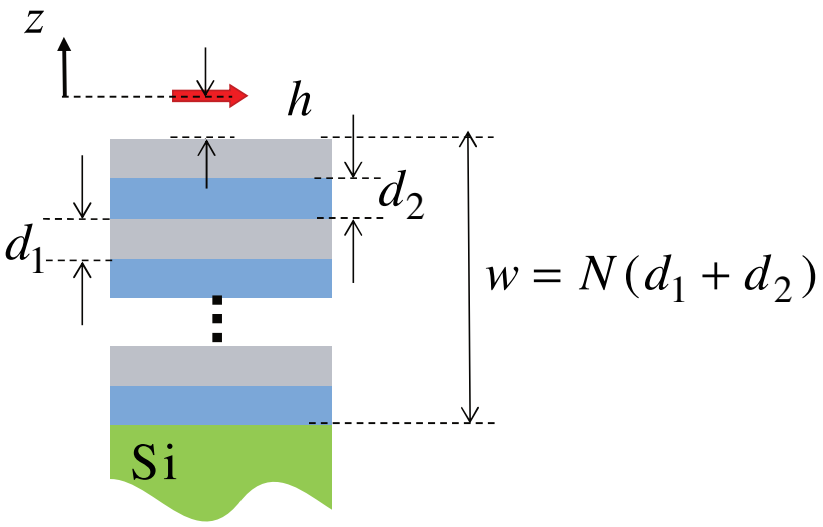

Fig. 5.7 HM substrate with finite thickness where *N* is the number of metal-dielectric bi-layers. This substrate configuration is investigated for both single dipolar source and an array of sources.

The spectral power density sampling scheme explained in the previous section stresses the relationship between the power emitted into FWs and the spectral power emitted by a single dipole. Therefore the study of spectral power due to a single source over a finite-thickness HM is fundamental to characterize the emission from an array in the same setup. We start by showing in Fig. 5.8 how the number of layers affects the spectral power distribution, generated by a single dipole polarized along *x*, for varying number of bi-layers $N = 1, 5, 10$ and $N \to \infty$, using the same HM composition as in the previous examples. We first observe that the power spectrum is strong over a wide wavevector space, a sign that large wavenumber waves are actually able to transport energy away from the array. Furthermore, we observe circular "belts" of spectral peaks in high k_x and k_y regions. The number of peaks depends on the number of metal-dielectric layers, in agreement with the bulk plasmon modes reported in [36]. As the number of layers *N* tends to infinity in Fig. 5.8(d), the field inside the HM is composed of a more uniform spectrum of propagating waves guided by the HM substrate. Next we stress the presence of the peak representing the wavenumber spectrum coupled to the SPP mode on the interface of free space and HM whose existence and wavenumber are determined in the Appendix A for the case of homogeneous HM. The power coupled to this mode is in the spectrum slightly larger than $|\mathbf{k}_t| = k_0$ circle and it is clearly visible in the close-up view in Fig. 5.8(d) which is present in all cases reported in Fig. 5.8, but not so well defined for *N*=1. We stress that this innermost circular peak of the spectrum in the vicinity of circle with the radius k_0, remains a distinct spectral feature as *N* increases, even when the aforementioned spectrum becomes uniform for $N \to \infty$. This

distinct spectral feature will, of course, affect the total emitted power by an array when some spectral sampling point lays on it, as discussed next.

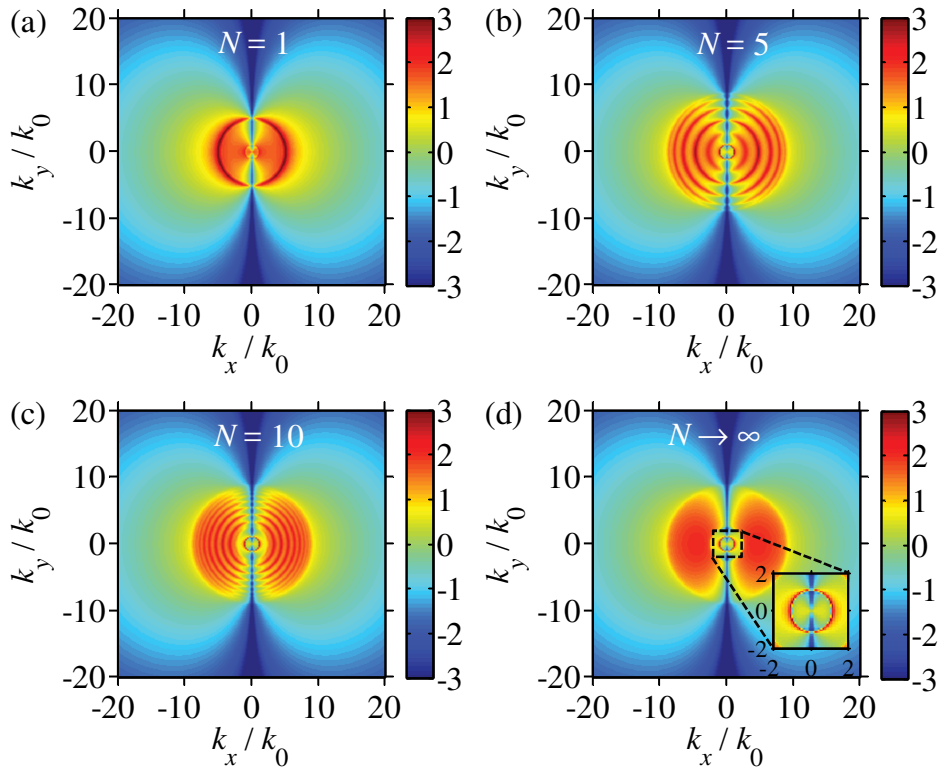

Fig. 5.8 Spectral power $\log_{10}\left[U_{\text{down}}^{\text{TM}}/\left(\text{Wm}^2\text{s}^2\right)\right]$ versus k_x and k_y emitted by the unit transverse dipole $\mathbf{p}_{00}=\hat{\mathbf{x}}$ Cm over a multilayer HM at 650 THz, for varying number of bi-layers *N*.

In Fig. 5.9, we report the emitted power enhancement $P/P_{\text{free space}}$ and the ratio of the power in the downward/upward direction $P_{\text{down}}/P_{\text{up}}$ as previously done in Fig. 5.3. The left panels are pertinent to the array of dipoles, whereas the right panels show the case of a single dipole for comparison. Various number of bi-layers $N=1,5,10$ and $N\to\infty$ are analyzed. Importantly, power enhancement is observed in all cases. Furthermore, in the case of array of dipoles on top of a HM substrate with finite *N*, the spectral sampling of the spectral peaks in Fig. 5.8 by the FW harmonics, which depends on the frequency, results in narrow

frequency peaks of the total emitted power and the power in the downward direction as in Fig. 5.9(a) and (c). This will be further justified by the discussion relative to Fig. 5.10.

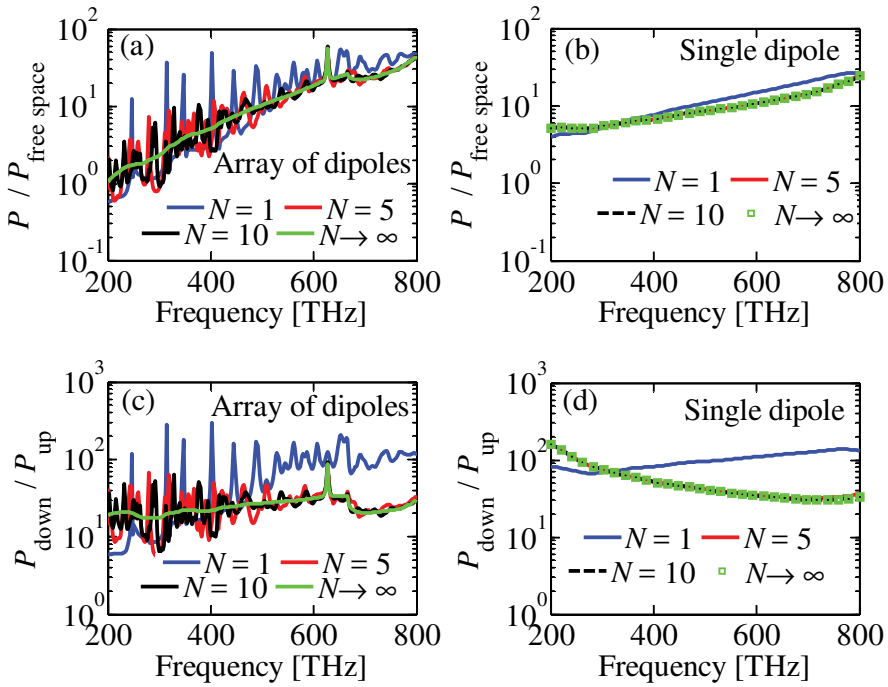

Fig. 5.9 Emitted power by an array of dipoles (normalized to the power emitted by the same array in free space) and ratio of power emitted towards HM and towards free space versus frequency, compared to the case of single dipole on HM. This result is calculated assuming a multilayer HM.

Moreover for array of dipoles, we observe that as *N* increases, $P / P_{\text{free space}}$ and $P_{\text{down}} / P_{\text{up}}$ become more stable versus frequency whereas for $N = 1$ the peaks are sharper and $P_{\text{down}} / P_{\text{up}}$ becomes lower than other cases at lower frequencies. This is due to several FW harmonics sampling the very sharp circular peak in spectral power [given in Fig. 5.8(a) for a certain frequency] when varying the frequency. In single dipole case, it is clear that even $N = 5$ is enough to emulate the effect of $N \to \infty$. Therefore, having greater *N* causes larger values of $P / P_{\text{free space}}$ and $P_{\text{down}} / P_{\text{up}}$ at low frequency with respect to the $N = 1$ case. For the

array of dipoles, when $N \to \infty$, we still observe a peak at 627.4 THz, absent in the single dipole case. This particular peak is due to the innermost peak circle in Fig. 5.8 [a close up view is provided in Fig. 5.8(d) representative for other cases as well] that corresponds to the SPP, briefly described in the Appendix A.

The power enhancement peaks for the array of dipoles can be explained by investigating the frequency evolution of the sampling points of the spectrum emitted by a single dipole. This is shown in Fig. 5.10 assuming N = 5 where $U_{\text{down}}^{\text{TM}}$ is plotted versus k_x / k_0 (x-axis) and frequency (y-axis), for $k_y = 0$. We also superimpose the frequency evolution of $k_{x,p} = \mathbf{k}_{t,pq} \cdot \hat{\mathbf{x}}$ normalized by k_0 (the p index is indicated on the top of the plot) denoted by dashed lines, assuming $\mathbf{k}_{t,00} = 0.5k_0\hat{\mathbf{x}}$. One can note that as the frequency increases more and more FW harmonics fall in the propagating spatial spectrum of HM. At certain frequencies a $k_{x,p}$ sample coincides with a spectral peak (observed as circular spectral regions in Fig. 5.8) and this causes the occurrence of a narrow frequency feature in Fig. 5.9. Since several FW wavenumbers can meet the peaks of the power spectrum in the HM, several power emission peaks can occur when varying frequency. Therefore the finite thickness HM has very narrow frequency features in power emission which can be useful in detection applications. It is important to note that the mode represented by the peak in the region where $|k_x|$ is slightly larger than k_0 does not belong to the propagating spectrum of HM, but it is the long-range SPP as shown in [36] and in Appendix A. The sampling of this mode by the FW with $p = -1$, $q = 0$ harmonic (pointed by the pink arrow in Fig. 5.10) results in the peak at 627.4 THz previously observed in Fig. 5.2 and Fig. 5.3. Note that this mode is distinct from the

propagating spectrum of HM and is present even for $N \to \infty$. On the other hand, for the single dipole case the wavenumber associated to the power coupled to this SPP mode is included in the integration domain of Eq. (5.26) at any frequency, thus we do not observe a power peak in Fig. 5.2.

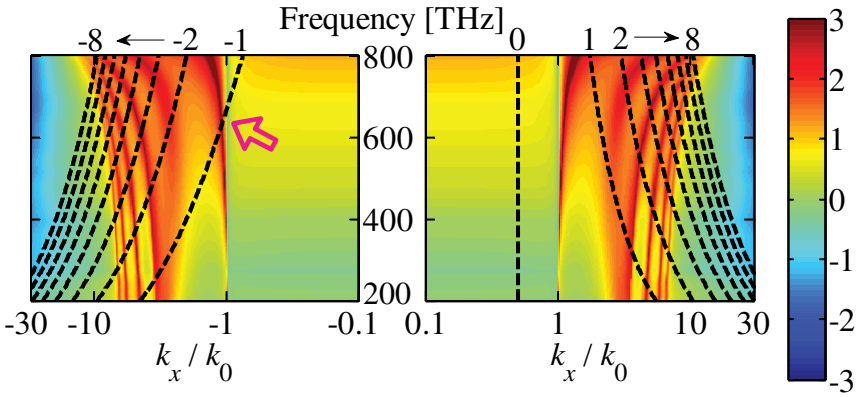

Fig. 5.10 Power spectrum of extraordinary TM waves carrying power in the negative z direction, $\log_{10}\left[U^{\mathrm{TM}}_{\mathrm{down}}(\mathbf{k}_t)/\left(\mathrm{Wm^2s^2}\right)\right]$, versus k_x (horizontal axis) and frequency (vertical axis) emitted by a single transverse dipole with $\mathbf{p}_{00} = \hat{\mathbf{x}}$ Cm on top of a finite thickness HM with N = 5 layers. Black dashed curves indicate spectral sampling lines corresponding to $\mathbf{k}_{t,p0} = k_{x,p}\hat{\mathbf{x}}$ for $p = -8,-7,\ldots,0,\ldots,7,8$ (denoted on top of the plot) when an array of dipoles in considered. This result is calculated assuming a multilayer HM.

Sec. 5.6 Effect of Source Spectrum

In the previous sections we have considered ideal (i.e., point like) dipoles as array elements. However in general, the size and physical domain of existence of the extended electric currents of the array elements also affect the amount of power coupled to the HM. This becomes especially important when the domain of the array-element current is no more extremely subwavelength. For example if we assume an extremely *impressed* flat current domain, then in Eqs. (5.20) and (5.21) the dipolar term $\mathbf{p}_{00}$ can no longer be assumed having

a constant spatial spectrum. It should be replaced by $\mathbf{p}_{00}(\mathbf{k}_t)$ evaluated in terms of the sheet electric current density $\mathbf{J}_{00}(x,y)$ flowing over the unit cell area *S*, at $z = 0$, as

$$\mathbf{p}_{00}(\mathbf{k}_t) = \frac{1}{-i\omega}\iint_S \mathbf{J}_{00}(x,y)\cdot e^{-i\left(k_x x + k_y y\right)}dxdy \tag{5.29}$$

As an example, consider a periodic array of flat rectangular current domains with dimensions l_x and l_y, as depicted in Fig. 5.11(a), on which a constant current $\mathbf{J}_{00}$ flows in the region $x \in (-l_x/2, l_x/2)$ and $y \in (-l_y/2, l_y/2)$. Then, the spectral power emitted by this array will be the FW sampling of the spectrum emitted by the isolated current sheet in Fig. 5.11(b), equivalent to the case described in Sec. 5.4 for imposed dipoles. The dipolar term $\mathbf{p}_{00}(\mathbf{k}_t)$ is a function of $\mathbf{k}_t$ and is given by

$$\mathbf{p}_{00}(\mathbf{k}_t) = \frac{1}{-i\omega}\left(\mathbf{J}_{00} l_x l_y\right)\frac{\sin k_x l_x}{k_x l_x}\frac{\sin k_y l_y}{k_y l_y} \tag{5.30}$$

It is clear that when $k_x l_x \ll 1$ and $k_y l_y \ll 1$, then $\mathbf{p}_{00}(\mathbf{k}_t)$ becomes constant (and independent of $\mathbf{k}_t$) approaching the discrete dipole case as

$$\mathbf{p}_{00} \approx \frac{1}{-i\omega}\mathbf{J}_{00} l_x l_y \tag{5.31}$$

Now let us show the impact of the source spatial spectrum on the total emitted power spectrum. For a fair comparison with the cases in Sec. 5.3, here we will assume $\left|\mathbf{p}_{00}(\mathbf{k}_t)\right|$ having unity maximum, determined by imposing $\left|\frac{1}{-i\omega}\mathbf{J}_{00}(x,y) l_x l_y\right| = 1$ Cm.

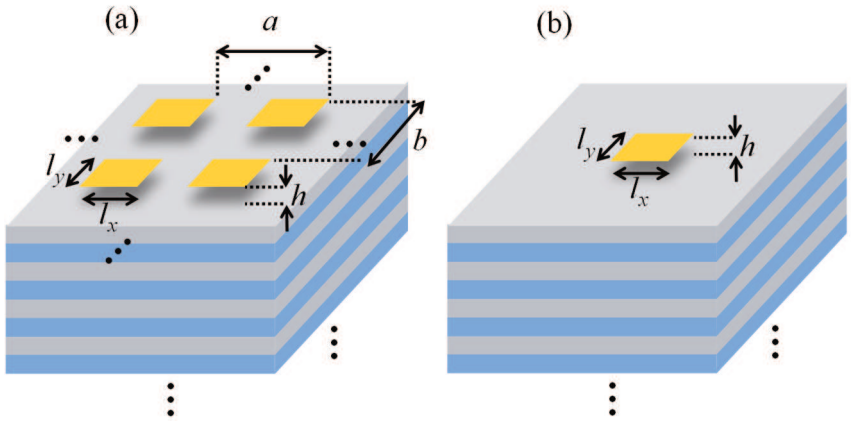

Fig. 5.11 The schematic of (a) a periodic array of rectangular current sheets on top of HM, and (b) a single rectangular current sheet on top of HM.

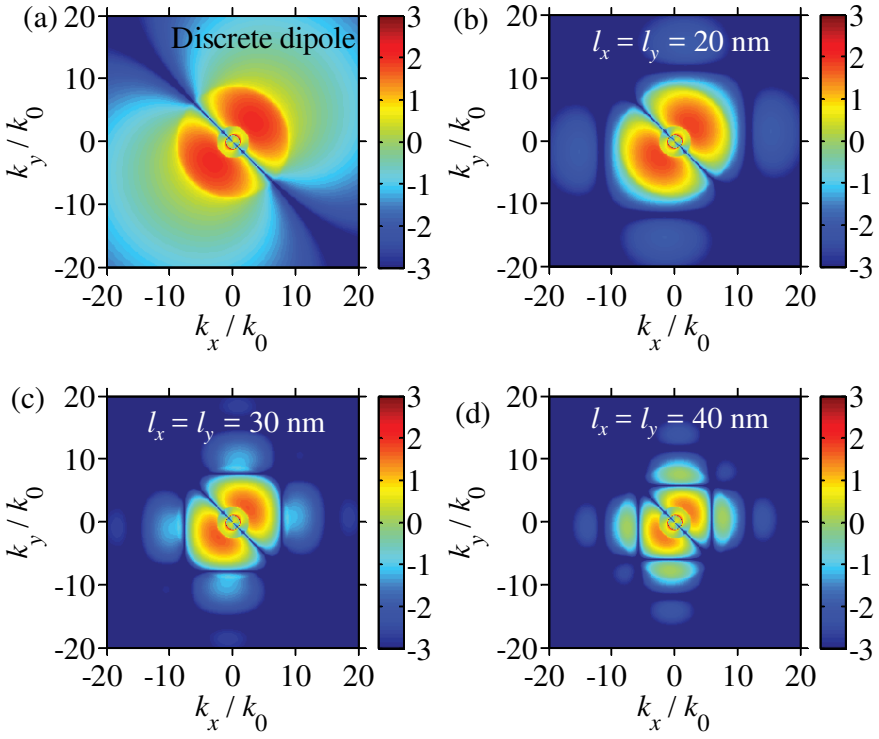

Fig. 5.12 Spectral power ($\log_{10}\left[\left(U_{\text{down}}^{\text{TM}}\right)/\left(\text{Wm}^2\text{s}^2\right)\right]$) versus k_x and k_y emitted at 650 THz (a) by the discrete dipole $\mathbf{p}_{00} = \left(\hat{\mathbf{x}} + \hat{\mathbf{y}}\right)/\sqrt{2}$ Cm and (b,c,d) by the constant sheet current $\mathbf{J}_{00} = -i\omega\mathbf{p}_{00}/\left(l_x l_y\right)$ flowing over a flat square sheet with sides $l_x = l_y = 20, 30, 40$ nm, respectively, centered at the origin. This result is calculated assuming a multilayer HM.

In Fig. 5.12(a) we report the power spectrum pertaining to an ideal elementary dipole with $\mathbf{p}_{00} = (\hat{\mathbf{x}} + \hat{\mathbf{y}})/\sqrt{2}$ Cm (note that $|\mathbf{p}_{00}| = 1$ Cm) and in Fig. 5.12(b)-(d) the ones pertaining to the sheet current $\mathbf{J}_{00} = -i\omega\mathbf{p}_{00}/(l_x l_y)$ for $l_x = l_y = 20, 30, 40$ nm, respectively. As clearly observed, the distributed current source truncates the high k_x - k_y spectrum due to the double *sinc* envelope in Eq. (5.30) imposed by the current domain's shape and dimensions. Moreover, by visual inspection of Fig. 5.12, it is clear that the power spectrum with large $\mathbf{k}_t$ (which would be able to couple to the HM) is suppressed in the distributed current domain case, when compared to the discrete dipole case. This causes a decrease of the power coupled to the HM, although for electrically small current domains its impact is limited. Therefore the total power emitted by an array of current sheets (evaluated by sampling of the spectrum in Fig. 5.12, as shown in Fig. 5.6) and the power emitted towards the HM will both decrease as either l_x or l_y increases if array periodicity is unchanged.

Sec. 5.7 Conclusion

In this work, the dynamics of Floquet waves emanating from a periodic set of emitters above HM substrate is studied analytically for the first time. The power coupled to the HM from the array of dipoles is shown to encompass numerous Floquet waves with high indices. The power emitted by an array of dipolar sources (over a unit cell) is highly enhanced with respect to free-space emission; moreover this power is mostly coupled to the HM substrate. We have also observed the interesting feature that the power emitted by the array, and the one coupled to the HM, exhibit narrow frequency peaks of very strong enhancement which can be useful in detection, probing and filtering applications. The physics behind this feature

associated to arrays over HM has been explained through the concept of sampling the power spatial spectrum of the isolated dipole on top of HM.

This chapter is reproduced based on the material in [C. Guclu, S. Campione, and F. Capolino, "Array of dipoles near a hyperbolic metamaterial: Evanescent-to-propagating Floquet wave transformation," *Phys. Rev. B*, vol. 89, 155128, 2014], © 2014 American Physical Society.

Appendix A A Surface Plasmon Polariton Mode Supported at the Interface of Free Space and HM

We derive here the transverse wavenumber of the SPP mode associated to the free space-HM interface. We use the transverse resonance method [42] applied at the interface, i.e.,

$$Z_{\mathrm{HM}}^{\mathrm{TM}}\left(k_t\right)+Z_0^{\mathrm{TM}}\left(k_t\right)=0 \tag{5.32}$$

where Z_0^{TM} and $Z_{\mathrm{HM}}^{\mathrm{TM}}$ are evaluated using Eqs. (5.10) and (5.11), respectively for the case of homogeneous HM. (In the case a multilayer HM, Eq. (5.32) is still valid but $Z_{\mathrm{HM}}^{\mathrm{TM}}$ could be evaluated using the transfer matrix method.) Then Eq. (5.32) leads to

$$\frac{k_{z1}}{\varepsilon_t}=-k_{z0}, \tag{5.33}$$

where for simplicity we have omitted the superscript TM for k_{z1}. Note that, when losses are neglected, a solution may exist only if both k_{z0} and k_{z1} are imaginary. Assuming a lossless case for simplicity, with $\varepsilon_t<0$ and $\varepsilon_z>1$ (recall that we analyzed the case with $\mathrm{Re}\{\varepsilon_t\}<0$

$\mathrm{Re}\{\varepsilon_z\}>1$ in Sec. 5.3-Sec. 5.5), solutions of imaginary k_{z0} and k_{z1} may be found in the range of transverse wavenumber as

$$k_0^2 < k_t^2 < \varepsilon_z k_0^2. \tag{5.34}$$

Solving Eq. (5.33) for k_t one has

$$\begin{aligned} &\left(k_{z1}\right)^2 = \left(-\varepsilon_t k_{z0}\right)^2, \\ &k_0^2 - \frac{1}{\varepsilon_z} k_t^2 = \varepsilon_t \left(k_0^2 - k_t^2\right) \end{aligned} \tag{5.35}$$

and both the left and right hand side members of the last equations should be positive. Thus,

$$\begin{aligned} &\left(\frac{1}{\varepsilon_z} - \varepsilon_t\right) k_t^2 = k_0^2 \left(1 - \varepsilon_t\right) \\ &k_t^2 = k_0^2 \frac{\varepsilon_z - \varepsilon_t \varepsilon_z}{1 - \varepsilon_t \varepsilon_z}. \end{aligned} \tag{5.36}$$

Note that the fraction term is a positive number larger than unity since $\varepsilon_z > 1$, implying that k_t^2 satisfies the original assumption in Eq. (5.34). The wavenumber of the SPP wave at the interface of free space and HM thus is

$$k_t = k_0 \sqrt{\frac{\varepsilon_z - \varepsilon_t \varepsilon_z}{1 - \varepsilon_t \varepsilon_z}} \tag{5.37}$$

when $\varepsilon_t < 0$ and $\varepsilon_z > 1$. For $\left|\varepsilon_t \varepsilon_z\right| \gg 1$ and $\left|\varepsilon_t \varepsilon_z\right| \gg \left|\varepsilon_z\right|$ this mode has k_t slightly greater than k_0 which can be observed in Fig. 5.10 particularly at smaller frequencies. This result is in agreement with previous predictions [51, 52]. No wave solutions can be found when $\varepsilon_t < 0$

and $0<\varepsilon_z<1$ since k_{z0} and k_{z1} cannot be imaginary simultaneously. Similarly, when $\varepsilon_t>0$ and $\varepsilon_z<0$, k_{z1} is never imaginary thus a bound mode at the surface is not supported.

Appendix B Example of the Derivation of Power Spectrum Expressions

This appendix provides the derivation details of Eq. (5.20) [the power spectrum for TM waves $U_{\text{down}}^{\text{TM}}$] starting from the 1st line of Eq. (5.18) [the real (i.e. the time-average) power density flowing in the –z direction]. This is given as an example, and the expressions for other polarization and up/down directions can be derived by an analogous treatment. In the 1st line of Eq. (5.18) the equality

$$\Gamma_{pq}e^{i2k_{z0,pq}h}=\frac{Y_{\text{up}}^{\text{TM}}\left(\mathbf{k}_{t,pq}\right)-Y_{\text{down}}^{\text{TM}}\left(\mathbf{k}_{t,pq}\right)}{Y_{\text{up}}^{\text{TM}}\left(\mathbf{k}_{t,pq}\right)+Y_{\text{down}}^{\text{TM}}\left(\mathbf{k}_{t,pq}\right)} \tag{5.38}$$

is used together with the admittance definition in Eq. (5.24) recalling that $Y_{\text{up}}^{\text{TM}}\left(\mathbf{k}_{t,pq}\right)=Y_0^{\text{TM}}\left(\mathbf{k}_{t,pq}\right)$. Then we rewrite $S_{\text{down}}^{\text{TM}}\left(\mathbf{k}_{t,pq}\right)$ as

$$\begin{aligned} S_{\text{down}}^{\text{TM}} &= \frac{1}{2}\text{Re}\left[\left|\mathbf{E}_{t,pq}^{\text{TM}-}\right|^2 Y_{\text{up}}^{\text{TM}*}\left[\frac{4Y_{\text{up}}^{\text{TM}}Y_{\text{down}}^{\text{TM}*}}{\left|Y_{\text{up}}^{\text{TM}}+Y_{\text{down}}^{\text{TM}}\right|^2}\right]\right], \\ &= 2\left|\mathbf{E}_{t,pq}^{\text{TM}-}\right|^2\left|Y_{\text{up}}^{\text{TM}}\right|^2\frac{\text{Re}\left[Y_{\text{down}}^{\text{TM}*}\right]}{\left|Y_{\text{up}}^{\text{TM}}+Y_{\text{down}}^{\text{TM}}\right|^2} \end{aligned} \tag{5.39}$$

where we have omitted the common dependence on $\left(\mathbf{k}_{t,pq}\right)$. Next, $\mathbf{E}_{t,pq}^{\mathrm{TM}-}$ is derived from Eqs. (5.2) and (5.3) for transverse dipoles' excitation $\mathbf{p}_{00} = p_x\hat{\mathbf{x}} + p_y\hat{\mathbf{y}}$ evaluated at the array plane $\left(z \to 0^-\right)$, and it is given by

$$\mathbf{E}_{t,pq}^{\mathrm{TM}-} = \frac{ie^{i\left(\mathbf{k}_{t,pq}\cdot\mathbf{r}\right)}}{2ab\varepsilon_0}\frac{k_{z0,pq}}{k_{t,pq}^2}\mathbf{k}_{t,pq}\left(\mathbf{k}_{t,pq}\cdot\mathbf{p}_{00}\right) \tag{5.40}$$

In Eq. (5.39), $\left|\mathbf{E}_{t,pq}^{\mathrm{TM}-}\right|^2$ is evaluated as

$$\begin{aligned}\left|\mathbf{E}_{t,pq}^{\mathrm{TM}-}\right|^2 &= \frac{1}{4\left(ab\right)^2}\frac{\left|\mathbf{p}_{00}\cdot\mathbf{k}_{t,pq}\right|^2}{\left|\mathbf{k}_{t,pq}\right|^2}\left|\frac{k_{z0,pq}}{\varepsilon_0}\right|^2 \\ &= \frac{\omega^2}{4\left(ab\right)^2}\frac{\left|\mathbf{p}_{00}\cdot\mathbf{k}_{t,pq}\right|^2}{\left|\mathbf{k}_{t,pq}\right|^2}\frac{1}{\left|Y_{\mathrm{up}}^{\mathrm{TM}}\right|^2}\end{aligned} \tag{5.41}$$

Substituting Eq. (5.41) in Eq. (5.39) yields

$$\begin{aligned}S_{\mathrm{down}}^{\mathrm{TM}}\left(\mathbf{k}_{t,pq}\right) &= \frac{\omega^2}{2\left(ab\right)^2}\frac{\left|\mathbf{p}_{00}\cdot\mathbf{k}_{t,pq}\right|^2}{\left|\mathbf{k}_{t,pq}\right|^2}\frac{\mathrm{Re}\left[Y_{\mathrm{down}}^{\mathrm{TM}*}\right]}{\left|Y_{\mathrm{up}}^{\mathrm{TM}}+Y_{\mathrm{down}}^{\mathrm{TM}}\right|^2} \\ &= \frac{\omega^2}{2\left(ab\right)^2}U_{\mathrm{down}}^{\mathrm{TM}}\left(\mathbf{k}_{t,pq}\right)\end{aligned} \tag{5.42}$$

where we have used the definition of $U_{\mathrm{down}}^{\mathrm{TM}}\left(\mathbf{k}_{t,pq}\right)$ in Eq. (5.20). The time-average power carried by the *pq*-th TM-polarized FW is $\iint_A S_{\mathrm{down}}^{\mathrm{TM}}\left(\mathbf{k}_{t,pq}\right)dA$, where *A* is the cross-section area of the unit cell orthogonal to the *z* axis. Note that $S_{\mathrm{down}}^{\mathrm{TM}}\left(\mathbf{k}_{t,pq}\right)$ has no *x* and *y*

dependence. The total time-average power of TM-polarized waves in the downward direction is the sum of the power carried by all FWs given as

$$\begin{aligned} P_{\text{down}}^{\text{TM}}\left(\mathbf{k}_{t,pq}\right) &= \sum_{p,q=-\infty}^{\infty}\left[\iint_A S_{\text{down}}^{\text{TM}}\left(\mathbf{k}_{t,pq}\right)dA\right] \\ &= \sum_{p,q=-\infty}^{\infty} S_{\text{down}}^{\text{TM}}\left(\mathbf{k}_{t,pq}\right)(ab) \\ &= \frac{\omega^2}{2ab}\sum_{p,q=-\infty}^{\infty} U_{\text{down}}^{\text{TM}}\left(\mathbf{k}_{t,pq}\right) \end{aligned} \tag{5.43}$$

References

[1] C. Guclu, S. Campione, and F. Capolino, "Hyperbolic metamaterial as super absorber for scattered fields generated at its surface," *Physical Review B,* vol. 86, p. 205130, 2012.

[2] M. A. K. Othman, C. Guclu, and F. Capolino, "Graphene-based tunable hyperbolic metamaterials and enhanced near-field absorption," *Opt. Express,* vol. 21, pp. 7614-7632, 2013.

[3] O. Kidwai, S. V. Zhukovsky, and J. E. Sipe, "Effective-medium approach to planar multilayer hyperbolic metamaterials: Strengths and limitations," *Physical Review A,* vol. 85, p. 053842, 2012.

[4] Z. Jacob, J. Y. Kim, G. V. Naik, A. Boltasseva, E. E. Narimanov, and V. M. Shalaev, "Engineering photonic density of states using metamaterials," *Applied Physics B,* vol. 100, pp. 215-218, 2010/07/01 2010.

[5] M. A. Noginov, H. Li, Y. A. Barnakov, D. Dryden, G. Nataraj, G. Zhu*, et al.*, "Controlling spontaneous emission with metamaterials," *Optics Letters,* vol. 35, pp. 1863-1865, 2010/06/01 2010.

[6] R. Kotyński, T. Stefaniuk, and A. Pastuszczak, "Sub-wavelength diffraction-free imaging with low-loss metal-dielectric multilayers," *Applied Physics A: Materials Science & Processing,* vol. 103, pp. 905-909, 2011.

[7] T. Tumkur, G. Zhu, P. Black, Y. A. Barnakov, C. E. Bonner, and M. A. Noginov, "Control of spontaneous emission in a volume of functionalized hyperbolic metamaterial," *Applied Physics Letters,* vol. 99, pp. 151115-3, 2011.

[8] A. N. Poddubny, P. A. Belov, P. Ginzburg, A. V. Zayats, and Y. S. Kivshar, "Microscopic model of Purcell enhancement in hyperbolic metamaterials," *Physical Review B,* vol. 86, p. 035148, 2012.

[9] H. N. S. Krishnamoorthy, Z. Jacob, E. Narimanov, I. Kretzschmar, and V. M. Menon, "Topological Transitions in Metamaterials," *Science,* vol. 336, pp. 205-209, April 13, 2012 2012.

[10] W. D. Newman, C. L. Cortes, and Z. Jacob, "Enhanced and directional single-photon emission in hyperbolic metamaterials," *J. Opt. Soc. Am. B,* vol. 30, pp. 766-775, 2013.

[11] J. Kim, V. P. Drachev, Z. Jacob, G. V. Naik, A. Boltasseva, E. E. Narimanov*, et al.*, "Improving the radiative decay rate for dye molecules with hyperbolic metamaterials," *Optics Express,* vol. 20, pp. 8100-8116, 2012/03/26 2012.

[12] J. B. Pendry and S. A. Ramakrishna, "Refining the perfect lens," *Physica B-Condensed Matter,* vol. 338, pp. 329-332, Oct 2003.

[13] K. J. Webb and M. Yang, "Subwavelength imaging with a multilayer silver film structure," *Optics Letters,* vol. 31, pp. 2130-2132, Jul 2006.

[14] X. Li and F. Zhuang, "Multilayered structures with high subwavelength resolution based on the metal-dielectric composites," *Journal of the Optical Society of America a-Optics Image Science and Vision,* vol. 26, pp. 2521-2525, Dec 2009.

[15] Y. Jin, "Improving subwavelength resolution of multilayered structures containing negative-permittivity layers by flatting the transmission curves," *Progress in Electromagnetics Research-Pier,* vol. 105, pp. 347-364, 2010.

[16] C. Della Giovampaola, M. Albani, and F. Capolino, "Investigation on subwavelength focusing properties of metal-dielectric multilayer," in *Metamaterials Congress, Barcelona, Spain, October 10-15, 2011*, 2011.

[17] Z. Liu, Z. Liang, X. Jiang, X. Hu, X. Li, and J. Zi, "Hyper-interface, the bridge between radiative wave and evanescent wave," *Applied Physics Letters,* vol. 96, pp. 113507-3, 2010.

[18] W. Yan, N. Asger Mortensen, and M. Wubs, "Hyperbolic metamaterial lens with hydrodynamic nonlocal response," *Opt. Express,* vol. 21, pp. 15026-15036, 2013.

[19] T. U. Tumkur, L. Gu, J. K. Kitur, E. E. Narimanov, and M. A. Noginov, "Control of absorption with hyperbolic metamaterials," *Applied Physics Letters,* vol. 100, p. 161103, 2012.

[20] T. U. Tumkur, J. K. Kitur, B. Chu, L. Gu, V. A. Podolskiy, E. E. Narimanov*, et al.*, "Control of reflectance and transmittance in scattering and curvilinear hyperbolic metamaterials," *Applied Physics Letters,* vol. 101, pp. 091105-4, 2012.

[21] E. E. Narimanov, H. Li, Y. A. Barnakov, T. U. Tumkur, and M. A. Noginov, "Reduced reflection from roughened hyperbolic metamaterial," *Opt. Express,* vol. 21, pp. 14956-14961, 2013.

[22] V. A. Podolskiy and E. E. Narimanov, "Strongly anisotropic waveguide as a nonmagnetic left-handed system," *Physical Review B,* vol. 71, p. 201101, 2005.

[23] G. V. Naik, J. J. Liu, A. V. Kildishev, V. M. Shalaev, and A. Boltasseva, "Demonstration of Al:ZnO as a plasmonic component for near-infrared metamaterials," *Proceedings of*

the National Academy of Sciences of the United States of America, vol. 109, pp. 8834-8838, Jun 2012.

[24] K. V. Sreekanth, A. De Luca, and G. Strangi, "Negative refraction in graphene-based hyperbolic metamaterials," *Applied Physics Letters,* vol. 103, pp. 023107-4, 2013.

[25] C. Argyropoulos, N. M. Estakhri, F. Monticone, and A. Alù, "Negative refraction, gain and nonlinear effects in hyperbolic metamaterials," *Opt. Express,* vol. 21, pp. 15037-15047, 2013.

[26] X. Ni, S. Ishii, M. D. Thoreson, V. M. Shalaev, S. Han, S. Lee*, et al.*, "Loss-compensated and active hyperbolic metamaterials," *Opt. Express,* vol. 19, pp. 25242-25254, 2011.

[27] M. A. K. Othman, C. Guclu, and F. Capolino, "Graphene–dielectric composite metamaterials: evolution from elliptic to hyperbolic wavevector dispersion and the transverse epsilon-near-zero condition," *Journal of Nanophotonics,* vol. 7, pp. 073089-073089, 2013.

[28] D. d. Ceglia, M. A. Vincenti, S. Campione, F. Capolino, J. W. Haus, and M. Scalora, "Second harmonic double resonance cones in dispersive hyperbolic metamaterials," *arXiv:1305.5430,* 2013.

[29] A. Ciattoni and E. Spinozzi, "Efficient second-harmonic generation in micrometer-thick slabs with indefinite permittivity," *Physical Review A,* vol. 85, p. 043806, 2012.

[30] T. S. Luk, I. Kim, S. Campione, S. W. Howell, G. S. Subramania, R. K. Grubbs*, et al.*, "Near-infrared surface plasmon polariton dispersion control with hyperbolic metamaterials," *Opt. Express,* vol. 21, pp. 11107-11114, 2013.

[31] C. Rizza, A. Ciattoni, E. Spinozzi, and L. Columbo, "Terahertz active spatial filtering through optically tunable hyperbolic metamaterials," *Optics Letters,* vol. 37, pp. 3345-3347, 2012/08/15 2012.

[32] I. V. Iorsh, I. S. Mukhin, I. V. Shadrivov, P. A. Belov, and Y. S. Kivshar, "Hyperbolic metamaterials based on multilayer graphene structures," *Physical Review B,* vol. 87, p. 075416, 2013.

[33] M. A. Noginov, Y. A. Barnakov, G. Zhu, T. Tumkur, H. Li, and E. E. Narimanov, "Bulk photonic metamaterial with hyperbolic dispersion," *Applied Physics Letters,* vol. 94, p. 151105, 2009.

[34] C. L. Cortes, W. Newman, S. Molesky, and Z. Jacob, "Quantum nanophotonics using hyperbolic metamaterials," *Journal of Optics,* vol. 14, p. 063001, 2012.

[35] S. V. Zhukovsky, O. Kidwai, and J. E. Sipe, "Physical nature of volume plasmon polaritons in hyperbolic metamaterials," *Opt. Express,* vol. 21, pp. 14982-14987, 2013.

[36] I. Avrutsky, I. Salakhutdinov, J. Elser, and V. Podolskiy, "Highly confined optical modes in nanoscale metal-dielectric multilayers," *Physical Review B,* vol. 75, p. 241402, 2007.

[37] P. Zhu, P. Jin, and L. Jay Guo, "Insight of limitations of effective media theory for metal–dielectric multilayer metamaterials," *Optics Communications,* vol. 305, pp. 8-12, 2013.

[38] F. Capolino, D. R. Jackson, and D. R. Wilton, "Field representations in periodic artificial materials excited by a source," in *Theory and Phenomena of Metamaterials*, F. Capolino, Ed., ed Boca Raton, FL: CRC Press, 2009, p. 12.1.

[39] P. Baccarelli, S. Paulotto, and C. D. Nallo, "Full-wave analysis of bound and leaky modes propagating along 2d periodic printed structures with arbitrary metallisation in the unit cell," *Microwaves, Antennas & Propagation, IET,* vol. 1, pp. 217-225, 2007.

[40] A. L. Fructos, S. Campione, F. Capolino, and F. Mesa, "Characterization of complex plasmonic modes in two-dimensional periodic arrays of metal nanospheres," *J. Opt. Soc. Am. B,* vol. 28, pp. 1446-1458, 2011.

[41] S. Campione, F. Mesa, and F. Capolino, "Magnetoinductive Waves and Complex Modes in Two-Dimensional Periodic Arrays of Split Ring Resonators," *Antennas and Propagation, IEEE Transactions on,* vol. 61, pp. 3554-3563, 2013.

[42] L. B. Felsen and N. Marcuvitz, *Radiation and Scattering of Waves*: Prentice-Hall, NJ, 1973.

[43] D. R. Smith and D. Schurig, "Electromagnetic Wave Propagation in Media with Indefinite Permittivity and Permeability Tensors," *Physical Review Letters,* vol. 90, p. 077405, 2003.

[44] D. M. Pozar, *Microwave Engineering*, 3rd ed.: John Wiley & Sons, 2005.

[45] N. Marcuvitz, "MODE REPRESENTATIONS IN UNIFORMLY STRATIFIED REGIONS," *Physical Review,* vol. 82, pp. 297-297, 1951.

[46] N. Marcuvitz and J. Schwinger, "ON THE REPRESENTATION OF THE ELECTRIC AND MAGNETIC FIELDS PRODUCED BY CURRENTS AND DISCONTINUITIES IN WAVE GUIDES .1," *Journal of Applied Physics,* vol. 22, pp. 806-819, 1951.

[47] F. Capolino, L. B. Felsen, and A. Della Villa, "Network Oriented Dyadic Time Domain Green's Function for a Sequentially Excited Infinite Planar Array of Dipoles in Free Space," *Antennas and Propagation, IEEE Transactions on,* vol. 55, pp. 2228-2238, 2007.

[48] P. B. Johnson and R. W. Christy, "Optical Constants of the Noble Metals," *Physical Review B,* vol. 6, pp. 4370-4379, 1972.

[49] P. A. Belov and Y. Hao, "Subwavelength imaging at optical frequencies using a transmission device formed by a periodic layered metal-dielectric structure operating in the canalization regime," *Physical Review B,* vol. 73, p. 113110, 2006.

[50] T. Maria, B. Svend-Age, M. Riccardo, and B.-A. Philippe, "On the limits of the effective description of hyperbolic materials in the presence of surface waves," *Journal of Optics,* vol. 15, p. 105101, 2013.

[51] C. H. Gan and P. Lalanne, "Well-confined surface plasmon polaritons for sensing applications in the near-infrared," *Optics Letters,* vol. 35, pp. 610-612, 2010.

[52] R. Warmbier, G. S. Manyali, and A. Quandt, "Surface plasmon polaritons in lossy uniaxial anisotropic materials," *Physical Review B,* vol. 85, p. 085442, 2012.

CHAPTER 6

RADIATIVE EMISSION ENHANCEMENT USING HYPERBOLIC METAMATERIAL RESONATORS

Sec. 6.1 Motivation

A hyperbolic metamaterial (HM) resonator is analyzed as a nano-antenna for enhancing the radiative emission of quantum emitters in its vicinity. It has been shown that the spontaneous emission rate by an emitter near a hyperbolic metamaterial substrate is enhanced dramatically due to very large density of states. However, enhanced coupling to the free-space, which is central to applications such as solid-state lighting, has not been investigated significantly. Here, it is numerically demonstrated that approximately 100 times enhancement of the free-space radiative emission at 660 nm wavelength is achieved by utilizing a cylindrical HM resonator with a radius of 54 nm and a height of 80 nm on top of an opaque silver-cladded substrate. Also the ways that the free-space radiation enhancement factor depends on the dipole orientation and the location of the emitter near the subwavelength resonator are shown. Furthermore, calculations are provided that an

array of HM resonators with subwavelength spacings can maintain most of the enhancement effect of a single resonator.

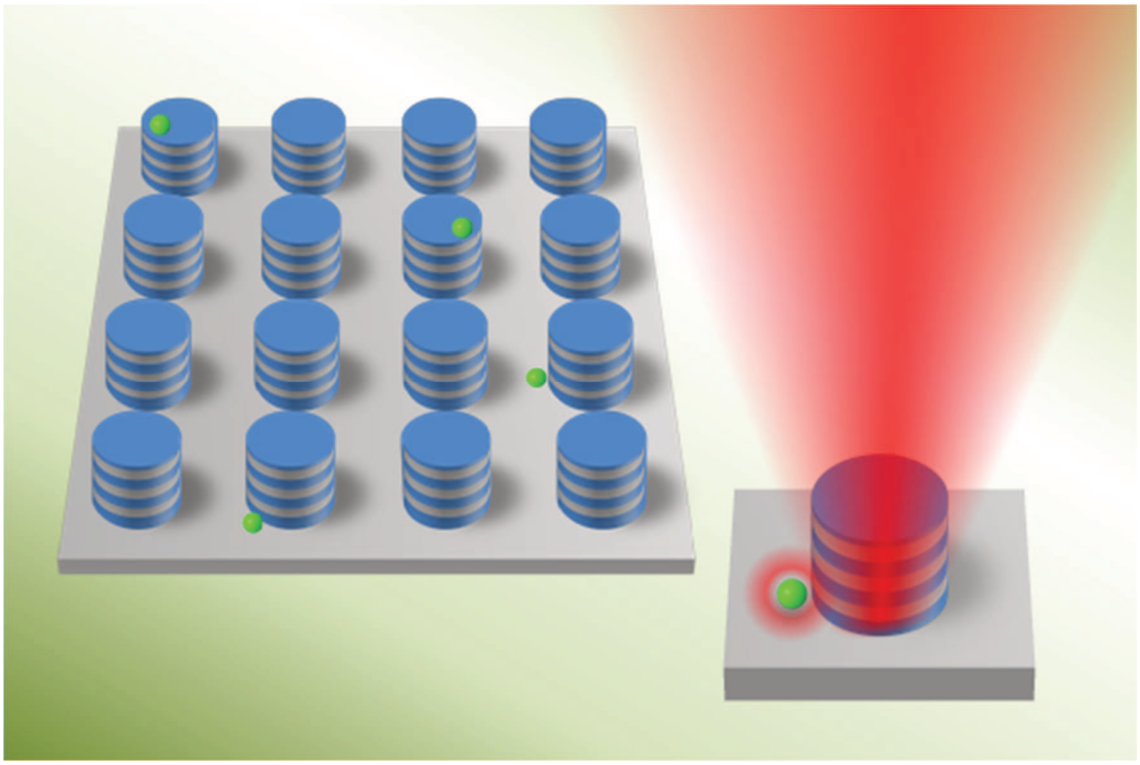

Fig. 6.1 The conceptual illustration of radiative emission enhancement of a dipolar radiator in the vicinity of a HM resonator nano antenna. The concept consists of an array of HM resonators antenna which are host to scattered point dipolar sources. Illustration is used as the cover figure of Applied Physics Letters volume 105.

Control of the spontaneous emission process is of fundamental and practical interest for enhanced light-matter interaction, quantum information processing, solid-state lighting, and biological sciences. Hyperbolic metamaterials (HMs) have been proposed for enhancing spontaneous emission rate owing to indefinite photonic density of states. HMs are characterized by an indefinite permittivity tensor (for example, $\underline{\boldsymbol{\varepsilon}}_r = \varepsilon_t\left(\hat{\mathbf{x}}\hat{\mathbf{x}} + \hat{\mathbf{y}}\hat{\mathbf{y}}\right) + \varepsilon_z\hat{\mathbf{z}}\hat{\mathbf{z}}$, where $\varepsilon_t\varepsilon_z$ is negative) and are in general made of metal-dielectric multilayers [1]–[3]; dielectric-semiconductor multilayers [4]; graphene-dielectric multilayers [5]–[7]; or by an

array of metallic nanopillars[8], [9]. HMs possess hyperbolic iso-frequency wavevector dispersion properties and can host ideally an infinite spectrum of propagating plane waves, which in turn leads to a dramatic increase in the photonic local density of states. The hyperbolic dispersion characteristic in a multilayer HM does not rely on building blocks with narrow-band resonances, therefore this property is maintained over a wide frequency band. Theoretical analysis of enhanced spontaneous emission due to a broadband Purcell effect in HMs is reported in [10], [11] and the spontaneous emission lifetime reduction of dyes deposited on HM substrates have been experimentally observed[12]–[14]. Directional single photon emission has also been reported[15]. However, in those studies, the emitted power is mostly directed into the HM substrate where it is eventually dissipated as heat[1]. This leads to a very low external quantum efficiency even though there is a significant increase in the decay rate. In many enhanced emission applications, such as solid-state lighting, it is important to enhance the free-space radiative emission, i.e., the power escaping out of the system and not just the emitted one by the source. While enhanced free-space radiative emission has been shown in a HM grating structure[16], three-dimensional HM resonator properties have not been explored. Here an approximately 100-fold enhancement in free-space radiation emission is calculated when using three-dimensional nanoscale HM subwavelength resonators.

It has been shown that HM resonators can possess high optical quality factor even in extreme subwavelength dimensions and that the radiated power by an excited HM resonator can be larger than the dissipated power[17], [18]. However, free-space radiative emission enhancement due to HM resonators was not studied in [17], [18]. Due to the anomalous resonance wavelength scaling with HM resonator size, one can adjust the resonator size

without changing the resonance wavelength in contrast to standard dielectric or plasmonic resonators. These properties are unique to HM resonators and allow one to optimize the radiation efficiency and radiative emission enhancement when a sub-wavelength HM resonator is used as a nano-antenna. Here it is explicitly shown that there is the strong enhancement of free-space *radiative* emission and quantum efficiency when a quantum emitter is placed close to a HM resonator. The concept in mind is summarily provided as an illustration in Fig. 6.1 and the details of the concept and the calculations thereof is presented in detail in the rest of this chapter.

Sec. 6.2 Definition of the Problem

In the following the first discussion is on the optical properties of an isolated cylindrical HM resonator (comprising silver-silica multilayers) located on top of an opaque silver-cladded substrate. Then the results are provided for the radiation enhancement for varying dipole position and orientation. Finally, elaborations are provided on the the radiation enhancement produced by a finite two-dimensional array of HM resonators with subwavelength spacings. The reported enhancement opens up a possibility for enhancing solid state lighting performance.

Consider a quantum dot (QD) emitter located very close to the HM resonator. The modeled QD emitter is at various locations relative to the resonator as a dipole with polarization oriented along the principal axes. A schematic view of the configuration is shown in Fig. 6.2

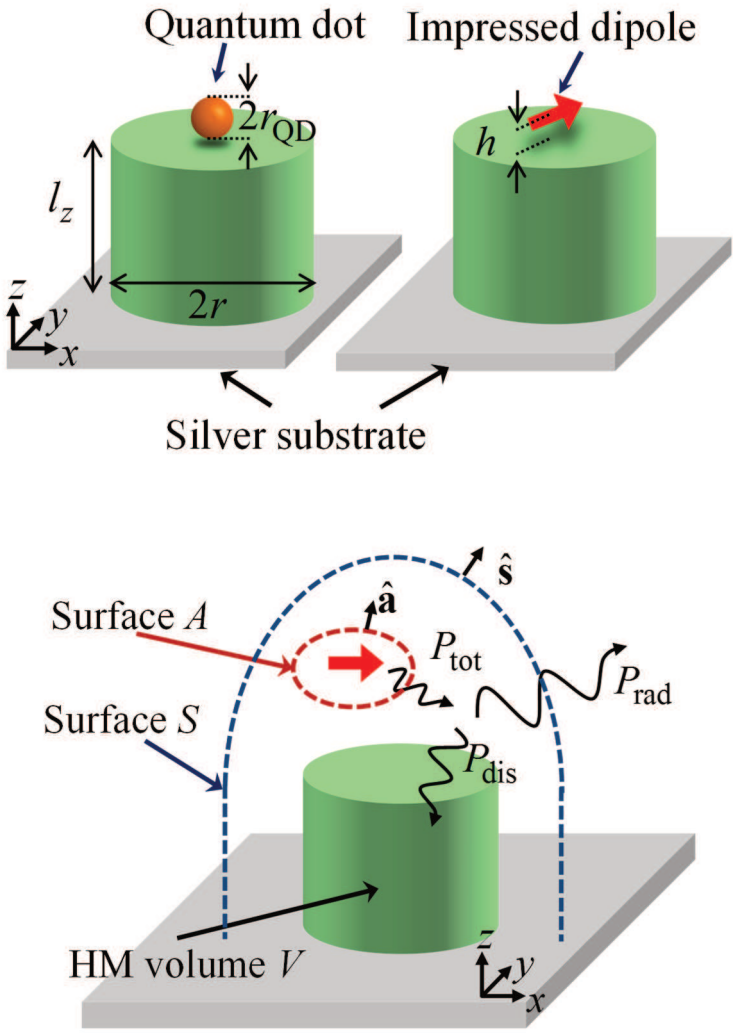

Fig. 6.2 Schematic view of a quantum dot (QD) emitter located on the top surface of a subwavelength HM resonator (top left). The QD is modeled as an impressed dipole with an arbitrary polarization (top right). The bottom panel shows the representation of the power radiated into the upper free-space (through the surface S) which is the difference of the total emitted power by the dipole P_{tot} (through the surface A) and the power dissipated in the HM resonator and substrate.

The QD modelled as a point dipole generates a very wide wavenumber-spectrum of waves enabling the emitted radiation to couple to modes in the HM resonator, and thus polarizes the HM resonator. Some excited mode is suitable for radiation enabling the use of the HM

resonator as a nano-antenna. Part of the total emitted power P_{tot} is dissipated as heat due to material losses (non-radiative process) in the HM, whereas the rest propagates away as radiation into the upper free space, P_{rad}. In this chapter, the focus is on enhancing the radiated power into the upper free-space, hence it is useful to define the radiative emission enhancement (*REE*) factor for each frequency as

$$REE = P_{\text{rad}} / P_{\text{fs}} \tag{6.1}$$

where P_{fs} is the power emitted by an isolated dipole in free space (vacuum). The *radiated* power P_{rad} is evaluated by integrating the real part of the Poynting vector over the surface *S*:

$$P_{\text{rad}} = \frac{1}{2}\int_S \text{Re}\left(\mathbf{E}\times\mathbf{H}^*\right)\cdot\hat{\mathbf{s}}dS \tag{6.2}$$

On the other hand, the total power *emitted* by the dipole, which includes the one dissipated in the materials and the radiated one into the upper space, is similarly evaluated as

$$P_{\text{tot}} = \frac{1}{2}\oint_A \text{Re}\left(\mathbf{E}\times\mathbf{H}^*\right)\cdot\hat{\mathbf{a}}dA \tag{6.3}$$

where the surface *A* is shown in Fig. 6.2. The dissipated power is $P_{\text{dis}} = P_{\text{tot}} - P_{\text{rad}}$, and can also be evaluated as

$$P_{\text{dis}} = \frac{1}{2}\int \text{Re}\left[\mathbf{E}\cdot\left(j\omega\mathbf{D}\right)^*\right]dV \tag{6.4}$$

where V is the volume of the substrate and the resonator. Most of previous work involving HMs focused on boosting the emission rate, i.e., on enhancing P_{tot}. Here, the quantity of interest is P_{rad}, the portion of P_{tot} that is radiated into the upper space. In the following, the evaluated values of these power quantities are obtained via full wave simulations based on the frequency-domain finite-element method[19]

Sec. 6.3 Resonator Example

The HM nano-antenna is designed to resonate at the wavelength of 660 nm, which is accessible using CdSe QDs. The multilayer HM resonator comprises silver (Ag) and silica glass (SiO_2) layers (Fig. 6.3). Measured relative permittivity functions of the constituent materials are used for modeling the materials and , at the wavelength of interest, $\lambda_0 = 660\,\text{nm}$, one has $\varepsilon_{\text{Ag}} = -17.19 - j0.69$ and $\varepsilon_{\text{SiO}_2} = 2.12$. The resonator is designed as a cylinder made of three pairs of alternating layers of SiO_2 (the bottom layer) and Ag (each with a thickness of 12.5 nm) and the top is capped with 5-nm-thick SiO_2 to protect Ag. The resonators are deposited on top of a Ag-cladded substrate as in Fig. 6.3(a). The resonator has a radius of 54 nm and a total height of 80 nm. Based on previous studies, three pairs of metal-dielectric planar structure are sufficient to exhibit hyperbolic metamaterial properties[2].

The calculated radiated power into the upper free space P_{rad}, as well as P_{dis} and P_{tot} versus wavelength for an *x*-directed dipole are shown in Fig. 6.3(b). The dipole is located at a height $h = 10\,\text{nm}$ above the top center of the resonator. These powers are normalized to P_{fs}. P_{tot} is enhanced by 30 folds due to Purcell effect, the radiative emission and dissipated power are enhanced by 19 (=*REE*) and 9 times, respectively, at the antenna resonance,

peaking around 660 nm. It is to be stressed that a large portion of the total power emitted is actually radiated into upper free-space. It is convenient to define the radiation efficiency as the fraction of radiated power over the total emitted one, $P_{\text{rad}} / P_{\text{tot}}$ (this coincides with the analogous definition used in antenna theory). Results in Fig. 6.3(b) show that $P_{\text{rad}} / P_{\text{tot}}$ is approximately 66% indicating that HM subwavelength resonators can be used as efficient nano-antennas. Using an alternative metric, for example as that in [16], the free-space radiation enhancement can be defined as the radiated power normalized to that radiated by the same dipole either over a flat Ag or over a HM substrate, leading to even larger enhancement factors of 102 and 143, respectively (plots not shown here for brevity).

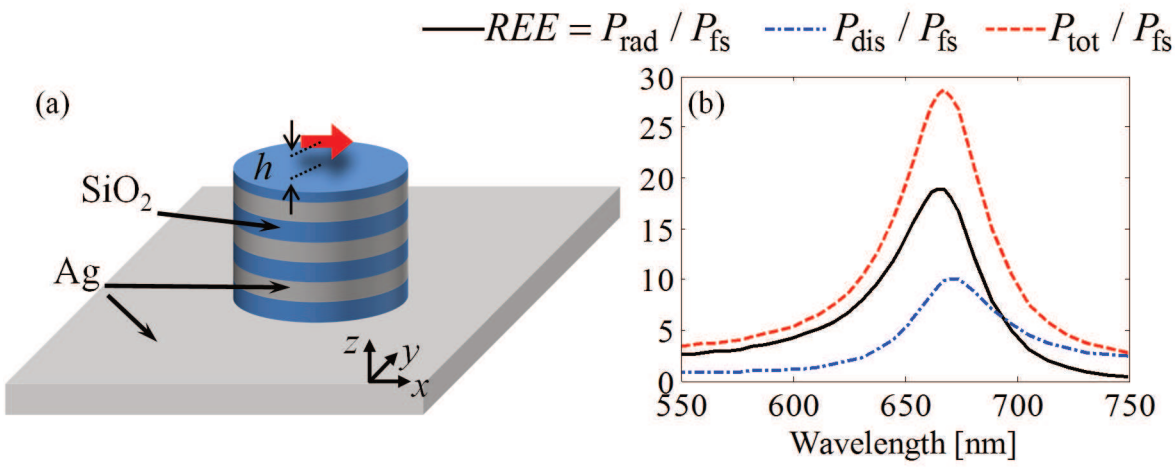

Fig. 6.3 (a) The illustration of the multilayer HM resonator on top of silver substrate. (b) Enhancement of radiated, dissipated and total power emitted relative to the power of the same dipole radiated in free-space (P_{fs})

Now the focus is how the dipole orientation affects the *REE*. In Fig. 6.4, *REE* is plotted for dipoles polarized along *x*, *y*, and *z*, showing maximum *REE* of 25, 20 and 100, respectively. In addition, it is also found that *REE* is sensitive to the location of the dipole relative to the HM resonator.

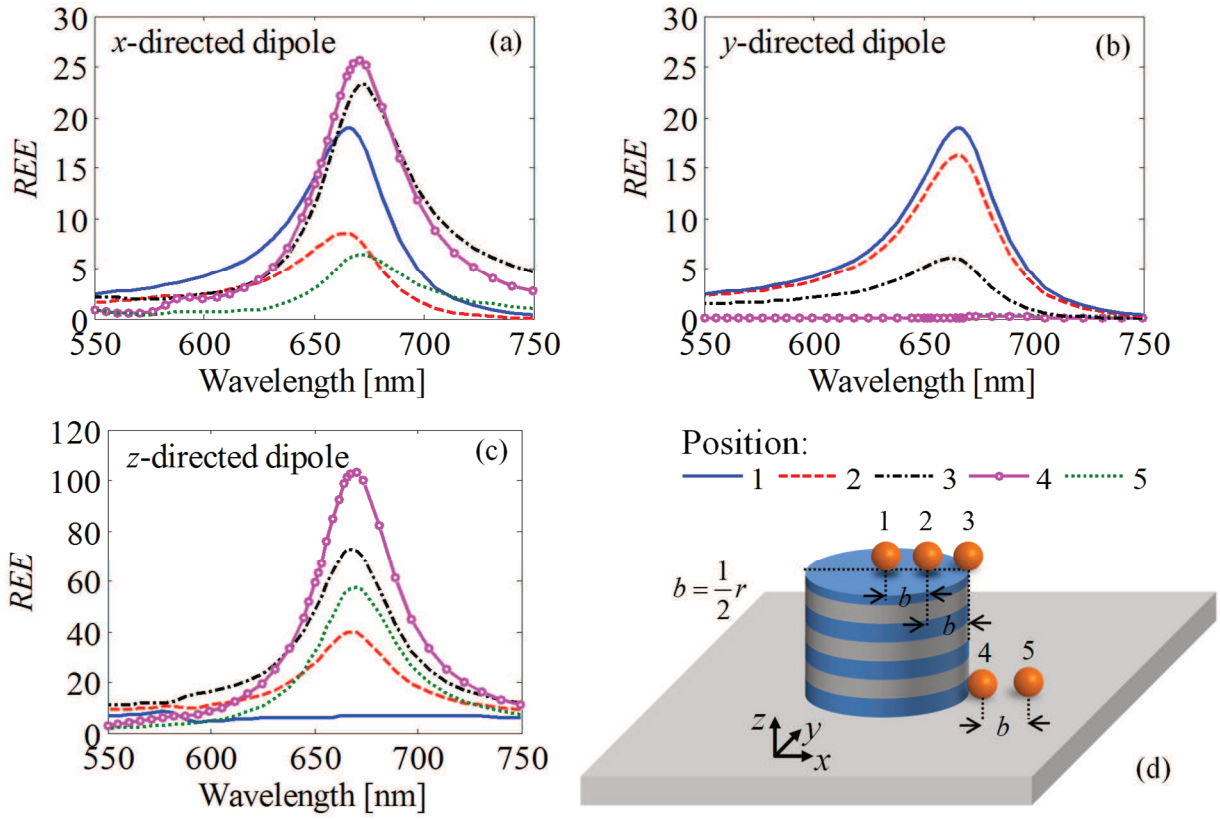

Fig. 6.4 Radiative emission enhancement *REE* of a QD versus wavelength model as a single dipole emitting with (a) *x*-, (b) *y*-, (c) *z*-polarization, for the enumerated QD positions in (d) (position 1: blue solid line, 2: red dashed line, 3: black dotted-dashed line, 4:, purple line with circle markers and 5: green dotted line)

The dipole positions explored are denoted by numbers $N=\{1,2,3,4,5\}$ in Fig. 6.4(d). For the *x*-directed dipoles at positions 1, 3, and 4 as well as for *y*-directed dipoles at positions 1 and 2 the enhancement factors are larger than 15 folds. On the other hand, for a *z*-directed dipole, all positions except position 1 yield enhancement factors larger than 30. The maximum enhancement is achieved for the *z*-directed dipole at position 4 with an enhancement factor larger than 100. Using the effective medium approach[1], [11] (EMA) to model the HM nano-antenna as a bulk anisotropic material, simulations are found to be 5% larger for the resonance wavelength and %20 smaller for the *REE*. In Fig. 6.5, the far-field

directivity patterns pertaining to dipoles polarized along x and z at positions 1 and 4, respectively, are reported. Here directivity is defined as $\text{Directivity}(\theta,\phi) = U(\theta,\phi)\,4\pi / P_{\text{rad}}$ where U is the radiation intensity per unit solid angle. The HM nano-antenna radiates with a single lobe in the +ve z direction and it is nearly symmetric about the z-axis with a half-power beam width of 95°. The maximum directivity is 5.7, which is almost 4 times that of a dipole in vacuum (For a point dipole, the maximum directivity is 1.5). Therefore the field intensity in +z direction is further enhanced due to enhanced directivity. In addition, the radiation patterns obtained using EMA are found to be in very good agreement with those using the multilayer HM simulations.

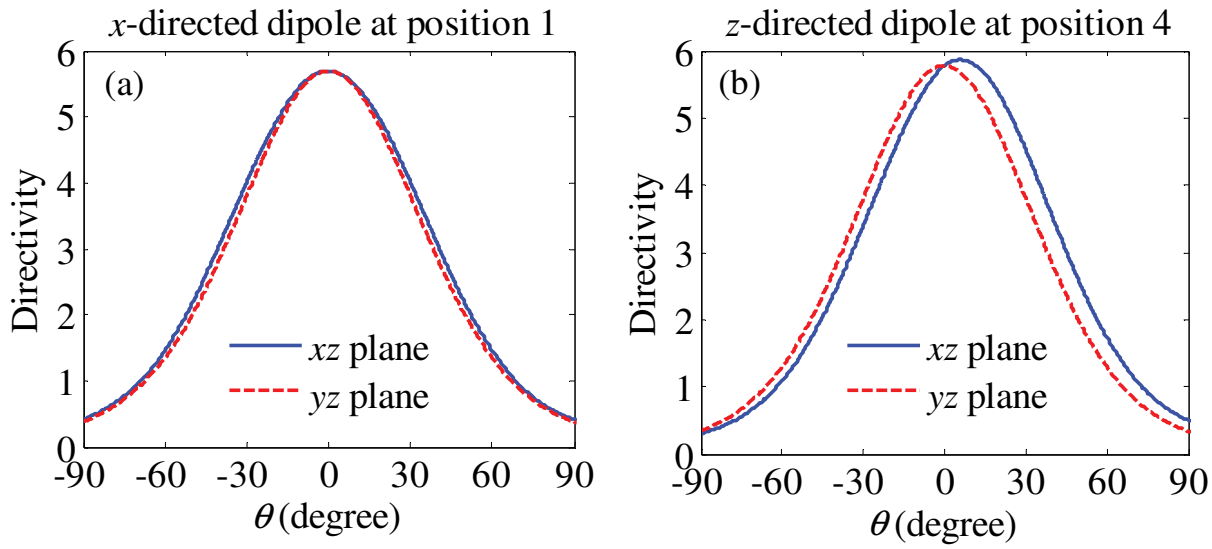

Fig. 6.5 Directivity patterns of (a) x-directed dipole at position 1 and (b) z-directed dipole at position 4.

In order to provide a physical insight into this characteristic, in Fig. 6.6 one can find the instantaneous electric field vector map at the 660 nm resonance when the resonator is excited by an x-directed dipole at position 1; the arrows indicate the E-field direction and the color indicates its magnitude. A similar E-field distribution is found for the z-directed dipole

at position 4, with the only difference being that the E-field is much stronger. The vector field map shown in Fig. 6.6 is basically the modal field of the resonance. From these field maps, one can correlate the emission enhancement factor to the position and dipole orientation. For example, when a *z*-directed dipole is place in location 4 where the *z*-component of the field is strong, the maximum enhancement factor is obtained. In contrast, the enhancement factor of the *x*-directed dipole at position 1 is smaller than that of the *z*-directed dipole at position 4, due to the fact that the *x*-component of the modal E-field in this position is weaker. Instead, the *x*-oriented dipole at location 3 matches the polarization of the modal E-field and therefore it exhibits a comparable enhancement factor as the *z*-oriented dipole at location 4. These results correlate with an increase of the local density of states. One can envision that further enhancement may be realized using different geometrical shapes that produce even stronger modal E-field intensities where a QD can be positioned.

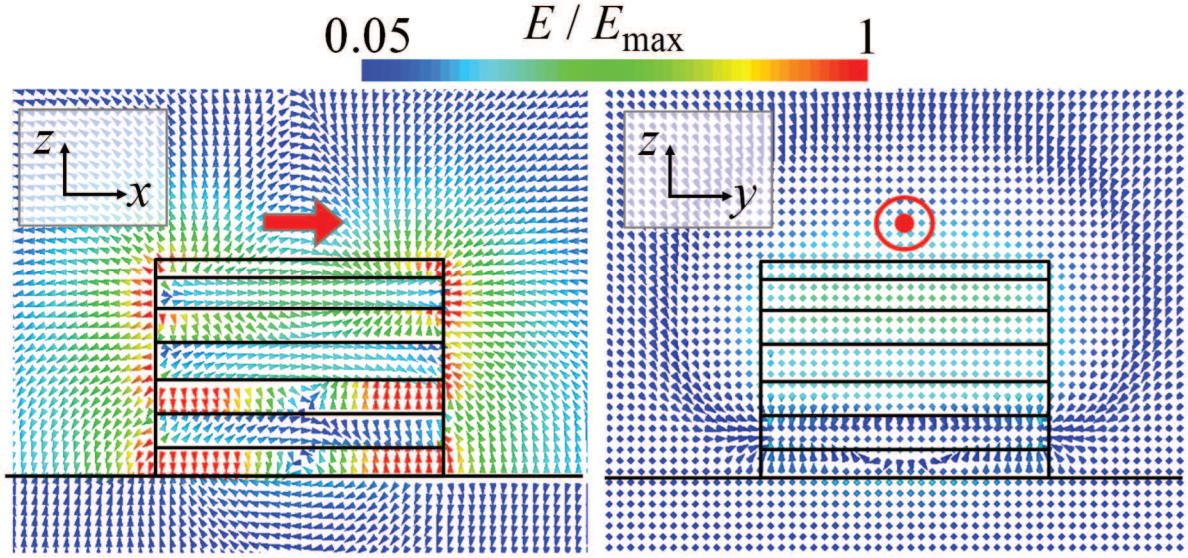

Fig. 6.6 Normalized electric field vector maps in the two principal planes at 660 nm wavelength. The color bar is in linear scale. The dipole is polarized along the *x*-axis as illustrated. Note that the field vector lies mainly on the *xz* plane.

Sec. 6.4 Array Effect

In a practical implementation, HM resonators are fabricated in a two-dimensional array and the QDs will be dispersed on the surface hosting the array. Here a discussion is presented on how nearby HM resonators affect the radiative emission enhancement. As mentioned earlier, an advantage of using HM resonators lies in the opportunity of high packing density due to their small size. In full-wave simulations the implementation of an infinitely periodic array with a single dipole excitation is impractical from numerical simulation standpoint even when taking advantage of the structure periodicity [20], therefore in the following the analysis of a finite array of resonators is provided. In particular a 3-by-3 square array of resonators identical to the one previously introduced is investigated showing the radiation enhancement pertaining to an *x*-directed dipole at position 1 and a *z*-directed dipole at position 4, as depicted in Fig. 6.7. The enhancement of radiated power *REE* is plot in Fig. 6.8 for four different periods $d_x = d_y$: 175, 200, 225, and 250 (all in nm). As a comparison also the enhancement for an isolated HM resonator (no-array) is reported.

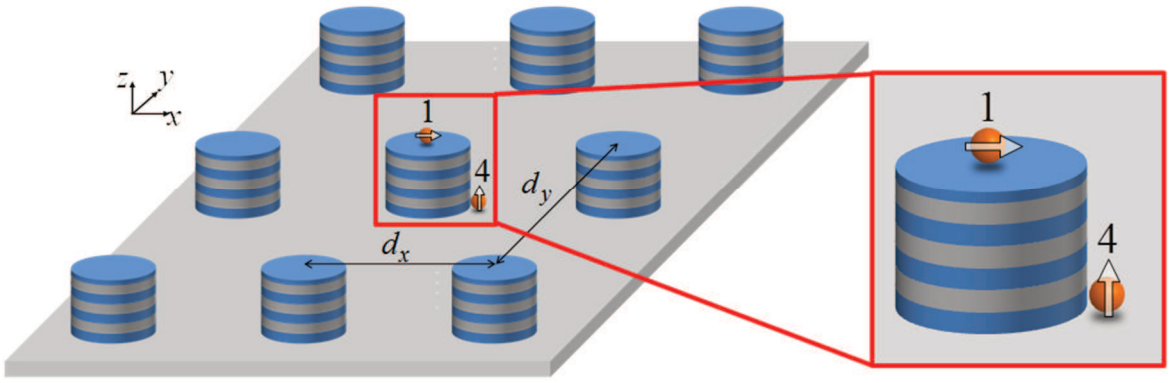

Fig. 6.7 A 3-by-3 array of cylindrical subwavelength HM resonators with a QD located in two possible positions.

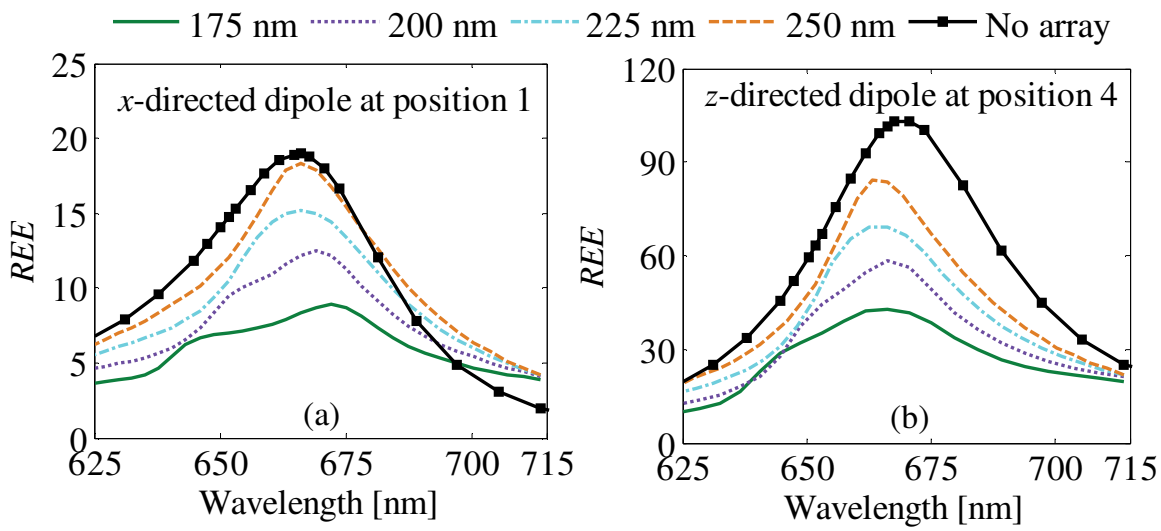

Fig. 6.8 Radiative emission enhancement *REE* versus wavelength for (a) an *x*-directed dipole at position 1 and (b) for a *z*-directed dipole at position 4, periods of $d_x = d_y$ = 175 nm (green solid line), 200 nm (purple dotted line), 225 nm (cyan dotted-dashed line), and 250 (orange dashed line) as in Fig. 6.7, and for the "no-array" case (black solid line with square markers).

Within the considered parameter range, the enhancement increases as the period $d_x = d_y$ is increased as shown in Fig. 6.8. For $d_x = 200\,\text{nm}$ ($\lambda_0 / 3.3$) the enhancement values are still high, and more than 50% of that of the no-array case. The case with largest spacing $d_x = 250\,\text{nm}$ ($\lambda_0 / 2.6$, i.e., still subwavelength) yields a level of enhancement comparable to the no-array case. This implies that HM resonators can be densely arranged in array configuration with subwavelength period still keeping large power enhancement levels. As in the single resonator case, the *z*-oriented dipole at position 4 in the array yields much higher *REE* than the other locations. For randomly oriented QDs, therefore, the average enhancement effect is expected to be smaller.

Sec. 6.5 Conclusion

It is shown for the first time, to the authors' knowledge, that subwavelength HM resonators can be used as efficient radiators (i.e., as efficient optical nano-antennas). They have the ability to enhance both the radiative emission and the Purcell factor of quantum emitters in their vicinity. It is shown that the total emission of a QD near a HM resonator nano-antenna is mostly coupled to the radiated power into the upper free space. The results show up to 100 times free-space radiation enhancement in the presence of HM resonators, indicating that these HM resonators are efficient radiators. The enhancement strongly depends on the dipole position and polarization. The combined effect of the enhanced REE and the directive emission produces further enhancement of field intensity in the broad side up to 400 times. Moreover significant enhancement levels are achieved also in the presence of surrounding nano-antennas in a two-dimensional array configuration. It is presented that the presence of nearby HM resonators in a 3-by-3 square array lead to large power enhancement levels, especially for QD at position 4 (i.e. for QD sitting next to the resonator, on top of the substrate), slightly lower than those for a single HM resonator. The conclusion is that nanostructures made of HM may prove useful for improvement of light-matter interaction and solid-state lighting applications.

This work was performed, in part, at the Center for Integrated Nanotechnologies, a U.S. Department of Energy, Office of Basic Energy Sciences user facility. The computational result was supported by Sandia LDRD program and the permittivity measurements performed at Sandia were supported by Sandia's Solid-State Lighting Science EFRC. Sandia National Laboratories is a multi-program laboratory managed and operated by Sandia Corporation, a wholly owned subsidiary of Lockheed Martin Corporation, for the U.S. Department of

Energy's National Nuclear Security Administration under contract DE-AC04-94AL85000. F.C. and C.G. are grateful to Ansys Inc. for providing HFSS. This chapter is reproduced based on the material in [C. Guclu, T. S. Luk, G. T. Wang, and F. Capolino, "Radiative Emission Enhancement Using Nano-antennas Made of Hyperbolic Metamaterial Resonators," *Applied Phys. Letters*, vol. 105, 123101, 2014],

References

[1] C. Guclu, S. Campione, and F. Capolino, "Hyperbolic metamaterial as super absorber for scattered fields generated at its surface," *Phys. Rev. B*, vol. 86, no. 20, p. 205130, Nov. 2012.

[2] T. S. Luk *et al.*, "Near-infrared surface plasmon polariton dispersion control with hyperbolic metamaterials," *Opt. Express*, vol. 21, no. 9, pp. 11107–11114, May 2013.

[3] C. Guclu, S. Campione, and F. Capolino, "Array of dipoles near a hyperbolic metamaterial: Evanescent-to-propagating Floquet wave transformation," *Phys. Rev. B*, vol. 89, no. 15, p. 155128, Apr. 2014.

[4] C. Rizza, A. Ciattoni, E. Spinozzi, and L. Columbo, "Terahertz active spatial filtering through optically tunable hyperbolic metamaterials," *Opt. Lett.*, vol. 37, no. 16, pp. 3345–3347, Aug. 2012.

[5] I. V. Iorsh, I. S. Mukhin, I. V. Shadrivov, P. A. Belov, and Y. S. Kivshar, "Hyperbolic metamaterials based on multilayer graphene structures," *Phys. Rev. B*, vol. 87, no. 7, p. 75416, Feb. 2013.

[6] M. A. K. Othman, C. Guclu, and F. Capolino, "Graphene-based tunable hyperbolic metamaterials and enhanced near-field absorption," *Opt. Express*, vol. 21, no. 6, pp. 7614–7632, Mar. 2013.

[7] M. A. K. Othman, C. Guclu, and F. Capolino, "Graphene–dielectric composite metamaterials: evolution from elliptic to hyperbolic wavevector dispersion and the transverse epsilon-near-zero condition," *J. Nanophotonics*, vol. 7, no. 1, pp. 073089–073089, 2013.

[8] E. E. Narimanov, H. Li, Y. A. Barnakov, T. U. Tumkur, and M. A. Noginov, "Reduced reflection from roughened hyperbolic metamaterial," *Opt. Express*, vol. 21, no. 12, pp. 14956–14961, Jun. 2013.

[9] M. A. Noginov, Y. A. Barnakov, G. Zhu, T. Tumkur, H. Li, and E. E. Narimanov, "Bulk photonic metamaterial with hyperbolic dispersion," *Appl. Phys. Lett.*, vol. 94, no. 15, p. 151105, Apr. 2009.

[10] Z. Jacob, I. I. Smolyaninov, and E. E. Narimanov, "Broadband Purcell effect: Radiative decay engineering with metamaterials," *Appl. Phys. Lett.*, vol. 100, no. 18, p. 181105, May 2012.

[11] O. Kidwai, S. V. Zhukovsky, and J. E. Sipe, “Effective-medium approach to planar multilayer hyperbolic metamaterials: Strengths and limitations,” *Phys. Rev. A*, vol. 85, no. 5, p. 53842, May 2012.
[12] Z. Jacob, J.-Y. Kim, G. V. Naik, A. Boltasseva, E. E. Narimanov, and V. M. Shalaev, “Engineering photonic density of states using metamaterials,” *Appl. Phys. B*, vol. 100, no. 1, pp. 215–218, Jul. 2010.
[13] M. A. Noginov *et al.*, “Controlling spontaneous emission with metamaterials,” *Opt. Lett.*, vol. 35, no. 11, pp. 1863–1865, Jun. 2010.
[14] J. Kim *et al.*, “Improving the radiative decay rate for dye molecules with hyperbolic metamaterials,” *Opt. Express*, vol. 20, no. 7, pp. 8100–8116, Mar. 2012.
[15] W. D. Newman, C. L. Cortes, and Z. Jacob, “Enhanced and directional single-photon emission in hyperbolic metamaterials,” *J. Opt. Soc. Am. B*, vol. 30, no. 4, pp. 766–775, Apr. 2013.
[16] D. Lu, J. J. Kan, E. E. Fullerton, and Z. Liu, “Enhancing spontaneous emission rates of molecules using nanopatterned multilayer hyperbolic metamaterials,” *Nat. Nanotechnol.*, vol. 9, no. 1, pp. 48–53, Jan. 2014.
[17] J. Yao, X. Yang, X. Yin, G. Bartal, and X. Zhang, “Three-dimensional nanometer-scale optical cavities of indefinite medium,” *Proc. Natl. Acad. Sci.*, Jun. 2011.
[18] X. Yang, J. Yao, J. Rho, X. Yin, and X. Zhang, “Experimental realization of three-dimensional indefinite cavities at the nanoscale with anomalous scaling laws,” *Nat. Photonics*, vol. 6, no. 7, pp. 450–454, Jul. 2012.
[19] Ansys, Inc., *High Frequency Structural Simulator (HFSS)*. 2013.
[20] R. Qiang, J. Chen, F. Capolino, D. R. Jackson, and D. R. Wilton, “ASM-FDTD: A Technique for Calculating the Field of a Finite Source in the Presence of an Infinite Periodic Artificial Material,” *IEEE Microw. Wirel. Compon. Lett.*, vol. 17, no. 4, pp. 271–273, 2007.

CHAPTER 7

ENHANCING FIELDS AND LIGHT EMISSION IN VICINITY OF ANISOTROPIC METAMATERIALS WITH NEAR ZERO PERMITTIVITY

Sec. 7.1 Motivation

Materials with extremely small permittivity, namely epsilon near zero (ENZ) materials have been on the focus of attention due to their natural existence in optical frequencies and their unprecedented properties. Realization of ENZ behavior has been achieved using multilayer stack of metal and dielectric [1], 3-D periodic array of dielectric-core metallic-shell nanospheres with fluorescent dyes in the core of each nanoparticle for the loss-compensation [2] or employing metal-coated waveguides at their cut-off frequency [3]. Owing to their extremely large velocity of phase propagation, such materials enable linear applications such as tailoring radiation emission [4]–[7], energy squeezing and supercoupling [8]. On the other hand ENZ materials can be utilized to achieve huge field enhancement. In [9] the field intensity enhancement (FIE) of a isotropic ENZ semi-infinite medium and a isotropic ENZ slab under TM (transverse magnetic) plane wave incidence is

theoretically investigated. Exploiting this ability, optical nonlinearities such as second or third harmonic generation [10]–[12] and Kerr nonlinearities [13] have been enhanced significantly.

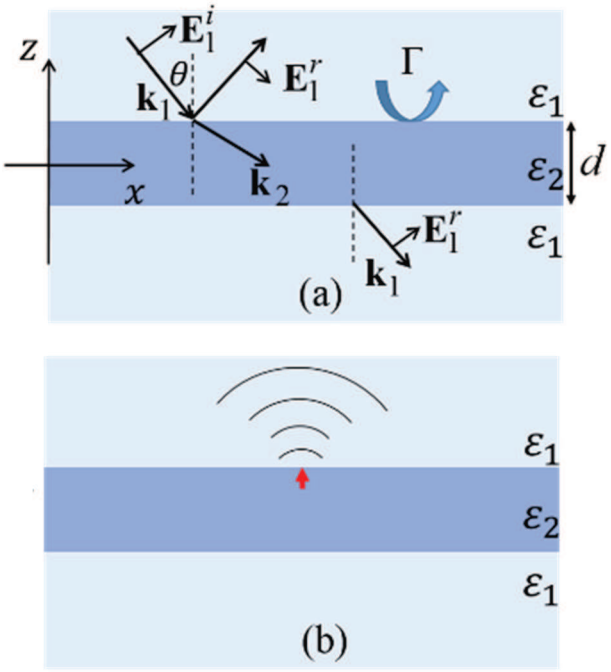

Fig. 7.1 Schematic of longitudinal epsilon near zero film (a) under TM-plane wave incidence and (b) with dipole located in the hotspot.

In the present letter we establish that under TM wave incidence a uniaxially anisotropic epsilon near zero film exhibits remarkably stronger FIE than isotropic epsilon near zero (hereafter we will use IENZ for isotropic epsilon near zero) studied in [9]. The film whose surfaces are normal to the *z* axis, shown in Fig. 7.1, is marked by the subscript '2', and modeled via a relative permittivity tensor $\underline{\varepsilon}_2 = \varepsilon_t\left(\hat{\mathrm{x}}\hat{\mathrm{x}}+\hat{\mathrm{y}}\hat{\mathrm{y}}\right)+\varepsilon_z\hat{\mathrm{z}}\hat{\mathrm{z}}$. Particularly we show that the specific type of anisotropy useful for super-field enhancement occurs when the *zz* entry of the permittivity tensor is near zero, which in the following we call it longitudinal epsilon near zero (LENZ) condition. Furthermore, through reciprocity, we demonstrate that a *z*-polarized dipole located at the E-field hotspot in the LENZ film radiates extremely strong far

field. We also show that FIE in LENZ films is not strongly dependent on and sensitive to the film thickness and remarkably it occurs for a wide angular incidence range unlike what happens in IENZ films. LENZ film can be realized in various ways, for example by a multilayered medium made of a stack of metallic and insulator layers or by stacking semiconductor layers.

Sec. 7.2 Statement of the Problem and the Analytical Model

The geometry of the investigated problem is depicted in Fig. 7.1. We investigate first the FIE in a film with thickness d under a TM plane wave as in Fig. 7.1(a), and then we investigate the radiative emission enhancement of a point dipole inside a LENZ film as illustrated in Fig. 7.1(b).

The electric field vector of the incident TM wave is in the $x-z$ plane, i.e., $\mathrm{E}_1^i = E_1^i\left(\cos\theta_i\hat{\mathrm{x}} + \sin\theta_i\hat{\mathrm{z}}\right)e^{i\mathrm{k}_1\cdot\mathrm{r}}$ where $\mathbf{k}_1$ is the wavevector of the impinging TM wave where $k_1 = |\mathbf{k}_1| = \omega\sqrt{\mu_0\varepsilon_0\varepsilon_1}$ is the wavenumber in medium 1. The transverse (to the z axis) wavenumber is k_t whereas the longitudinal wavenumber outside the film is $k_{z1} = \sqrt{k_1^2 - k_t^2}$. A monochromatic, time harmonic convention $e^{-i\omega t}$ is implicitly assumed. In the LENZ film the entries of the relative permittivity tensor are $\varepsilon_t = \varepsilon_t' + i\varepsilon_t''$ and $\varepsilon_z = \varepsilon_z' + i\varepsilon_z''$. We will use $k_{z2} = \sqrt{\varepsilon_t k_0^2 - (\varepsilon_t/\varepsilon_z)k_t^2}$ for denoting the longitudinal wavenumber in the film. Owing to the continuity of the normal displacement field component at $z = d/2$:

$$\varepsilon_1 E_{z1}\big|_{z=(d/2)^+} = \varepsilon_z E_{z2}\big|_{z=(d/2)^-} \tag{7.1}$$

in which E_{z1} and E_{z2} are the longitudinal components of the *total* electric field in media 1 and 2 respectively. By replacing the value of the E_{z1} in the abovementioned equation one obtains [9]

$$\varepsilon_1 E_1^i (1-\Gamma)\sin\theta_i = \varepsilon_z E_{z2} \tag{7.2}$$

where Γ is the reflection coefficient towards the $-z$ direction, seen from the upper interface and is given by

$$\Gamma(d,\theta_i) = \frac{-i\left(k_{z2}^2 - k_{z1}^2\hat{\varepsilon}_t^2\right)s_h}{2k_{z1}k_{z2}\hat{\varepsilon}_t\, c_h - i\left(k_{z2}^2 + k_{z1}^2\hat{\varepsilon}_t^2\right)s_h} \tag{7.3}$$

with $s_h = \sin(k_{z2}d)$, $c_h = \cos(k_{z2}d)$ and $\hat{\varepsilon}_t = \varepsilon_t / \varepsilon_1$. Therefore, assuming $\hat{\varepsilon}_z = \varepsilon_z / \varepsilon_1$, it is convenient to define the local *z*-polarized field intensity enhancement at $z = (d/2)^-$ as

$$\text{FIE} = \left|\frac{E_{z2}}{E_1}\right|^2 = \left|\frac{(1-\Gamma)\sin\theta}{\hat{\varepsilon}_z}\right|^2 \tag{7.4}$$

which is the ratio of the electric field in the longitudinal direction in the film to the incident electric field amplitude at the same place in the absence of the film. In the following, unless stated otherwise, FIE is always calculated just below the top surface of the film at $z = (d/2)^-$. The field intensity enhancement depends strongly on the choice of ε_z, i.e., by choosing ε_z close to zero FIE gets large. FIE is also strongly dependent upon the reflection coefficient Γ, which is in general complex, and if it gets close to unity then FIE vanishes. We will compare the LENZ and IENZ cases for their field enhancement and radiation enhancement capabilities using examples and analytical calculations.

As an example, in Fig. 7.2, we consider a film with thickness $d = \lambda / 3$, with $\lambda = 2\pi / k_1$, made of LENZ material surrounded by vacuum i.e. $\varepsilon_1 = 1$. In Fig. 7.2(a) we assume that the film has longitudinal permittivity of $\varepsilon_z = 0.001 + i0.001$ and transverse permittivity of $\varepsilon_t = \varepsilon_t' + i0.001$ at wavelength λ. We report the FIE at $z = (d/2)^-$, i.e. just below the top surface of the film, versus the real part of the transverse permittivity of the film ε_t' and the angle of incidence of the impinging TM-polarized wave. The IENZ case, as a subset of LENZ cases reported in Fig. 7.2(a), is marked with white dashed line where $\varepsilon_t' = \varepsilon_z'$. Notably, we observe that FIE is the lowest for the IENZ case compared to LENZ cases with larger ε_t'. As the anisotropy of the film becomes starker, the FIE increases, in other words it is better not to have a vanishing ε_t'. This figure clearly exhibits the superior field enhancement capability of LENZ over IENZ. Also provided in Fig. 7.2(b) is the comparison of FIE in IENZ case and LENZ case with $\varepsilon_t = 2.5 + i0.001$ as a function of angle of incidence. The FIE of the reported LENZ case is 23 folds of the FIE of the IENZ case. Moreover the angular range at which FIE occurs is much wider in the LENZ case than in the IENZ case. Using angular full width at half maximum (FWHM) of FIE defined as the range of angles in which FIE is higher than the half of its maximum value, the angular FWHM of FIE in LENZ case is at least 45° whereas for the isotropic case is less than 5°. We can state that LENZ leads to not only larger FIE, but also to a wider angular span of large FIE. To differentiate the IENZ and LENZ behavior mathematically, assuming $\varepsilon_1 = 1$ we substitute Γ from (7.3) in (7.4)

$$\mathrm{FIE} = \left| \frac{2k_{z1}k_{z2}\varepsilon_t c_h - 2ik_{z1}^2\varepsilon_t^2 s_h}{\varepsilon_z \left[2k_{z1}k_{z2}\varepsilon_t c_h - i\left(k_{z2}^2 + k_{z1}^2\varepsilon_t^2\right) s_h \right]} \sin\theta \right|^2 \tag{7.5}$$

From this equation one may observe that for an isotropic film with permittivity $\varepsilon_2 \to 0$ and $\theta \neq 0$ equation (7.5) can be written as

$$\mathrm{FIE}_{\mathrm{IENZ}} = \left| \frac{2\cos\theta \cos\left(-ik_1 d \sin\theta\right)}{\sin\left(-ik_1 d \sin\theta\right)} \right|^2 \tag{7.6}$$

which is a finite (i.e., not large) value unless θ or d (or both) tends to zero. Note that for an assigned θ, $\mathrm{FIE}_{\mathrm{IENZ}}$ is not infinity even if we have assumed that $\varepsilon_2 \to 0$. It is also worth mentioning that the maximum of IENZ case in Fig. 7.2(b) does not go to infinity as θ tends to zero due to nonzero ε_2. Instead, for the LENZ case assuming near zero values for ε_z and angles such that $\varepsilon_z \ll \sin^2\theta$ (because the proper limit is for $\varepsilon_z / \sin^2\theta \to 0$), by simplifying the numerator and denominator of (7.5), assuming finite values of ε_t and d, we obtain

$$\mathrm{FIE}_{\mathrm{LENZ}} \approx \left| \frac{2\sqrt{\varepsilon_t}}{\sqrt{\varepsilon_z}} \cos\theta \right|^2 \approx 4 \left| \frac{\varepsilon_t}{\varepsilon_z} \right| \cos^2\theta \tag{7.7}$$

Here the denominator goes to zero as $\varepsilon_z \to 0$ which causes the FIE to tend to infinity for the LENZ case. Note that to obtain giant FIE is not necessary to illuminate with small incidence angle θ, whereas in the IENZ case only for small θ one can get giant FIE. In contrast to (7.6) which does not depend on ε_2, FIE in LENZ case as reported in (7.7) depends on permittivity tensor entries. It shows that having large ε_t is favorable for having large FIE, contrary to the assumption that IENZ is supposed to be good for field enhancement.

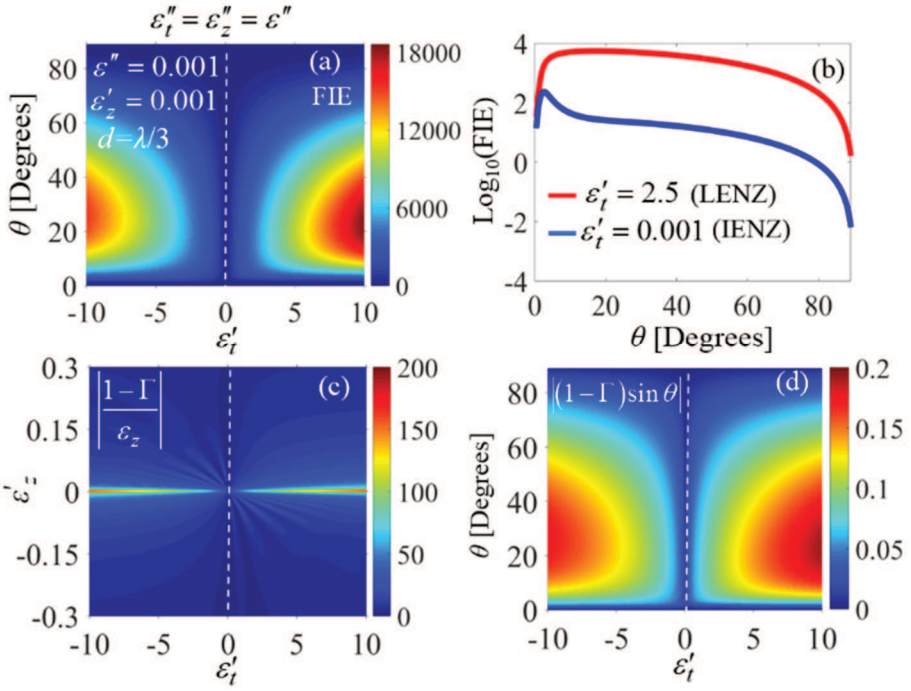

Fig. 7.2 (a) FIE at $z=(d/2)^-$ in the geometry of Fig. 7.1 with $d=\lambda/3$ and $\varepsilon_z=0.001+i0.001$ and $\varepsilon_t=\varepsilon_t'+i0.001$ as a function of ε_t' and incident angle θ (b) Comparison of the FIE at $z=(d/2)^-$ between the IENZ case (blue line) with $\varepsilon_2=0.001+i0.001$ and the LENZ case (red line) with $\varepsilon_t=2.5+i0.001$ (c) Value of $\left|(1-\Gamma)/\varepsilon_z\right|$ versus ε_t' and ε_z' for $\theta=40^o$ and $\varepsilon_t''=\varepsilon_z''=0.001$ (d) $\left|(1-\Gamma)\sin\theta\right|$ as a function of incident angle and ε_t' with $\varepsilon_t''=\varepsilon_z''=0.001$.

Sec. 7.3 Numerical Computations of Field Enhancement

In this section, the numerical calculation carried out with exact formulae are presented. The approximated formulae that are derived in previous sections are used for guidance in selecting distinctive cases demonstrating the advantages of LENZ slabs. The initial interpretation of (7.7) was that the FIE is enhanced for high transverse permittivity in general, a case not observed in IENZ. This fact is clearly shown in Fig. 7.2(c) where $\left|(1-\Gamma)/\varepsilon_z\right|$ of (7.4) is reported versus real part of the transverse and longitudinal

permittivities for slab with $d=\lambda/3$ and $\varepsilon_t''=\varepsilon_z''=0.001$. It is clear that as ε_z tends to zero the abovementioned value increases. It is also worth noting that as the film becomes more anisotropic (larger $|\varepsilon_t'|$) FIE increases as well. Fig. 7.2(d) shows the value of $|(1-\Gamma)\sin\theta|$, i.e. the numerator inside the absolute value function in (7.5), as a function of ε_t' and θ for the same slab of Fig. 7.2(a). As it is clear from this figure, $|(1-\Gamma)\sin\theta|$ is much larger than ε_z for LENZ cases which leads to giant FIE. On the line denoting IENZ in Fig. 7.2(d) the behavior of $|(1-\Gamma)\sin\theta|$ is a signature of the reflection coefficient Γ which tends to 1 unless when d tends to zero. However, for LENZ case the real part of Γ does not tend to 1, paving the way toward increasing FIE, over a wide range of angles. To sum up, the FIE is remarkably higher for the anisotropic case than the isotropic case.

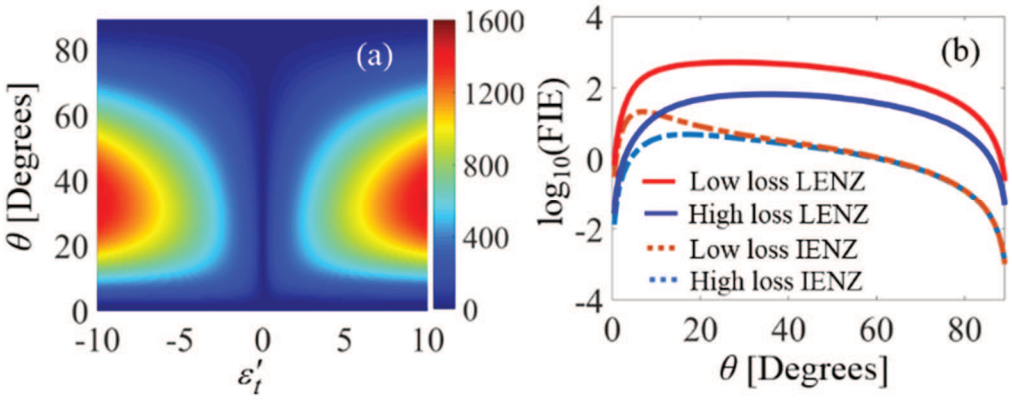

Fig. 7.3 (a) FIE at $z=(d/2)^-$ with $d=\lambda/3$ as a function of ε_t' and θ for $\varepsilon_z=0.001+i0.01$ and $\varepsilon_t''=0.01$ (b) Comparison of IENZ (dotted lines) with $\varepsilon_2'=0.001$ and LENZ (solid lines) with $\varepsilon_t'=2.5$ and $\varepsilon_z'=0.001$ for different losses: $\varepsilon_t''=\varepsilon_z''=0.01$ (low loss), $\varepsilon_t''=\varepsilon_z''=0.05$ (high loss).

One of the most important factors in determining the FIE in LENZ film is the loss represented by the imaginary parts of the transverse and the longitudinal permittivities. To

investigate the effect of the loss in Fig. 7.3(a) we reproduce the same set of cases as in Fig. 7.2(a) but with higher film loss modeled by $\varepsilon_t'' = \varepsilon_z'' = 0.01$ reporting that FIE decreased drastically due to the loss in the film. However, LENZ still yields higher FIE compared to IENZ (marked with dashed white line). To better appreciate FIE superiority of LENZ over IENZ over a wide angular range both in low and high loss cases, in Fig. 7.3(b) FIE is plotted versus incident angle for IENZ with $\varepsilon_2' = 0.001$ and LENZ with $\varepsilon_t' = 2.5$ and $\varepsilon_z' = 0.001$. The high loss cases have $\varepsilon_2'' = 0.05$ for IENZ and $\varepsilon_t'' = \varepsilon_z'' = 0.05$ for LENZ; the low loss cases have $\varepsilon_2'' = 0.01$ for IENZ and $\varepsilon_t'' = \varepsilon_z'' = 0.01$ for LENZ. The outstanding performance of LENZ is demonstrated in this figure by noting that high loss LENZ provides much higher FIE even than low loss IENZ for angles of incidence $\theta > 10^{\circ}$. Assuming similar imaginary permittivity, the FIE of LENZ is *two* orders of magnitude higher than that for IENZ for a wide range of angles of incidence.

So far we have investigated FIE at $z = (d/2)^{-}$. Another important quality of FIE is its profile within the film. This is reported in Fig. 7.4(a) as a function of z/d and d/λ for a specific case of $\theta = 40^{\circ}$, $\varepsilon_z = 0.001 + i0.035$ and $\varepsilon_t = 2.5 + i0.035$. As it is clear from the results, the FIE is maximum at the interface between the film and the air and it decreases by getting deeper into the film. For small thicknesses, when $d < 0.1\lambda$, the FIE has a more uniform distribution inside the film, and the FIE is at similar levels as in thicker films. In Fig. 7.4(b) the dependence of FIE on the film thickness has been studied as a function of ε_t', analyzing three cases with $d/\lambda = 1$, $d/\lambda = 0.1$ and even $d/\lambda = 0.01$, assuming incidence at $\theta = 40^{\circ}$, $\varepsilon_z = 0.001 + i0.01$ and $\varepsilon_t'' = 0.01$. An important result from this figure is that in films with thickness larger than $d/\lambda = 0.1$ increasing anisotropy (larger $|\varepsilon_t|$) will boost FIE. This can

be simply understood from equation (7.7) in which numerator increases with ε_t. Importantly, from Fig. 7.4(b) we observe also that very thin films (e.g., $d/\lambda = 0.01$) can provide high FIE almost independently of $|\varepsilon_t|$. Indeed, FIE is inversely proportional to the thickness and for the IENZ case it is readily explained by simplifying equation (7.6) for $d \to 0$ and using $\cos(-ik_1 d\sin\theta) \approx 1$ and $\sin(-ik_1 d\sin\theta) \approx -ik_1 d\sin\theta$ that leads to

$$\mathrm{FIE}_{\mathrm{IENZ}} \approx \left| \frac{2\cos\theta}{-ik_1 d\sin\theta} \right| \tag{7.8}$$

The presence of d at the denominator explains the mentioned behavior.

We consider an example of a LENZ case obtained from a multilayer structure in Fig. 7.5(a) and compare it to a IENZ case. The multilayer structure is made of alternate layers, of equal thickness, of silver with permittivity described using Drude model given in [9] and alumina with permittivity taken from [14]. We assume thicknesses small enough such that the homogenization model is valid. LENZ condition for this homogenized structure happens at f_0 = 974 THz in which [using effective medium approximation (EMA)] $\varepsilon_z = i0.044$ and $\varepsilon_t = 1.62 + i0.011$. In Fig. 7.5(b) we compare the FIE of this structure with bulk silver at its ENZ frequency at at $f_0 = 962\ \mathrm{THz}$ with $\varepsilon = i0.022$. Films have thicknesses $d = \lambda/3$. As it can be seen, not only FIE for the multilayer (LENZ) is higher for all angles of incidence than bulk silver (IENZ) but also its maximum is 6 folds of that of the IENZ, even when $\mathrm{Im}(\varepsilon_z)$ is twice $\mathrm{Im}(\varepsilon)$ of the IENZ. We also provided the FIE calculated via the transfer-matrix method (TMM) alternating five layers of silver (in its ENZ frequency with $\varepsilon = i0.022$) and five of silica,

all with thicknesses $\lambda/30$. The FIE just below the top surface of the top layer (silver) is even higher than that in the homogenized LENZ.

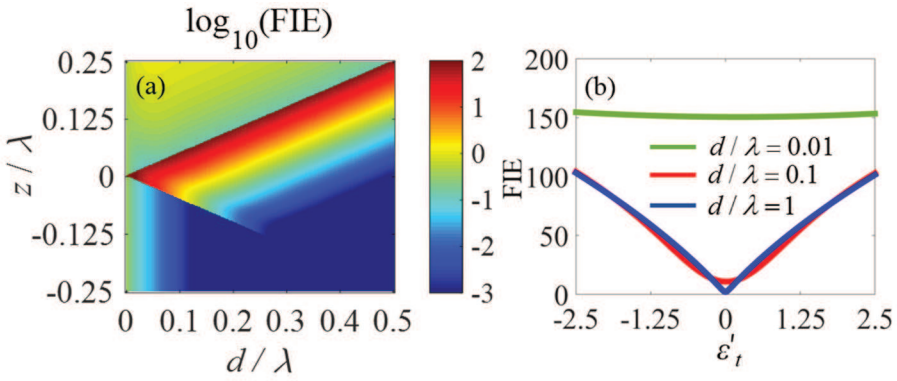

Fig. 7.4 FIE for $\theta = 40^{o}$ and $\varepsilon_t'' = \varepsilon_z'' = 0.035$ and $\varepsilon_z' = 0.001$ (a) in the film profile for $\varepsilon_t' = 2.5$ and (b) as a function of ε_t' for various thicknesses, $d = \lambda$ (blue), $d = 0.1\lambda$ (red) and $d = 0.01\lambda$ (green), at $z = (d/2)^{-}$.

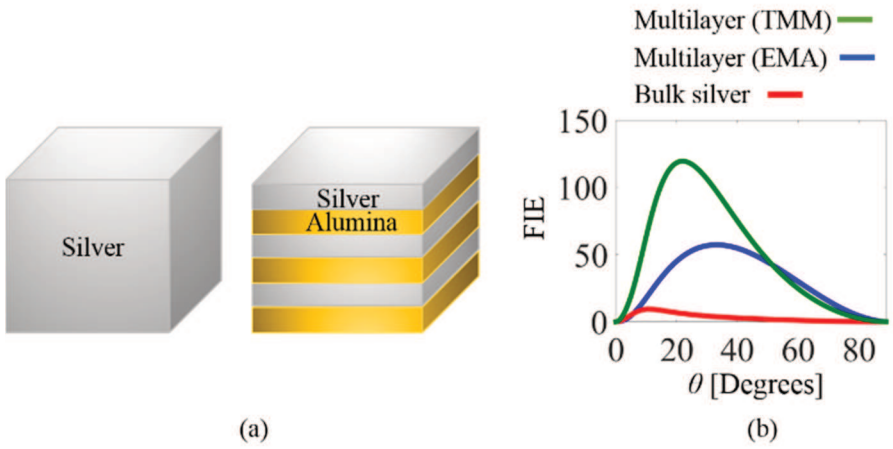

Fig. 7.5 (a) LENZ design based on multilayer structure of silver and alumina compared to bulk silver. (b) FIE versus angle of incidence for homogenized LENZ with $\varepsilon_z = i0.044$ and $\varepsilon_t = 1.62 + i0.011$ and IENZ case with $\varepsilon = i0.022$. The FIE in the top layer using the TMM is also shown, showing even higher FIE.

Sec. 7.4 Radiative Emission Enhancement of an Impressed Dipole in LENZ

Giant *z*-polarized E-field enhancement inside the film for a wide range of angles of incidence in LENZ also implies, via the reciprocity theorem, that, a *z*-polarized dipole located at the E-field hotspot in a LENZ film radiates *very strong far-fields over a wide angular region*. With this in mind, we next investigate the capability of LENZ films to enhance a dipole radiation emission. The main parameter we are interested in is the radiative emission enhancement, REE, defined as

$$\mathrm{REE} = P_{\mathrm{rad}} / P_{\mathrm{fs}} \tag{7.9}$$

where P_{rad} is the amount of power radiated by a dipole inside the anisotropic film (in both vacuum half-spaces) and P_{fs} is the total power emitted by the same dipole in free space. P_{rad} does not account for the power emitted by that dipole which is then dissipated as loss in the LENZ film. In Fig. 7.6, REE of a *z*-polarized dipole inside the LENZ film with thickness $d = \lambda / 3$ at an infinitesimal distance from the top surface is plotted versus ε_t' and ε_z' for the lossless case in (a) and when $\varepsilon_t'' = \varepsilon_z'' = 0.01$ in (b). We observe that regardless of the sign of ε_z', when it is small, REE is large. Moreover REE increases as ε_t' increases in absolute value. In the lossless case, the REE is maximized when $\varepsilon_t' < 0$ and $\varepsilon_z' > 0$ or $\varepsilon_t' > 0$ and $\varepsilon_z' < 0$, however when losses are introduced, this behavior is less pronounced.

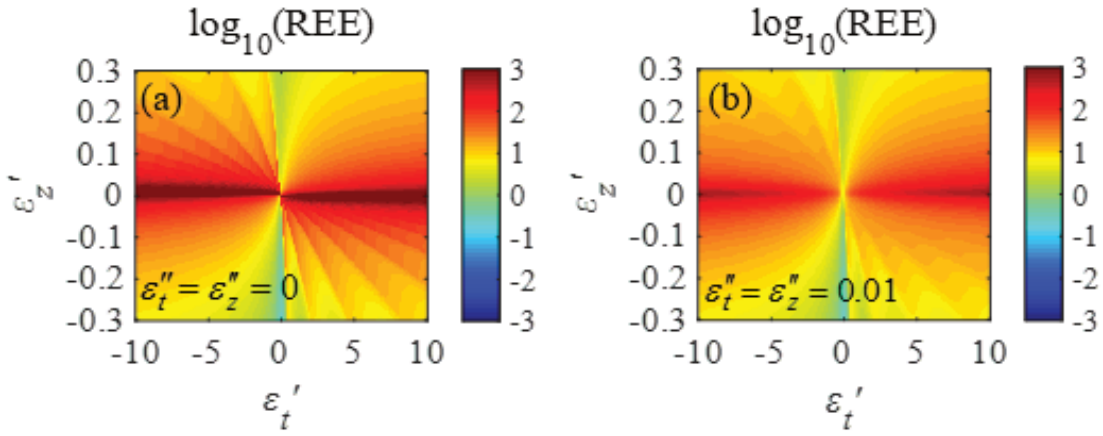

Fig. 7.6 REE, the radiative emission enhancement, versus ε_t' and ε_z' when a z-polarized dipole is right below the top surface of a LENZ film of thickness $d = \lambda/3$, (a) for the lossless case (the color legend is saturated for values more than 1000) and (b) for a lossy case with $\varepsilon_t'' = \varepsilon_z'' = 0.01$.

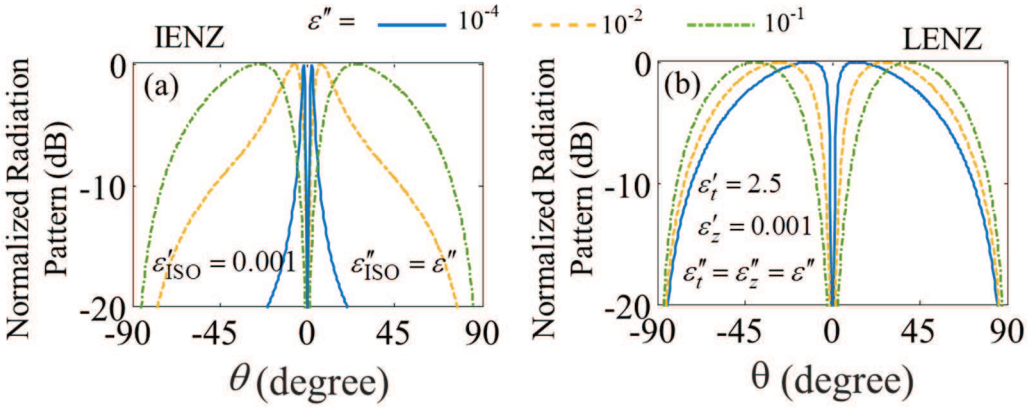

Fig. 7.7 The normalized radiation pattern in dB (a) for the IENZ case and (b) for the LENZ case with a film thickness of $d = \lambda/3$ in both cases for various values of imaginary part of permittivities.

A main difference between the radiation from the *z*-polarized dipole in an LENZ film and that in an IENZ film arises in the radiation patterns. In Fig. 7.7(a) and (b), the normalized radiation patterns of the dipole in IENZ and LENZ, respectively, are provided for various loss levels. IENZ case represents a very sharp radiation peak when loss is very low. On the other hand LENZ leads to a much wider beam than IENZ even in the extremely low loss case which

relates to its superior REE performance, as it leads to intense radiation over a wide solid angle. The pattern in both IENZ and LENZ cases gradually gets less directive and the radiation peak moves away from the bore side as losses increase. Dipoles in LENZ films radiate over a wider angular region than in IENZ fields and are thus suitable for boosting the power through radiative emission, i.e. far-field radiation, of dipolar emitters.

Sec. 7.5 Conclusion

In conclusion, we have investigated the ability of LENZ films for electric field enhancement in proximity of the film interface and demonstrated its superiority over IENZ. We have showed that for the same level of loss, LENZ gives much higher FIE than IENZ and also it occurs for a wider range of angles of incidence compared to the IENZ, while being also less sensitive to the thickness of the film than the IENZ case. Finally, radiative emission in LENZ is higher than in IENZ films.

Acknowledgment

M.K, C.G and F.C gratefully acknowledge support from the National Science Foundation, NSF-SNM-1449397.

References

[1] G. Subramania, A. J. Fischer, and T. S. Luk, "Optical properties of metal-dielectric based epsilon near zero metamaterials," *Appl. Phys. Lett.*, vol. 101, no. 24, p. 241107, Dec. 2012.

[2] S. Campione, M. Albani, and F. Capolino, "Complex modes and near-zero permittivity in 3D arrays of plasmonic nanoshells: loss compensation using gain [Invited]," *Opt. Mater. Express*, vol. 1, no. 6, p. 1077, Oct. 2011.

[3] A. Alù and N. Engheta, "Boosting Molecular Fluorescence with a Plasmonic Nanolauncher," *Phys. Rev. Lett.*, vol. 103, no. 4, p. 43902, Jul. 2009.

[4] A. Alù, M. G. Silveirinha, A. Salandrino, and N. Engheta, "Epsilon-near-zero metamaterials and electromagnetic sources: Tailoring the radiation phase pattern," *Phys. Rev. B*, vol. 75, no. 15, p. 155410, Apr. 2007.

[5] G. Lovat, P. Burghignoli, F. Capolino, D. R. Jackson, and D. R. Wilton, "Analysis of directive radiation from a line source in a metamaterial slab with low permittivity," *IEEE Trans. Antennas Propag.*, vol. 54, no. 3, pp. 1017–1030, Mar. 2006.

[6] G. Lovat, P. Burghignoli, F. Capolino, and D. R. Jackson, "High directivity in low-permittivity metamaterial slabs: Ray-optic vs. leaky-wave models," *Microw. Opt. Technol. Lett.*, vol. 48, no. 12, pp. 2542–2548, Dec. 2006.

[7] G. Lovat, P. Burghignoli, F. Capolino, and D. R. Jackson, "Combinations of low/high permittivity and/or permeability substrates for highly directive planar metamaterial antennas," *Antennas Propag. IET Microw.*, vol. 1, no. 1, pp. 177–183, Feb. 2007.

[8] B. Edwards, A. Alù, M. E. Young, M. Silveirinha, and N. Engheta, "Experimental Verification of Epsilon-Near-Zero Metamaterial Coupling and Energy Squeezing Using a Microwave Waveguide," *Phys. Rev. Lett.*, vol. 100, no. 3, p. 33903, Jan. 2008.

[9] S. Campione, D. de Ceglia, M. A. Vincenti, M. Scalora, and F. Capolino, "Electric field enhancement in $\ensuremath{\varepsilon}$-near-zero slabs under TM-polarized oblique incidence," *Phys. Rev. B*, vol. 87, no. 3, p. 35120, Jan. 2013.

[10] T. S. Luk *et al.*, "Enhanced third harmonic generation from the epsilon-near-zero modes of ultrathin films," *Appl. Phys. Lett.*, vol. 106, no. 15, p. 151103, Apr. 2015.

[11] M. A. Vincenti, S. Campione, D. de Ceglia, F. Capolino, and M. Scalora, "Gain-assisted harmonic generation in near-zero permittivity metamaterials made of plasmonic nanoshells," *New J. Phys.*, vol. 14, no. 10, p. 103016, 2012.

[12] D. de Ceglia, S. Campione, M. A. Vincenti, F. Capolino, and M. Scalora, "Low-damping epsilon-near-zero slabs: Nonlinear and nonlocal optical properties," *Phys. Rev. B*, vol. 87, no. 15, p. 155140, Apr. 2013.

[13] C. Argyropoulos, P.-Y. Chen, G. D'Aguanno, N. Engheta, and A. Alù, "Boosting optical nonlinearities in $\ensuremath{\epsilon}$-near-zero plasmonic channels," *Phys. Rev. B*, vol. 85, no. 4, p. 45129, Jan. 2012.

[14] "CRC Handbook of Laser Science and Technology Supplement 2: Optical Materials," *CRC Press*, 28-Dec-1994. [Online]. Available: https://www.crcpress.com/CRC-Handbook-of-Laser-Science-and-Technology-Supplement-2-Optical-Materials/Weber/p/book/9780849335075. [Accessed: 17-Sep-2016].

CHAPTER 8

ENHANCING MAGNETIC FIELD-MATTER INTERACTIONS

Sec. 8.1 Motivation

Natural magnetism at optical frequencies is rather weak when compared to electric response of matter [1]. Indeed, optical spectroscopy and microscopy systems mainly work based on electric dipolar transitions in matter rather than their magnetic counterparts. On the other hand, even though natural optical magnetism vanishes, metamaterials with equivalent magnetic dipolar responses have been widely studied in the past decade. For example, arrays of magnetic meta atoms are employed in engineering bulk effective permeability [2]–[7]. Several studies have been devoted to generating artificial magnetism (i.e., effective relative permeability different from unity) for such structures leading to effective permeability engineering. However, artificial magnetism for magnetic near-field enhancement is a rather newer subject of research and its application to boost the weak natural magnetism in matter at the short wavelength range of the electromagnetic spectrum for microscopy applications is rather unexplored yet.

The building blocks of metamaterials are scatterers that possess scattering modes modeled via multipolar expansion. The magnetic dipolar term in the scattering multipolar expansion of such scatterers is always present alongside the electric dipolar response. Magnetic resonances in such meta atoms have been used also to generate high-quality resonances owing to the reduced radiative losses. In particular, clusters of plasmonic nanoparticles such as the spherical constellations [8]–[10] have been suggested to generate effective bulk permeability when arranged in array configuration. Also circular clusters of

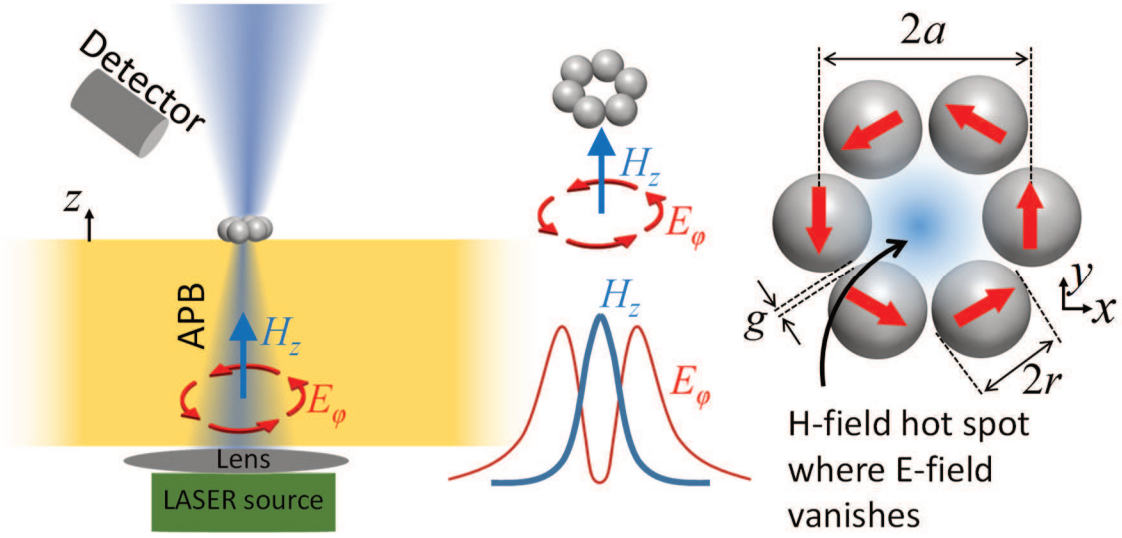

Fig. 8.1 Illustration of the exemplary setup in which generation of a large magnetic to electric field contrast could be beneficial in detection of (or interaction with) a weakly magnetic response of a matter sample placed at the center of the cluster. The nanoantenna studied here, called magnetic nanoprobe, is made of a resonating circular cluster excited by an APB with longitudinal magnetic field and it generates a strong magnetic field at its center

plasmonic particles, which are of interest in this chapter, have been suggested with the purpose of engineering negative effective permeability [5], for achieving Fano resonances [11]–[15], and in the quest for detectable photoinduced magnetic forces via artificial magnetism [16]. The characterization of the near-field signature of magnetic nanoprobes

may be functional in adding an extra dimension to optical spectroscopy using photoinduced force microscopy [17]. The extra dimension based on magnetic near-field signature could be provided in addition to the electric dipolar near-field signature.

The utilization of a magnetic nanoprobe for enhancing the magnetic transitions and suppressing the electric dipolar ones in matter requires: (i) excitation of the magnetic mode of the nanoprobe leading to enhanced magnetic near field, (ii) suppressing the electric near field where magnetic field is enhanced. To help in the latter magnetic to electric field contrast aspect, symmetry in the magnetic nanoprobe and in its excitation plays an important role as we show in this chapter. This entails the suppression of the electric dipolar mode and the rest of the higher order electric multipoles in the magnetic nanoprobe. In the quest of selective excitation of the magnetic dipolar mode of the nanoprobe, we turn our attention to vector beams with cylindrical symmetry, so-called cylindrical vector beams [18]–[21], which have been proved to be experimentally functional in the selective excitation of Mie resonances in dense dielectric particles [22], [23]. Cylindrically symmetric vector beams with spatially-dependent electric field vectors, namely radially [18]–[21], [24]–[28] and azimuthally [18]–[21], [29]–[32] polarized vector beams, have been thoroughly investigated specially under tight focusing [24], [27]. A particular cylindrically symmetric vector beam category useful for selective excitation of the magnetic dipolar moment is the azimuthally electric polarized vector beams which hosts a strong longitudinal magnetic field along the beam axis where electric field vanishes [29]–[33]. In the following, we call such beams simply as *azimuthally polarized beam (APB)* referring to the local orientation of their vector electric field. An APB does not only have the capability to selectively excite the magnetic dipolar moment of a magnetic nanoprobe, but also to boost intensity and resolution of the

magnetic near-field scattered by a nanoprobe. Owing to the rotational symmetry of the APB and nano probe setup (Fig. 8.1), one can obtain large magnetic to electric field ratio, denoted also as local field admittance, around the magnetic nanoprobe center when aligned with the beam axis. In [32], the authors quantify electric and magnetic fields of the tightly focused APB within a region with a very large local field admittance and report that scattering by a dense dielectric nanosphere placed in the focal plane of the focused APB leads to enhanced magnetic field with resolution below the diffraction limit.

In this chapter, we elaborate on the excitation of a magnetic nanoprobe consisting of a cluster of plasmonic nanospheres which provides significant accessible area with enhanced magnetic field for placing matter samples (i.e., molecules, quantum dots, etc.). The near field of such a plasmonic nano clusters is characterized in terms of newly introduced figures of merit quantifying the magnetic and electric field enhancements and the magnetic to electric field contrast, i.e., the local field admittance. The magnetic nano cluster therefore significantly boosts the total magnetic field and increases spatial magnetic resolution. Such nano clusters when excited with an APB could be useful in boosting the magnetic dipolar transitions of materials located at the cluster's center which are in general weak and overshadowed by stronger electric dipolar transitions. The setup proposed in this chapter is depicted in Fig. 8.1 where a magnetic-dominant region with a strong magnetic field and a vanishing electric field is generated.

Sec. 8.2 Large Local Field Admittance and Enhanced Magnetic Field

In the selective excitation of the magnetic dipolar transitions with magnetic-based spectroscopic applications in mind, the main goal is to investigate the physics of magnetic

field enhancement within a region where electric field vanishes, so-called magnetic-dominant region. To this purpose we investigate a circular cluster of plasmonic nanospheres that supports a "magnetic" resonance, excited by an APB, whose electric field vanishes on the beam axis aligned with the cluster center. These kinds of nanoantennas are here called magnetic nanoprobes because they are used to enhance the magnetic near field. Several concepts developed in this chapter for a circular cluster of plasmonic nanospheres are also applicable to other kinds of magnetic nanoantennas.

We introduce some figures of merit to characterize the quality of magnetic nanoprobes and their excitation. The goal is to quantify the magnetic field enhancement and the magnetic to electric field ratio, i.e., the absolute value of local field admittance normalized by that of a plan wave $1/\eta = \sqrt{\varepsilon/\mu}$, defined as

$$F_H = \frac{\left|\mathbf{H}^{\text{tot}}(\mathbf{r})\right|}{\left|\mathbf{H}^{\text{ext}}(\mathbf{r})\right|}, \quad F_Y = \frac{\eta\left|\mathbf{H}^{\text{tot}}(\mathbf{r})\right|}{\left|\mathbf{E}^{\text{tot}}(\mathbf{r})\right|}, \tag{8.1}$$

where the superscripts "tot" and "ext" refer to the total field and external excitation field, respectively. For completeness we define also the electric field enhancement as

$$F_E = \frac{\left|\mathbf{E}^{\text{tot}}(\mathbf{r})\right|}{\left|\mathbf{E}^{\text{ext}}(\mathbf{r})\right|} \tag{8.2}$$

although in this chapter the goal is to boost only the figures of merit in (8.1). The subscripts of figures of merit *H*, *E*, and *Y* stand for magnetic field, electric field and local field admittance, respectively. In this chapter bold fonts denote phasor vector quantities with time-harmonic

convention $\exp(-i\omega t)$ where ω and t refer to real angular frequency and time, respectively. A hat "^" is used to denote unit vectors.

To have large values of figures of merit, we propose to use an APB to illuminate the magnetic nanoprobe as in Fig. 8.1. The external electric field of the APB is given by the expression

$$\begin{aligned}\mathbf{E}^{\mathrm{APB}}(\mathbf{r}) &= \frac{-i}{\sqrt{2}}\left[\frac{\hat{\mathbf{x}}+i\hat{\mathbf{y}}}{\sqrt{2}}E^{\mathrm{LG}}_{l=-1}(\mathbf{r}) - \frac{\hat{\mathbf{x}}-i\hat{\mathbf{y}}}{\sqrt{2}}E^{\mathrm{LG}}_{l=+1}(\mathbf{r})\right] = \\ &= \hat{\boldsymbol{\varphi}}E^{\mathrm{APB}}_{\varphi} = \hat{\boldsymbol{\varphi}}E^{\mathrm{LG}}_{l=\pm 1}e^{\mp i\varphi}\end{aligned} \tag{8.3}$$

where E^{LG}_{l} is the field expression of a Laguerre-Gaussian beam with orbital angular momentum (OAM) order of l, and radial mode number p = 0 that propagates in the +z direction. Note that the choice of + or - sign in (8.3) is irrelevant. The APB ideally does not possess longitudinal electric field anywhere, while possessing a longitudinal magnetic field that reaches its maximum on the beam axis. On the beam axis, for symmetry reasons, there are no transverse electric and transverse magnetic fields [30]. Note that Laguerre-Gaussian beams are solutions to the wave equation under paraxial approximation [34]. The expression of the Laguerre-Gaussian mode with OAM order[30] $l=\pm 1$ and radial order $p=0$ is

$$\begin{aligned}&E^{\mathrm{LG}}_{l=\pm 1}(\mathbf{r}) = V\frac{2\rho}{\sqrt{\pi}w^2}e^{-\left(\frac{\rho}{w}\right)^2\zeta}e^{-2i\tan^{-1}\left(\frac{z}{z_R}\right)}e^{\pm il\varphi}e^{ikz} \\ &w = w_0\sqrt{1+\left(\frac{z}{z_R}\right)^2}, \quad \zeta = \left(1-i\frac{z}{z_R}\right)\end{aligned} \tag{8.4}$$

where $\rho = \sqrt{x^2 + y^2}$ and φ are the cylindrical coordinates, $k = 2\pi / \lambda$ and λ are the wavenumber and wavelength in the host medium, w_0 is the beam parameter and represents the spatial extent of the beam at $z = 0$ that is the beam's minimum-waist plane, and the Rayleigh range is defined as $z_R = \pi w_0^2 / \lambda$. Note that at any given *z*, the azimuthal electric field is maximum at the radius $\rho = \rho_M$ where $\rho_M = w / \sqrt{2}$ [32], and its maximum value is equal to

$$\left| E_\varphi^{\mathrm{APB}}(\rho_M, z) \right| = |V| \frac{2\rho}{\sqrt{\pi} w^2} e^{-\left(\frac{\rho}{w}\right)^2} \Bigg|_{\rho=\rho_M} = |V| \frac{1}{w} \sqrt{\frac{2}{\pi e}} \tag{8.5}$$

The magnetic field of the APB is then calculated via $\mathbf{H} = \nabla \times \mathbf{E} / (i\omega\mu)$ with the electric field of the APB given in Eq. (8.3). The *z* component of the magnetic field is

$$H_z^{\mathrm{APB}} = \frac{V}{\eta} \frac{-2i}{\sqrt{\pi^3}} \frac{\lambda}{w^2} e^{-\left(\frac{\rho}{w}\right)^2 \zeta} e^{-2i \tan^{-1}\left(\frac{z}{z_R}\right)} e^{ikz} \left(1 - \frac{\rho^2}{w^2} \zeta\right) \tag{8.6}$$

which is not only nonzero on the beam axis ($\rho = 0$) but also reaches its maximum magnitude

$$\left| H_z^{\mathrm{APB}}(\rho = 0) \right| = \frac{|V|}{\eta} \frac{2}{\sqrt{\pi^3}} \frac{\lambda}{w^2} \tag{8.7}$$

Here note that the maximum electric field magnitude is inversely proportional to *w* whereas the maximum longitudinal magnetic field is inversely proportional to w^2. Therefore, when keeping the power in the APB constant, one can boost maximum magnetic field relatively more than the maximum electric field by focusing the beam to tighter spots. Note that APB

excitation ideally provides a $F_Y \to \infty$ on the beam axis, hence it is ideal for obtaining regions with large local field admittance. The radial magnetic field is accordingly found as

$$H_\rho^{\mathrm{APB}} = -\frac{1}{\eta} E_\varphi^{\mathrm{APB}} \left[1 + \frac{1}{kz_R} \frac{\rho^2 - 2w_0^2}{w^2} \right] \tag{8.8}$$

It is observed that when $kz_R >> 1$ the radially polarized magnetic field component follows mainly the same intensity profile as the azimuthally polarized electric field. For very tight beams, however, the second term inside the brackets in (8.8) becomes non negligible, and a slight difference between the intensity profiles of H_ρ^{APB} and E_φ^{APB} starts to appear. The formula of the power of the APB, *P*, as a function of *V* and w_0 / λ is given in Appendix.

Next we emphasize the relative increase of the longitudinal magnetic field of an APB and its resolution as w_0 decreases. In Fig. 8.2 all the field components of APBs with $w_0 = \lambda$ and $w_0 = 0.5\lambda$ are reported, keeping the power carried in the beams constant and equal to 1 mW. We observe that the longitudinal magnetic field is boosted relatively more than the transverse magnetic and electric field components when the beam is tighter, i.e., when w_0 decreases. Therefore, just using an APB with a tighter spot is on its own an intriguing way to boost the magnetic field, the magnetic field resolution and the figure of merit F_Y. Moreover, in the following we will analytically prove that a magnetically polarizable cluster further enhances the magnetic field at its center, almost independently of the beam parameter of the incident APB.

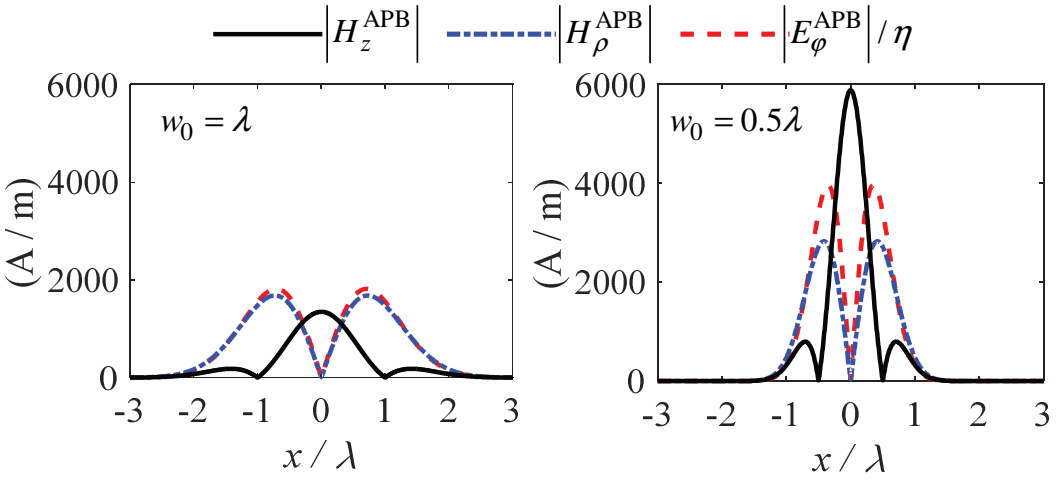

Fig. 8.2 Field profiles of an APB in vacuum with two different beam parameters, $w_0 = \lambda$ and $w_0 = 0.5\lambda$ at $\lambda = 632$ nm keeping the power in the beam constant and equal to 1 mW (i.e., with $V = 0.972$ V for $w_0 = \lambda$ and $V = 0.891$ V for $w_0 = 0.5\lambda$). Longitudinal magnetic field H_z^{APB} is boosted in tight beams (i.e., with small beam parameter w_0).

We define a figure of longitudinal magnetic field at the minimum waist (i.e., at $z = 0$), quantifies the magnetic field strength independent of the power of the beam. It is equal to the longitudinal magnetic field of an APB normalized by the magnetic field of a plane wave whose power intensity is equal to the power of the APB divided by an area λ^2

$$h_z = |H_z| / \sqrt{\frac{2P}{\eta\lambda^2}} \tag{8.9}$$

where P is the power in the APB which possesses the longitudinal magnetic field H_z. The figure h_z, evaluated at the minimum waist is only a function of w_0 / λ and its explicit formula is provided in Appendix. In Fig. 8.3, we report such figure of magnetic field and it clearly shows that the magnetic field of an APB is significantly boosted as the beam parameter decreases, especially when $w_0 < \lambda$.

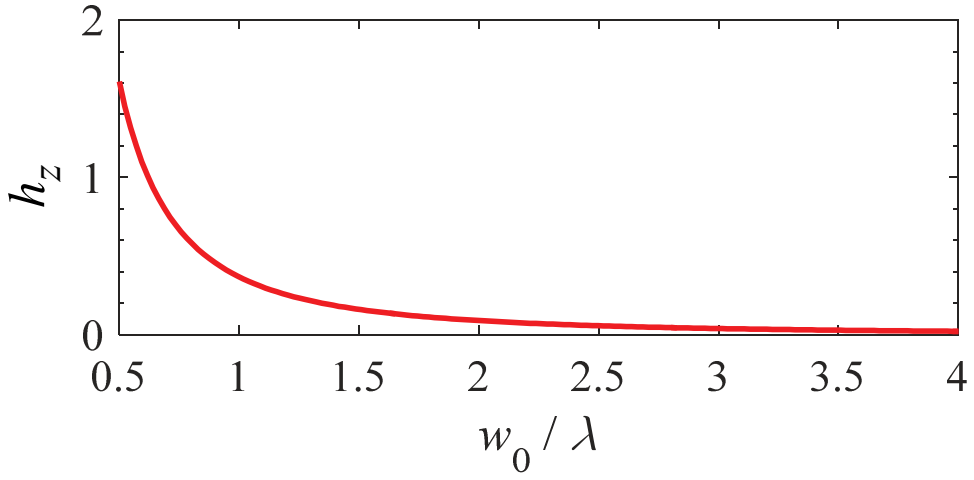

Fig. 8.3 The nondimensional figure of longitudinal magnetic field defined in (8.9).

In the following, we introduce the analytical equations used in the single dipole approximation (SDA) calculations for quantifying the two main figures of merit in (8.1), the magnetic field enhancement and the normalized absolute local field admittance, and then explain the physics behind the capability of the cluster for boosting these two figures of merit. Note that in our characterization of the cluster under APB illumination, we put special emphasis on the magnetic field enhancement, i.e., on F_H, achieved in the presence of the ring cluster as a way of boosting natural magnetism, rather than the cluster's magnetic polarizability as done in several previous publications [15].

Sec. 8.3 Analytical Model of Cluster Scattering

We briefly summarize the analytical model utilized in solving a scattering problem where a cluster made of electrically polarizable *plasmonic* nanospheres in homogeneous free space, vacuum, is excited by an external field. For comparison we also consider external field such as a single plane wave and a superposition of two plane waves.

The nano cluster is made of N plasmonic particles at positions $\mathbf{r}_n$, displaced in the x-y plane (Fig. 8.1). For simplicity we assume that each particle is a nanosphere modeled by a scalar (isotropic) electrical polarizability α_n where $n \in \{1,\ldots,N\}$. The local electric field exciting the n^{th} particle is evaluated as

$$\mathbf{E}^{\text{loc}}(\mathbf{r}_n) = \mathbf{E}^{\text{ext}}(\mathbf{r}_n) + \sum_{\substack{m=1 \\ m\neq n}}^{N} \underline{\mathbf{G}}_{Ep}(\mathbf{r}_n, \mathbf{r}_m) \cdot \mathbf{p}_m \tag{8.10}$$

where the superscript 'ext' denotes the external excitation (i.e., the illuminating APB) and $\underline{\mathbf{G}}_{Ep}(\mathbf{r}_n, \mathbf{r}_m)$ is the dyadic Green's function that gives the electric field at $\mathbf{r}_n$ generated by the electric dipole $\mathbf{p}_m$ at $\mathbf{r}_m$, and here we use the fully dynamic and exact expression in Chapter 8 of [35]. Each nanosphere's electric dipole moment is evaluated via the Mie polarizability of the nanosphere and the local field at the nanosphere's center as $\mathbf{p}_n = \alpha_n \mathbf{E}^{\text{loc}}(\mathbf{r}_n)$, where the local field is the sum of the external field and the field scattered by all the other nanospheres. Thus (8.10) is rewritten in terms of the unknown electric dipole moments as

$$\mathbf{p}_n - \alpha_n \sum_{\substack{m=1 \\ m\neq n}}^{N} \underline{\mathbf{G}}_{Ep}(\mathbf{r}_n, \mathbf{r}_m) \cdot \mathbf{p}_m = \alpha_n \mathbf{E}^{\text{ext}}(\mathbf{r}_n) \tag{8.11}$$

By writing (8.11) for n = 1, …, N, we construct a linear system of N equations as

$$[A] \begin{bmatrix} \mathbf{p}_1 \\ \vdots \\ \mathbf{p}_N \end{bmatrix} = \begin{bmatrix} \alpha_1 \mathbf{E}^{\text{ext}}(\mathbf{r}_1) \\ \vdots \\ \alpha_N \mathbf{E}^{\text{ext}}(\mathbf{r}_N) \end{bmatrix} \tag{8.12}$$

where $[A]$ is a $3N \times 3N$ matrix made of 3×3 sub-blocks $\underline{\mathbf{A}}_{nm}$ with $n,m \in \{1,\ldots,N\}$ that are given by

$$\underline{\mathbf{A}}_{nm} = \begin{cases} \underline{\mathbf{I}} \text{ when } m = n \\ -\alpha_n \underline{\mathbf{G}}_{Ep}(\mathbf{r}_n, \mathbf{r}_m) \text{ otherwise} \end{cases} \tag{8.13}$$

where $\underline{\mathbf{I}}$ is the 3×3 identity matrix. The system of linear equations in (8.12) is solved for the electric dipole moments under external excitation. Subsequently the electric and magnetic fields scattered by the cluster are evaluated using the fully dynamic and exact dyadic Green's functions $\underline{\mathbf{G}}_{Hp}$ (Section 2.3 in [36]) and $\underline{\mathbf{G}}_{Ep}$ which provide the magnetic and electric fields due to an electric dipole, respectively. The total electric and magnetic fields at an observation point $\mathbf{r}$ are evaluated as

$$\begin{aligned} \mathbf{E}^{\text{tot}}(\mathbf{r}) &= \mathbf{E}^{\text{ext}}(\mathbf{r}) + \sum_{n=1}^{N} \underline{\mathbf{G}}_{Ep}(\mathbf{r}, \mathbf{r}_n) \cdot \mathbf{p}_n, \\ \mathbf{H}^{\text{tot}}(\mathbf{r}) &= \mathbf{H}^{\text{ext}}(\mathbf{r}) + \sum_{n=1}^{N} \underline{\mathbf{G}}_{Hp}(\mathbf{r}, \mathbf{r}_n) \cdot \mathbf{p}_n. \end{aligned} \tag{8.14}$$

For simplicity, in the following section (Sec. 8.4) we assume that all nanospheres are identical and we drop the subscript *n* in the polarizability symbol.

Sec. 8.4 Physics of Cluster Azimuthal Excitation, Resonance, and Field Enhancement

A cluster made of plasmonic nanospheres offers a large degree of flexibility in tuning the magnetic resonance wavelength. In general, we define the *real* magnetic resonance wavelength as the wavelength at which the magnitude of the magnetic dipole moment of the cluster under a time harmonic field peaks. The magnetic dipole moment of the cluster as in Fig. 8.1 is defined as

$$\mathbf{m} = \frac{i\omega}{2}\sum_{n=1}^{N}\mathbf{r}_n \times \mathbf{p}_n \tag{8.15}$$

The cluster has the significant cross-sectional area only on the plane normal to the *z* axis, i.e. the main magnetic moment of the cluster will be aligned along *z* under various types of excitations. The magnetic moment of the cluster is proportional to the local magnetic field (assumed not varying significantly over the cluster area). Therefore we define the magnetic polarizability of the cluster as a way of modeling its magnetic response. The magnetic polarizability is in general represented as a tensor, however here we are interested in the *z*-directed magnetic moment induced by the *z*-component of the external magnetic field (i.e., an APB with strong longitudinal magnetic field along its propagation axis *z*). Accordingly, the magnetic polarizability of the cluster centered at the origin is

$$\alpha_{zz}^{mm} = \frac{m_z}{H_z^{\text{ext}}(\mathbf{r}=\mathbf{0})} \tag{8.16}$$

Due to symmetry, the magnetic dipole moment is generated by circulating electric dipolar moments (Fig. 8.1), which are excited by an APB. The cluster in Fig. 8.1 is made of nanospheres equally spaced on a perfect circle with the cluster radius $a = (2r+g)/\left[2\sin(\pi/N)\right]$ where *r* is the nanosphere radius and *g* is the inter-nanosphere gap distance. The cluster is excited by an ideal APB whose electric field E_φ^{APB} is purely azimuthal, i.e., transverse to *z* and along the φ direction. Under rotational symmetry, all the induced electric dipole moments are polarized azimuthally and equal in magnitude given by

$$p_\varphi = \frac{\alpha E_\varphi^{\mathrm{APB}}\left(\rho = a\right)}{1 - \alpha \sum_{n=2}^{N} \hat{\boldsymbol{\varphi}}_1 \cdot \underline{\mathbf{G}}_{Ep}\left(\mathbf{r}_0, \mathbf{r}_n\right) \cdot \hat{\boldsymbol{\varphi}}_n} \tag{8.17}$$

where $\hat{\boldsymbol{\varphi}}_n = -\sin\left[\left(n-1\right)\delta\right]\hat{\mathbf{x}} + \cos\left[\left(n-1\right)\delta\right]\hat{\mathbf{y}}$ with $\delta = 2\pi / N$. In the following the denominator in (8.17) is called

$$D = 1 - \alpha \sum_{n=2}^{N} \hat{\boldsymbol{\varphi}}_1 \cdot \underline{\mathbf{G}}_{Ep}\left(\mathbf{r}_1, \mathbf{r}_n\right) \cdot \hat{\boldsymbol{\varphi}}_n \tag{8.18}$$

and it reaches its minimum absolute value at the "magnetic" resonance.

Since the electric dipole moments and the position vectors ($\mathbf{p}_n$ and $\mathbf{r}_n$) lie on the same plane (orthogonal to *z*) the magnetic dipole moment of the cluster would be purely in the *z* direction based on (8.15). This leads to an equivalent cluster magnetic dipole moment and the magnetic cluster polarizability as

$$m_z = N \frac{i\omega}{2} a p_\varphi, \qquad \alpha_{zz}^{mm} = N \frac{i\omega}{2} a \frac{p_\varphi}{H_z^{\mathrm{APB}}\left(\mathbf{0}\right)} \tag{8.19}$$

By substituting (8.17) in (8.19), the cluster magnetic polarizability (v16) is found as

$$\alpha_{zz}^{mm} = N \frac{i\omega}{2} a \frac{\alpha}{D} \frac{E_\varphi^{\mathrm{APB}}\left(\rho = a, z = 0\right)}{H_z^{\mathrm{APB}}\left(\mathbf{0}\right)} \tag{8.20}$$

The $E_\varphi^{\mathrm{APB}} / H_z^{\mathrm{APB}}$ field ratio is found by looking at (8.3) and (8.6):

$$\frac{E_{\varphi}^{\mathrm{APB}}(\rho,z)}{H_z^{\mathrm{APB}}(\rho=0,z)}=\eta\frac{\pi\sqrt{2}}{2}\frac{\rho}{\lambda}e^{-\left(\frac{\rho}{w}\right)^2\xi},$$
$$\frac{E_{\varphi}^{\mathrm{APB}}(\rho=a,z=0)}{H_z^{\mathrm{APB}}(\mathbf{0})}=\eta\frac{\pi\sqrt{2}}{2}\frac{a}{\lambda}e^{-\left(\frac{a}{w_0}\right)^2}, \tag{8.21}$$

and reaches maximum when $a=\rho_M=w_0/\sqrt{2}$.

From (8.1) the longitudinal magnetic field enhancement at the cluster center is

$$F_H(\mathbf{0})=\left|\frac{H_z^{\mathrm{ext}}(\mathbf{0})+H_z^{\mathrm{scat}}(\mathbf{0})}{H_z^{\mathrm{ext}}(\mathbf{0})}\right|=\left|1+\frac{H_z^{\mathrm{scat}}(\mathbf{0})}{H_z^{\mathrm{ext}}(\mathbf{0})}\right| \tag{8.22}$$

where $H_z^{\mathrm{ext}}\equiv H_z^{\mathrm{APB}}$. The scattered magnetic field enhancement is

$$\begin{aligned}\frac{H_z^{\mathrm{scat}}(\mathbf{0})}{H_z^{\mathrm{APB}}(\mathbf{0})}&=N\frac{\omega k}{4\pi}\frac{e^{ika}}{a}\left[1+\frac{i}{ka}\right]\frac{p_{\varphi}}{H_z^{\mathrm{APB}}(\mathbf{0})}\\&=N\frac{\omega k}{4\pi}\frac{e^{ika}}{a}\left[1+\frac{i}{ka}\right]\frac{\alpha}{D}\frac{E_{\varphi}^{\mathrm{APB}}(\rho=a,z=0)}{H_z^{\mathrm{APB}}(\mathbf{0})}\end{aligned} \tag{8.23}$$

which is the most significant term in the magnetic field enhancement reported in (8.22) when maximized. In the expressions in (8.20) and (8.23) we see the common term $E_{\varphi}^{\mathrm{APB}}/H_z^{\mathrm{APB}}(\mathbf{0})$ given in (8.21).

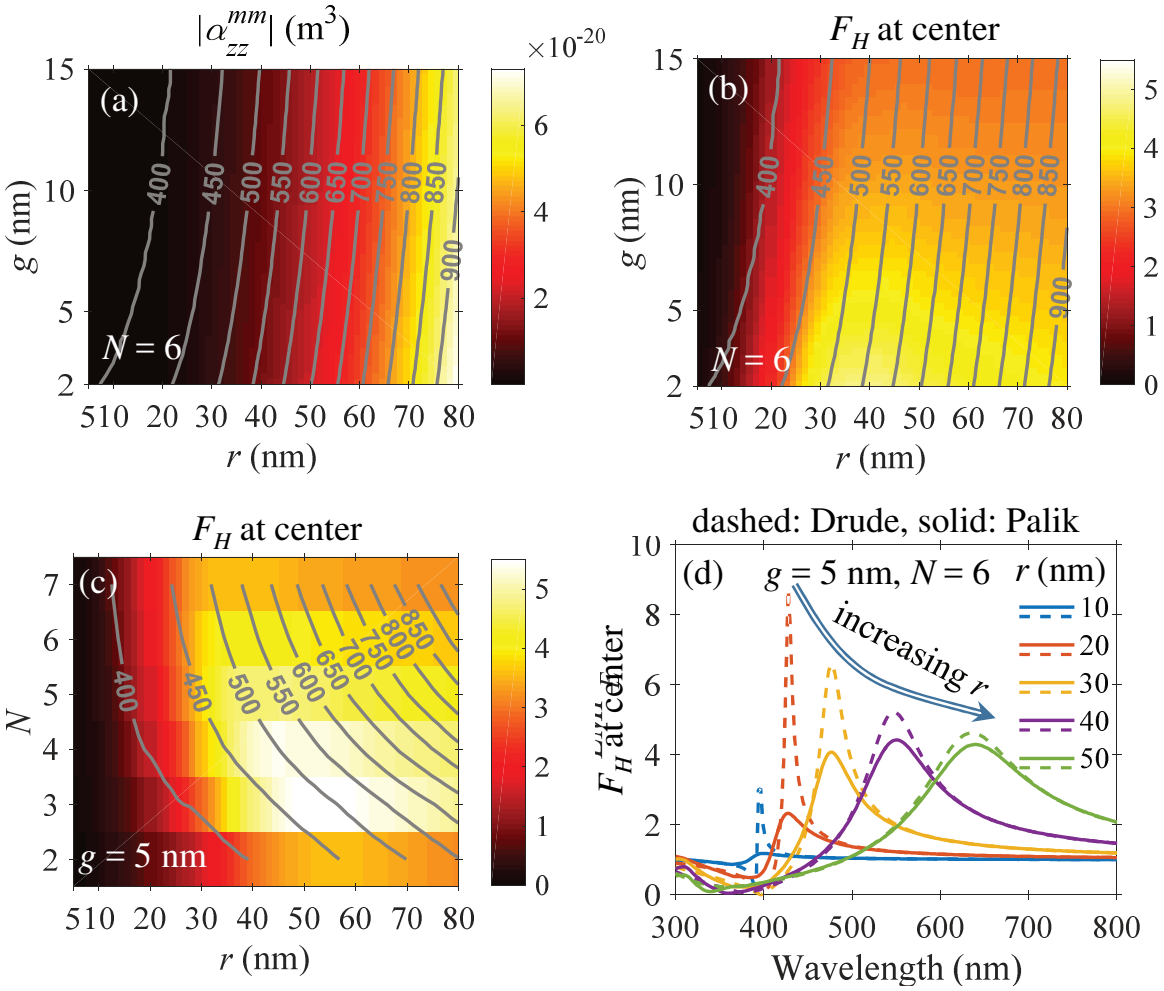

Fig. 8.4 (a) Cluster magnetic polarizability and (b) magnetic field enhancement F_H at the cluster's center (purely z-polarized owing to the symmetry of the cluster geometry and APB excitation), at the respective wavelengths where each peaks, versus nanosphere radius r and gap g between neighboring nanospheres when N = 6. (c) F_H at the wavelength where it peaks, versus N and r when gap is fixed at g = 5 nm. The superimposed iso-wavelength contours annotated with the wavelengths in nm denote the wavelength at which the reported quantity peaks. (d) F_H versus wavelength for various r and the effect of losses on the maximum magnetic field enhancement at the wavelengths where it peaks using two different silver permittivity functions, Drude's model and experimental Palik data.

The optimum cluster design that maximizes either one of the magnetic polarizability and the magnetic field enhancement does not necessarily maximize the other one. In this chapter

the main quantity of interest is not the magnetic moment or the magnetic polarizability of the cluster but rather the magnetic field enhancement in the central area of the cluster. The magnetic field enhancement at the cluster center is purely due to enhancement of the longitudinal (*z*-directed) magnetic field and we will use the figure of merit (F_H) to quantify it.

We plot in Fig. 8.4(a, b) the peak of the cluster magnetic polarizability α_{zz}^{mm} and the peak of the magnetic field enhancement F_H of a cluster made of 6 silver nanospheres excited by an APB with beam parameter $w_0 = \lambda$, versus nanosphere radius *r* and inter-sphere gap *g* using SDA model. The cluster is placed at the APB minimum waist plane (i.e, at $z = z_0$) and nanospheres' silver is described by the "Palik" permittivity function taken from [37]. The iso-wavelength contours, annotating the wavelength in nm at which these peaks occur is shown in Fig. 8.4(a-c). The colormaps are generated by calculating the peak values (that are wavelength dependent) for each pair of *g, r* or *N*, *r* parameters. Note that as the nanospheres radius increases the peak magnetic polarizability increases monotonically *in the reported range*, whereas the field enhancement peaks at a certain nanosphere radius, for each gap distance. Moreover the magnetic polarizability and magnetic field enhancement peaks occur almost at the same wavelength. As the gap *g* increases and *r* is kept constant, the peak magnetic polarizability and the peak magnetic field enhancement decreases. Therefore small gaps are important for achieving strong resonances.

In Fig. 8.4(c) the magnetic field enhancement peak is plotted versus *N*, the number of nanospheres, and nanospheres radius *r* where the inter-sphere gap is fixed at $g = 5\,\text{nm}$. Similarly, there appears to be an optimum nanosphere radius for each *N*. Also it is observed

that N = 3 or 4 lead to largest field enhancement values, however it may be preferable to use N = 6 which leads to a larger accessible area of magnetic field enhancement inside the cluster.

It is observed in Fig. 8.4(a,b) that for a specified N and when keeping r constant, the resonance wavelength decreases very *slightly* as g increases. On the other hand, when N and g are kept constant, the resonance wavelength of the cluster increases significantly as r increases. In Fig. 8.4(c) where g is fixed to 5 nm, the resonance wavelength increases notably, either with increasing r and keeping N constant or with increasing N and keeping r constant. Recalling that the cluster radius is $a = (2r + g) / \left[2\sin(\pi / N) \right]$, as either r or N gets larger the cluster radius increases. Furthermore, when $r >> g$, a becomes proportional to r as $a \approx r / \sin(\pi / N)$. Therefore, the *main* trend in Fig. 8.4(a-c) is that the resonance wavelength increases when the cluster radius a increases due to an increase of r or N.

Finally, in Fig. 8.4(d) the magnetic field enhancement versus wavelength is plotted for various nanosphere radii using the Palik permittivity function [37] (as in the other map plots in Fig. 8.4) and Drude's model [38] which underestimate losses in silver at smaller wavelength range and leads to larger magnetic field enhancement values.

The optimum magnetic field enhancement occurs at certain nanosphere radius and number of nanospheres N whereas the magnetic polarizability is monotonically increasing with the increase of nanosphere radius in the reported range. Therefore, it is apparent that different design considerations apply to maximize either magnetic field enhancement or magnetic polarizability. The cluster is equivalent to a circulating electric current as an effective magnetic dipole. The radius a of the cluster is a crucial parameter because a larger cross-sectional area of the cluster leads to a larger magnetic polarizability but not necessarily

to a larger magnetic field enhancement. Next we interpret the observations based on the analytical formulas.

The term *D* at the denominator in (8.17) [given in (8.18)] determines the resonance of the cluster, and it appears in both the magnetic polarizability (8.20) and the scattered magnetic field enhancement (8.23). These quantities are proportional to the electric polarizability α of each nanosphere which grows as $\alpha \propto r^3$. Keep in mind that as *r* increases, the cluster radius $a=(2r+g)/\left[2\sin(\pi/N)\right]$ also increases. Next, the term $E_{\varphi}^{\mathrm{APB}}(a)\big/H_z^{\mathrm{APB}}(\mathbf{0})$ in (8.21) is common for both the magnetic polarizability in (8.20) and the scattered magnetic field enhancement in (8.23). Here we emphasize that, when neglecting the signature of *D*, both α_{zz}^{mm} and $E_{\varphi}^{\mathrm{APB}}(a)\big/H_z^{\mathrm{APB}}(\mathbf{0})$ tend to grow with the cluster radius *a* (i.e., with increasing *r* or *N*), assuming that $a^2 << w_0^2$. When this assumption is not verified, the exponential function $\exp\left[-(a/w_0)^2\right]$ in the common term (8.21) limits the growth of $E_{\varphi}^{\mathrm{APB}}/H_z^{\mathrm{APB}}$. We now focus on the cluster radius that maximizes either α_{zz}^{mm} or the scattered field enhancement $H_z^{\mathrm{scat}}(\mathbf{0})/H_z^{\mathrm{APB}}(\mathbf{0})$. To do so we utilize the dimensionless ratio

$$\frac{\left|H_z^{\mathrm{scat}}(\mathbf{0})\big/H_z^{\mathrm{APB}}(\mathbf{0})\right|}{\left|\alpha_{zz}^{mm}\right|/\lambda^3}=\frac{4\pi^2}{(ka)^2}\sqrt{1+\frac{1}{(ka)^2}} \tag{8.24}$$

in order to assess the relative dependence of α_{zz}^{mm} and the scattered field enhancement on the cluster radius *a*. The ratio in (8.24) does not depend on the term *D* in (8.18) and it grows when *a* decreases. It is clear that among different resonant designs, the cluster with smaller cluster radius tends to have relatively large field enhancement compared to the absolute

magnetic polarizability normalized by λ^3. As *a* increases, the magnetic cluster polarizability grows faster than the magnetic field enhancement with an extra a^3 factor dependence when $(ka)^2 << 1$. On the other hand as *a* increases further, the term $\exp\left(-a^2 / w_0^2\right)$ causes both quantities in (8.20) and (8.23) to reach a peak and then decrease. However, α_{zz}^{mm} in (8.20) and the scattered field enhancement in (8.23) reach maximum at different cluster radii. We observe in Fig. 8.4(a,b) that when keeping *g* and *N* constant, the magnetic field enhancement F_H reaches peak value for certain *r* values in the reported range whereas the magnetic polarizability α_{zz}^{mm} grows monotonically in the reported *r* range and it is expected to reach peak value at a large *r* out of the reported range. Thus, α_{zz}^{mm} peaks at larger cluster radii than the one where F_H peaks, when *g* and *N* are kept constant.

The cluster here is seen as a current loop and this analogy helps us conceive the physics behind maximizing the magnetic field enhancement rather than the magnetic polarizability. The magnetic polarizability of a current loop is proportional to the loop area squared, thus proportional to a^4. Moreover, the current induced on a loop is proportional to the area and the incident magnetic field. Accordingly, the magnetic field at the center of a current loop is proportional to the loop current but inversely proportional to *a*, thus the magnetic field enhancement is proportional to the loop radius *a*. Eventually we observe a factor difference of a^3 in the dependences of the magnetic polarizability and the magnetic field enhancement on *a* which is in agreement with the formula in (8.24) for a cluster when $(ka)^2 << 1$.

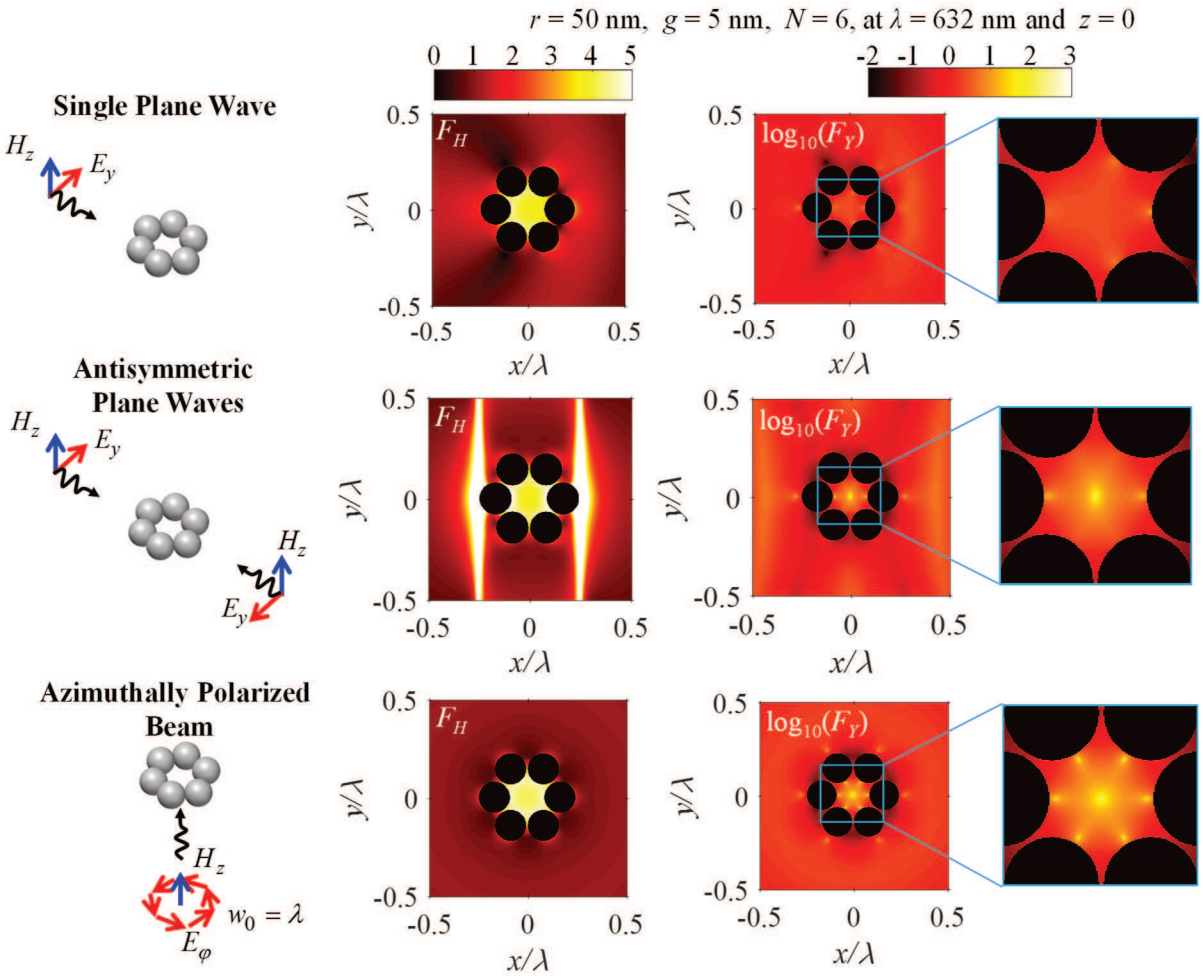

Fig. 8.5 Local magnetic field enhancement F_H (First column of plots) and normalized local field admittance F_Y (second column of plots), both evaluated on the transverse symmetry plane of the cluster for three different excitation schemes: (i) single plane-wave incidence, (ii) two antisymmetric plane-wave incidence, (iii) normally incident APB.

Having discussed the characterization of the cluster magnetic resonance and the magnetic field enhancement, in the following we stress the advantages of exciting the nano cluster with an APB compared to other possible excitation schemes. In Fig. 8.5, we compare the two figures of merit, the magnetic field enhancement F_H and the normalized absolute local field admittance F_Y, both evaluated at the cluster plane using three different excitation schemes:

(i) TE (with respect to *z*) plane wave propagating in the *x* direction, (ii) two antisymmetric plane waves propagating in +/- *x* directions, (iii) APB with $w_0 = \lambda$ whose beam axis coincides with the cluster axis (the *z* axis). The case with two plane waves has a vanishing electric field at the cluster center. All the excitation schemes excite the magnetic resonance significantly and lead to a magnetic field enhancement of about 4.2. This indicates that, under a scanning microscopy setup, the magnetic mode of the cluster would be excited sharply as the illumination beam's strong longitudinal (axial) magnetic field is aligned with the cluster center. The cluster has a dominant magnetic dipolar mode with a rather high quality factor at the reported wavelength. Therefore, the presence of the *z*-directed external magnetic field leads to a dominant magnetic dipole response which is observed for the three illumination schemes reported in Fig. 8.5. Accordingly, this justifies the similar F_H observed in all cases reported in Fig. 8.5. It is noteworthy that there are very bright vertical bands of exceptionally large F_H in Fig. 8.5 for the antisymmetric plane waves case, this is due to the standing wave pattern of the incident magnetic field, which has two nulls separated by half a wavelength. Therefore, any scattered magnetic field at these bands corresponds to *locally* huge magnetic field enhancement. Furthermore, the single plane wave case does not lead to an increased local admittance, the two plane-waves provide high local field admittance, and the APB excitation leads to the largest value and widest area of enhanced local admittance, representing a wide magnetic-dominant region. Note that even though the two antisymmetric plane-wave scheme also results in a large local field admittance in the cluster's center, it is difficult to phase synchronize these plane waves in practical cases such that their electric fields cancel out exactly at the cluster's center, whereas vanishing electric field at the cluster center is a natural property of the APB.

Sec. 8.5 Field Characteristics under Azimuthally Polarized Beam Excitation

At this point we have only plotted the characteristic field maps of the nano cluster excited by an APB with $w_0 = \lambda$. In this section, we first characterize the cluster magnetic response versus the beam parameter w_0 of the APB and then report the figures of merit at several planes, when illuminated by an APB propagating in +*z* direction as in Fig. 8.6.

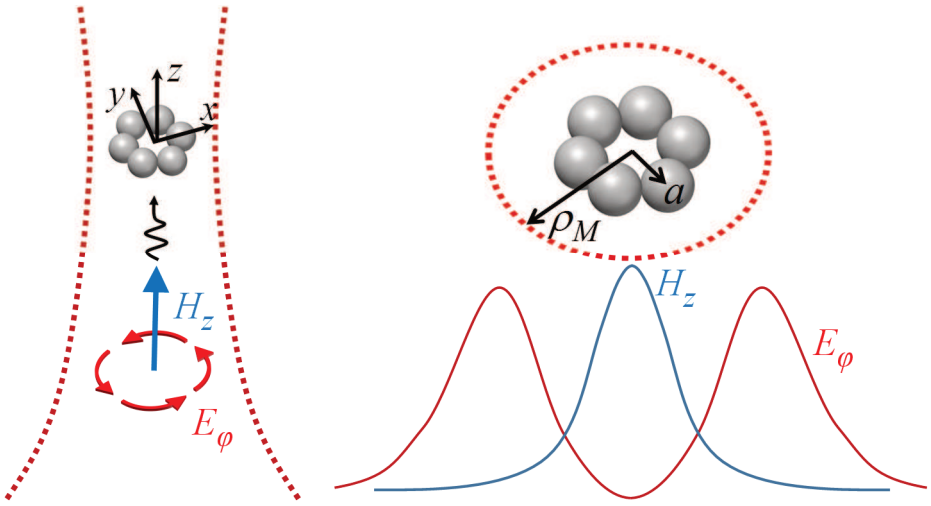

Fig. 8.6 Illustration of the cluster located at the minimum waist plane of an APB propagating in the +*z* direction. The radial distance ρ_M where the electric field is maximum is denoted by a dashed line.

In general, the figures of merit, investigated quantitatively in Sec. 8.4, depend on the beam parameter w_0 of the illuminating APB that determines also the radial location $\rho_M = w_0 / \sqrt{2}$ of the maximum of the electric field. Note that the cluster considered in this section with parameters $r = 50\,\text{nm}$, $g = 5\,\text{nm}$, $N = 6$ resonates at a wavelength of $\lambda = 632\,\text{nm}$, and its radius is $a \approx \lambda / 6$. In order to ensure that the APB electric field maximum coincides with the cluster radius, so $\rho_M = a$, the beam parameter of the APB should be $w_0 \approx 0.24\lambda$. However the field features of such an APB is beyond the diffraction limit, and cannot constitute a propagating beam as investigated in [32]. However, it is still important to assess the impact

of the beam parameter w_0, i.e. the spatial extent and amplitude distribution of the excitation field, on the magnetic field enhancement of the cluster-APB system. Therefore, we report in Fig. 8.7 the magnetic cluster polarizability α_{zz}^{mm} and the magnetic field enhancement F_H at the cluster center versus beam parameter. In both plots we observe the signature of $E_{\varphi}^{\mathrm{APB}} \big/ H_z^{\mathrm{APB}}(\mathbf{0})$ term [appearing as a function of w_0 in (8.20) and (8.23)] as a slight decrease with w_0 since the exponential term in (8.24) becomes significant. It is shown that for $w_0 > \lambda$ both quantities plotted in Fig. 8.7 saturate, and around $w_0 \approx \lambda$ the reported quantities take values close to the saturated ones. Note here that even though the APB's maximum electric field location, as illustrated in Fig. 8.6, moves farther from the cluster radius, when w_0 is increased; the magnetic field enhancement does not change significantly. Smaller w_0 indicates tighter field features that start to be comparable to the cluster size, thus the magnetic polarizability and the magnetic field enhancement decrease slightly as w_0 decreases. However, the slight decrease in the magnetic field enhancement F_H with decreasing w_0 does not mean that the APBs with tighter features should be avoided. In fact, we recall that F_H is defined in (8.1) as the ratio of the total field over the incident (external) field, and despite the slight decrease of F_H with decreasing w_0, the incident (external) magnetic field of a tighter beam is much stronger, assuming that the power of the beam is kept constant. This is easily understood by looking at the magnetic field of the incident APB in Fig. 8.2 for a tightly focused APB ($w_0 = \lambda/2$) and a weakly focused APB ($w_0 = \lambda$). It is clear from Fig. 8.2 that the incident magnetic field with $w_0 = \lambda/2$ is almost 3 times the one with

$w_0 = \lambda$, whereas in Fig. 8.7 we observe only a 10% drop in enhancement from $w_0 = \lambda$ to $w_0 = \lambda/2$. Eventually, we still stress that tighter beams lead to larger total magnetic fields. In Fig. 8.7, the sweep of w_0 is started at $w_0 = \lambda/2$ because as the beam parameter w_0 decreases to values smaller than $\lambda/2$ the plane wave spectrum of its field starts to extend over to the evanescent spectrum and these beams are no more composed of a spectrum of propagating waves and the paraxial approximation in (8.1) loses accuracy [32]. The field features throughout this chapter are calculated using an APB with $w_0 = \lambda$ which represents a self-standing beam whose field spectrum is only confined to the propagating plane-wave spectrum.

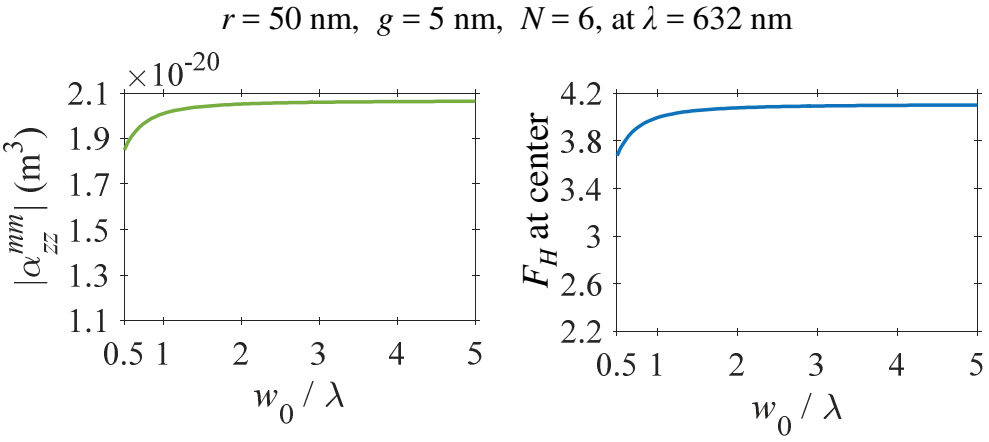

Fig. 8.7 α_{zz}^{mm} and F_H at the origin, i.e., center of the cluster, versus the beam parameter of APB.

In Fig. 8.8(a-c), we report F_H, F_E, and F_Y and then along the *x* and *y* axes at several *z*-planes, from $z = -0.5\lambda$ to $z = 0.5\lambda$ where we assume the cluster is centered at the minimum waist plane $z = 0$ and the APB is incident from below as in Fig. 8.6. It is observed that the field enhancement features are mainly confined to the cluster plane, and the normalized absolute local field admittance F_Y is maximum around the *z* axis and in contrast to the other

figures of merit, it maintains its large value at different z values. It is important to note here that F_Y ideally tends to infinity on the z axis, and is there truncated (for graphic representation) at a maximum of 10^3 (or 60 dB) in the plots. Lastly we report the magnetic field enhancement F_H along the z axis, whose maximum value occurs at $z = 0$. Importantly, we see the destructive interference signature of the incident magnetic field and the scattered one as a minimum at $z = -0.25\lambda$.

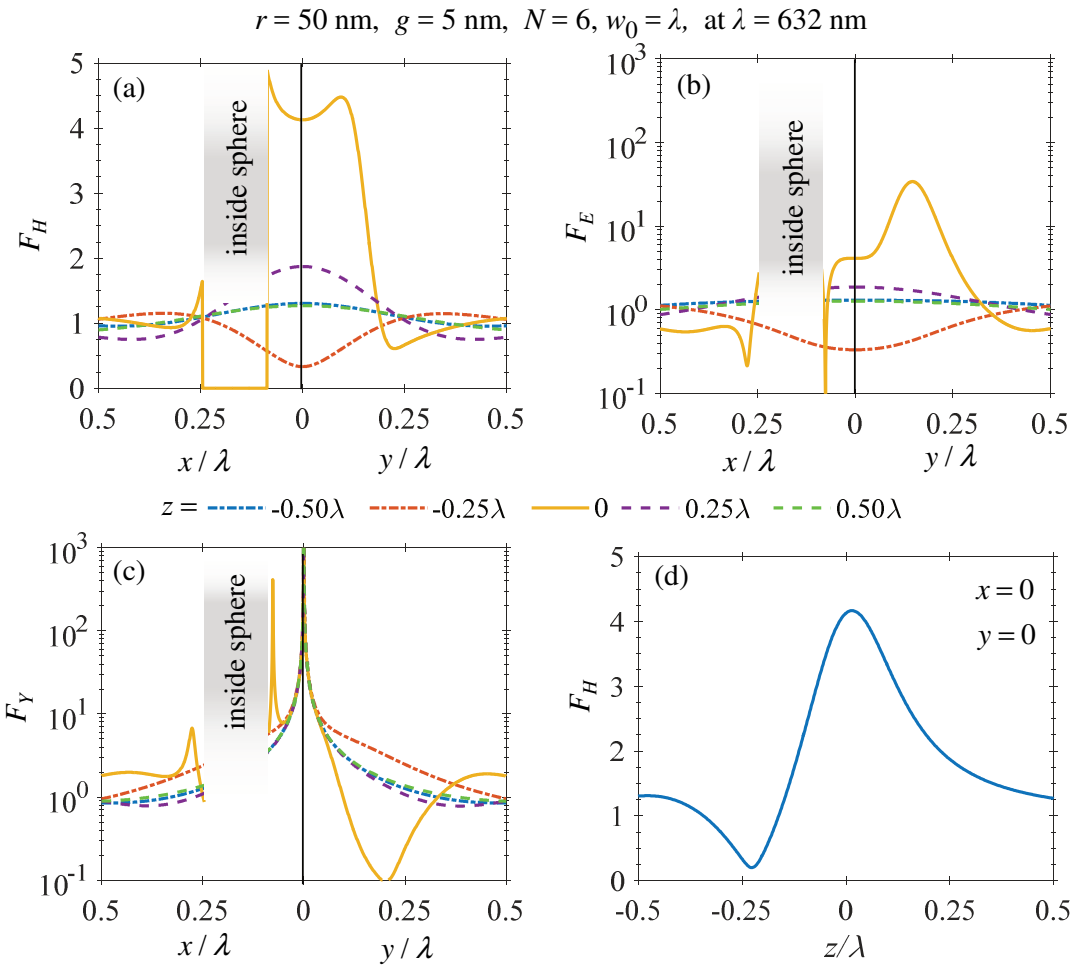

Fig. 8.8 (a) Magnetic and (b) electric field enhancement (F_H and F_E). (c) Normalized absolute local field admittance F_Y versus x and y at various z planes. (d) The magnetic field enhancement on z axis showing destructive interference at $z \approx -0.25\lambda$ and a maximum at $z/\lambda \approx 0$.

Sec. 8.6 Effect of Cluster Defects and Beam Alignment on Figures of Merit

In the Sec. 8.5, we have shown that the normalized absolute local field admittance F_Y around the center of the nano cluster excited by the APB is ideally very large alongside a magnetic field enhancement F_H around 4.2. In addition to an increase of F_H due to the nano cluster, stronger incident magnetic field is also achieved with tighter APBs. However, it is supposable that the perfect alignment of the beam axis with the cluster axis and also the ideal symmetry of the circular cluster may not be easily achieved in practical applications. In this section, we provide a short assessment of the sensitivity of advantages of the APB illumination obtained with the proposed setup in Fig. 8.1 with respect to some defect scenarios.

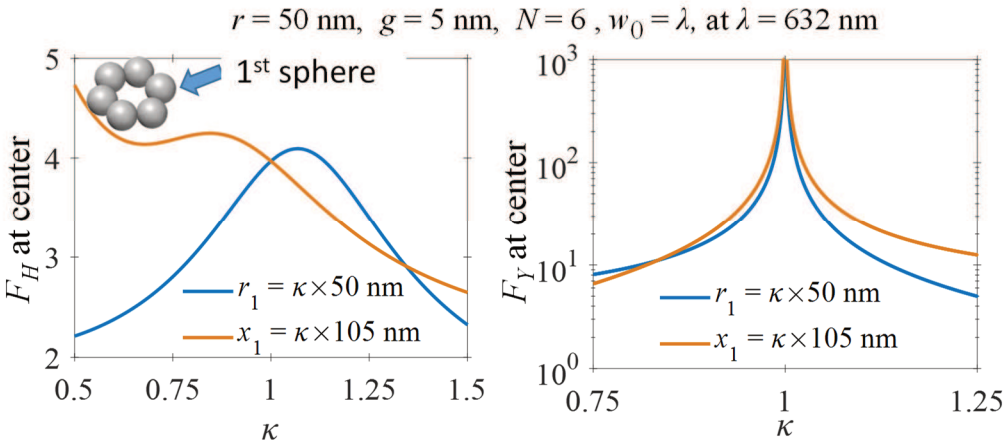

Fig. 8.9 F_H and F_Y at the origin, i.e., center of the cluster, versus two defect scenarios, either (i) only the radius of 1st sphere in the cluster, or (ii) only the position of the 1st sphere in the cluster is scaled by a factor κ with respect to the ideally symmetric cluster. The reference nanosphere radius is set to 50 nm and the reference distance of the nanospheres from the origin is equal to 105 nm.

We investigate two possible defect scenarios of nano clusters where the nanosphere on the +*x* axis (1st sphere) (i) has a different radius than the rest of the nanospheres, and (ii) is

displaced along the *x* axis. To examine the effect of these defects in the nano cluster on its figures of merits, the radius and position of the 1st nanosphere in the regular symmetric cluster are, respectively, scaled by a coefficient κ, namely equal to $r_1 = \kappa(50\,\text{nm})$ and $x_1 = \kappa(105\,\text{nm})$, respectively. It is observed in Fig. 8.9 that by scaling the 1st nanosphere's radius with $\kappa = 0.9$ to $\kappa = 1.25$, one still has a magnetic field enhancement F_H at the cluster center larger than 90% of its nominal value with $\kappa = 1$. In addition, the magnetic field enhancement F_H increases as the nanosphere is placed closer the cluster center. In contrast to the magnetic field enhancement, the magnetic to electric field ratio F_Y at the cluster center

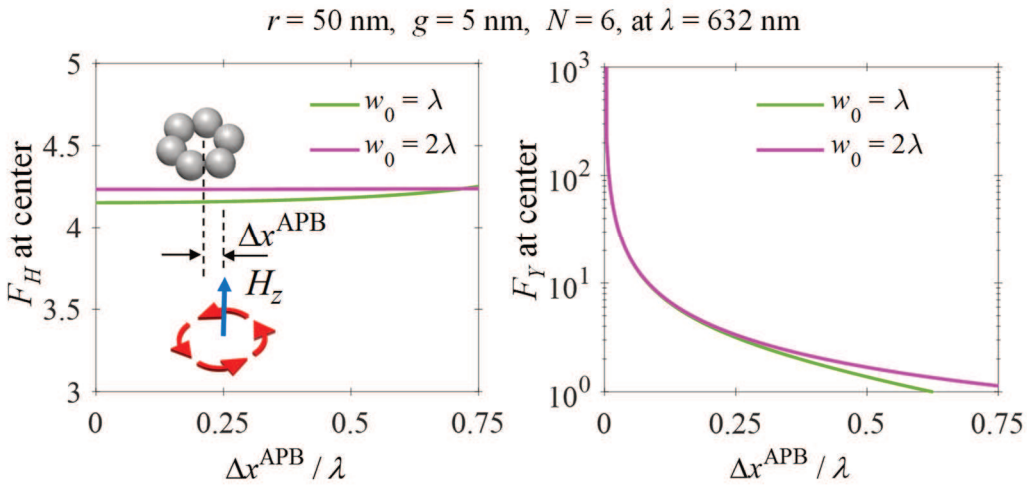

Fig. 8.10 Effect of beam axis displacement from the center of the cluster Δx^{APB} on the magnetic field enhancement F_H (left) and the normalized absolute local field admittance F_Y (right) at the cluster center. It is shown that independently of the beam parameter w_0 the field enhancement is resilient to the beam alignment whereas the normalized absolute local field admittance is highly sensitive, and remains larger than 10 at the cluster center for $0 \le \Delta x^{\text{APB}} < 0.08\lambda$.

shows a very strong dependence on the physical defects in the cluster. We recall that in an ideal symmetric setting $F_Y = \infty$ when $\kappa = 1$. However even 10% variation in the radius or the position of the 1st sphere can lead to a decrease to $F_Y = 15$ due to the loss of the radial symmetry in the cluster-APB setup. For variations within $0.83 < \kappa < 1.13$ one still has $F_Y >$ 10.

Next, we plot in Fig. 8.10, the magnetic field enhancement F_H and normalized magnetic to electric field ratio F_Y at the cluster center versus the *displacement* Δx^{APB} of the APB beam axis along the +*x* direction from the center of the circular nano cluster. While the magnetic field enhancement F_H is not strongly affected by the offset of the beam axis, the normalized local admittance F_Y drops significantly. However, for small displacements within $0 \le \Delta x^{\mathrm{ABP}} / \lambda < 0.08$ one still has $F_Y >$ 10 at the cluster center, since ideally one has $F_Y = \infty$ there. Recalling that the spatial extent of the APB depends on the beam parameter w_0, in Fig. 8.10 we report the figures of merit for two different values w_0. We stress that different choices of the beam parameter do not create a significant difference on the figures of merit when it comes to the effects of beam's misalignment Δx^{APB}. The strong dependence of F_Y on the relative position of the beam axis with respect to the nanoprobe center indeed may have a role in high resolution in scanning probe microscopy.

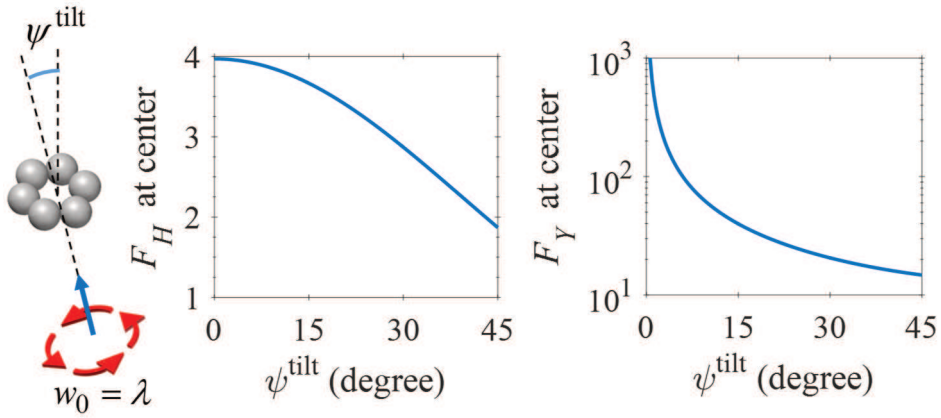

Fig. 8.11 Effect of beam tilt angle ψ^{tilt} between the beam axis and the normal of the cluster plane on the magnetic field enhancement F_H (left) and the normalized absolute local field admittance F_Y (right) evaluated at the cluster center.

The final possible scenario under examination is regarding the tilt of beam axis. For illustrating the impacts of such a problem, in Fig. 8.11 we report the magnetic field enhancement F_H and the normalized magnetic to electric field ratio F_Y evaluated at the cluster center versus the beam tilt angle ψ^{tilt} between the beam axis and the normal of the cluster plane. The beam tilt up to 15˚ results in a 10% decrease in F_H and it drops below 2 at a tilt angle of 45˚. Similarly, the normalized local field admittance F_Y, which is ideally infinite (out of the limits of the plot) when the beam is not tilted, decreases down to 100 at a tilt angle of 6˚. F_Y decreases down to 15 at the maximum reported tilt angle of 45˚. Note that F_Y is rather sensitive to tilt angle and this parameter should be kept in check during the efforts of maximizing F_Y. Here we also remind that the vertical displacement of the focus plane with respect to the cluster plane is inherently studied in Fig. 8.7, as the vertical displacement of focus is equivalent to changing the beam parameter. As a result, we conclude that the magnetic field enhancement F_H is insensitive to the vertical displacement of the

focus, whereas F_Y is ideally infinite as long as the beam axis coincides with the center of the cluster.

Sec. 8.7 Conclusion

A circular cluster of nanoparticles excited by an azimuthally polarized beam (APB) is utilized as a magnetic nanoprobe for enhancing the magnetic near-field and the spatial resolution of the enhanced magnetic field in a magnetic-dominant region. In the same region a huge local field admittance is achieved, much larger than that of a plane wave, meaning that the magnetic to electric field ratio is very high. We demonstrate that large magnetic field enhancement is robust to small physical defects in the nano cluster and to small misalignments of the APB with respect to the cluster's center, though the latter decreases the local field admittance. In this chapter circular clusters of nanospheres as magnetic nanoprobes excited by APBs have been studied as an example, but similar conclusions are expected to hold for other magnetic nanoprobes with symmetry properties. Moreover, any required improvement of the model regarding specific fabrication methods and experimental setups (for example the presence of a substrate) should be accounted for in future studies. We remind that different types of magnetic nanoprobes such as silicon spheres or clusters made of different geometries of nanoparticles may provide advantages in experimental setups, tuning wavelength of operation and controlling the magnetic field enhancement level and the area of the magnetic-dominant region. The enhanced magnetic fields in magnetic-dominant regions with resolutions beyond the diffraction limit obtained using magnetic nanoprobes may prove useful in optical spectroscopy and microscopy applications based on detection of magnetic field interacting with matter.

Acknowledgment

This chapter is reproduced based on the material in [C. Guclu, M. Veysi, F. Capolino, "Photoinduced Magnetic Nanoprobe Excited by an Azimuthally Polarized Vector Beam," *ACS Photonics*, vol. 3, pp. 2049-2058, 2016], © 2016 American Chemical Society. The authors acknowledge support by the W. M. Keck Foundation (USA).

Appendix A - Power in the Azimuthally Polarized Beam under Paraxial Approximation

The power P carried by the beam in the + z direction, in the figure of longitudinal magnetic field defined in (8.9) is given by

$$\begin{aligned} P &= \frac{1}{2}\int_0^{2\pi}\int_0^{\infty} \mathrm{Re}\left\{-E_\varphi^{\mathrm{APB}}\left(H_\rho^{\mathrm{APB}}\right)^*\right\}_{z=0} \rho d\rho d\varphi \\ &= \frac{|V|^2}{2\eta}\left(1-\frac{1}{2\pi^2\left(\frac{w_0}{\lambda}\right)^2}\right) \end{aligned} \tag{8.25}$$

whose derivation is shown in [32]. Therefore h_z in (8.9), evaluated at z = 0 is

$$h_z = \frac{1}{\left(\frac{w_0}{\lambda}\right)^2}\frac{\frac{2}{\sqrt{\pi^3}}}{\sqrt{1-\frac{1}{2\pi^2\left(\frac{w_0}{\lambda}\right)^2}}} \tag{8.26}$$

and it is a function of only w_0 / λ.

References

[1] L. D. Landau, E. M. Lifshitz, and L. P. Pitaevskii, *Electrodynamics of Continuous Media*. Elsevier, 1984.

[2] J. B. Pendry, A. J. Holden, D. J. Robbins, and W. J. Stewart, "Magnetism from conductors and enhanced nonlinear phenomena," *IEEE Trans. Microw. Theory Tech.*, vol. 47, no. 11, pp. 2075–2084, 1999.

[3] M. S. Wheeler, J. S. Aitchison, and M. Mojahedi, "Three-dimensional array of dielectric spheres with an isotropic negative permeability at infrared frequencies," *Phys. Rev. B*, vol. 72, no. 19, p. 193103, Nov. 2005.

[4] A. Alù and N. Engheta, "Polarizabilities and effective parameters for collections of spherical nanoparticles formed by pairs of concentric double-negative, single-negative, and/or double-positive metamaterial layers," *J. Appl. Phys.*, vol. 97, no. 9, p. 94310, May 2005.

[5] A. Alù, A. Salandrino, and N. Engheta, "Negative effective permeability and left-handed materials at optical frequencies," *Opt. Express*, vol. 14, no. 4, p. 1557, 2006.

[6] S. Campione, S. Lannebère, A. Aradian, M. Albani, and F. Capolino, "Complex modes and artificial magnetism in three-dimensional periodic arrays of titanium dioxide microspheres at millimeter waves," *J. Opt. Soc. Am. B*, vol. 29, no. 7, pp. 1697–1706, Jul. 2012.

[7] S. Lannebère, S. Campione, A. Aradian, M. Albani, and F. Capolino, "Artificial magnetism at terahertz frequencies from three-dimensional lattices of TiO_2 microspheres accounting for spatial dispersion and magnetoelectric coupling," *J. Opt. Soc. Am. B*, vol. 31, no. 5, p. 1078, May 2014.

[8] C. R. Simovski and S. A. Tretyakov, "Model of isotropic resonant magnetism in the visible range based on core-shell clusters," *Phys. Rev. B*, vol. 79, no. 4, p. 45111, Jan. 2009.

[9] A. Vallecchi, M. Albani, and F. Capolino, "Collective electric and magnetic plasmonic resonances in spherical nanoclusters," *Opt. Express*, vol. 19, no. 3, pp. 2754–2772, Jan. 2011.

[10] A. Vallecchi, M. Albani, and F. Capolino, "Effect of irregularities of nanosatellites position and size on collective electric and magnetic plasmonic resonances in spherical nanoclusters," *Opt. Express*, vol. 21, no. 6, pp. 7667–7685, Mar. 2013.

[11] S. N. Sheikholeslami, A. García-Etxarri, and J. A. Dionne, "Controlling the Interplay of Electric and Magnetic Modes via Fano-like Plasmon Resonances," *Nano Lett.*, vol. 11, no. 9, pp. 3927–3934, Sep. 2011.

[12] B. Luk'yanchuk *et al.*, "The Fano resonance in plasmonic nanostructures and metamaterials," *Nat. Mater.*, vol. 9, no. 9, pp. 707–715, Sep. 2010.

[13] M. Hentschel, M. Saliba, R. Vogelgesang, H. Giessen, A. P. Alivisatos, and N. Liu, "Transition from Isolated to Collective Modes in Plasmonic Oligomers," *Nano Lett.*, vol. 10, no. 7, pp. 2721–2726, Jul. 2010.

[14] N. Liu *et al.*, "Manipulating Magnetic Plasmon Propagation in Metallic Nanocluster Networks," *ACS Nano*, vol. 6, no. 6, pp. 5482–5488, Jun. 2012.

[15] S. Campione, C. Guclu, R. Ragan, and F. Capolino, "Enhanced Magnetic and Electric Fields via Fano Resonances in Metasurfaces of Circular Clusters of Plasmonic Nanoparticles," *ACS Photonics*, vol. 1, no. 3, pp. 254–260, Mar. 2014.

[16] C. Guclu, V. A. Tamma, H. K. Wickramasinghe, and F. Capolino, "Photoinduced magnetic force between nanostructures," *Phys. Rev. B*, vol. 92, no. 23, p. 235111, Dec. 2015.

[17] J. Jahng *et al.*, "Linear and Nonlinear Optical Spectroscopy at the Nanoscale with Photoinduced Force Microscopy," *Acc. Chem. Res.*, vol. 48, no. 10, pp. 2671–2679, Oct. 2015.

[18] K. Youngworth and T. Brown, "Focusing of high numerical aperture cylindrical-vector beams," *Opt. Express*, vol. 7, no. 2, pp. 77–87, Jul. 2000.

[19] D. P. Biss and T. G. Brown, "Cylindrical vector beam focusing through a dielectric interface," *Opt. Express*, vol. 9, no. 10, p. 490, Nov. 2001.

[20] Q. Zhan and J. Leger, "Focus shaping using cylindrical vector beams," *Opt. Express*, vol. 10, no. 7, p. 324, Apr. 2002.

[21] Q. Zhan, "Cylindrical vector beams: from mathematical concepts to applications," *Adv. Opt. Photonics*, vol. 1, no. 1, p. 1, Jan. 2009.

[22] P. Woźniak, P. Banzer, and G. Leuchs, "Selective switching of individual multipole resonances in single dielectric nanoparticles," *Laser Photonics Rev.*, vol. 9, no. 2, pp. 231–240, Mar. 2015.

[23] M. Neugebauer, P. Woźniak, A. Bag, G. Leuchs, and P. Banzer, "Polarization-controlled directional scattering for nanoscopic position sensing," *Nat. Commun.*, vol. 7, p. 11286, Apr. 2016.

[24] S. Quabis, R. Dorn, M. Eberler, O. Glöckl, and G. Leuchs, "Focusing light to a tighter spot," *Opt. Commun.*, vol. 179, no. 1–6, pp. 1–7, May 2000.

[25] L. Novotny, M. R. Beversluis, K. S. Youngworth, and T. G. Brown, "Longitudinal Field Modes Probed by Single Molecules," *Phys. Rev. Lett.*, vol. 86, no. 23, pp. 5251–5254, Jun. 2001.

[26] N. Davidson and N. Bokor, "High-numerical-aperture focusing of radially polarized doughnut beams with a parabolic mirror and a flat diffractive lens," *Opt. Lett.*, vol. 29, no. 12, p. 1318, Jun. 2004.

[27] R. Dorn, S. Quabis, and G. Leuchs, "Sharper Focus for a Radially Polarized Light Beam," *Phys. Rev. Lett.*, vol. 91, no. 23, p. 233901, Dec. 2003.

[28] E. Y. S. Yew and C. J. R. Sheppard, "Tight focusing of radially polarized Gaussian and Bessel-Gauss beams," *Opt. Lett.*, vol. 32, no. 23, p. 3417, Dec. 2007.

[29] J. R. Zurita-Sánchez and L. Novotny, "Multipolar interband absorption in a semiconductor quantum dot. II. Magnetic dipole enhancement," *J. Opt. Soc. Am. B*, vol. 19, no. 11, p. 2722, Nov. 2002.

[30] M. Veysi, C. Guclu, and F. Capolino, "Vortex beams with strong longitudinally polarized magnetic field and their generation by using metasurfaces," *J. Opt. Soc. Am. B*, vol. 32, no. 2, pp. 345–354, Feb. 2015.

[31] M. Veysi, C. Guclu, and F. Capolino, "Large magnetic to electric field contrast in azimuthally polarized vortex beams generated by a metasurface (Presentation Recording)," 2015, p. 954408.

[32] M. Veysi, C. Guclu, and F. Capolino, "Focused Azimuthally Polarized Vector Beam and Spatial Magnetic Resolution below the Diffraction Limit," *ArXiv160300038 Phys.*, Feb. 2016.

[33] M. Kasperczyk, S. Person, D. Ananias, L. D. Carlos, and L. Novotny, "Excitation of Magnetic Dipole Transitions at Optical Frequencies," *Phys. Rev. Lett.*, vol. 114, no. 16, p. 163903, Apr. 2015.

[34] L. Allen, M. W. Beijersbergen, R. J. C. Spreeuw, and J. P. Woerdman, "Orbital angular momentum of light and the transformation of Laguerre-Gaussian laser modes," *Phys. Rev. A*, vol. 45, no. 11, pp. 8185–8189, Jun. 1992.

[35] F. Capolino, *Metamaterials Handbook*. CRC Press, 2009.

[36] S. Campione and F. Capolino, "Ewald method for 3D periodic dyadic Green's functions and complex modes in composite materials made of spherical particles under the dual dipole approximation," *Radio Sci.*, vol. 47, no. 6, p. RS005031, 2012.

[37] E. D. Palik, *Handbook of Optical Constants of Solids, Volumes I, II, and III: Subject Index and Contributor Index*. Elsevier Science & Tech, 1985.

[38] I. El-Kady, M. M. Sigalas, R. Biswas, K. M. Ho, and C. M. Soukoulis, "Metallic photonic crystals at optical wavelengths," *Phys. Rev. B*, vol. 62, no. 23, pp. 15299–15302, Dec. 2000.